Dynamic Magnetic Effects in Amorphous Microwires for Sensors and Coding Applications

by

Serghei Sandacci

Thesis submitted to the University of Plymouth

in partial fulfilment for the degree of

Doctor of Philosophy

30 September 2004

ABSTRACT

DYNAMIC MAGNETIC EFFECTS IN AMORPHOUS MICROWIRES FOR SENSORS AND CODING APPLICATIONS

This work is devoted to the study of the dynamic properties of magnetic amorphous wires, in particular, glass-coated microwires, which have small diameters (5-30 microns), outstanding soft magnetic behaviour with a high permeability and low coercivity, yet, possess a well-defined magnetic structure.

First part of my PhD research has been devoted to the investigation of a bi-stable magnetisation reversal in glass-coated amorphous microwires. In contrast to traditional approaches, where characteristics of the magnetisation reversal are analysed as a consequence of the eddy current effect, I have applied stochastic methods for modelling the remagnetisation reversal in the microwires with axial anisotropy. While the eddy current approach, widely discussed in literature, was based on the single domain model, proposed stochastic approach takes into account a multi-domain state of studied samples. A modified stochastic Néel-Brown model of the magnetisation reversal has been proposed enabling the explanation of number of characteristic parameters of the microwires with axial magnetisation. Such important parameters of Barkhausen discontinuity as a mean switching field and a standard deviation of the switching field distribution have been investigated experimentally for understanding the influence of extrinsic factors such as a slew rate of the alternating magnetic field on applications operation.

A deep understanding of the remagnetisation process in amorphous the microwires with axial anisotropy was successfully applied in development of a new type of the remote magnetic interrogation system. My reading system allows the large Barkhausen jump to be detected without actual contact between the magnetic microwire and the magnetic field detector. Experiments show that the detection will be possible at a distance of approximately 100-150 mm from the detecting sensor. A very low cost and easily repetitive amorphous microwires with axial anisotropy are incontrovertibly best materials for Electronic Article Surveillance (EAS) applications.

During the study of the microwires with axial anisotropy and development of the application based on them, I took part in the investigation of unusual coding methods of the amorphous microwires using a localised laser annealing treatment. This treatment produces a multi-pulse code within the wire and therefore adds to the information contained within the wire, improving reliability and security. I developed and used a magnetic interrogation system allowing an accurate and reliable test and analysis of the studied samples.

The second part of my PhD research has included investigations of microwires with circumferential and helical anisotropies. The main interest in these materials is due to their applications for high-performance magnetic and stress sensors. Within this research project, the microwires with circumferential/helical anisotropy have been studied in a broad range of frequencies. A number of dynamic effects have been experimentally obtained and analysed. In particular, a detailed investigation of dynamic circular hysteresis (10kHz-300kHz) has been carried out allowing explanation of different behaviour of the materials with circumferential/helical anisotropy at different frequencies. The experimental curves are proposed to be analysed in terms of field dependence of characteristic permeabilities: domain wall displacements (reversible and irreversible) and magnetisation rotation. It was established that these permeabilities have different field behaviour. That explains different MI patterns at relatively low frequencies (less than a few MHz) and relatively high frequencies (more than 10 MHz).

Further, some special features of the Magneto-Impedance effect in the microwires with a circumferential anisotropy such as off-diagonal impedance and microwave impedance have been considered. In this research, the former presents a considerable interest for development of linear magnetic sensors and the latter can find application in tuneable microwave materials and devices. As a result of this study several types of linear, bi-directional MI sensors were developed. I also developed new MI sensing approaches (such as off-diagonal response) and a new high performance detection technique allowing us to improve sensitivity, bandwidth, and linearity at low cost and simple construction..

The last part of the PhD research has been devoted to an investigation of the stress-impedance in the ultra high-frequency (UHF) band (300MHz-3 GHz). Based on the experimental investigation, a new type of a stress-sensitive composite material is proposed. The microwave effective permittivity of such material depends on mechanical stresses. These composite materials opens up new possibilities for remote monitoring of stress with the use of microwave "free-space" techniques. This kind of composite material can be characterised as a "sensing medium", which images the mechanical stress distribution inside construction or on its surface.

AUTHOR'S DECLARATION

At no time during the registration for the degree of Doctor of Philosophy has author been registered for any other University awards.

This study was supported with the aim of a studentship from OSR/EPSRC award scheme. A programme of advanced study was undertaken including a list of guided reading and advanced thematic seminars in the measuring techniques and magnetic sensors.

The work contained in this thesis was partially presented at several international conferences and thematic schools. Eleven papers have been submitted/published in research journals. Copies of the most essential publications are enclosed in the appendix of this thesis.

Total number of words in this thesis is 35652.

Signature: 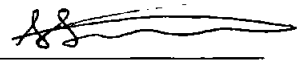

Date: 30.09.2004

ACKNOWLEDGEMENTS

I would like to express my sincerest thanks to all people, who I worked with in the last three years, especial,

To my first supervisor Prof. L. V. Panina for giving me an opportunity to work on this challenging topic and for providing continuous constructive supervision and expert guidance, support and steadfast encouragement throughout the study, and without whom this thesis would not have been possible.

To my second supervisor Prof. D. J. Mapps for useful discussions and continuous help during my study at the University of Plymouth

To Dr. Sasha Grigorenko who helped me finding the right directions in my research in the early stages and offered extension help, especially during my first year at the University.

To Dr. Dmitriy Makhnovskiy for useful discussions and suggestions regarding some theoretical aspects of my research.

To Mr. Nick Fry, Mr. Phil Brown and Mr. Stewart Warner for their friendship and technical assistance.

On a more personal note, I would like to thank my family and fiancée Victoria. Without their love, support and constant encouragement this work would not have been possible.

Thank you all for your patience and support. I greatly appreciate you help.

CONTENT

List of Figures

Chapter 2

Chapter 3

Chapter 4

Chapter 5

Chapter 6

Chapter 7

Chapter 8

Appendix A

List of Tables

Chapter 3

Chapter 4

Chapter 7

Chapter 1. Introduction

Amorphous metallic materials present a considerable interest for fundamental research and a wide range of applications due to their unique and favourable association of mechanical, electrical, magnetic and chemical properties related to the absence of long-range order. The use of preparation methods that allow rapid condensation of atoms or rapid solidification of liquid metallic melts in order to avoid crystallization is necessary to achieve the energetically metastable amorphous state. Presently known amorphous metallic materials have been obtained in the form of thin films [1], ribbons [2], powders [3], wires [4] and very recently bulk materials with dimensions in the range of millimetres [5]. Among those materials, amorphous metallic wires are of a special interest emerging from their degree of symmetry. A range of applications includes high performance resistors, inductive elements, radio and microwave frequency shields; stress, temperature and pressure sensors. This work is devoted to properties and applications of magnetic amorphous wires, in particular, glass-coated microwires [6,7], which have small diameters (5-30 microns), outstanding soft magnetic behaviour with a high permeability and low coercivity, yet, possess a well-defined magnetic structure.

Depending on the alloy composition, technological regime and post-production treatment, a wide spectrum of magnetic characteristics can be obtained, which makes magnetic microwires suitable for a large number of applications, especially in the field of electronic devices and sensors. Presently, amorphous magnetic microwires are used in such applications as pulse generators [8], position and displacement sensors [9], biomedical sensors [10], magnetic and stress sensors [11]. Driven by application demands, the magnetic properties of microwires have been extensively studied and there is voluminous literature on the subject (see, for example, reviews [12], [13] and references therein). However, a number of physical effects require further investigations and some new effects can be predicted. The work in this direction is foreseen to generate new exciting ideas and applications. For example, a completely new problem of magnetic behaviour related to 'modulated' wires, where wires can have imperfections introduced to change their properties. In this work, I investigate dynamic magnetisation processes in two kinds of microwires, characterised by bistable or linear static magnetisation curves, and develop such applications as magnetic labels utilising bistable microwires, high performance magnetic sensors and stress-sensitive

microwave materials based on magneto-impedance effect in wires with a circumferential anisotropy.

The work is organised as follows. In Chapter 2, some general physical principles of ferromagnetism will be discussed. The parameters characterising reversible and irreversible processes in the ferromagnetic materials will be introduced since they are playing key role in the magnetisation process. Several models of magnetisation reversal in amorphous wires with uniaxial anisotropy will be considered, including: classical Stoner-Wohlfarth model, expanded model of rotational magnetisation reversal in the presence of transverse magnetic field and quantitative model of magnetisation reversal in the presence of various stresses. The later models are very useful for further analysis of rotational processes in magnetic materials under the effects of external mechanical stresses and nevertheless difficult to find elsewhere.

In Chapter 3, I will consider the basic technology of microwire production with relation to their geometry, microstructure (amorphous or microcrystalline), and residual stress distribution. I will also briefly discuss mechanical, electrical and general magnetic properties.

In Chapter 4, detailed analysis of amorphous microwires with an axial anisotropy will be given. In the case of microwires with axial anisotropy the magnetisation reversal takes place by a large Barkhausen discontinuity. This rapid remagnetisation process, which generates a sharp voltage pulse, is useful for such applications as magnetic encoding, magnetic labelling and security sensors. Growing interest in the low-cost magnetic labelling applications utilising amorphous microwires motivate the detailed investigation of the Fe-based amorphous microwires.

In Section 4.2, the investigation of the dynamic properties of the amorphous wires will be represented within the framework of the stochastic theory of thermal activation. This new approach of stochastic domain wall activation over pinning barrier is considered for the first time in this thesis. Such important parameters of Barkhausen discontinuity as a mean switching field and standard deviation of the switching field distribution have been investigated experimentally for understanding the influence of extrinsic factors such as slew rate of the alternating magnetic field on applications operation. A modified Néel-Brown model of the magnetisation reversal has been proposed enabling the explanation of number of characteristic parameters of the microwires with axial magnetisation.

Further, in Section 4.3 a new selective treatment method for writing continuous magnetic "bar-code" on the microwires by using argon laser irradiation will be proposed.

Local annealing by an argon laser has resulted in the formation of weakly interacting heterogeneous structures with different magnetic properties. Such wires possessing the weakly interacting multi-domain structure with different magnetisation may be of great interest for magnetic coding applications as a data storage element.

In Section 4.4, a low-frequency identification system utilizing microwires with an axial magnetisation will be presented. The idea of utilizing amorphous microwires exhibiting very rapid change in magnetisation as magnetic labels has been known for a number of years [14-17]. This kind of labelling has potential uses in anti-theft applications, counting objects and security identification systems. One method of labelling makes use of counting wires having the same magnetic switching characteristic. Here, the object with attached magnetic label is passed through a detection system, which triggers a counting event. Another group of magnetic labels can be made from wires with different magnetic characteristics, in particular, different switching fields. For this a more sophisticated detection system is required to identify the different magnetic labels attached to various types of objects. Until now, such a detection system has only been developed in prototype form. My present work involves the development of the existing technology to create a new remote sensing system. This system will allow the large Barkhausen jump to be detected without actual contact between the magnetic label and the magnetic field detector. My recent research suggests that detection will be possible at distances of approximately 100-150 mm from the detecting sensor. Very low cost and easily repetitive amorphous microwires with axial anisotropy are incontrovertibly best materials for Electronic Article Surveillance (EAS) applications.

In Chapters 5-8, I analyse the magnetisation dynamics including the magnetoimpedance (MI) effect in microwires with circumferential and helical anisotropies and developing few sensing applications. Since the discovery of the MI effect in 1994 [18], the interest in amorphous microwires of Co-based compositions with circumferential anisotropy has increased considerably. The recent works of L. Panina [18-22], D. Makhnovskiy [20-22] and other authors have established the theoretical models quantitatively describing the MI effect in wires with different types of anisotropy. However, experimental results were lacking to support this theory. For example, the data on dynamic circular hysteresis obtained in this work were needed to understand different impedance behaviour at relatively low and moderate frequencies. I also investigated the MI effect at very high frequencies up to a few

GHz, providing that in this frequency range the impedance change is governed by the dc magnetisation and can exhibit so-called 'valve'-like behaviour.

Chapter 5 is devoted to the detailed investigation of dynamic circular hysteresis (10kHz-300kHz). The experimental curves are proposed to analyse in terms of a field dependence of characteristic permeabilities describing domain wall displacements (reversible and irreversible) and magnetisation rotation. I have established that these permeabilities have completely different field behaviour, which explains different MI patterns at relatively low frequencies (less than a few MHz) and relatively high frequencies (more than 10 MHz).

In Chapter 6 I will consider some special features of the MI effect in microwires with a circumferential anisotropy such as off-diagonal impedance and microwave impedance. The former presents a considerable interest for developing linear magnetic sensors and the latter can found application in tuneable microwave materials and devices. I will start with an introduction into MI effect in terms of the surface impedance tensor for wires with a circumferential anisotropy, when the skin effect is essential and the permeability is due to a coherent magnetisation rotation described by the linearised Landau-Lifshitz equation. The permeability will be considered in Section 6.2. Giving background research on MI, I will proceed with the comparative study of the diagonal and off-diagonal impedances (Section 6.3). Finally, in Section 6.4, I will study the MI effect at GHz frequencies, demonstrating that the field remains very high (up to 50% per few Oe) but only for low magnetic fields less then the anisotropy field.

Chapter 7 will be devoted to MI sensors. Along with the analysis of previous MI sensor designs [23, 24], I will present several types of linear, bi-directional MI sensors developed in this work. I have proposed new MI sensing approaches (as off-diagonal response) and a new high performance detection technique allowing us to improve sensitivity, bandwidth, and linearity, at low cost and simple construction.

The last and most exciting part (Chapter 8) will represent a completely new research of the effect of stress on microwire impedance. On the basis of the carried out experimental investigation, a new type of stress-sensitive composite material is proposed. The microwave effective permittivity of such composite material depends on the applied mechanical stresses. This composite material opens up new possibilities for remote monitoring of stress with the use of microwave "free-space" techniques. This kind of composite material can be

characterised as a "sensing medium", which images the mechanical stress distribution inside a construction or on its surface.

References

[1] R. W. Cahn *"Background to rapid solidification processing"* Liebermann H. H. (ed.) Rapidly Solidified Alloys, Materials Engineering Series. Dekker, Parsippany, NJ, (1993) Vol. 3, pp. 1-15.

[2] R. Boll, H. R. Hilizinger, H. Warlimont *"Magnetic material properties and applications of metallic glasses"* Hasegawa R. (ed.) The Magnetic, Chemical and Structural Properties of Glassy Metallic Alloys, CRC Press, Boca Raton, FL, (1983) pp. 183-200.

[3] M. Yagi, I. Endo, I. Otsuka, H. Yamamoto, R. Okuno, H Kashimoto, A. Shintari *"Magnetic properties of Fe-based amorphous powder cores produced by a hot-pressing method"* J.Magn.Mater. (2000) Vol. 215-216, pp. 284-7.

[4] I. Ogasawara, S. Ueno *"Preparation and properties of amorphous wires"* IEEE Trans. Magn. (1995) Vol. 31, pp. 1219-123.

[5] A. Inoue *"Stabilization of metallic super-cooled liquid and bulk amorphous alloys"* Acta Mater. (2000) Vol. 48. pp. 279-306.

[6] S. Baranov, V. Larin, A.Torcunov *"Cast microwire in glass insulation with amorphous metal core"* Amorphous soft magnetic alloys and its application in secondary power supply, (1990) 110 - 113.

[7] J. Lluma, M. Vazquez, J. Hernandez, J. Ruiz, J. Garcia-Beneytez, A. Zhukov, X. Zhang and J. Tejada *"Low temperature magnetization and resistivity measurements in co based soft magnetic microwires"* JMMM, (1999) Vol. 196-197, 821-823.

[8] K. Mohri *"Review on Recent Advances in the Field of Amorphous-Metal Sensors and Transducers"* IEEE Trans. Magn. (1984) Vol. 20, 942

[9] E. Hristoforou and D. Niarchos *"Mechanical Sensors Based on Re-Entrant Flux Reversal"* IEEE Trans. Magn (1992) Vol. 28, 2190

[10] K. Mohri *"Detections of Secondary Current and Toque of Induction-Motors using Amorphous Micro Field Sensors"* J. Magn. Japan (1986) Vol. 10, 371

[11] K. Mohri, F. Humphrey, J. Yamasaki *"Large Barkhausen Effect and Mateucci Effect in Amorphous Magnetosstristive Wires for Pulse Generator Elements"* IEEE Trans. Magn (1984) Vol. 20, 1409

[12] K. Mohri, H. Takamido "*Large Barkhausen effect of 6.3% SiFe single crystal wire*" IEEE Trans. Magn (1990) Vol. 26, 1783

[13] G. Rauscher, C. Radeloff "*Article surveillance magnetic markers*" IEEE Trans. Magn (1991) Vol. 27, 5238

[14] F. Humphrey "*Article surveillance magnetic marker having an hysteresis loop with large Barkhausen discontinuities*" USA Patent 4660025 (1984)

[15] L. Panina and K. Mohri "*Mechanism of the magneto-impedance effect in negative magnetostrictive amorphous wires*" J. Magn. Soc. of Japan, (1994) Vol. 18, 245-249

[16] L. Panina and K. Mohri "*Magneto-impedance effect in amorphous wires*" Appl. Phys. Lett., (1994) Vol. 65, 1189-1191

[17] D. Makhnovskiy, L. Panina, and D. Mapps "*Field-dependent surface impedance tensor in amorphous wires with two types of magnetic anisotropy: helical and circumferential*" Phys. Rev. B, (2001) Vol. 63, 144424

[18] L. Panina, D. Makhnovskiy, D. Mapps, K. Mohri, and P. Nikitin "*Effect of frequency and dc current on ac-biased asymmetrical magneto-impedance in wires*" Materials Science Forum, (2001) Vol. 373/376, 741

[19] D. Makhnovskiy, L. Panina, and D. Mapps "*Measurement of field-dependent surface impedance tensor in amorphous wires with circumferential anisotropy*" J. Appl. Phys., (2000) Vol. 87, 4804

[20] Y. Honkura "*Magneto-impedance sensors*" J. Magn. Magn. Mater. (2002) Vol. 249, 375

[21] K. Mohri, T. Uchiyama and L. Panina "*Recent Advances of Micro Magnetic Sensors and Sensing Application*" Sens. Act. A (1997) Vol. 59, 1

Chapter 2. Background research

2.1 Introduction to magnetic materials

This section reviews some physical principles of ferromagnetism, in order to provide a background for understanding magnetisation processes in the studied materials.

Generally speaking, every material, which is subjected to a *magnetic field*, $\boldsymbol{H}$ acquires a magnetic moment. The dipole moment per unit volume is defined as the *magnetisation*, and will be denoted here by the vector $\boldsymbol{M}$. In most materials, $\boldsymbol{M}$ is proportional to the applied field, $\boldsymbol{H}$. The relationship is then written as:

$$\boldsymbol{M} = \chi \boldsymbol{H} \tag{2.1}$$

Where χ is called the *magnetic susceptibility* of the material. The *magnetic flux density* $\boldsymbol{B}$ is given by a linear relationship in terms of $\boldsymbol{H}$ and $\boldsymbol{M}$:

$$\boldsymbol{B} = \mu_0 \boldsymbol{H} + \gamma_B \boldsymbol{M} \tag{2.2}$$

Here γ_B is a parameter introduced by Brown [1] to include different systems of units. In particular, $\gamma_B = 1$ and $\mu_0 = 4\pi \cdot 10^{-7}$ H/m for SI units, while for Gaussian units, $\gamma_B = 4\pi$ and $\mu_0 = 1$. In general in this work, I will use Gaussian units, unless SI units are preferred for the simplification of the required model. If (2.1) is fulfilled, it is also possible to rewrite (2.2) as

$$\boldsymbol{B} = \mu \boldsymbol{H} \tag{2.3}$$

where,

$$\mu = \mu_0 + \gamma_B \chi = \mu_0 \mu_r \tag{2.4}$$

In most materials, the relative magnetic susceptibility $\chi_r = \chi / \mu_0$ is very small (in the range of $10^{-5} - 10^{-3}$), however, in some cases it can be as large as 10^6. The value of χ can take positive and negative values. Sometimes, the relation between $\boldsymbol{M}$ and $\boldsymbol{H}$ is not linear, so that χ depends on the intensity of magnetic field. It is possible to interpret the type of behaviour of χ in terms of the magnetic nature of the material. From this point of view, the various kinds of magnetic materials are classified as follows.

i. Diamagnetism (negative $\chi_r < 0$ of a small magnitude of 10^{-5})

ii. Paramagnetism (positive $\chi_r > 0$ of a magnitude ranging $10^{-5} - 10^{-3}$)

iii. Magneto-ordered materials such as ferro-, ferri- and antiferro- magnetics, characterised by much larger values of χ_r dependent on the external magnetic field.

In the case of ferromagnetism, the atomic spins are aligned parallel to each another because of strong positive interaction acting between the neighbouring spins. Since such magnetisation is produced without the action of any external magnetic field, it is called a spontaneous magnetisation. As the temperature increases, the arrangement of the spins is disturbed by thermal agitation, thus resulting in a temperature dependence of spontaneous magnetisation. Above the Curie point, the susceptibility obeys the Curie-Weiss law [6], which states that $1/\chi$ rises from zero at the Curie point and increases linearly with temperature. Ferromagnetic substances can often have a magnetisation that is much smaller than the saturation value. This can be explained by assuming that the sample of material is actually composed of a number of small regions called domains; within each the local magnetization is saturated. However, the direction of this magnetisation varies in different domains. The same effects are observed in polycrystalline samples, for which the resultant magnetic moment becomes zero by virtue of a random distribution of the local magnetic moments in different granules. The increase of the resultant magnetic moment in the whole sample under the applied action of an applied magnetic field arises from two mechanisms:

1. An increase in the volume of domains, which are favourably oriented with respect to the field at the expense of unfavourably, oriented domains.
2. Rotation of the directions of magnetizations towards the direction of the field.

In weak fields, the resultant magnetization changes mostly due to the domain wall motion, whereas in strong fields it takes place by means of the rotation of magnetic moments. Ferromagnetism is exhibited mostly by metals such as: iron, cobalt, nickel and their alloys.

The alloys may also contain small amount of other elements such as Cr, Mn, B, Si in order to achieve homogeneous nano-crystalline or amorphous structure [3].

The origin of anti-ferromagnetism lies in the strong negative exchange interaction between the adjacent spins so that the energy is minimised by their anti-parallel alignment. The temperature dependence of the susceptibility of this magnetism is, however, characterised by the occurrence of a kink in the $\chi - T$ curve at the so-called Néel temperature [2,3]. The reason for this is that below this temperature an anti-parallel spin arrangement is established in which the plus and minus spins completely cancel each other, and the susceptibility decreases with a decrease in temperature. Above the Néel point the spin arrangement becomes random, so that the susceptibility decreases with an increase of temperature.

Ferri-magnetism is the term first proposed by Néel [2] to describe the magnetism of ferrites. In these materials the magnetic ions can occupy two kinds of lattice sites, designated here as A and B. The ionic spins on A sites all point in the plus direction, where as all those situated at B sites point in the minus direction because of a strong negative interaction acting between the two spin systems. Since the number of magnetic ions and the individual magnitude of spins of individual ions are different on the A and B sites, such an ordered arrangement of spins gives rise to a resultant magnetisation, which is typically smaller than that of ferromagnetic materials.

In spite of the presence of spontaneous magnetisation, a block of ferro- or ferri-magnetic material is usually not spontaneously magnetised but exists rather in a demagnetised state. This is because the interior of the block is divided into many *magnetic domains*. Since only the direction of magnetisation inside domains varies from domain to domain, the resulting magnetisation can be changed from zero to the value of the spontaneous magnetisation. If the field is reduced, the magnetisation is decreased, but does not come back to the original value. Such *an irreversible process* is called *hysteresis*. The change of the resulting magnetic moment of the whole magnetic specimen under the action of an applied magnetic field arises from two mechanisms:

(a) a change in the volume of domains which are favourably oriented with respect to the external field at the expense of unfavourably oriented domains, and

(b) rotation of the directions of magnetisation towards the direction of the field.

In the next sections, I will consider some basic magnetisation reversal mechanisms involving magnetisation rotation and domain wall displacements in ferromagnetic bodies. The dependence of the susceptibility χ on the applied magnetic field, temperature, frequency and some other parameters, will be discussed. This analysis is very important for the present research.

2.2 Equilibrium magnetisation in a ferromagnetic sample.

Any analysis of the magnetisation behaviour starts with establishing the equilibrium magnetic structure, which can be done by the minimisation of the free energy of the ferromagnetic sample. [4,5]. The total magnetic energy includes a number of terms of different origins. In general, the following contributions are important: *magneto-crystalline energy* U_K, *magnetostatic energy* U_{sh} associated with the demagnetising field (shape effect), *energy* U_H due to *an external magnetic field*, and *magnetoelastic energy* U_{me} related with magnetostriction:

$$U_E = U_K + U_{sh} + U_{me} + U_H \tag{2.5}$$

In amorphous ferromagnetics, which are the main interest of the present work, the magneto-crystalline anisotropy is absent and it will be excluded from further discussion. The preferable magnetisation direction is decided via the magnetostrictive interaction by the residual stress distribution induced during the solidification process and further treatments. In the case of elastically uniform material the magnetoelastic energy can be expressed in the following form [4]:

$$U_{me} = -\frac{3}{2}\lambda\sigma\cos^2\alpha \tag{2.6}$$

where α is the angle between the stress σ and the direction of magnetisation, and λ is the

saturation magnetostriction. In (2.5), the *exchange energy* is also excluded since a uniform magnetisation is first analysed (single domain state) and we are interested only in the direction of the magnetisation vector considering that its magnitude is constant (at a certain temperature).

In the next sections I will describe several examples of the rotational magnetisation reversal in a ferromagnetic sample with a uniaxial effective anisotropy, which are directly related to the present study.

a. Rotational magnetisation reversal (Stoner-Wohlfarth model)

I will start with the case when the internal stress σ has the angle θ_0 with the applied magnetic field $\boldsymbol{H}$. This case corresponds to the Stoner-Wohlfarth model for the uniaxial anisotropy ($\mathbf{n_k}$) [5]. The applied field $\boldsymbol{H}$ causes the rotation of the magnetisation direction $\boldsymbol{M}$ (which makes an angle θ with $\boldsymbol{H}$ (Fig. 2.1). If the shape effect is ignored, the energy of this system U_0 can be expressed as follows:

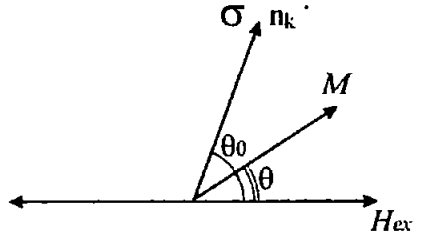

Fig. 2.1 Rotation of magnetisation reversal from an easy axis under the effect of applied magnetic field.

$$U_0 = -\frac{3}{2}\sigma\lambda\cos^2(\theta-\theta_0) - M_0 H\cos\theta \tag{2.7}$$

Here, I will introduce the parameter $H_K = {}^{3\lambda\sigma}/_{M_0}$, which plays the role of the effective *anisotropy field*, M_0 is saturation magnetisation. The equilibrium direction of magnetisation is obtained by the extreme energy condition,

$$\frac{\partial U_0}{\partial\theta} = \frac{H_K}{2}\sin 2(\theta-\theta_0) + H\sin\theta = 0 \tag{2.8}$$

In order to choose the solutions corresponding to local energy minima, the following condition must be imposed:

$$\frac{\partial^2 U_0}{\partial\theta^2} > 0 \tag{2.9}$$

In general, there are two minimums related to the two metastable states. When the magnetic

field is reversed in the negative direction, the magnetisation continues to rotate gradually, being still positive (because of the energy barrier). The height of the barrier decreases with increasing negative field and it disappears when

$$\frac{\partial^2 U_0}{\partial \theta^2} = 0 \tag{2.10}$$

The equilibrium state becomes unstable and M suddenly rotates toward the direction of the field. The field at which this sudden magnetisation flip happens is refereed to as a critical field H^* of the irreversible magnetisation rotation. It can be found from equations (2.8) and (2.10) which have to be solved together

$$\begin{aligned} \sin 2(\theta - \theta_0) &= -2p \sin\theta \\ \cos 2(\theta - \theta_0) &= -p \cos\theta \end{aligned} \tag{2.11}$$

where

$$p = \frac{H^*}{H_K} \tag{2.12}$$

Eliminating $\sin\theta$ or $\cos 2(\theta - \theta_0)$ from the preceding equations, we obtain

$$\sin\theta = \sqrt{\frac{1-p^2}{3p^2}}, \quad \cos\theta = \pm 2\sqrt{\frac{p^2 - 1/4}{3p^2}} \tag{2.13}$$

On putting these values into (2.11), we can solve for $\sin 2\theta_0$:

$$\sin 2\theta_0 = \frac{2}{p^2}\left(\frac{1-p^2}{3}\right)^{3/2}. \tag{2.14}$$

Figure 2.2 shows p plotted as a function of θ_0. It is seen that the critical field H^* has a minimum when $\theta_0 = 45^0$. When the field deviates by 45^0 from the easy axis, the reversal of magnetisation takes place most easily. The critical field is, then,

$$H^* = H_K / 2 \tag{2.15}$$

The critical field becomes larger as θ_0 deviates from 45^0 and finally reaches the maximum value of

$$H^* = H_K \tag{2.16}$$

at $\theta_0 = 0^0$ and 90^0.

Such a process results in the magnetisation curves shown in Fig. 2.3 for various values of θ_0. The vertical lines correspond to irreversible rotation, and the curved portions

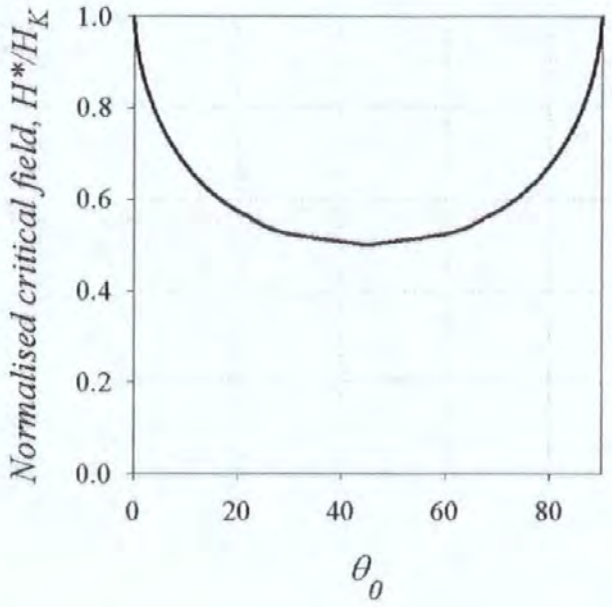

Fig. 2.2 Critical field H plotted as a function of the angle θ_0 between the effective anisotropy (determined by stress in this model) and the magnetising field.*

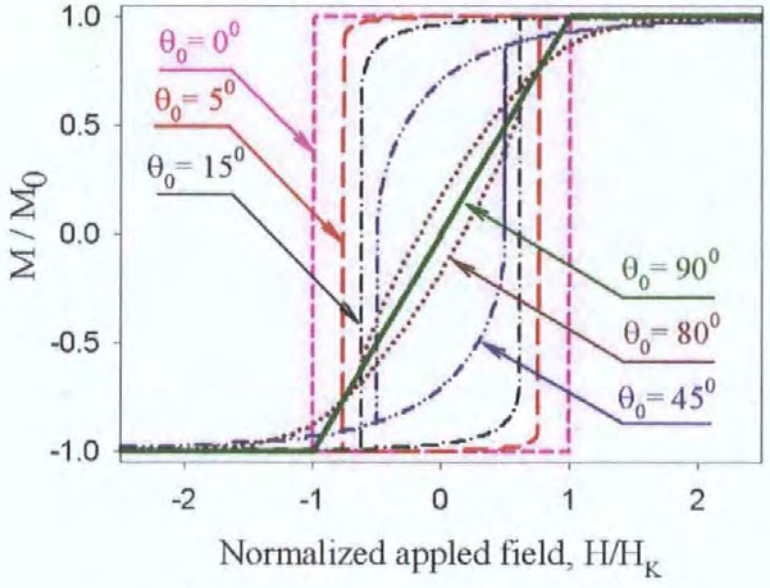

Fig. 2.3 Calculated rotational hysteresis curves for different anisotropy angles.

correspond to reversible rotation. For $\theta_0 > 45^0$ the range of reversible rotation covers a fairly large portion of the magnetisation curves. If a magnetic field is applied in the negative direction and then removed, before the occurrence of irreversible rotation, the magnetisation comes back to the original residual magnetisation.

b. Rotational magnetisation reversal under the effect of a transverse magnetic field.

The next example considers the effect of a transverse field on the magnetisation reversal by rotation. It is assumed that the easy anisotropy axis and the driving field are parallel ($\theta_0 = 0^0$). This model, hereafter, will be used to explain the effect of the axial field on circumferential magnetisation process in amorphous microwires with a circumferential anisotropy. The overall energy of the system can be expressed in the following form:

$$U_0 = -\frac{H_K}{2}\cos^2\theta - H\cos\theta - H_\perp \sin\theta \tag{2.17}$$

Using the same scenario, the stable direction of the magnetisation can be determined by

$$\frac{\partial U_0}{\partial \theta} = \frac{H_K}{2}\sin 2\theta + H\sin\theta - H_\perp \cos\theta = 0 \tag{2.18}$$

Putting $\cos\theta = x$, (2.18) becomes

$$x^4 + 2px^3 + (r^2 + p^2 - 1)x^2 - 2px - p^2 = 0 \tag{2.19}$$

where $r = H_\perp / H_K$. Solving equation (2.19) produces rotational plots *x(p)* with the transverse field as a parameter, as shown in Fig. 2.4.

The analysis demonstrates that the application of $H_\perp$ activates the reversible rotational processes, since it results in the magnetisation inclination from the anisotropy axis. The critical field of the irreversible magnetisation jump decreases considerably according to

$$H^* / H_K = (1 - r^{2/3})^{3/2}$$

which implies that when $H_\perp = H_K$, the hysteresis disappears.

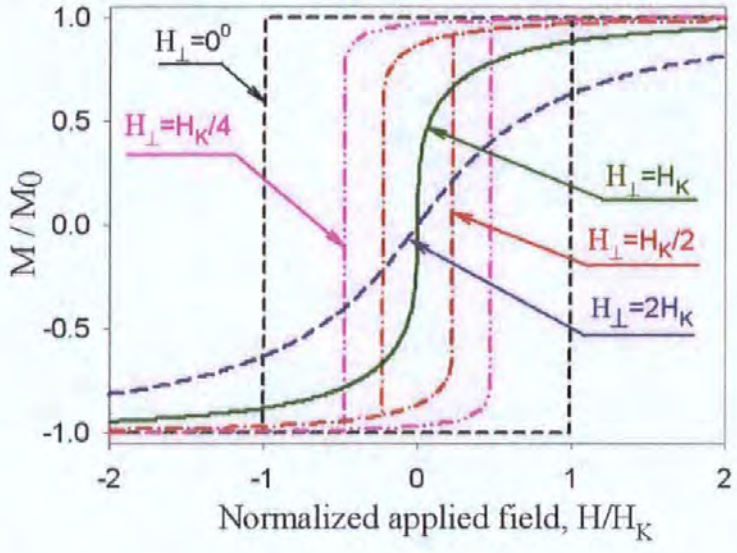

Fig. 2.4 Calculated rotational hysteresis with the transverse magnetic field as a parameter.

c. Rotational magnetisation reversal in the presence of various stresses

In amorphous ferromagnetic materials where magnetostrictive processes play the main role in establishing the magnetic anisotropy, the applied stress may influence the magnetisation reversal substantially. I will present here an accurate quantitative analysis that is difficult to find elsewhere (also the model fundamentals are similar to a general rotational hysteresis analysis). The stress effect on the rotational hysteresis will be demonstrated taking an example of an amorphous wire with a negative magnetostriction, which has two types of internal (or applied) stresses: an axial tension and a twist. The former has intensity σ_1 and the latter represents the combination of tension and compression σ_{2+} and σ_{2-} with equal intensity ($\sigma_{2+} = \sigma_{2-} = \sigma_2$) at 90^0 to each other and at 45^0 to the wire axis, as shown in Fig. 2.5.

The combined action of all the stresses results in the effective magnetostrictive energy of the form (see vector diagram on fig. 2.5b):

$$U_{me} = -\frac{3}{2}\lambda(\sigma_1 \cos^2\theta + \sigma_2 \cos^2(\theta - 45^0) - \sigma_2 \cos^2(\theta + 45^0)) \qquad (2.20)$$

This can be simplified as

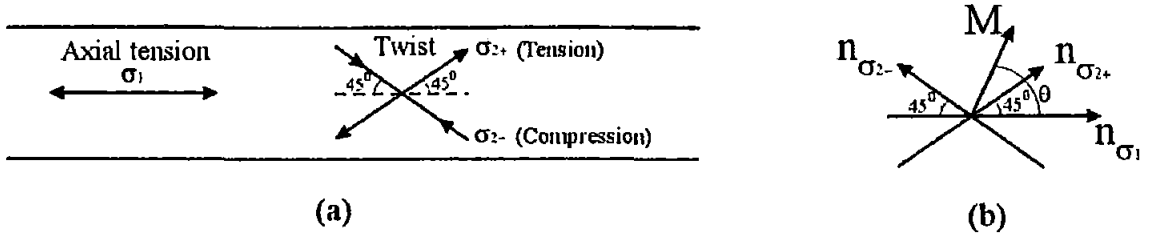

Fig. 2.5. Stress components in an amorphous microwires in (a) and principle components vector directions in (b).

$$U_{me} = -\frac{3}{2}\lambda(\sigma_1 \cos^2\theta + \sigma_2 \sin 2\theta) \tag{2.21}$$

If the driving external magnetic field is applied along the wire axis, the total energy becomes:

$$U_0 = -\frac{3}{2}\lambda(\sigma_1 \cos^2\theta + \sigma_2 \sin 2\theta) - MH\cos\theta \tag{2.22}$$

Then the stable direction of magnetisation can be determined by

$$\frac{\partial U_0}{\partial \theta} = -\frac{3}{2}\lambda(2\sigma_2 \cos 2\theta - \sigma_1 \sin 2\theta) + MH\sin\theta = 0 \tag{2.23}$$

Putting $\cos\theta = x$, (2.23) becomes

$$x^4(4b^2 + a^2) + 2ax^3 - (4b^2 + a^2 - 1)x^2 - 2ax + b^2 - 1 = 0 \tag{2.24}$$

where $a = 3\lambda\sigma_1/MH$, $b = 3\lambda\sigma_2/MH$. After determining x from this equation, we can plot the magnetisation curves with σ_1 and σ_2 as parameters for given $M = 500$ G, as shown in Fig. 2.6. The given examples clearly demonstrate that internal and applied stresses strongly influence the magnetisation reversal in amorphous wires. Thus, in the case of negative magnetostriction (Fig. 2.6) the axial hysteresis is very small when the torsional stress is small (the tensile stress-induced anisotropy is circumferential). Increasing torsion results in the inclination of the effective anisotropy axis from a circumferential direction towards the axis (but the angle between the effective anisotropy and the circumferential direction will be always smaller than 45°) and the hysteresis area increases.

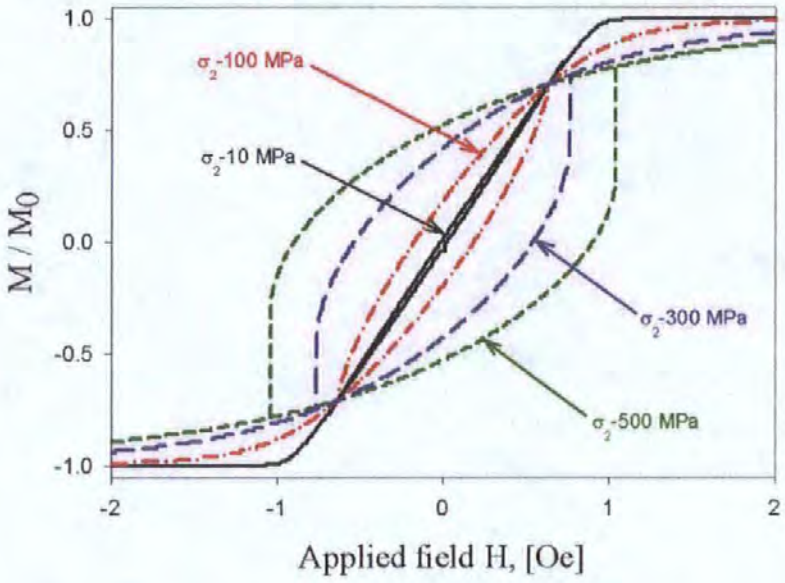

Fig. 2.6 Rotational hysteresis M(H) with the applied twist σ_2 as a parameter whilst the axial tension $\sigma_1 = 500\ MPa$, $\lambda = -3 \cdot 10^{-7}$ and M=500 G are kept constant. This corresponds to the axial hysteresis in Co-based negative magnetostrictive wires under the effect of twist.

d. Model of domain walls displacement.

The rotational models analysed above can be applied for multi domain samples as they describe the rotational processes within the domains (reversible portions of the magnetisation curves) [4]. The magnetisation flip, however, typically takes place by the domain wall movement, rather than the irreversible rotation as the coercivity is typically considerably smaller than the effective anisotropy field (which can include the contribution from the demagnetising field).

Here we assume that a plain domain wall is displaced in some material with irregularities, which cause variations of energy for the displacement of the wall. These irregularities may result from, for example, micro-defects, surface imperfections or cracks. The energy U_{dw} of the wall per unit area is assumed to be changing with the displacement of the wall, s, as shown in Fig. 2.7.

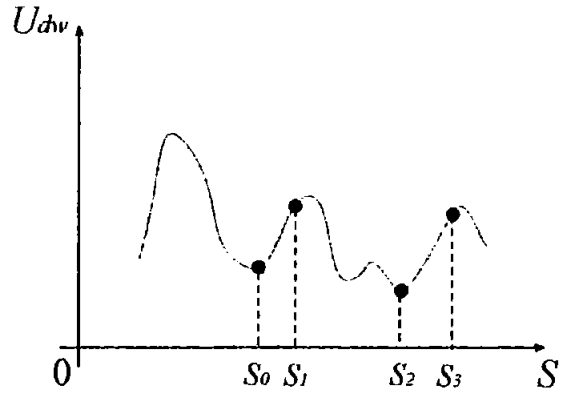

Fig. 2.7 Variation of the wall energy as a function of position of a domain wall.

In the absence of a magnetic field, the wall stays at some minimum point s_0, where $\partial U_{dw}/\partial s = 0$. The energy can be expressed in the first approximation as

$$U_{dw} = \frac{1}{2}\alpha s^2 \tag{2.25}$$

in the vicinity of a stable point. If a magnetic field $\boldsymbol{H}$ is applied in a direction, which makes an angle θ with M_0, the energy supplied by the magnetic field is

$$U_H = -2sM_0H\cos\theta \tag{2.26}$$

for an 180^0 wall, because the displacement s of the wall results in a change in the magnetisation of $2sM_0$ per unit area of the wall. From the condition of minimising the total energy,

$$U_0 = U_{dw} + U_H = \frac{1}{2}\alpha s^2 - 2sM_0H\cos\theta \tag{2.27}$$

or

$$\frac{\partial U_0}{\partial s} = \alpha s - 2M_0H\cos\theta \tag{2.28}$$

we have

$$s = \frac{2M_0\cos\theta}{\alpha}H \tag{2.29}$$

If we assume that the gradient of the energy U_{dw} has a maximum at s_1 (Fig. 2.7), further increase of the field intensity will result in an irreversible displacement of the wall from s_1 to, say s_3 where the gradient is larger and thus can counterbalance the stronger magnetic field

"pressure". If the field is reduced from this state, the wall will come back, not to s_0, but to the minimum point, which is closest to s_3. If the largest maximum of the gradient exist at s_3, the wall will finally reach s_3 and then will discontinuously move to the final goal upon an additional increase of $\boldsymbol{H}$. Thus the critical field H^* for one domain wall can be expressed in the following form:

$$H^* = \frac{1}{2M_0 \cos\theta}\left(\frac{\partial U_{dw}}{\partial s}\right)_{\max} \tag{2.30}$$

A considerable cause of the fluctuation in the energy of a domain wall as shown in Fig. 2.7 is the internal stress, as first proposed by Kondorsky [6] and developed by Kersten [7]. A sinusoidal variation of internal stress has been used

$$\sigma = \sigma_0 \cos 2\pi \frac{s}{l} \tag{2.31}$$

where l is the wavelength of spatial variation of the internal stress. The anisotropy constant is, therefore,

$$K = K_u - \frac{3}{2}\lambda\sigma_0 \cos 2\pi \frac{s}{l} \tag{2.32}$$

where K_u is an averaged effective anisotropy constant. If the wavelength l is sufficiently large compared to the wall thickness δ, it can be assumed that the anisotropy constant does not change inside the wall; then the surface energy of the wall is given by

$$\gamma = 2\sqrt{A\left(K_u - \frac{3}{2}\lambda\sigma_0 \cos 2\pi \frac{s}{l}\right)} \tag{2.33}$$

Then

$$\left(\frac{\partial \gamma}{\partial s}\right)_{\max} = \frac{3\pi\lambda\sigma_0}{l}\left(\sqrt{\frac{A}{K_u - \frac{3}{2}\lambda\sigma_0 \cos 2\pi \frac{s}{l}}} \sin 2\pi \frac{s}{l}\right)_{\max} = \frac{\pi\lambda\sigma_0}{l}\delta, \tag{2.34}$$

where $\delta = 3\sqrt{A/K_u}$ is the thickness of the wall. Since the wall does not change its area ($U_{dw} = \gamma$), (2.30) becomes

$$H^* = \frac{\pi\lambda\sigma_0}{2M\cos\theta}\frac{\delta}{l} \tag{2.35}$$

In the Kersten model it is supposed that the wall is constrained at two points and that it is

expands under the action of the applied magnetic field (Fig. 2.8). The radius of the curvature of the wall is given by

$$\frac{\gamma}{r} = 2MH\cos\theta, \tag{2.36}$$

It is seen that the radius should decrease with an increase of H. Actually, r is reduced as the wall expands as shown by curves a, b, and c in Fig. 2.8, but, if the wall expands beyond curve c where r is equal to the one-half of the separation of two constraining points l, the radius of the curvature, r, is again increased with further expansions of the wall. The wall will, therefore, expand discontinuously after it passes through curve c. The critical field H^* is obtained by setting $r = l/2$ in (2.36); then we have

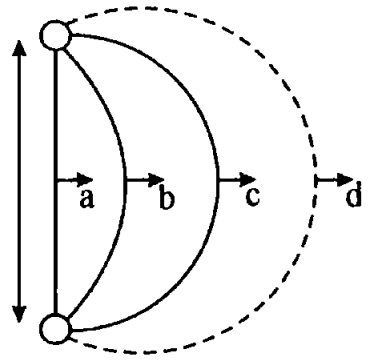

Fig. 2.8. Reversible and irreversible expansion of the domain wall.

$$H^* = \frac{\gamma}{Ml\cos\theta} \tag{2.37}$$

In this model, the critical field is proportional to the domain wall energy γ. The value of γ can be reduced by applying a transverse field, which is similar to the effect of the transverse field on the rotational critical field. Therefore, in both cases of rotational and wall displacement mechanisms, the effect of the transverse field reduces the hysteresis area and makes the switching process faster. This effect will be employed to control circumferential magnetisation reversal in amorphous wires by applying an axial magnetic field.

2.3 Thermally activated irreversible magnetisation reversal. Néel-Brown model.

As it is clearly seen, from previous discussion, the critical field is a random variable. It turned out that stochastic methods are more appropriated in the study of the parameters of irreversible magnetisation reversal, such as fluctuations of the critical field and the field of irreversible domain nucleation. One of the models describing nucleation of domains in ferromagnetic samples is the Néel-Brown model of thermally activated magnetisation reversal [1, 2, 8-10]. In this model the magnetisation reversal is assumed to occur via nucleation of domains happening at a certain applied field, which is called the switching field H_{sw}. In the

Néel-Brown model, a single domain particle has two equivalent ground states of opposite magnetisation separated by an energy barrier due to for instant shape and crystalline anisotropy. The system can escape from one state to the other either by thermal activation over the barrier at high temperature, or by quantum tunnelling at low temperatures. At sufficiently low temperatures and at zero field, the energy barrier between two states of opposite magnetisation is too high for an escape process to be observed. However, the barrier can be lowered by applying a magnetic field in the opposite direction to that of the particle's magnetisation. When the applied field is close enough to the switching field at zero temperature H_{sw}^0, thermal fluctuations are sufficient to allow the system to overcome the barrier, and the magnetisation reverses. For modelling this process, Brown proposed to add a random field term to the Gilbert equation, which is assumed to be of white noise type. On the basis of this assumption, he was able to derive a Fokker-Planck equation for the distribution of magnetisation orientation. Brown did not solve this differential equation. Instead he tried some analytical approximations and asymptotic expansion for the case of the field parallel or perpendicular to the easy axis of magnetisation. More recently, Coffey et al. [11-13, 16] have found by numerical methods an exact solution of Brown's differential equation for uniaxial anisotropy and an arbitrary applied field direction.

There are two main experimental methods for investigation of stochastic escaping process: waiting time and switching field approaches.

a. The waiting time method

The waiting time method consists in measuring the probability that the magnetisation has not switched after a certain time. At a given temperature, the magnetic field H is increased to a waiting field H_w near the switching field H_{sw}^0. Next, the elapsed time until the magnetisation switches is measured (Fig. 2.9(a)). This process is repeated several hundreds times, yielding a waiting time histogram. The integral of this histogram and proper normalization yields the probability that the magnetisation has not switched after a time t.

According to the model, the probability that the magnetisation has not switched after a time t is given by:

$$P(t) = e^{-t/\tau} \tag{2.38}$$

and τ (inverse of the switching rate) can be expressed by an Arrhenius law of the form:

$$\tau^{-1}(\varepsilon) = \tau_0^{-1} e^{-A\varepsilon^b} \tag{2.39}$$

where $\varepsilon = (1 - H/H_{sw}^0)$; τ_0^{-1} is constant (pre-exponential factor), parameters A and b depend on damping, temperature, energy barrier height and reversal mechanism (thermal or quantum) [17, 18].

b. Switching field measurements

It is often more convenient to study magnetisation reversal by ramping the applied field at a given rate and measuring the field value as soon as the sample magnetisation switches. Next, the field ramp is reversed and the process repeated. After several hundred cycles, switching field histograms are established, yielding the mean switching field $\langle H_{sw} \rangle$ and the width σ_{sw} (rms. deviation). Both mean values are measured as a function of the field sweeping rate and temperature (Fig. 2.9(b)). From the point of view of thermally activated magnetization reversal, switching field measurements are equivalent to waiting time measurements as the time scale for the sweeping rate is typically more than 8 orders of

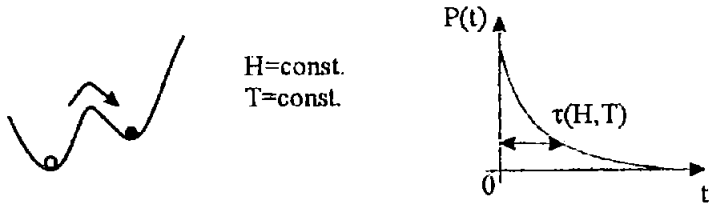

(a) Waiting time measurements

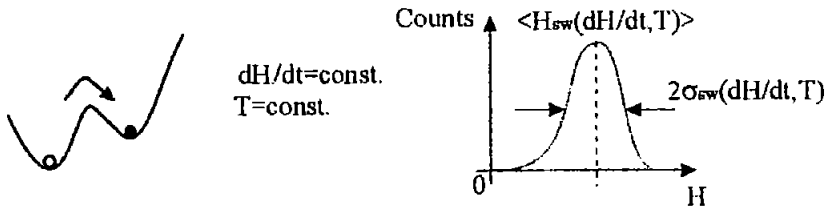

(b) Switching field measurements

Fig. 2.9 Diagrams illustrating two approaches for investigation of stochastic escaping process: waiting time (a) and switching field (b) methods.

magnitude greater than the time scale of the pre-exponential factor a typical value of which is $10^{-10}s$.

Therefore the Néel–Brown model described above can be applied to define parameters of irreversible magnetisation reversal.

References

[1] W. F. Brown *"The Effect of Dislocations on Magnetization Near Saturation"* Phys. Rev. (1941) 60, 139

[2] L. Néel "*Influence of the thermal fluctuation on the domains of ferromagnetic materials*" C. R. Acad. Science (1949) 228, 664

[3] C. Kittel "*Introduction to Solid State Physics*" John Wiley&Sons Inc., New York, (1971).

[4] S. Chikazumi "*Physics of Magnetism*" John Wiley&Sons Inc., New York, London, Sydney (1964).

[5] E. C. Stoner and E. P. Wohlfarth *"A Mechanism of Magnetic Hysteresis in Heterogeneous Alloys"* Phil. Trans. Roy. Soc. (1948) A 240, 599.

[6] E. Kondorsky *"Physik"* Z. Sowjetunion (1937) 11, 597

[7] M. Kersten, Z. Angew "*Fractal domain structures in thin amorphous films*" Phys. (1956) 7, 313

[8] W. F. Brown *"Relaxational Behavior of Fine Magnetic Particles"* J. Appl. Phys. (1959) 30, 130.

[9] W. F. Brown "*Dynamic properties of a system of cobalt nanoparticles*" J. Appl. Phys. (1963) 34, 1319.

[10] W. F. Brown *"Thermal Fluctuations of a Single-Domain Particle"* Phys. Rev. (1963) 130, 1677.

[11] W. T. Coffey, D. S. F. Crothers, J. L. Dormann, Yu. P. Kalmykov and J. T. Waldron *"Effect of an oblique magnetic field on the superparamagnetic relaxation time"* Phys. Rev. B (1995) 52, 15951.

[12] W. T. Coffey, D. S. F. Crothers, J. L. Dormann, Yu. P. Kalmykov, E. C.Kennedy, and W. Wernsdorfer *"Thermally Activated Relaxation Time of a Single Domain*

Ferromagnetic Particle Subjected to a Uniform Field at an Oblique Angle to the Easy Axis: Comparison with Experimental Observations" Phys. Rev. Lett. (1998) 80, 5655.

[13] W. T. Coffey, D. S. F. Crothers, J. L. Dormann, Yu. P. Kalmykov, E. C.Kennedy, and W. Wernsdorfer *"Thermally activated escape rates of uniaxial spin systems with transverse field: Uniaxial crossovers"* J. Phys. Cond.Mat. (1998) 10, 9093.

[14] I. Klik and L. Gunther *"1st-Passage-Time Approach to Overbarrier Relaxation of Magnetization"* J. Stat. Phys. (1990) 60, 473.

[15] I. Klik and L. Gunther *"Experimental Evidence of the Néel-Brown Model of Magnetization Reversal"* J. Appl. Phys. (1990) 67, 4505.

[16] W. T. Coffey *"Thermal fluctuation in multi-domain ferromagnetic clusters"* Adv. Chem. Phys. (1998) 103, 259.

[17] A. Garg *"Escape-field distribution for escape from a metastable potential well subject to a steadily increasing bias field"* Phys. Rev. B (1995) 51, 15592.

[18] J. Kurkijarvi *"Intrinsic Fluctuations in a Superconducting Ring Closed with a Josephson Junction"* Phys. Rev. B (1972) 6, 832.

[19] H. L. Richards, S. W. Sides, M. A. Novotny, and P. A. Rikvold *"Kinetic Ising Systems as Models of Magnetization Switching in Submicron Ferromagnets"* J. Appl. Phys. (1996) 79, 5749.

[20] J.M. Gonzalez, R. Ramirez, R. SmirnovRueda, and J. Gonzalez *"Non-Arrhenius relaxation in micromagnetic models of systems with many degrees of freedom"* J. Appl. Phys. (1996) **79**, 6479.

[21] D. GarciaPablos, P. GarciaMochales, and N. Garcia *"Nonhomogeneous magnetization reversal in 2D Ising clusters"* J. Appl. Phys. (1996) **79**, 6021.

[22] D. Hinzke and U. Nowak *"Magnetisation switching in a Heisenberg model for small ferromagnetic particles"* Phys. Rev. B (1998) 58, 265.

[23] E. D. Boerner and H. Neal Bertram *"Local Relaxation and Collective Stochastic Dynamics"* IEEE Trans. Mag. (1997) 33, 3052.

Chapter 3. Production methods and general magnetic properties.

A large number of applications in which an amorphous wire is used as a magnetic sensing element are based on the possibility of establishing in these materials a unique magnetic structure with well-defined magnetic anisotropy. The type of anisotropy and hence, domain structure is determined by such factors as residual stress distribution, applied stress, the value and sign of the magnetostriction constant. The latter is an internal characteristic, which depends on the alloy composition and can be used to classify the wires. Three main groups of amorphous wires can be distinguished:

1. Fe-based alloys with positive and relatively large magnetostriction (of the order of 10^{-6})

2. Co-based alloys with negative and relatively large magnetostriction (of the order of 10^{-6})

3. Co-based alloys with small additions of Fe exhibiting vanishing magnetostriction (of the order of 10^{-7}).

Amorphous microwires of the first and second groups, so-called Fe-based and Co-based microwires, are characterised by the axial anisotropy in the inner region. The magnetisation reversal in these materials takes place by a large Barkhausen jump between two bistable states, producing nearly squared hysteresis loops [1]. This rapid remagnetisation process, which generates a sharp voltage pulse, is useful for such applications as pulse generators, magnetic encoding, magnetic labelling and security sensors. In the outer region, the domain structure is radial and circular, respectively for Fe-based and Co-based microwires. On applying external stress to Fe-based wires or using a special treatment, the outer region can be reduced so that the axial anisotropy occupies almost the total volume. Therefore, the bistability properties can be easily enhanced. On the contrary, for Co-based wires the effect of external stress would increase the area with the circumferential anisotropy. Wires of the third group having small magnetostriction typically do not exhibit bistable magnetisation reversal. In this case, practical interest is related to wires with a small negative magnetostriction that is still sufficient to preserve the circular domain structure. This type of microwire is well known as one of the best materials for magneto-impedance sensors.

In this section, we will briefly review the basic technology of microwire production with relation to their geometry, microstructure (amorphous or microcrystalline), mechanical properties, residual stress distribution and finally general magnetic properties. For example, different types of magnetic structures originate from the balance between magnetostatic and magneto-elastic energies contributions. The magneto-elastic anisotropy in its turn is a consequence of the internal stresses frozen in during the fabrication process. The internal stresses (axial, radial and circular) are induced by strong thermal gradient during the fabrication process. After-production treatments such as annealing under stress or magnetic field and drawing can modify the stress distribution considerably, resulting in modifications of the magnetisation configurations.

3.1 Production methods

There are two main techniques of microwire fabrication, namely, in the water rotating melting Unitika method and Taylor-Ulitovsky method based on glass-capillary drawing.

a. UNITIKA technique

The first technology has been developed by UNITIKA Ltd. R&D (Kyoto, Japan). The basic features of this method are as follows [2-7]. The master alloy is loaded into a quartz nozzle and melted by induction heating. The temperature is monitored with an optical pyrometer. A jet of molten metal is ejected under pressure through the orifice of the quartz nozzle into the rotating water layer. Fig. 3.1 shows a schematic representation of the experimental apparatus. The diameter of the amorphous wire is controlled by the orifice, ejection pressure, ejection angle and drum rotational speed. The most important factor in the spinning process is to control the ratio of the jet velocity V_j to the water velocity V_w. Figs. 3.2 (a, b) show the optimal range in V_j / V_w as a function of orifice diameter for preparing continuous amorphous Fe-Si-B and Co-Fe-Si-B wires at the ejection angle of about 60 degrees. This indicates that continuous amorphous wires with various diameters (50-250 μm) are produced if the water velocity in the drum exceeds the jet velocity by about 2-6 %. The deviation in the diameter can be made within 8-10%

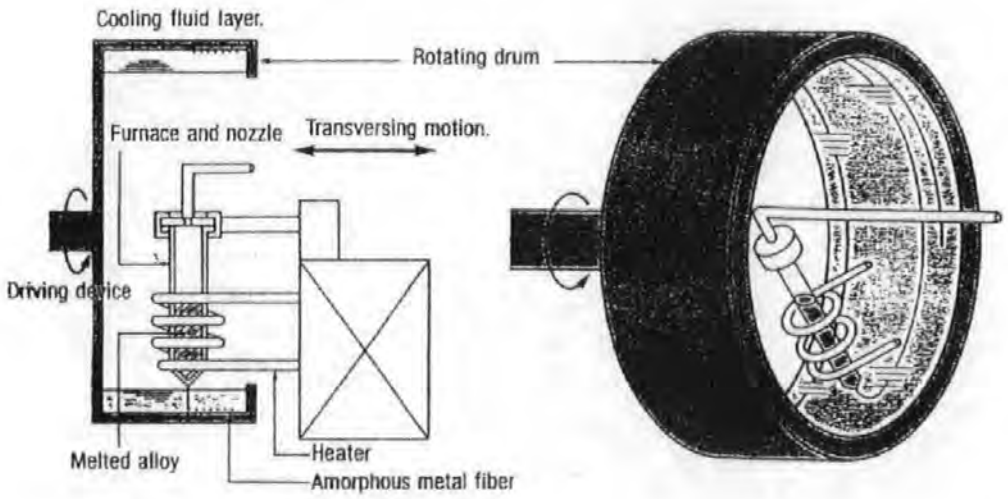

Fig. 3.1. Schematic illustration of the UNITIKA spinning apparatus.

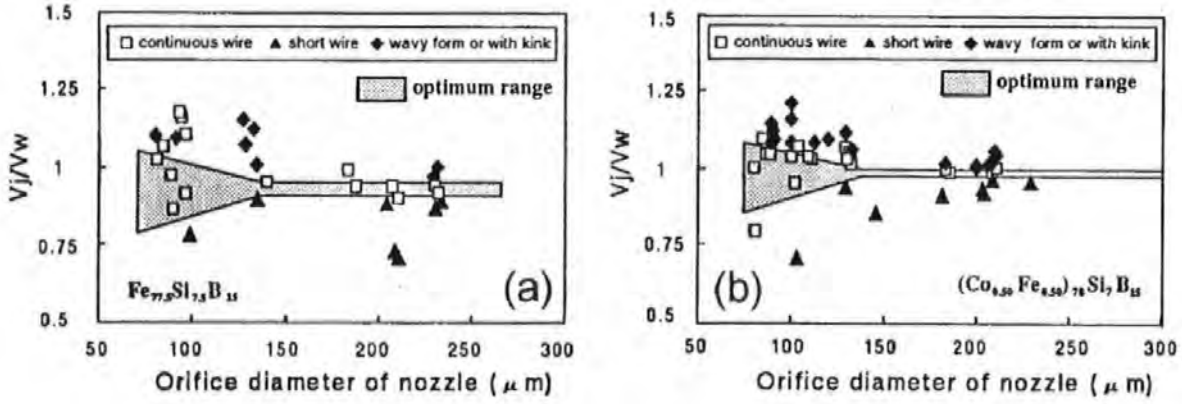

Fig. 3.2. Optimum range in Vj/Vw for amorphous Fe-Si-B wires in (a) and Co-Fe-Si-B wires in (b).

b. Taylor-Ulitovsky technique

The process for making extremely thin glass-coated wires, which are a primary interest for this work, was first invented by Taylor in 1924 [8]. A drop of molten metal was put inside a heated glass pipe, which was pulled very quickly. This transformed the metal into several microns thick wire coated by glass. In the early 1952, Ulitovsky et al. [8,9] developed an industrial process based on the Taylor method. In 1970, Wiesner and Schneider obtained for

the first time such glass-coated microwire with an amorphous metal core. The Taylor-Ulitovsky process can be described as follows [8-15]. The drop of the master alloy is delivered inside a glass tube and heated by a large high-frequency electromagnetic field. Hot metal melt softens glass, which is drawn to form a glass capillary wherein melting metal penetrates (Fig. 3.3).

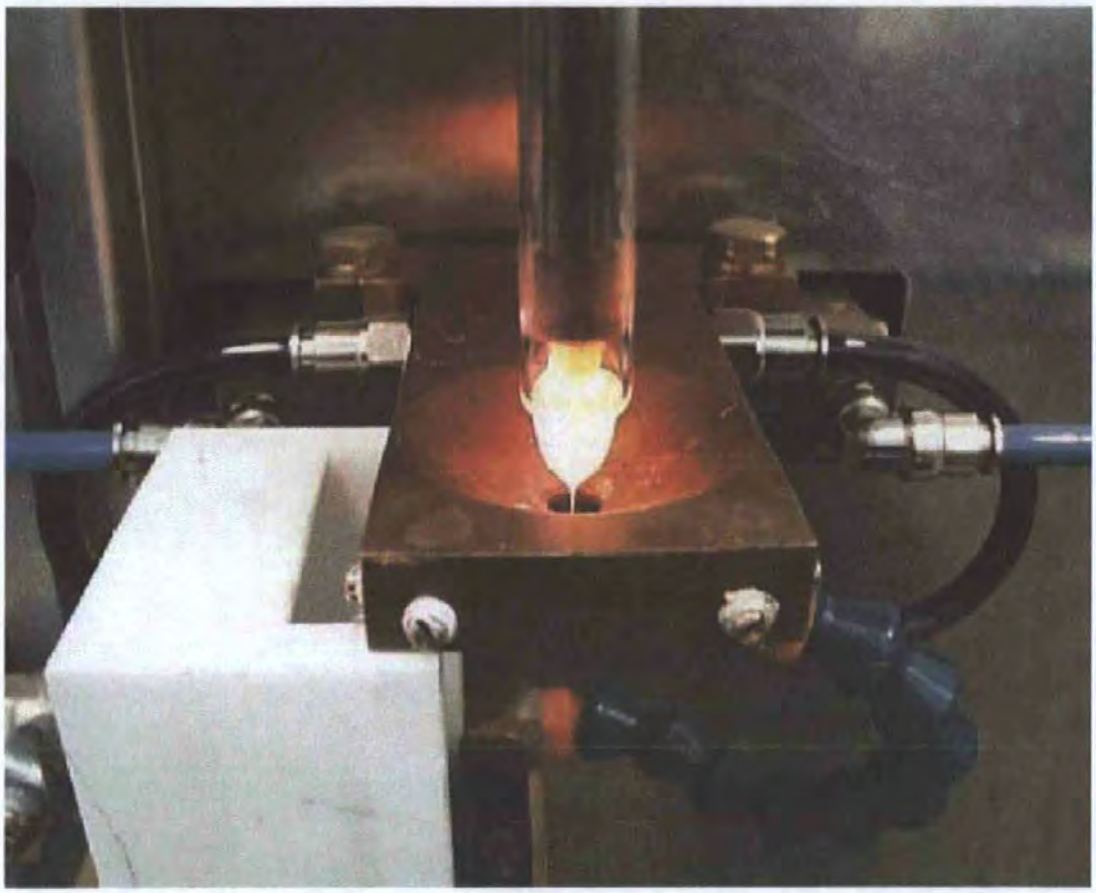

Fig. 3.3. The melted drop inside a glass tube

Thus, a micro wire is formed, which has a metal core covered by glass (Fig. 3.4). The micro wire on its way to the receiving coil is cooled in the stream of water to obtain a metallic core in an amorphous or fine microcrystalline state.

The glass used in the preparation of microwires must be of a very high purity to prevent hairline cracks and have a melting point comparable to the melting point of the metal used in the experiment. When high melting point metals are used, glasses with high softening temperatures, i.e., high silicon content, are needed.

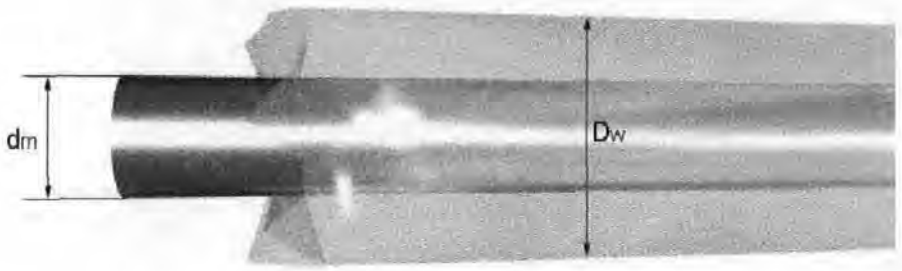

Fig. 3.4. Glass coated microwire.

The metal drop is heated up to the melting point T_m of the alloy; at this temperature the glass softens and forms an envelope for the metal. Then, the metal is superheated and kept at a temperature $T_S = T_m + \Delta T$ for a time t. The melting temperature T_m of the magnetic alloy will typically fall in the range of from 1230 to 1400°C. The alloy is typically superheated (ΔT) from 10 to 300°C above its melting point. The parameter t is found empirically for a given alloy composition, conductive and magnetic properties and values of the metallic core diameter and the glass thickness. To find a suitable time t, the process of casting microwires is repeated several times with different times t. The conductive and magnetic properties of the obtained samples are then measured as a function of t. Using extrapolation methods, the exposure time for the required magnetic and geometrical parameters may then be determined.

The glass heated by the melted alloy softens because of the dramatic reduction of its viscosity. As a result, two coaxial flows arise: one of the melted metal in the centre and the other of softened glass around it. After leaving the heating zone, both flows transport through a water or oil stream (Fig. 3.5), cooling and solidifying. The glass coating solidifies before the metal core as the wire passes through the cooling zone. When cooling is rapid, the metallic core is in a strained state of extension and the glass coating is in a state of compression. The strain is induced by the differences in the coefficients of thermal expansion of glass and metal. The molten metal tries to contract on cooling but is constrained by the already solidified glass. Resistance, mechanical strength and magnetic properties benefit from this situation. This will be considered in more details in the next section. The microstructure of a microwire and hence, its properties depend mainly on the cooling rate, which can be controlled by a cooling mechanism.

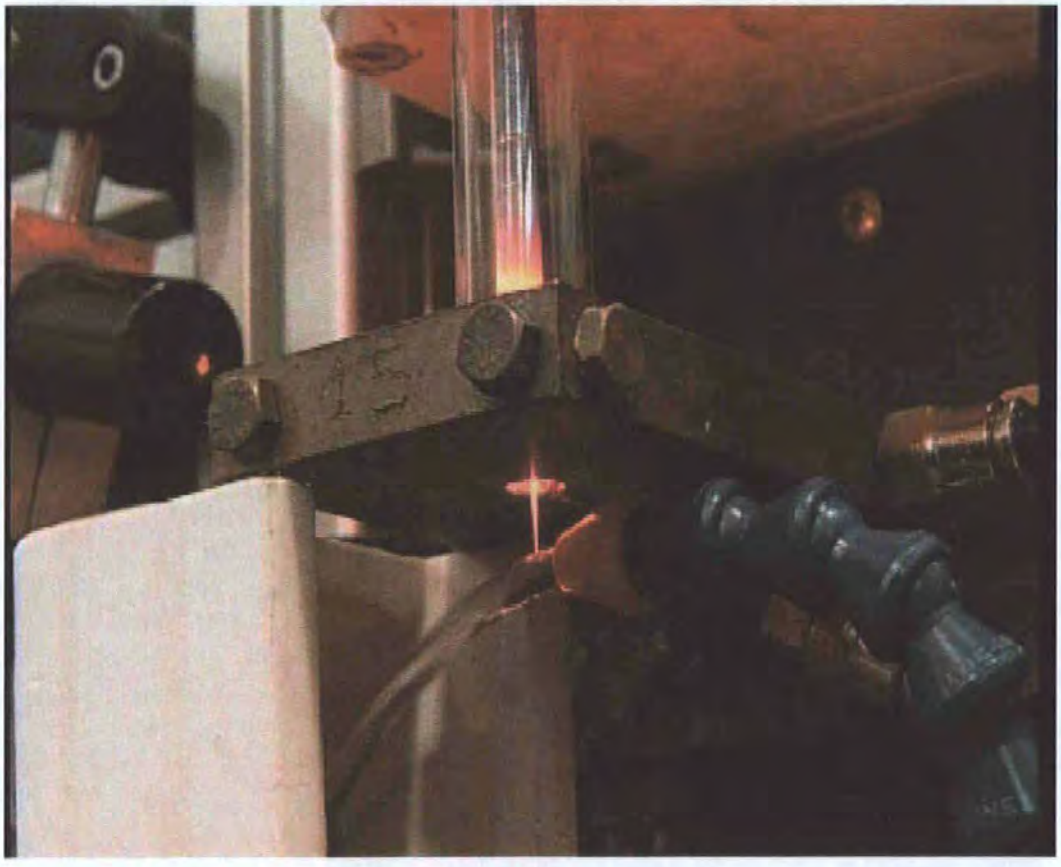

Fig. 3.5. Process of cooling wire by a water stream.

The velocity at which the microwire is wound on a bobbin is from a few meters, to some hundreds of meters per minute. In total, this multi-parameter process, requiring sophisticated control methods and special methods for the preliminary treatment of the metal and glass raw materials.

The diameter of the microwire influences the final microstructure because the rate of heat loss changes with diameter. Microwires greater than 40 μm in diameter are usually microcrystalline. Microwires less than 20 μm are usually amorphous. Microwires in the range of 40 to 20 μm will have a microstructure strongly influenced by the processing parameters. For example, increasing the additive load in the metal, lengthening the cooling stream path length, reducing the distance between the cooling and heating zones and increasing the degree of super-heating and super-cooling of the metal all promote an amorphous microstructure. In general, rapid cooling is typically required to obtain amorphous and microcrystalline microstructures. The amorphous or microcrystalline structure is controlled by choice of

amorphisizers, cooling rate, nature of the cooling liquid, location of the cooling stream, dwell time in the cooling stream and degree of superheating and super-cooling.

Typically, a multi component alloy is required for microwire production to satisfy a number of properties. In the case of magnetic wires, the alloy is preferably a *Fe* and/or *Co*-based alloy to get high magnetisation along with a number of controlled parameters such as the magnetostriction constant. As the content of *Fe* is increased, the magnetostrictive constant monotonically increases going through zero at 4-4.5%. This allows a magnetic system with the effective anisotropy field varying within a wide range (0.1-50 Oe) to be designed. The magnetic properties can be further refined using such additives as *Mn* and *Cr*. To produce a microwire having a metallic core in an amorphous or microcrystalline state, the elements responsible for amorphization such as *Si, B, Ge* are used. Their total content must not exceed a certain limit to avoid relaxation of properties with time. Along with this, certain requirements on composition may be imposed by the technological regime. Amorphous metals have no grain boundaries, can be readily doped, and possess good electrical and magnetic properties. The electrical resistance of the amorphous wires increases 20 times up to 2500 KΩ/m in comparison with crystalline alloys, which makes the wires suitable for high frequency applications. In the case of magnetically soft amorphous microwires, the initial magnetic permeability increases 5-7 times, and can be as high as $2 \cdot 10^4$. The mechanical elasticity of these amorphous microwires increases. It is interesting to note that non-magnetic microwires can be of interest for such applications as micro-cables for telecommunications, miniature high-voltage transformers. Thin sub-ten micron silver microwires can be used as conductors at high frequencies, and planar DC-to-DC converters.

I can conclude that due to their unique characteristics, amorphous microwires can be considered as a novel class of high performance conductive and magnetic materials.

3.2 General magnetic properties

The recent interest in amorphous microwires lies in their magnetic properties. As it was shown in the previous Chapter, the magnetic behaviour in amorphous materials is determined

by the shape anisotropy and the magnetoelastic anisotropy arising from the coupling between magnetostriction λ and internal stresses σ frozen-in during the fabrication process. These internal stresses originate from a strong thermal gradient during the fabrication process. This results in a substantial radial distribution of stress with tensile stress in the inner core and compressive stress in the outer region (if no additional stress is set up during the post fabrication process). Accordingly, the easy directions for magnetisation are different in the inner core and outer shell regions. The combination of shape anisotropy and tensile stress produces an axial easy anisotropy in the inner core (irrespective of sign of λ), whereas there is either radial ($\lambda > 0$) or circumferential ($\lambda < 0$) anisotropy in the outer shell. The typical domain structure in wires with positive (Fe-based) and negative (Co-based) magnetostriction is shown in Fig. 3.6.

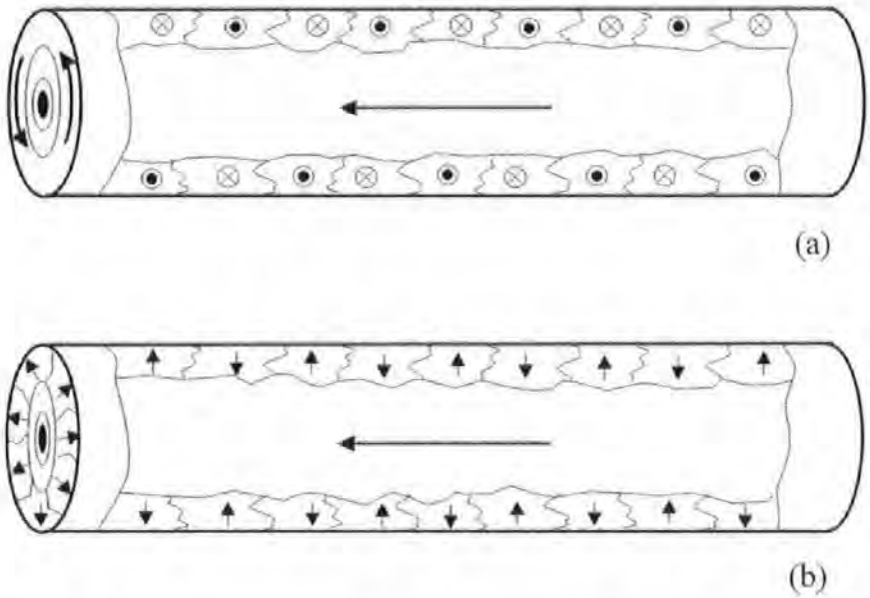

Fig. 3.6. Schematic view of the domain structure determined by the distribution of internal stresses in wires with negative magnetostriction (a) and positive magnetostriction (b).

Let us consider stress distribution in Fe-based glass-coated amorphous microwires. The model of stress distribution in glass-coated amorphous microwires has been developed in works by Chiriac et al [16]. Their method is based on distinguishing two separate stages in the preparation process of this material, which are accomplished in successive time and temperature intervals. During the first stage, the melting metal solidifies, which is assumed to take place simultaneously with the hardening of the glass at the glass transition temperature

T_g. The second stage is the cooling of the metal-glass ensemble from T_g to room temperature T_{RT}. In the first stage, internal stresses are induced due to the solidification of the metal as the solidification front proceeds radially inward to the centre of the wire. In the second stage, internal stresses are induced due to the contraction of the two materials (metal and glass) having different thermal expansion coefficients. In addition, there is an axial tensile stress continuously applied on the wire due to the drawing during the preparation process. In this approach, the tensile axial stress induced due to continues drawing process specific for this technology is neglected. Figure 3.7 shows plots of the stress components (axial σ_{zz}, radial σ_{rr} and azimuthal $\sigma_{\varphi\varphi}$) as functions of distance x from the wire centre. One observes that the shape of the curve $\sigma_{zz}(r)$ and $\sigma_{\varphi\varphi}(r)$ are the same, but the positive values of σ_{zz} are almost twice the positive values of $\sigma_{\varphi\varphi}$. After reaching a maximum, both $\sigma_{zz}(r)$ and $\sigma_{\varphi\varphi}(r)$ decrease down to zero (at approximately 82% of r_w, where r_w is the wire radius) and go to large negative values at the surface. The radial stress $\sigma_{rr}(r)$ is tensile everywhere in the wire.

In the central region of the wire, $\sigma_{zz}(r)$ is the component with the highest value and it is positive (zone I). From ~ 85% of r_w to ~ 88% of r_w there is a second region, much narrower than the first one, in which σ_{rr} is the highest stress component and it is positive (zone II). The remaining part up to r_w constitutes a third region, dominated by the high negative values (compression) of σ_{zz} and $\sigma_{\varphi\varphi}$ (zone III). For positive magnetostriction alloy, the easy anisotropy axis is in the direction of the dominant tensile stress and in the direction perpendicular to the dominant compressive stress. Considering zone II as a small transition region, this confirms the existence of basically a two-region magnetisation model shown in Fig. 3.6b with the axially magnetised core and radial maze domain structure in the shell. For the considered case, the radius of the cylindrical inner core is approximately 85% of r_w.

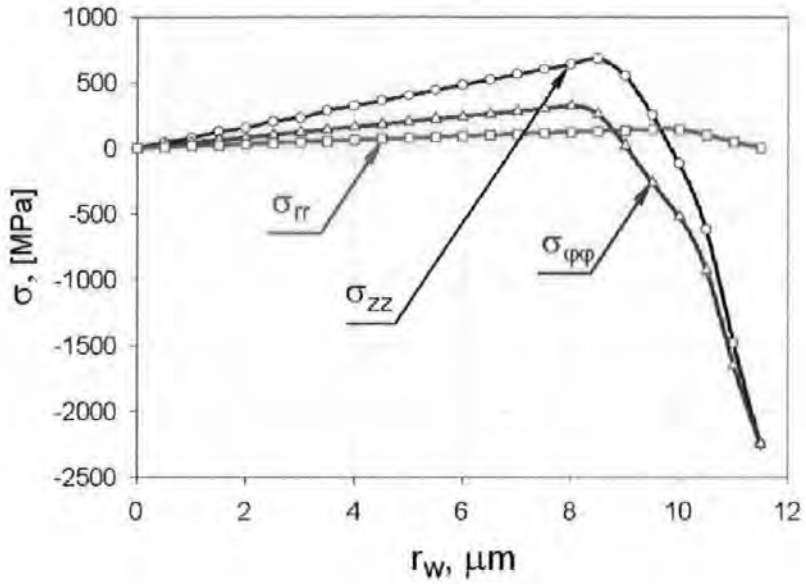

Fig. 3.7. Stress distribution in $Fe_{77.5}Si_{7.5}B_{15}$ wire vs. radius as a result of solidification. The calculation is done for the core diameter of 23 μm and glass thickness of 3.65 μm. Adapted from Chiriac et al. [16].

In the case of Co-based amorphous microwires, magnetostriction determined by the alloy composition is negative. It is assumed that the internal stress distribution for Co-based microwires is similar to that for Fe-based ones, shown in Fig. 3.7. The negative magnetostriction coupled with the compressive stress results in the easy anisotropy axis in the direction of the dominant compressive stress, that is, in a helical direction in the outer shell (combination of σ_{zz} and $\sigma_{\varphi\varphi}$). The core magnetisation seems to be mostly dominated by the shape anisotropy and is in the axial direction, as in the case of $\lambda > 0$. Then, both types of wires irrespective of the sign of magnetostriction exhibit an essentially rectangular hysteresis loop with B_r / B_s determined by the ratio of core and shell thickness (where B_r is the remanent magnetic induction and B_s is the saturation induction). However, the experimentally determined remanence ratio B_r / B_s is much larger in the case of $\lambda > 0$ (figure 3.8, red and black curves) and smaller for $\lambda < 0$ (figure 3.8, pink and blue curves). If the glass is removed, the value of B_r / B_s is nearly equal to the core to shell ratio. It implies that in the preparation process of the glass covered wires an additional tensile axial stress appears due to the drawing of the wire. Then, there is a dominant axial tensile stress everywhere in the wire. As a result, positive magnetostrictive wires have an axial anisotropy and negative magnetostrictive wires have a circumferential anisotropy, in almost the entire wire region.

As I noted above the magnetostriction constant is determined by the alloy composition. Alloys with high iron content, for example $Fe_{77.5}Si_{12.5}B_{10}$, have large positive magnetostriction of the order of 10^{-5}, whilst Co-rich alloys have large negative magnetostriction (of the order of 10^{-6}). Examples of alloys systems having large positive and negative magnetostrictions are given in Table 3.1.

Alloys component	Fe-based microwire with large positive magnetostriction	Co-based microwire with large negative magnetostriction
Iron (*Fe*)	55-80 at.%,	0 – 3 at.%,
Cobalt (*Co*)	0-12 at.%	50- 85 at.%,
Manganese (*Mn*)	0-8 at.%	0 – 12 at.%,
Boron (*B*)	5-15 at.%,	3 – 12 at.%,
Silicon (*Si*)	8-14 at.%,	5 – 15 at.%,

Table 3.1 Alloy systems constituting amorphous microwires with large magnetostriction.

The gap between these two groups is filled by alloys with low magnetostriction constant, if it is negative, the wire still preserves a well-defined circular domain structure due to supplementary tensile stress. Such wires exhibit nearly linear hysteresis loops, as shown in figure 3.8 (pink or blue curves). An example of an alloy system having small but negative magnetostriction is given in Table 3.2. A microwire formed using such an alloy system with core diameter between 8-22 μm and glass thickness 2-5 μm exhibits almost linear B-H curves with a very small hysteresis area.

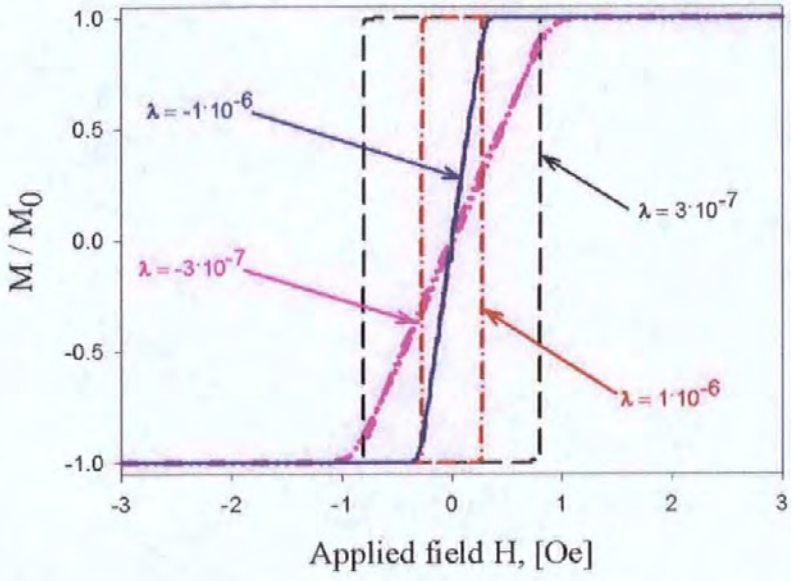

Fig. 3.8. Hysteresis loops for Fe-based and Co-based microwires with different magnetostrictions.

Alloy component	Atomic mass percent (at.%)
Iron (*Fe*)	6.5 - 7.5 at.%,
Cobalt (*Co*)	66.6 - 69.4 at.%,
Manganese (*Mn*)	0.5 - 0.8 at.%,
Boron (*B*)	14 - 14.5 at.%,
Silicon (*Si*)	9.6 - 10.6 at.%,

Table 3.2 Typical alloy systems having small negative magnetostriction.

In this Chapter I briefly discussed the basic microwire properties with relation to their geometry, composition, microstructure (amorphous or microcrystalline), and residual stress distribution. These are based on a number of magnetisation models developed over last two decades. However, the dynamics of the magnetisation in these materials is still relatively poor understood. The following Chapters where I present mine original results on the dynamic hysteresis in microwires with positive and negative magnetostriction are covering this gap.

References

[1] L. Panina, H. Katoh, M. Mizutani, K. Mohri and F. Huphrey "*Domain collapse in amorphous magnetostrictive wires* " IEEE Trans. Magn., (1992) Vol. 28, No. 5, 2922-2924

[2] I. Ogasawara, S. Ueno "*Preparation and Properties of Amorphous Wire*" IEEE Trans. Magn., (1995) vol. 31, No. 2, 1219-1223

[3] F. Humphrey, K. Mohri, J. Yamasaki, H. Kawamura, R. Malmahall and I. Ogasawara *"Re-entrant magnetic reversal in amorphous wires"* Proc. Symp. "Magnetic properties of amorphous metals" edited by H. Hernando (1987) 110-114

[4] I. Ohnaka, T. Fukusako, T. Ohmichi, T. Masumoto, A. Inoue and M. Hagiwara "*Production of amorphous filament by in-rotating-liquid spinning method*" Proc. 4th Inter. Conf. On rapidly quenched metals edited by T. Masumoto and K. Suzuki (1982) 31-34

[5] M. Hagiwara, A. Inoue and T. Masumoto "*Mechanical properties of FeSiB amorphous wires produced by in-rotating-water spinning method* " Metall. Trans., (1982) Vol. 13A, 373-382

[6] Y. Abe, K. Miyazawa, M. Nakamura and T. Ohashi "*The behaviour of melt jet in the in-rotating-water spinning method* " Trans. ISIJ, (1987) Vol. 27, 929-935

[7] Y. Waseda, S. Ueno, M. Hagiwara and K. Aust "*Formation and mechanical properties of Fe- and Co-based amorphous alloy wires produced by in-rotating-water spinning method*" Progr. Mat. Sci., (1990) Vol. 34, 149-260

[8] G. Taylor "*Process and apparatus for making filaments*" US Patent 1,793,529 (1931)

[9] A. Ulitovsky, N. Avernin "*Method of fabrication of metallic microwire*" Patent No. 161325 (1964)

[10] A. Ulitovsky, I. Maianski, A. Avramenco "*Method of continuous casting of glass-coated microwires*" Patent No. 128427 (1960)

[11] V. Larin, A. Torcunov, A. Zhukov, J. Gonzalez, M. Vazquez, L. Panina "*Preparation and properties of glass-coated microwires*" J. Magn. Magn. Mat, (2002)Vol. 249, 39-45

[12] Z. Zelikovski, S. Zotov, I. Nesterovski "*On conditions of simultaneous extraction of metallic nucleus and glass capillary during the microwire fabrication*" Microwire and Electrical Resistance Devices (Chisinau, Cartea Moldaveniasca), (1971) Vol. 8, 3-8

[13] S. Zotov, K. Kabisov, I. Silkes "*Formation of parameters of cast microwires*" Microwire and Electrical Resistance Devices, (1974) 3-17

[14] A. Zhukov, E. Sinnecker, D. Paramo, F Guerrero, V. Larin, J. Gonzalez and M. Vazquez "*Fabrication and magnetic properties of glass coated microwire from immiscible elements*" J.Appl.Phys., (1999) Vol. 85, 4482-4484

[15] E. Sinnecker, D. Paramo, V. Larin, A. Zhukov, J. Gonzalez and M. Vazquez "*Fabrication and magnetic properties of glass coated microwire from immiscible elements*" J.Magn.Magn.Mater., (1999) Vol. 54, 203

[16] H. Chiriac, T. Ovari and Gh. Pop "*Internal stress distribution in glass-covered amorphous magnetic wires* " Phys. Rev. B., (1995) Vol. 52, N. 14, 104-113

[17] F. Humphrey, K. Mohri, J. Yamasaki, H. Kawamura, R. Malmhall and I. Ogasawara "*Magnetic properties of amorphous Metals*" ed. A. Hernando et al., Amsterdam:Elsevier (1993) 110

[18] A. Hernando, M. Barro, G. Rivero, D. Chen and M. Vazquez "*Magnetoelastic Effects and applications*" ed. L. Lanotte, Amsterdam: Elsevier (1993) p.39

[19] D. Raskin and C. Smith "*Amorphous Metallic Alloys*" ed. F.E. Luborsky, London: Butterworths (1992) 381

[20] A. Hernando and M. Vazquez "*Rapidly Solidified Alloys*" ed. H.H. Liebermann, New York: Marcel Dekker (1993) 110

[21] M. Vazquez and A. Hernando "*A soft magnetic wire for sensor applications*" J. Phys. D: Appl. Phys., (1996) Vol. 29, 939-949

Chapter 4. Amorphous microwires with large magnetostriction: magnetisation process and applications.

This chapter is devoted to the investigation into re-entrant magnetic flux reversal of amorphous microwires with positive magnetostriction. This process leading to very fast magnetisation switching makes wire elements unique for applications in magnetic tagging technology. The content of this chapter is divided into four parts. I start with a more detailed review of the quasi-static axial magnetisation processes in Section 4.1, which is determined by the combined effects of the shape and magnetoelastic anisotropies. This gives the necessary background to proceed to the investigation of dynamic hysteresis (up to 200 kHz) in Section 4.2. The results obtained in this study on the transformations in hysteresis curves with increasing frequency are discussed by considering the Néel-Brown model of stochastic activation over domain wall pinning barrier. This is a new approach to model magnetisation dynamics and relaxation processes in magnetic bistable materials. Thus, the frequency dependence of the nucleation (or switching) field is evaluated by considering a "waiting time" for closure domain wall to escape the pinned state, rather than involving eddy current mechanism. The domain wall propagation and domain wall configuration in established stage would be consistent with quasi dc models, however. Section 4.3 concerns the controllable selective treatment of glass-coated magnetic microwires by laser irradiation. This local annealing by an argon laser results in the formation of weakly interacting heterogeneous structures with different magnetic properties. In the case of wire with positive magnetostriction, this treatment allows a "magnetic bar-code" to be written on a small piece of microwire. To the best of my knowledge, this possibility was demonstrated for the first time. Finally, Section 4.4 presents a specific security application utilising re-entrant magnetisation reversal. I proposed to use a number of glass-coated microwires with different switching fields, each of which constitutes a bit of information. Therefore, the assembly of these microwires can be used to set a specific magnetic bar code. I also have designed the reading apparatus for the remote information detection (at a distance of about 15 cm).

4.1 Domain structure and quasi dc axial magnetisation process.

Amorphous microwires with high magnetostriction are characterised by a core and sheet domain structure with the magnetisation parallel to the wire axis in the inner core and radial (or circumferential) in the outer region. This structure is caused by the combination of the residual stress distribution and wire geometry, as discussed in Sections 2 and 3. The axial anisotropy is important for the re-entrant reversal, which occurs in the core and takes place by the propagation of a domain wall along the wire.

In thin wires with axial easy magnetisation a domain wall is very elongated in shape as shown in Fig. 4.1. The elongated shape, diluting magnetic free poles over larger volume, decreases stray fields. Assuming that the domain wall shape at equilibrium is one half of a prolate ellipsoid, minimizing the total energy with respect to the domain length, l_d, yields an energy balance between the wall energy and magnetostatic energy [1]. It is most convenient to express these energies in terms of fields, so that:

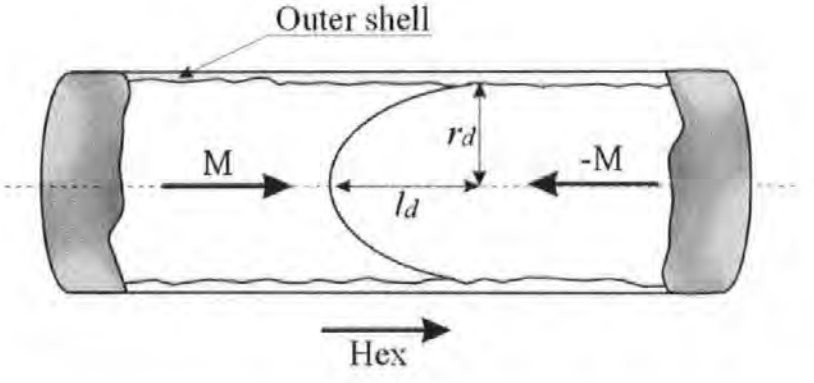

Fig. 4.1 Formation of an elongated domain wall in the core with uniaxial anisotropy.

$$H_w - H_d + H_{ex} = 0, \tag{4.1}$$

$$H_w = 3\pi\gamma / 8M_s r_d \ , \ \gamma = 4\left\langle\sqrt{KA}\right\rangle, \tag{4.2}$$

$$H_d = 4\pi M_s \left(\frac{r_d}{l_d}\right)^2 \left(\ln\left(\frac{2l_d}{r_d}\right) - 1\right). \tag{4.3}$$

Here H_{ex} is the field required to move DW (typically, smaller than the nucleation field), H_w is the effective field resulting from DW surface tension, γ is DW energy per unit area, M_s is the saturation magnetisation, r_d is the radius of the domain, A is the exchange constant, K is an anisotropy constant, H_d is the demagnetising field. The expression for H_d is valid only when $r_d / l_d << 1$. For a moving wall, the damping essentially balances the applied field H_{ex} so the wall moves with little or no changes in shape, which is consistent with what is observed. If r_d is constant, equation (4.1) determines the domain length l_d:

$$l_d^2 = \frac{32 M_S^2 r_d^3 [\ln(2l_d / r_d) - 1]}{3\gamma} \tag{4.4}$$

It is seen that the length l_d decreases with increasing DW energy γ.

This model can be applied for the consideration of the closure domain structure at the wire ends. I can assume that this elongated DW is spontaneously nucleated at the end and extends into the wire to a distance of the order of l_d, which can be then understood as a correlation length denoting the balance between the energies from magnetostatic and magneto-elastic origins. In order to observe bistability, the wire length must be longer than l_d. For wires prepared by in-water rotating process, the critical length is in the range of 2-7 cm [1]. In the case of glass-coated wires, which have much higher internal stress and hence much higher DW surface energy γ, the critical length can be as small as few millimetres [2].

In short wires, which are typically used as sensor elements, closure domains structure plays a very important role. The experimental evidence of the existence of closure domains of the elongated shape is reported in Ref. 3,4. Figure 4.2 shows the domain pattern of an axially polished amorphous wire close to one end. The presence of various axial domains at the end of the inner is clearly seen.

Fig. 4.2. Existence of the closure domain structure at the ends of Fe-based amorphous wire as demonstrated by the magneto-optical Kerr effect (the picture was taken at the end of an axially polished wire) Figure adapted from Ref [3].

When applying a longitudinal magnetic field opposite to the remanence, the already existing closure domain structures at the ends enlarge towards the centre of the wire. At the switching field H_s, the domain wall from one end of the wire breaks through the pinning site and irreversibly moves towards the other end, giving rise to the sharp change in magnetisation. This DW propagation mode can be either alternating, from a different end after each reversal, or unidirectional, depending on the external agents such as magnetic fields or applied stresses. The propagation wall velocity depends on the strength of the anisotropy in the core and on the field intensity. During a steady-state propagation, the shape of the wall does not change being ellipsoidal or conical [5]. There are some works wherein a quasi-planar DW model was proposed [6]. This would result in an axially asymmetrical domain structure, which is not supported by the experiment. In this work, I will consider only symmetrical ellipsoidal DW. Magnetic bistable behaviour appears in samples with a well-defined quasi-single-domain inner core. The particular value of the switching field H_s depends on the thermal history as well as on the applied mechanical stresses [7].

The considered model estimates the DW shape for steady-state processes. There is no mechanism involved which would describe the DW transformation during its breaking

through the pinning site. Some modifications are needed to apply the model to describe dynamical processes. It is known that DW dynamics in ferromagnetic systems exhibits intrinsic stochastic properties [8,9]. Magnetic viscosity can be understood in terms of thermal or other noise activation over energy barriers. This mechanism explains the increase in switching field with increasing frequency.

4.2 Dynamic hysteresis in amorphous wires with positive magnetostriction.

In this Section, the experimental study of dynamical hysteresis in bistable wires is presented followed by the discussion in terms of modified Néel-Brown model of the magnetisation reversal due to the activation over energy barrier [10,11]. Most of experiments of hysteresis in these materials (and in general) are performed under dc or quasi dc conditions. As operational frequencies become progressively higher, there is an interest in studying the magnetisation reversal at corresponding frequencies. Here, the magnetisation curves in of Fe-based glass-coated microwires have been measured for frequencies up to 200 kHz with help of specially designed miniature hysteresis tracer. The frequency dependence of the switching field is evaluated by considering a "waiting time" for closure domain wall to escape the pinned state.

a. Experimental set-up for dynamic hysteresis measurements.

For dynamic hysteresis study, glass covered amorphous wires of the composition $Fe_{15}Co_{55.4}Mn_{7.2}B_{12.4}Si_{10}$ were used (kindly provided by "AmoTec" Ltd, Moldova). The wires had a core of 12.4-16.1 μm in diameter covered by glass with total diameter of 18.6-22.1 μm. A special hysteresis loop tracer was designed for high frequency measurements (Fig. 4.3.). Two pick-up coils, (3) and (4), of 0.15 cm in diameter, 1 cm long with 30 turns are placed inside a driving solenoid, (2), of 0.75 cm in diameter, 6 cm long with 180 turns. The driving solenoid is connected to a signal generator, (1), and produces the ramping fields of the

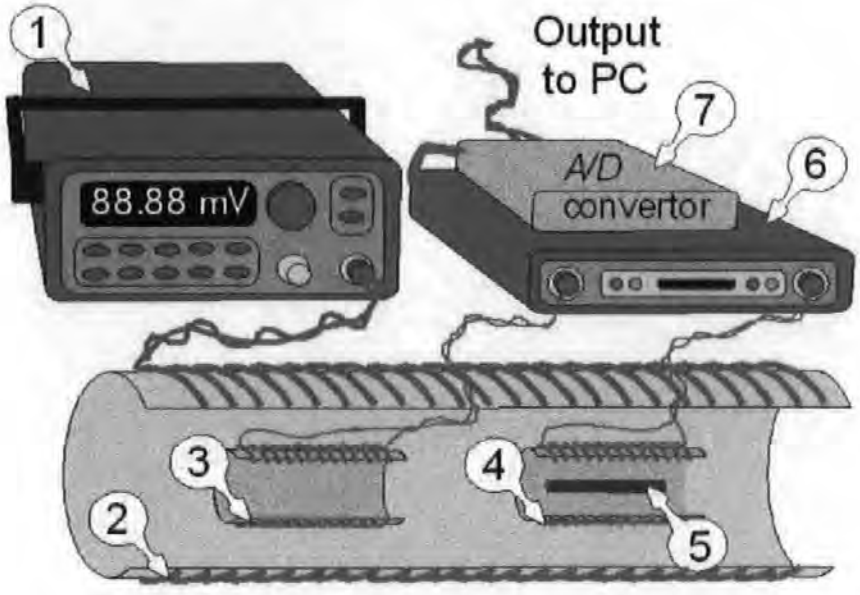

Fig. 4.3. Compensation magnetometer: (1) Signal generator, (2) driving solenoid, (3) compensation coil, (4) pick-up coil, (5) sample, (6) processing electronics, and (7) A/D converter.

different forms and frequencies. The wire element (5) 2 cm long was placed in one pick-up coil, (4), which was used for detection of magnetization changes while the other, (3), is designed for compensation of the driving field. A differential detection system, (6), contains amplifiers and high frequency band-pass filters to suppress noise. For frequencies higher than a few kilohertz, the effect of distributed inductance and capacitance becomes significant introducing distortions into the output voltage signal. The hysteresis tracer was calibrated using an integro-differential correction function. The parameters of the correction function at different frequencies were calculated and checked by measuring the system response to various periodic input signals (of sinusoidal, rectangular, triangular forms). The driving field amplitude was 7 Oe, which was sufficient to realize the magnetization switching at frequencies up to 200 kHz.

Figure 4.4 shows a typical set of hysteresis loops reconstructed from measured signals at different frequencies of periodic driving field of constant amplitude. At low frequencies, the magnetization process is well described in terms of a large Barkhausen jump, which happens at a switching field of about 1 Oe. Three important features characterize dynamic hysteresis in the wires studied. First, the field at which the large Barkhausen jumps occur (switching field) considerably increases with frequency and changes from 1 Oe at low

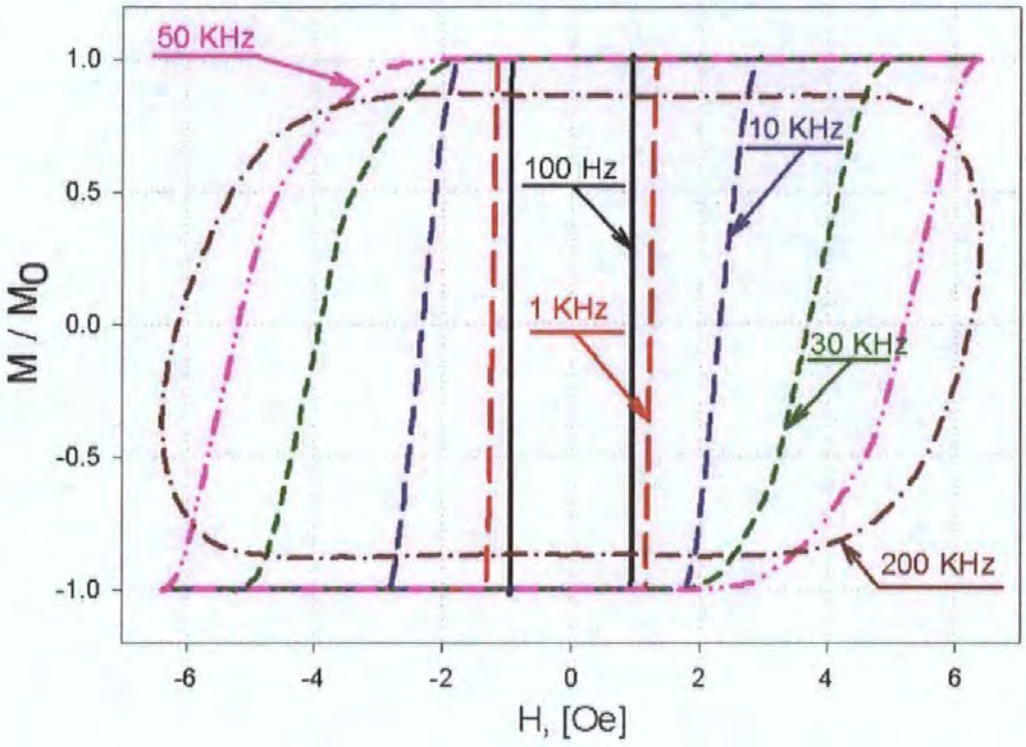

Fig. 4.4. Dynamic hysteresis loops in a glass covered amorphous wire.

frequencies to 2 Oe at a frequency of 20 kHz. Second, the time of magnetic field ramping becomes comparable with the time of magnetization changes at frequencies above 10 kHz and the hysteresis loop opens up. Third, the domain walls that carry magnetization reversal fail to reach sample edges at frequencies above 200 kHz and hysteresis loops acquire an elliptical shape. It was also found that time of a large Barkhausen jump decreases with an increase of frequency of a driving field.

b. Modified Néel-Brown model

To quantify the frequency dependence of the switching field we make use of the Néel-Brown model of magnetization reversal, which was originally developed for description of the magnetization flip in uniaxial magnetic particles due to thermal activation over the anisotropy barrier. Generally, the modification of the hysteresis curves in conducting magnetic materials due to higher frequency magnetising fields is described introducing an additional energy

dissipation resulting from eddy current losses [12,13]. However, in regard to bystable systems, within this approach it is not possible to explain an increase in the switching field with a frequency since the rate of the magnetisation change is zero before the flip. I suggest that the switching field H_s in my experiments is defined by the closure DW activation over the initial barrier ΔU and modify the Néel-Brown model to account for this scenario.

According to the model, the probability rate $p(t)$ of DW to overcoming the barrier is given by

$$p(t) = v_0 \exp\left(-\frac{\Delta U - H(t)MV}{D}\right), \tag{4.5}$$

where v_0 is the attempt frequency, $H(t)$ is the ramping magnetic field, M is the magnetization, V is an activation volume and D is the noise parameter. Assumptions are made here that the initial energy barrier ΔU does not depend upon magnetic field, the frequency of the magnetic field is much lower than the attempt frequency and magnetic field is treated as a perturbation for simplicity. The probability $Q(t)$ of DW to stay in the pinned state obeys the following equation

$$dQ/dt = -p(t)\cdot Q. \tag{4.6}$$

Assuming that a jump will eventually happen at some small value of Q_0 and using equation (4.5), we obtain an implicit equation for the jump time t_j

$$\int_{t_0}^{t_j} \exp\left(\frac{H(t)MV}{D}\right)dt = \frac{\ln(1/Q_0)}{v_0}\exp\left(\frac{\Delta U}{D}\right) \tag{4.7}$$

where t_0 is the time at which a reversal nucleus appears and DW is able to jump. Taking a saw-tooth dependence of the magnetic field $H(t) = H_0\omega t$ and assuming that the time t_0 corresponds to some field H_{S0} (when ω tends to be zero) we finally get the switching field of the large Barkhausen jump as

$$H_S = \frac{D}{MV}\ln\left(\frac{\omega}{\omega_0}+1\right) + H_{S0} \tag{4.8}$$

where

$$\omega_0 = \frac{Dv_0}{\ln(1/Q_0)H_0MV}\exp\left(-\frac{\Delta U - H_{s0}MV}{D}\right)$$

Equation (4.8) agrees excellently with the measured dependence of the switching field H_s upon frequency of dynamical hysteresis loops. Figure 4.5 demonstrates that the agreement between theory and experiment extends over a wide frequency range 0.1-30 kHz (where the ramping field amplitude was enough to drive the sample into saturation). Equation (4.8) worked well for different bistable wires in a large temperature range down to the temperature of liquid nitrogen. Careful comparison of the change in the logarithm slope with decrease of temperature shows that the temperature activation accounts for only less than 10% of total noise. This implies that fluctuating external magnetic fields were the main source of noise. Extracting the logarithmic pre-factor from the graph shown in Fig.4.5, I estimate a lower limit of an activation volume as $V \approx 8 \cdot 10^{-17}$ cm^3 which gives linear dimension of activation as $d \approx 2 \cdot 10^{-6}$ cm. This scale is close to the domain wall width in this material.

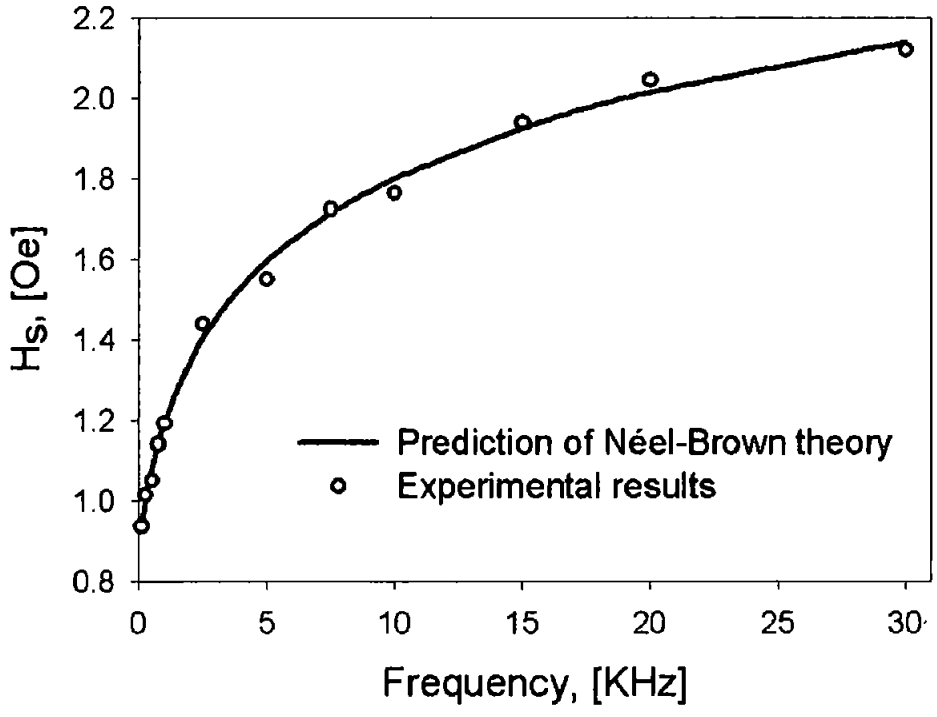

Fig. 4.5. Average switching field of a large Barkhausen jump as a function of frequency at room temperature.
Simulation equation is H_S= 0.3 ln (1+ω/624.5) +0.93.*

An activation process always leads to the distribution of a switching field. This important feature of the Néel-Brown model was also observed in my experiments. The distribution was Gaussian and its width was higher at lower frequencies in accordance with the model.

c. Domain wall propagation

Once activated, DW propagates forming an elongated shape to minimise the demagnetising energy [14]. During this process, some additional demagnetising field H_d assists its movement. For a moving wall, the damping essentially balances the effective field H_{eff}, which includes the applied field, demagnetisation field and coercivity field. The DW velocity is of the form:

$$u = \frac{2M_S}{\beta} H_{eff}(t), \tag{4.9}$$

where β is the damping parameter. Since the switching field increases with the frequency of field ramping it means that DW moves in higher fields at higher frequencies. Considering that the damping parameter does not change essentially with frequency, equation (3.7) leads to an increase of an average DW velocity $\langle u \rangle$ and hence to a decrease of the time of magnetization reversal which can be estimated as $l/\langle u \rangle$, where l is the sample length (or distance between nucleation sites). For fast reversal processes we can assume that the external field does not change during the jump and take $H_{eff}(t) \approx H_S$. Then, it follows from (4.9), that the time of magnetization reversal τ has to be inversely proportional to the switching field H_S. This is proven in Fig. 4.6 where the plot $1/\tau$ vs H_S is given. The data used cover the frequency range from 100 Hz to 100 kHz. The interception with the field axis of the linear regression to the experiment gives an average demagnetisation field of about 1.6 Oe. Finally, we can combine the expression for switching field (4.8) with linear dependence for the inverse time and estimate the frequency at which τ becomes of the order of the period of the driving field. A straightforward evaluation gives the frequency of about 100 kHz for my samples. This coincides with the experimental results showing elliptical hysteresis loops at frequencies

higher than 100 kHz.

It should also be stated that with increasing frequency the time of magnetization reversal drops (Fig. 4.7). The change of the magnetization time with frequency is attributed to the change of the switching field. At the end of this chapter, in the section "Application based on Barkhausen jump" I will demonstrate importance of dynamic features of the magnetic microwires with positive magnetostriction.

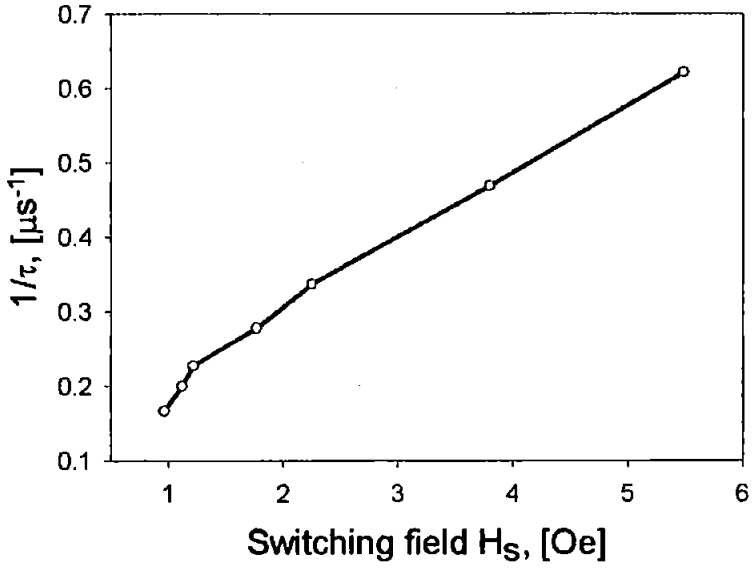

Fig. 4.6. Inverse of reversal time τ as a function of switching field H_S

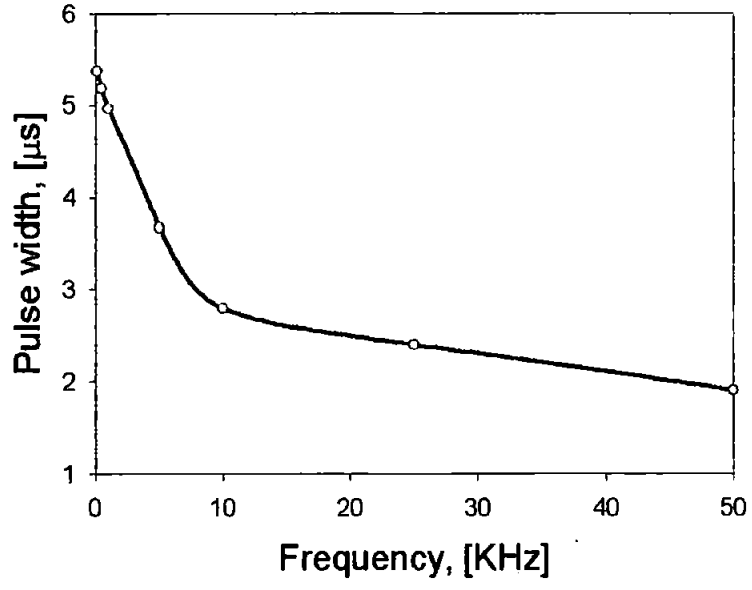

Fig. 4.7. Reversal time as a function of frequency

Summarizing results of this section, I have found that the dynamic hysteresis in bistable amorphous wires under a periodic magnetic field is described well by Néel-Brown theory of activation of a closure domain wall over a pinning barrier. The switching field follows a logarithmic function of frequency. The evaluated size of an activation volume is comparable to the size of the domain wall in amorphous materials. Pulse width drops with increasing frequency and time of magnetization reversal τ is inversely proportional to the switching field H_S.

4.3 The effect of a laser annealing on magnetic properties of amorphous microwires.

I already noted above, that the anisotropy and the domain structure are determined by the balance between the magnetoelastic and magnetostatic (shape) contributions. Annealing under stress and/or magnetic field results in a particular frozen-in stress distribution, changing the magnetoelastic energy. Then, various kinds of magnetic structures can be realised by a suitable postproduction treatment, which normally affects the whole sample. A local processing, which influences only a part of an amorphous material, is also possible. For example, laser radiation was used to achieve local crystallization of amorphous CoP alloys [15], to change locally the anisotropy of metallic glasses [16, 17]. However, little work has been done to investigate the effect of a local treatment of amorphous materials with the aim to produce heterogeneous magnetic structures. In particular, the development of a method for the predetermined, spatially patterned modification of glass-coated amorphous wires would be a very attractive proposition.

In this section I present my results on the effect of local laser annealing of glass-coated amorphous magnetic wires. I demonstrate that magnetic properties of amorphous wires can be locally and controllably tuned by argon laser processing due to the formation of magnetic heterostructures. In particular, the use of this treatment for wires exhibiting large Barkhausen effect produces a number of portions switching at different fields. This can be of great interest for magnetic tag application. I used wire of the following compositions: $Fe_{74}B_{13}Si_{11}Co_2$ (sample 1) and $Fe_{66}B_{13}Si_{11}Co_{10}$ (sample 2) with large positive magnetostriction for which an

axial anisotropy and re-entrant magnetization reversal are typical. In the experiment, we exposed wires to the laser light and investigated the changes in the bistable behavior of samples before and after the treatment.

The sketch of the installation is shown in Fig. 4.8, which was designed in collaboration with Aston University. In the experiment, the magnetic wires were exposed to the emission of an argon laser operating at a wavelength of 488nm. The laser beam was focused into an elliptical spot, aligned with the wire, by a positive cylindrical lens. The width of the spot across the wire was about of 25 μm. An additional negative cylindrical lens was used for expanding the laser spot along the wire. Depending on the position of the negative lens, the spot length varied from ~2 to 10 mm. It was possible to focus the beam tighter, down to a length of 60 μm, by substituting the negative lens with a microscope objective.

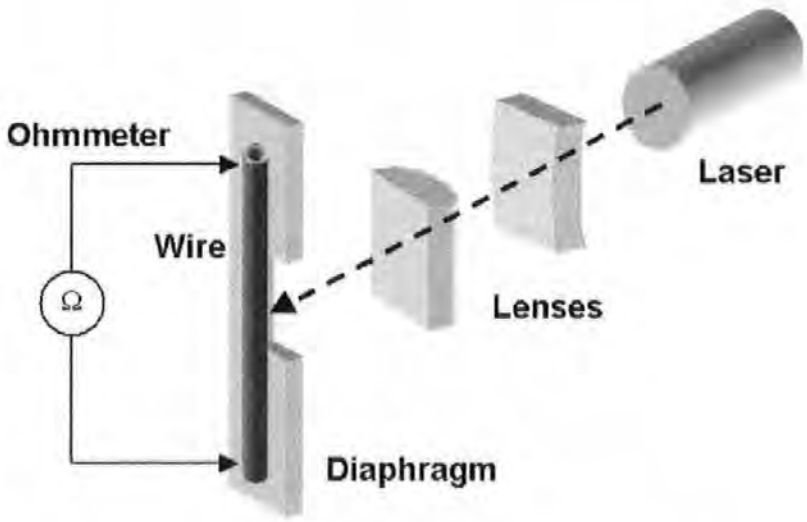

Fig. 4.8. Schematic diagram of argon laser processing installation due to the formation of magnetic heterostructures.

The wire was fixed on bracket holder that allowed an exposure of the middle section of the wire. A three-coordinate translation stage provided precise alignment of the holder. The maximum power in the beam was 6.5W, corresponding to the maximum intensity in the focus in excess of 10^4 W/cm^2. A change in the wire resistance was used as a reference parameter for the laser treatment. The dependence of the wire resistance upon temperature has been

calibrated in a thermal bath prior to processing. The wire resistance changed with temperature at a rate $\eta=\Delta R/(R\cdot\Delta T)=1.2\times10^{-4}\ C^{-1}$. Therefore, knowing the length of the exposed section, we can roughly evaluate the local temperature of the treated wire from the total resistance of the sample. When a wire was exposed to relatively low laser intensity below 10^3 W/cm^2, its resistance changed reversibly, i.e., the resistance increased and returned to the initial value after irradiation. At a higher level of exposure, the wire resistance dropped irreversibly by 1%–3%. The likely reason for that is a crystallization of the sample and a higher conductivity of a crystalline state. During the experiments, care was taken to avoid the crystallization process. The annealing procedure consisted of an increase and a decrease of laser power until the total wire resistance fell to a predetermined value below the initial value. The exposure time was typically one minute.

I investigated the effect of laser treatment on the characteristics of the magnetisation reversal. The magnetisation curves were measured by a conventional inductive method (described in previous Section) using two differential pickup coils of 30 turns, 0.5 mm in inner diameter (0.8 mm in outer diameter) and 1 cm long. Figures 4.9(a) and 4.9(c) show the measured differential response of an unprocessed wire and that of a partially laser treated wire (sample 1), respectively. The total sample length was 2 cm and the length of the treated portion was about 5 mm. For as-cast wires, a sharp voltage pulse was detected at a magnetic field of 0.4 Oe (see Fig. 4.9(a)). This pulse is characteristic of a large Barkhausen jump. Placing the processed wire in such a way that the detection coil contained both treated and non-treated portions, I detected two voltage pulses (two large Barkhausen jumps) shown in Fig. 4.9(c). The first pulse corresponds to the field 0.6 Oe and the other occurs at higher field of 2 Oe. On the other hand, if the treated portion was outside the detection coil there was no change in the magnetization reversal behaviour in comparison with as-cast wires (Fig. 4.9(a)).

Therefore, the laser annealing induced a local change in coercivity and produced no measurable effect on the adjacent areas. By reducing the width of the pickup coils and measuring local magnetisation loops, I confirmed that the magnetisation reversal happens in treated and non-treated portions by means of a large Barkhausen jump occurring at different fields. As a result, the differential response shown in Fig. 4.9(c) has two pulses corresponding to the coercivity of processed and unprocessed material. Similarly, one can compare the reconstructed hysteresis loops in Fig. 4.9(b) (unprocessed wire) and Fig. 4.9(d) (partially annealed sample 1). The hysteresis loop of sample 1 consists of a superposition of two rectangular hysteresis loops with two distinctly different coercivities. It means that a locally laser treated bistable wire represents an interesting prototype of a simple 2-bit element for product labelling.

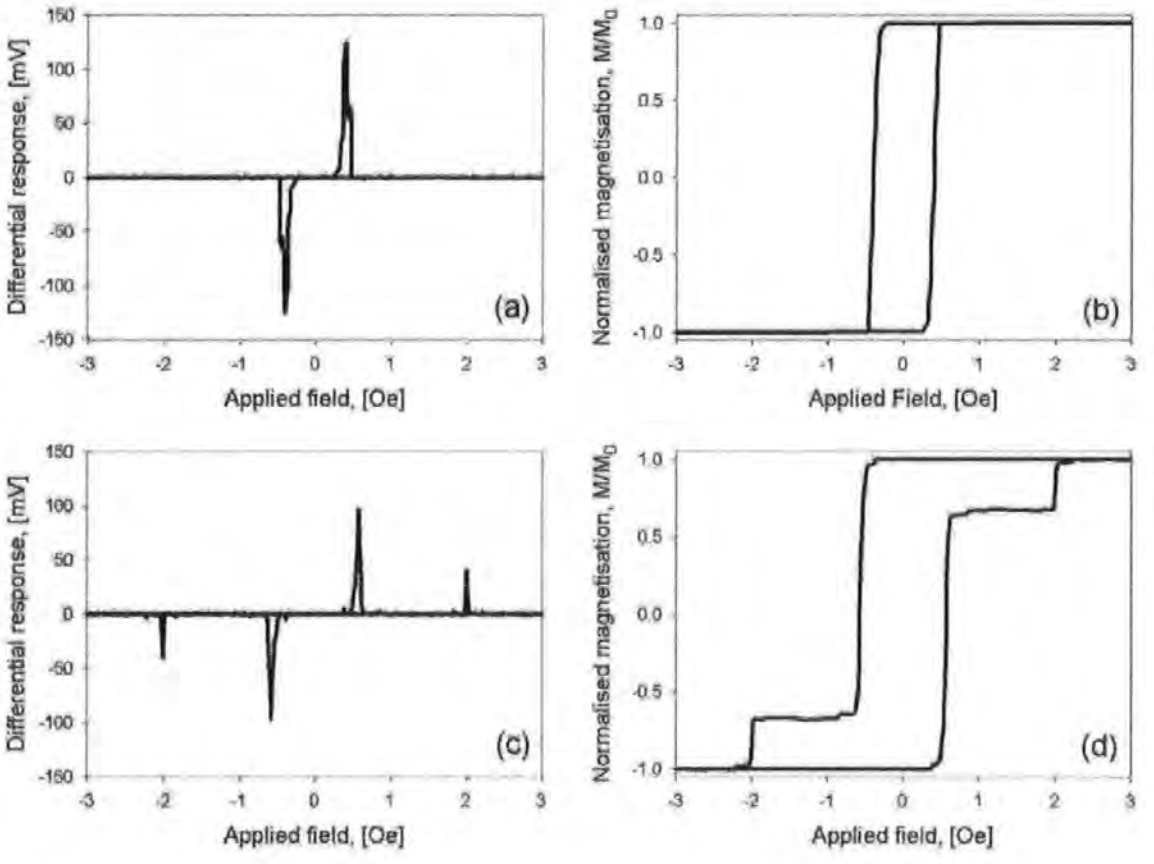

ERROR: undefined
OFFENDING COMMAND: r

STACK:

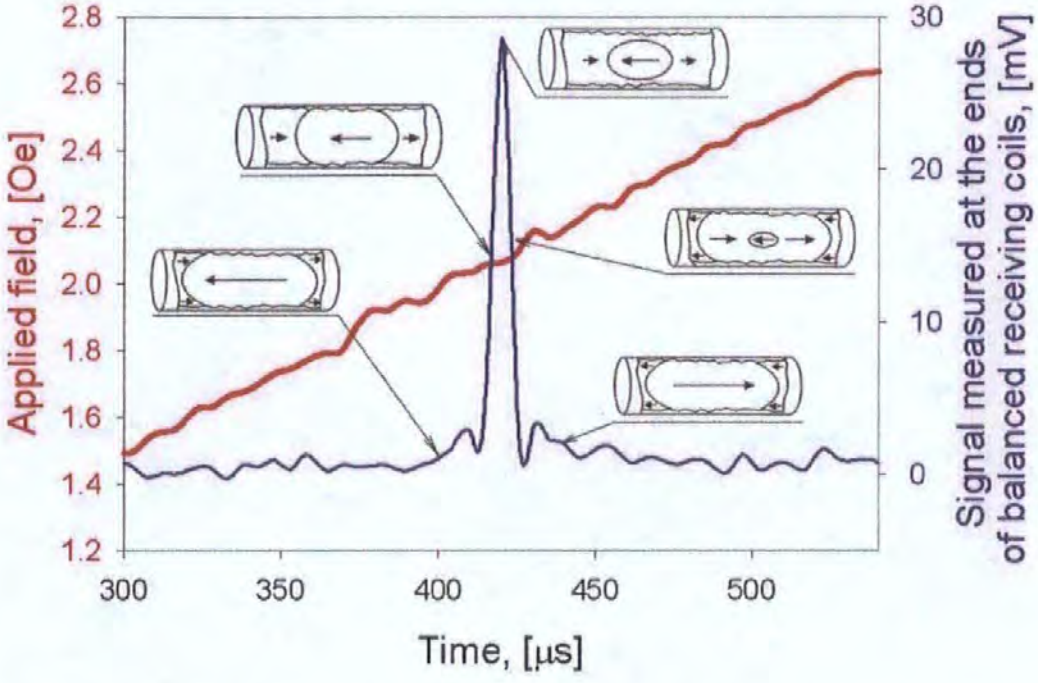

Fig. 4.13. Zoomed region of Fig 4.12 at the point where remagnetisation process appears with inserts of wire magnetisation model at different remagnetisation stages.

characteristics, which is related to the corresponding critical length of bistability [1,2]. These characteristics can be improved considerably using glass-coated Fe-based microwires, which can produce voltage peaks with the width smaller than 30 μs and the height is around 0.03 mV per turn (for 12 μm metallic core diameter). Furthermore, the minimum critical length is about 2 mm. The switching field is in the range of 0.1-8 Oe.

4.4.1 1-D interrogation system

The detection apparatus (Reader) consists of a means for generating a uniform a.c. magnetic field in an interrogation volume and a differential pick-up coil arrangement for detecting a generated voltage signal from the wires. The system also comprises several recognising and displaying electronic units for different types of recycling devices.

a. Coil's system

Figure 4.14 illustrates the concept for a 1-D scanned interrogation system. Such a system can operate with one tag in the interrogation volume, whose orientation is in parallel with the filed direction. This type of the system has a simple form and is convenient to use to explain the system operation. The magnetic tag is excited by the magnetic field produced by four transmit coils. The transmit coils generate a substantially uniform magnetic field in the central part of the interrogation volume. The "term uniform" is used to describe a vector field that has substantially the same amplitude and direction over a spatial volume.

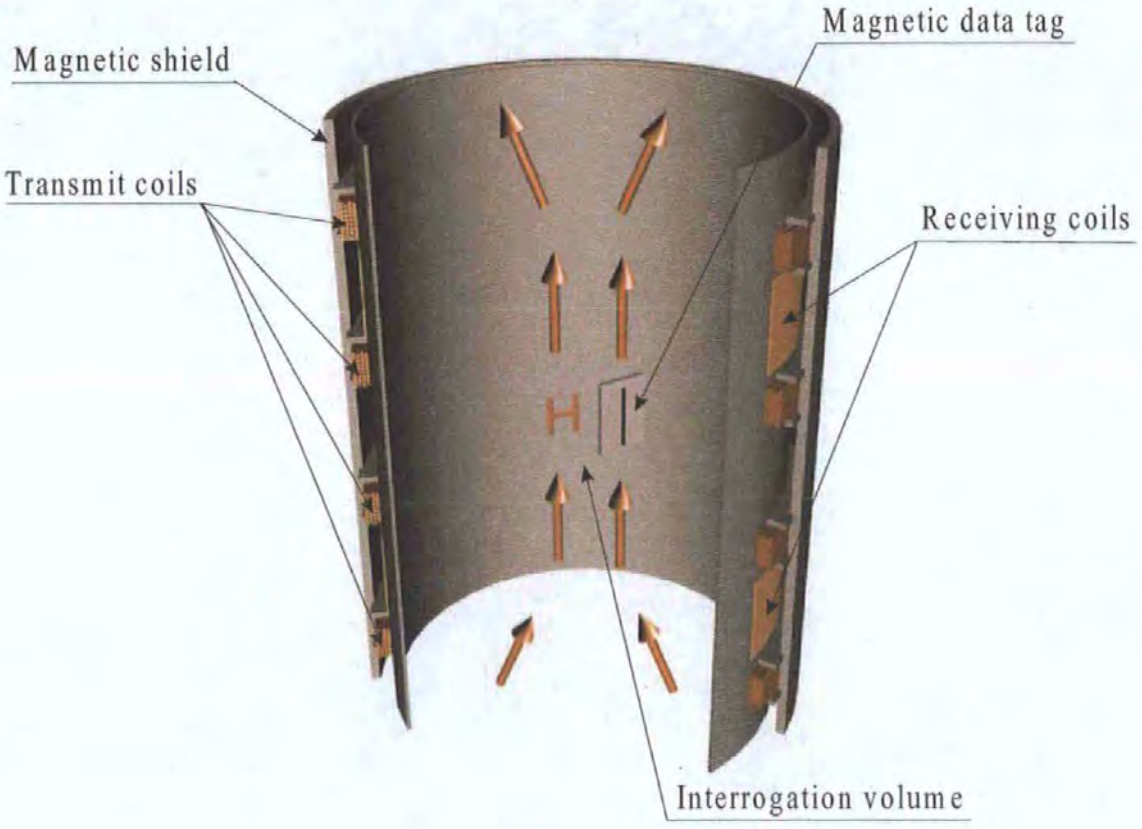

Fig. 4.14. 1-D scanned interrogation system

The receiving coils are both arranged such that their magnetic axis (defined as the vector along which an impinging magnetic field vector produces maximum electromotive force - emf) is aligned to the magnetic field direction. Each receiving coil comprises a short solenoid coil. The receiving coils are 100 mm in diameter and 50 mm long having 200 turns

of 0.25 mm diameter enamelled copper wire (ecw). The receive coils have approximately 4 mH inductance and 20 Ω resistance.

The transmitting coils are electrically connected in series and their arrangement is similar to a Helmholtz configuration. Each coil comprises 100 turns wound over 10 layers with 1mm ecw and is a short solenoid 10 mm long and 100 mm in diameter. The combined inductance of the coils is 3.3 mH. The coils are separated a distance apart along their magnetic axis. The important feature is that the magnetic field produced around the tag is substantially uniform. The field produced by coils in the central part of the interrogation volume is about 6 Oe.

The operation of the receiving coils is as follows. The receiving coils are designed such that in the presence of the transmit magnetic field, the emfs produced by receiving coils are equal and opposite. Such an arrangement is referred to as differential or balanced and is achieved by a number of well-known techniques [20]. The methods include varying the turn's ratio between the coils, slight distortions in the enclosed coil area or very small orientation changes. When a magnetic material is placed inside one of the receiving coils, its property of permeability causes the magnetic field flux lines to link with the material. The effect is to cause more flux to flow inside the coil than would be the case with no magnetic material. The coil output emf is proportional only to the ratio of change of linked flux, whilst being insensitive to the transmitting magnetic field. This feature is known art and is employed by magnetometers and other instruments used to characterise magnetic material properties.

All the scanning system is covered by a dual mu-metallic magnetic shield to reduce an influence of the external magnetic noise.

b. Magnetic data tag

The tag element material was a glass-coated microwire with a positive magnetostriction attached to a plastic or paper substrate. The wires had a metallic core of 18-22 μm in diameter covered by glass with total diameter of 20-25 μm. The wire length was 10 mm. Table 4.1 shows basic properties of the microwires, which have been chosen for LFID application.

Alloy	Metal diameter (average value) ±3 μm	Glass thickness (average value) ±0.5 μm	Coercivity force (average value) ±0.2 Oe
$Fe_{55.4}Co_{15}Mn_{7.2}B_{12.4}Si_{10}$	18.6 μm	2.2 μm	0.8 Oe
$Fe_{65.4}Co_{8}Mn_{4.2}B_{12.4}Si_{10}$	19.6 μm	3.6 μm	1.4 Oe
$Fe_{60.1}Co_{12}Mn_{3.9}B_{12}Si_{10}$	21.4 μm	2.8 μm	2.1 Oe

Table 4.1. Basic characteristics of the materials chosen for the `Recycling project`

c. Processing electronics

As a part of research, several prototypes have been developed and tested to find the best solution in term of reasonable cost, sensitivity and quality. The first one is a computer-based version of the Reader (see Fig. 4.15). The voltages induced in receiving coils are assigned numerical values by A/D converter and analysed by specially created computer software for recovering and displaying data from the magnetic tag. The computer-based prototype made it possible to demonstrate the feasibility of using magnetic microwires as magnetic tags in such kind of systems.

Fig. 4.15. View of the computer-based recognition system.

Considering that mass-production facility has to be inexpensive, the second version of the Reader based on analogue electronics solely was developed. Fig. 4.16 shows outward of the analogue system. The analogue-based prototype is portable.

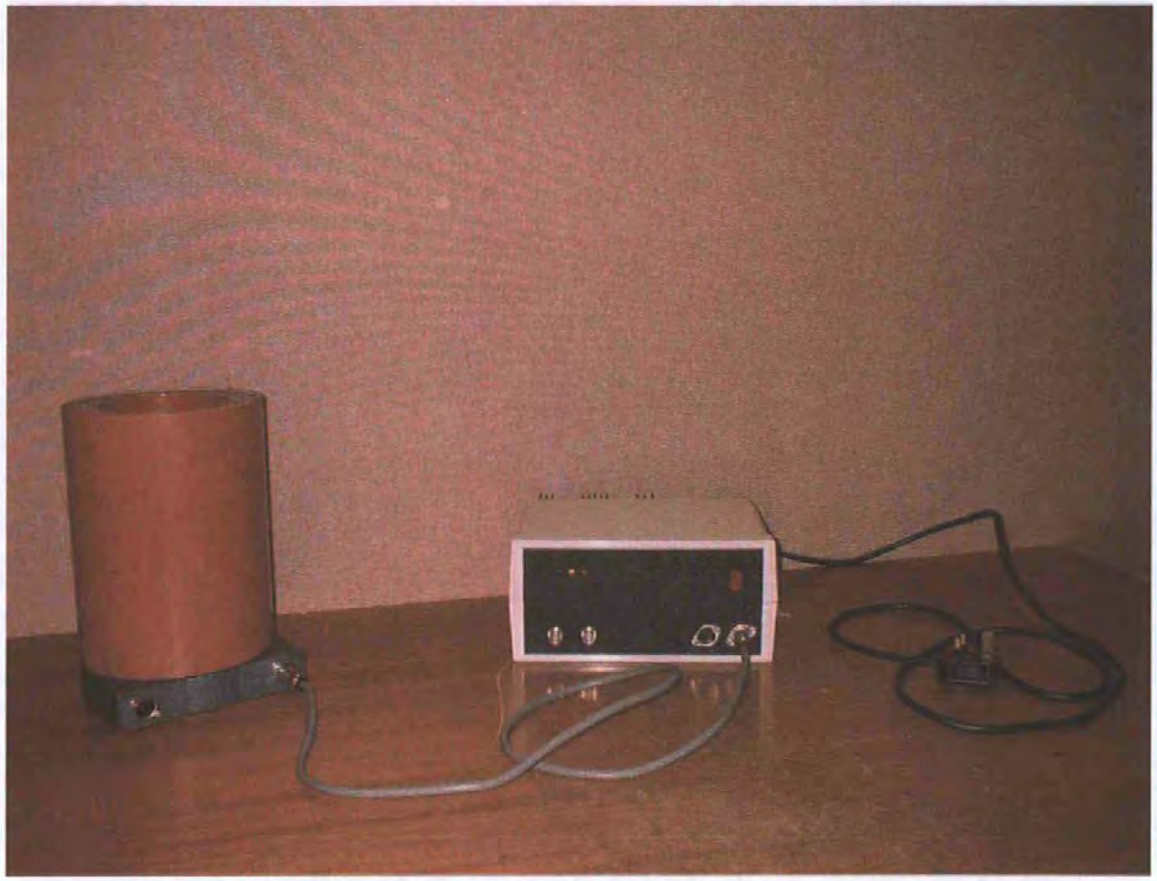

Fig. 4.16. View of the analogue system.

The basic principles of recognition are common for both modifications of the Reader and can be demonstrated using the simple analogue based prototype. Analogue Reader contains three circuits: driving circuit, amplifying-filtering circuit and identifying circuit.

The driving circuit is schematically shown in fig 4.17. It operates as follow. A sine generator (microchip MAX038) generates a 200 Hz signal with amplitude 2Vp-p. The signal frequency can be adjusted with R_F. A pre-amplifier (microchip TL081) is used for adjusting the amplitude of the signal applied to the transmitting coils by adjusting the value of the variable resistor R_A. The high power amplifier (chip OPA549T) provides the drive for the transmitting coils. The drive current is set to achieve the appropriate transmitting field level. The voltage applied to the transmitting coils is about 8Vp-p. This generates the transmitting current of about 1.6A rms (measured by means of R_I), yielding the transmitting field of approximately 6 Oe. The upper limit of this field level is determined by the tag material

saturation, with the consequent suppression of the sharp magnetisation transition, which encode the data. The detailed diagram of the driving circuit is given in Appendix A.1.

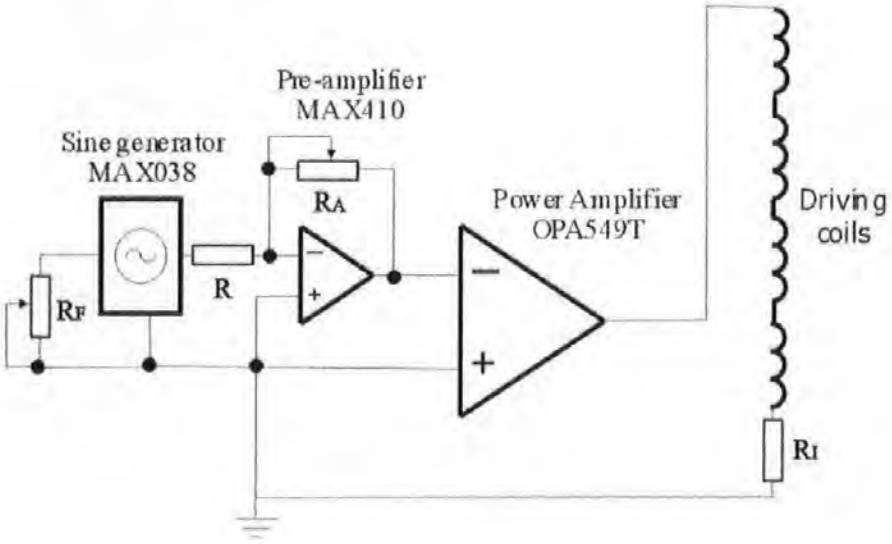

Fig. 4.17. Schematic view of the driving circuit.

The amplifying-filtering circuit is given in Fig.4.18 (the details can be found in Appendix A.2). The balanced receive coils are connected to the amplifying and filtering electronics. The receive coils are designed such that in the presence of the transmit magnetic field, the emfs in them are equal and opposite. However, it is quite difficult to achieve the full compensation only by mechanical means. The variable resistor R_B is used for compensating residual distortion. The band-pass filter (BPF) removes the residual low frequency distortion

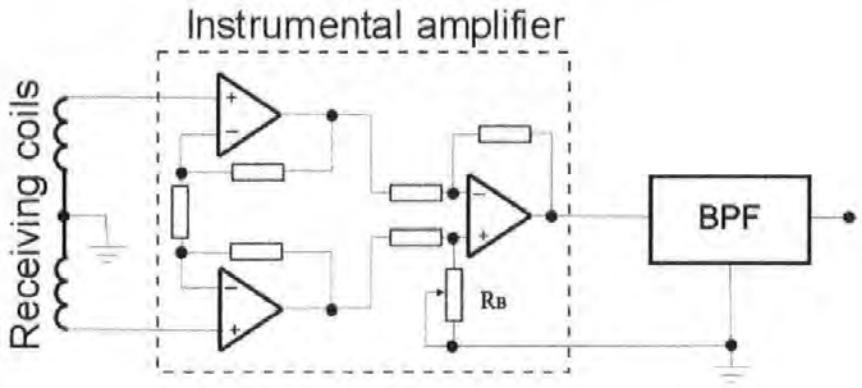

Fig. 4.18. Schematic view of the amplifying-filtering circuit.

in the transmitter as well as the low frequency distortion in the receiver caused by unwanted receive coil imbalance or any other magnetic materials placed in the interrogation volume. The filter also limits high frequency noise, the sources of which are thermal, electronic (amplifier), and interfering ac magnetic signals. In addition, it is desirable that the receiver bandwidth is matched with the characteristics of the tag element impulse response induced by the transmitter. In practice, a high-band of the filter set at 25 kHz is an efficient compromise. Fig. 4.12 shows a typical response after the amplification and filtering stage (green curve). The sinusoidal signal (red curve) is the voltage measured across the resistor R_I (Fig 4.17). This voltage is proportional to the current flowing through the coil. The magnetic field, in turn, is a function of current. The amplification and filtering boards also contain a so-called selector circuit (Fig. 4.19). It is designed for eliminating negative pulses and to modify the positive pulses to be square, which will be used as strobe signal for running the following digital electronics. At the output of this circuit only positive pulse at the positive portion of the sine waveform appear as it illustrated in Fig 4.20.

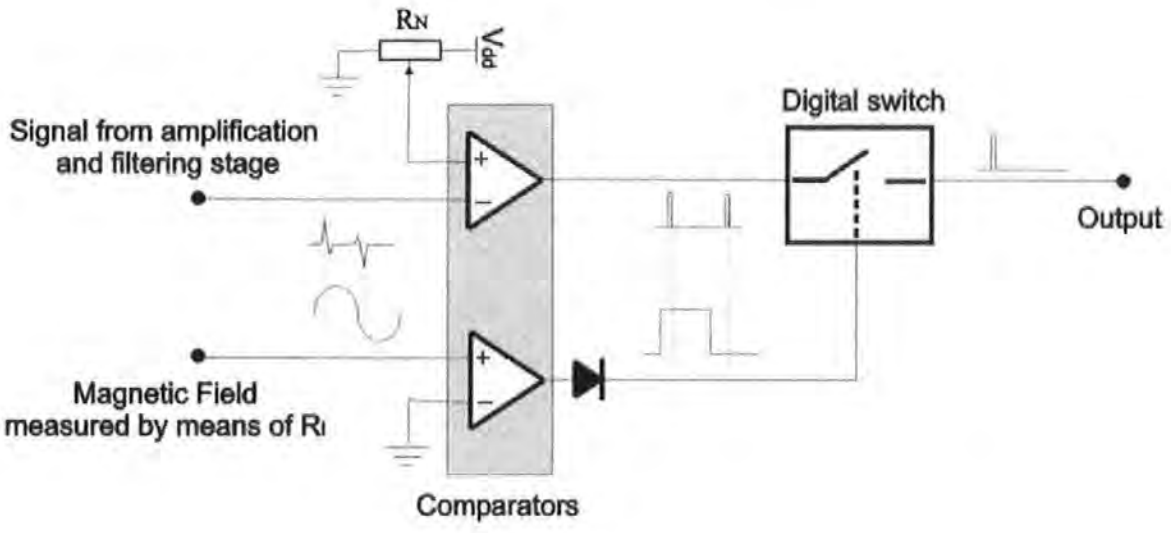

Fig. 4.19. Schematic view of selector circuit

This enables the signal level to be measured. This signal is proportional to the magnetic field applied to the wire at the point where the Barkhausen jumps appear (switching

field). The "Sample and Hold" device LF398 was used for sampling signals. The sampling

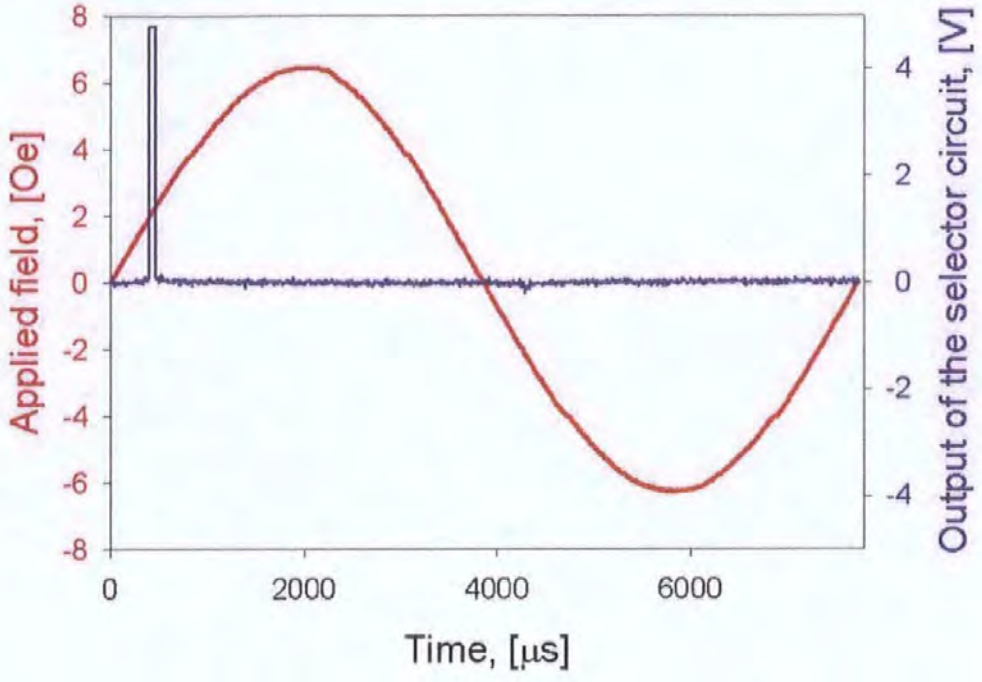

Fig. 4.20. Output of the selector circuit. Digital pulse can be used as a strobe signal for sampling level which is proportional to the switching field H_S.

and identifying circuit is shown schematically in Fig. 4.21. When the square pulse appears at the strobe input V_C, LF398 samples the signal, which is applied to the input V_{in}. When this pulse is not seen, LF398 holds the sampled level. This level is proportional to the switching

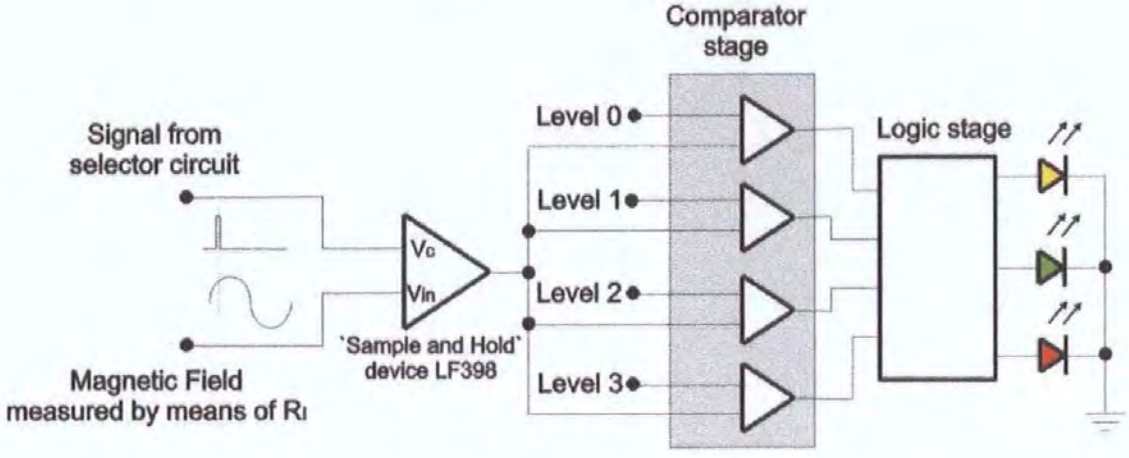

Fig. 4.21. The identifying circuit.

field H_S.

At this stage, it is worth mention the following limitation for the analogue prototype. The analogue prototype is able to work with a fixed numbers of different magnetic tags. In our case, recognising three different magnetic tags was required. According to this the comparator, logic and displaying stages were designed.

The comparator stage was designed for separating magnetic tags with different switching fields. The "levels" inputs at the comparator stage are adjustable and used for setting levels determining the deviation of switching fields of certain magnetic tags. After a simple logic stage, whose truth table is shown in table 4.2 the data are ready for display.

Comp N1 (higher than noise level)	*Comp N2 (higher than Level 1)*	*Comp N3 (higher than Level 2)*	*Comp N4 (higher than Level 3)*	*Yellow diode*	*Green diode*	*Red diode*
0	*0*	*0*	*0*	*0*	*0*	*0*
1	*0*	*0*	*0*	*1*	*0*	*0*
1	*1*	*0*	*0*	*0*	*1*	*0*
1	*1*	*1*	*0*	*0*	*0*	*1*
1	*1*	*1*	*1*	*0*	*0*	*0*

Table 4.2 Truth table of logical stage.

The analogue prototype can be used only for the purpose of demonstrating the possibility of using glass-coated microwires as magnetic tags. Mass production equipment would include communication unit, deactivation unit, protection unit and many other features.

4.4.2 2-D interrogation system

The 1-D system can be extended to recognize data tags randomly oriented in the plane. Figure 4.22 illustrates the concept of 2-D interrogation system. The transmit coils are arranged in pairs, each pair producing an orthogonal magnetic field: (H_x, H_y). The coil pairs are electrically connected in series. Each coil comprise 100 turns wound of 1mm diameter enameled copper wire over 10 layers and are a short rectangular solenoid 120mm wide, 180mm high and 10mm thick. The combined inductance of the coil pair is 3.3 mH. The coil pairs are 150mm apart along their magnetic axes. The important feature is that the magnetic fields produced by each pair in the interrogation volume are uniform and orthogonal. Each coil pair is driven by a current sine waveform to produce the field of the form:

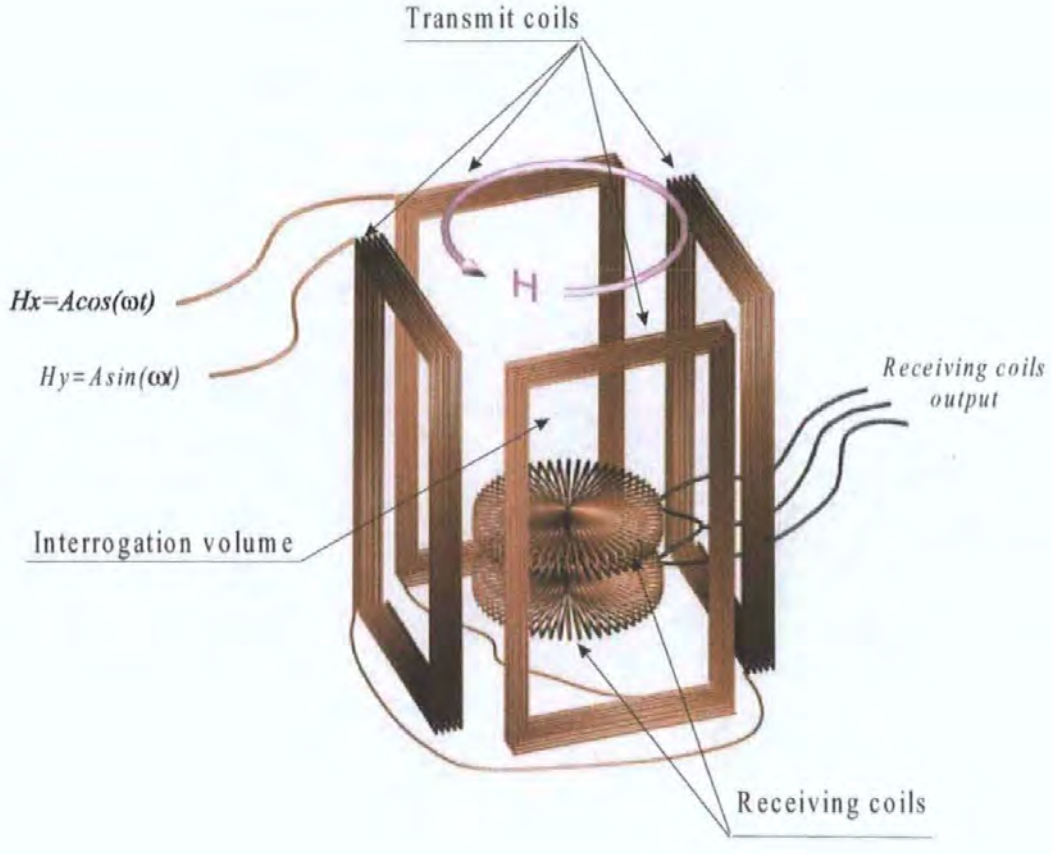

Fig. 4.22. 2-D scanned interrogation system

$$H_x = A \cdot \cos(2 \cdot \pi \cdot f \cdot t)$$
$$H_y = A \cdot \sin(2 \cdot \pi \cdot f \cdot t)$$

where the maximal value is about 8 Oe. The resultant field vector produced has a constant magnitude and is situated in the xy-plane, spinning around the z-axis at the rate ω radians per second. The value of ω was set to be about 1256 rad/s. The a.c. signal source (microchip MAX038) generating a signal at $f = 200Hz$ is split and filtered by an active phase shifting circuit designed to give differential phase about 90^0 (fig. 4.23).

The receiving coils have a toroidal form as shown in figure 4.24. They are placed in the xy-plane perpendicular to the z-axes. According to the requirements, receive coils are designed for detecting the magnetic data tags, which are placed perpendicular to the radial

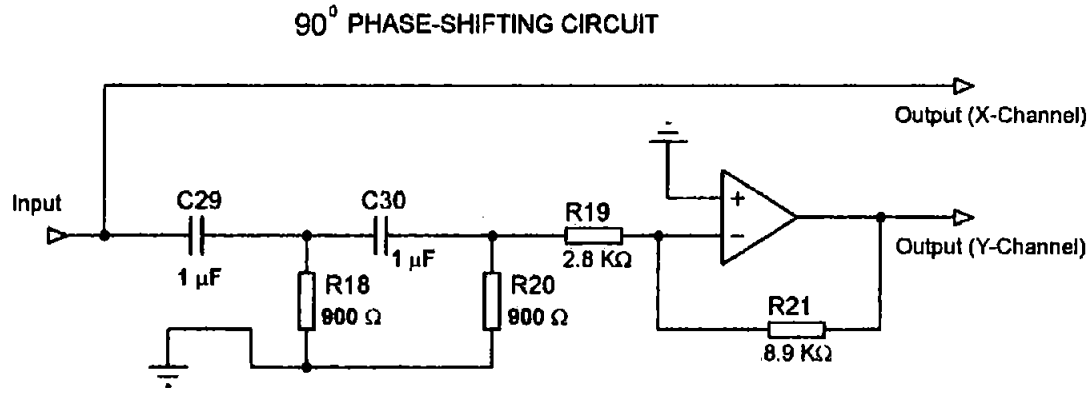

Fig. 4.23. 90^0 phase-shifting circuit.

direction and apart from the coil center as shown in figure 4.25. The receive coils are designed such that the emfs produced by transmit coils are equal and opposite. Each coil comprise 150 turns wound in a single layer with 0.25 mm ecw and are a toroidal solenoids 80 mm in diameter, 12 mm height and 40 mm thickness. The combined inductance of the coil pair is 1.1 mH. For the 2-D scanning system I used the receive circuit similar to that for 1-D system.

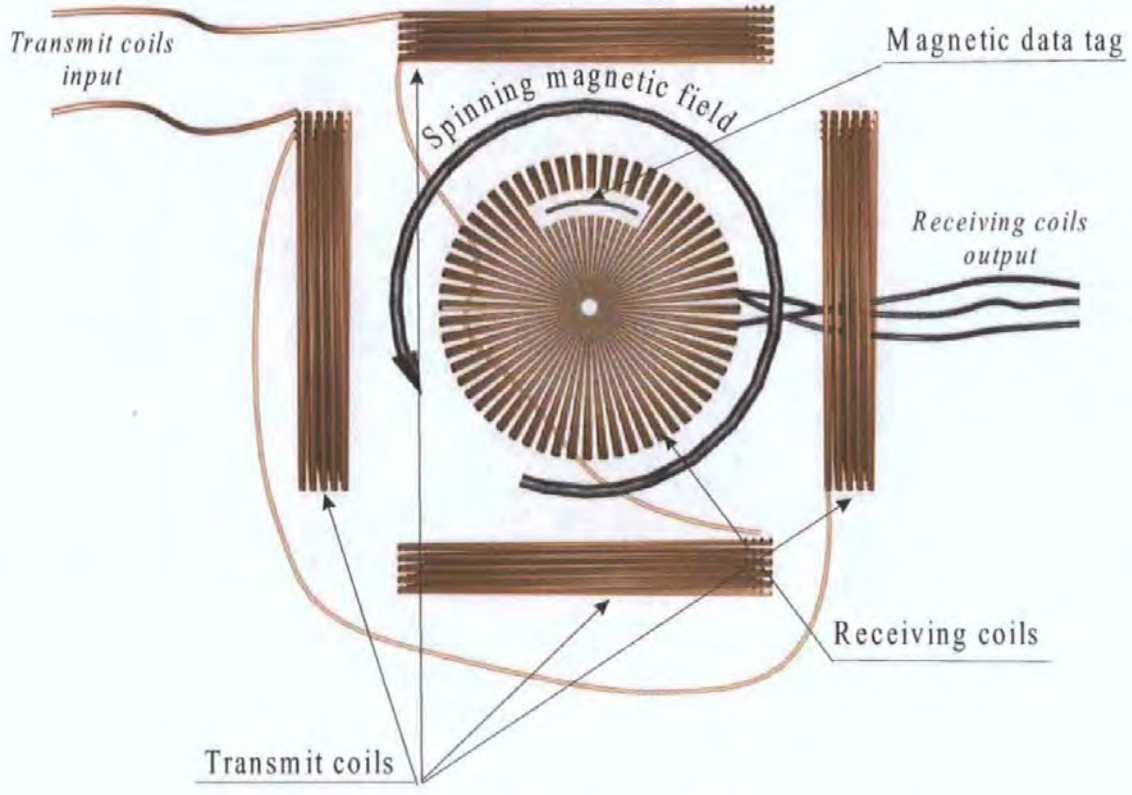

Fig. 4.24. 2-D scanned interrogation system (top view).

The 2-D system was developed on a conceptual level and only the principle operation has been realised. There are still many practical issues to be addressed, however, this is beyond the aims of this work.

Summarising the accomplished work, 1-D and 2-D interrogation scanning detection systems have been designed. Whilst 1-D detector is able to detect magnetic label with microwire oriented in parallel with the applied external field, 2-D detector can detect magnetic labels randomly oriented in the plane. A computer-based prototype allows optimal parameters of detection system such as operational frequency, amplification and filtering bandwidth to be chosen. The next modification, an analogue based prototype, demonstrates the possibility of producing inexpensive and portable detection system. This version can be used for specific purposes where security and reliability options are not very important, for example, for recycling.

References

[1] L. Panina, H. Katoh, M. Mizutani, K. Mohri and F. Humphrey *"Domain Collapse in Amorphous Magnetostrictive Wires"* IEEE Trans. Magn., (1992) Vol. 28, No. 5, 2922-2924

[2] A. Zhukov, M. Vazquez, J. Velazquez, H. Chiriac and V. Larin *"The remagnetization process of thin and ultrathin Fe-rich amorphous wires"* JMMM (1995) Vol. 151, 132

[3] M. Vazquez, C. Gomez-Polo and D. Chen *"A soft magnetic wire for sensor applications"* IEEE Trans. Magn. (1992) Vol. 28, 3147

[4] T. Reininger, H. Kronmuller, C. Gomez-Polo and M. Vazquez *"Magnetic domain observation in amorphous wires"* J. Appl. Phys. (1993) Vol. 73, 5357

[5] K. Mohri, F. Humphrey, K. Kawashima, K. Kimura and M. Mizutani *"Large Barkhausen and Matteucci Effects in FeCoSiB, FeCrSiB, and FeNiSiB Amorphous Wires"* IEEE Trans. Magn. (1990) Vol. 26, 1789

[6] M. Vazquez and D. Chen *"Stress dependence of the hysteresis loops of Co-rich amorphous wire"* IEEE Trans. Magn. (1995) Vol. 31, 1229

[7] A. Mitra , M. Vazquez *"Stress- and annealing-dependent magnetic properties of amorphous wires"* J. Phys. D: Appl. Phys. (1990) Vol. 23, 228

[8] P. Gaunt *"The frequency constant for thermal activation of a ferromagnetic domain wall"*, J. Appl. Phys, (1977) Vol. 48, 3470-3474

[9] A. Grigorenko *"Experimental Observation of Magnetostochastic Resonance"*, J. Appl. Phys., (1994) Vol. 76, 6335-6337

[10] L. Neel, *"Influence of the thermal fluctuation on the domains of ferromagnetic materials"* C. R. Acad, Sciences, (1949) Vol. 228, 664-671

[11] W. Brown *"Micromagntics"*, New York: Wiley, (1963)

[12] D. Jiles *"Frequency dependence of hysteresis curves in conducting magnetic materials"*, J. Appl. Phys., (1994) Vol. 76, 5849-5855

[13] J. Szczyglowski *"Influence of eddy currents on magnetic hysteresis loops in soft magnetic materials"*, JMMM, (2001) Vol. 223, 97-102

[14] L. Panina et al., *"Domain dynamics at large Barkhausen discontinuity in magnetostrictive amorphous wires"*, IEEE Trans. Magn, (1991) Vol. 27, 5331-5333

[15] M. Zheng, M. Yu, Y. Liu, R. Skomski, S. H. Liou, D. J. Sellmyer, V. N. Petryakov, Y. K. Verevkin, N. I. Polushkin, and N. N Salashchenko "*Magnetic nanodot arrays produced by direct laser interference lithography*" Appl. Phys. Lett. (2001) Vol. 79, 2606

[16] M. Sorescu and E. T. Knobbe *"Induced anisotropy and phase transformation in metallic glasses by pulsed-excimer-laser irradiation"* Phys. Rev. B (1994) 49, 3253–3265

[17] Monica Sorescu *"Direct evidence of laser-induced magnetic domain structures in metallic glasses"* Phys. Rev. B (2000) Vol. 61, 14338–14341

[18] H. Chiriac *"Fe-rich Glass Covered Amorphous Wires for article survelance applications"* Mater. Sci. Eng. A, (2001) Vol. 304, 166

[19] K. Mohri *"Review on Recent Advances in the Field of Amorphous-Metal Sensors and Transducers"* IEEE Trans. Magn. (1984) Vol. 20, 942

[20] HoloTag Ltd. "*System for article identification*", UK patent GB0120035.1 (2001)

[21] R. O'Handley "*Domain wall kinetics in soft ferromagnetic metallic glasses*" J. Appl. Phys., (1975) Vol. 46, 4996

[22] F. Humphrey, K. Mohri, J. Yamasaki, K. Kawamura, R. Malmhall, and I. Ogasawara "*Magnetic Properties of Amorphous Metals*" New York (1987).

[23] H. Chiriac, T. Ovari, M. Vazquez, and A. Hernando "*Magnetic hysteresis in glass-covered and water-quenched amorphous wires*" J. Magn. Magn. Mater., (1998) Vol. 177, 205

[24] L. Panina and K. Mohri *"Magneto-Impedance effect in amorphous wires"* Appl. Phys. Lett., (1994) Vol. 65, 1189

[25] M.Vazquez *"Giant magneto-impedance in soft magnetic wire"* J. Magn. Magn. Mater., (2001) Vol. 226, 693

[26] R. Malmhal, K. Mohri, F. Humphrey, T. Manabe, H. Kawamura, J. Yamasaki, and I. Ogasawara *"Bistable Magnetization Reversal in 50-μm Diameter Annealed Cold-Drawn Amorphous Wires"* IEEE Trans. Magn. (1987) Vol. 23, 3242

Chapter 5. Dynamic hysteresis and magneto-inductive effect in amorphous microwires with negative magnetostriction.

Quasi-static models of rotational magnetisation reversal of microwires with negative magnetostriction were briefly analysed in Chapter 2 under the effect of such factors as applied stresses and magnetic fields. Hereafter I will describe the dynamic effects of magnetisation reversal in conjunction with the magneto-inductive effect.

At low frequencies when the skin effect is weak, the change in the circumferential magnetisation due to the ac current generating an inductive voltage across the wire, the value of which is quite large and very sensitive to the dc axial magnetic field H_{ex}, reflecting the behaviour of the dynamic circumferential magnetisation reversal under the effect of H_{ex} [1, 2]. The axial field is a hard axis field with respect to the circumferential anisotropy. It strongly suppresses the circular magnetisation via the domain wall movement, but encourages the rotational processes. This process can be described in terms of an ac non-linear permeability, the field dependence of which defines the field behaviour of the inductive voltage (or inductive part of the impedance). This effect is also referred to as a magneto-inductive effect. Here I give an introduction into low frequency magnetic permeability (Section 5.1) and MI effect (Section 5.2), and Section 5.3 presents the original results on the dynamic circular magnetisation reversal in Co-based wires. The low-frequency analysis is useful to clarify the MI behaviour at higher frequencies when the skin effect is essential. For example, the obtained results explain the transformation of the MI plots: from curves with one central peak at zero field to characteristics with two peaks at the anisotropy field as frequency is increased and the DW processes become progressively damped.

5.1 Dynamical domain wall permeability

In the low frequency range, the essential field dependence of an ac voltage $V_w = V_R + V_L$ results from only the inductive part V_L, whereas the resistive component V_R corresponds to the dc voltage. In Co-based amorphous wires the value of V_L can be quite

large at relatively low frequencies ($V_L / V \approx 10\%$ at frequency of 10 kHz) and highly sensitive to the external dc field. This effect is knows as a *magneto-inductive effect [3-5]*, or low frequency magneto-impedance. Such a large inductive component is due to a circular magnetic structure for which a passing current induces an easy axis driving magnetic field. The inductive voltage is proportional to the circumferential permeability consisting of contributions from domain wall movement and magnetization rotation in the presence of the axial magnetic field given by:

$$\mu_\varphi = 1 + 4\pi(\chi_{rot} + \chi_{dw}) \tag{5.1}$$

where χ_{rot}, χ_{dw} are rotational and domain wall susceptibilities, respectively. (In this chapter Gaussian units are used following the original works [1, 2, 8, 10]).

For circular magnetic structure, both χ_{dw} and χ_{rot} are very sensitive functions of the external field. Typically, χ_{dw} dominates at relatively low frequencies less than the characteristic relaxation frequency ω_{dw} of the domain wall movement, whereas at higher frequencies χ_{rot} becomes important, since the relaxation is much faster in the case of the rotational processes. At low frequencies, the rotational part χ_{rot} can be considered frequency independent. The domain susceptibility χ_{dw} is of a relaxation type due to eddy currents generated by wall movements.

In the effective medium approximation, the dynamical magnetic susceptibility χ_{dw} due to the domain wall movements is defined from $< \chi^0_{dw} \cdot H >= \chi_{dw} < H^0 >$, where <...> indicates averaging over the volume larger than the domain spacing, χ^0_{dw} is a static domain wall susceptibility, and H^0 is an external driving field, which is in our case a circular field generated by a passing current [1-5]. The calculation of χ_{dw} depends on a specific domain structure. Following [1], I assume

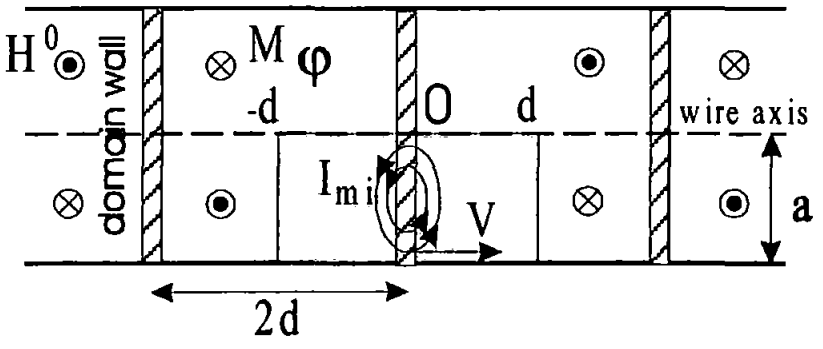

Fig. 5.1 Circular domain structure for eddy current field calculation.

that circular domains cross the entire wire of radius a periodically with spacing 2d, as shown in Fig. 5.1. A rigid domain wall model is also assumed, when the wall shifts as a whole under the influence of the averaged field $< H >$, which incorporates, H^0 and the eddy current field H_{mi} generated by the wall displacements. The induced electric field E_{mi} is potential ($curlE_{mi} = 0$), except within the wall, and satisfies the Laplace equation

$$\Delta\psi = 0, \quad E_{mi} = -grad\psi \tag{5.2}$$

The eddy current field H_{mi} is calculated by the solution of (5.2) as:

$$curlH_{mi} = \frac{4 \cdot \pi \cdot \sigma}{c} \cdot E_{mi} \tag{5.3}$$

The problem is solved in the cylindrical co-ordinates r, φ, z with the origin in the centre of a circular domain wall [12]. Because of the symmetry the hatched area in Fig. 5.1 is considered. The boundary conditions are:

$$\begin{aligned} &(\partial\psi / \partial r)_{r=a} = 0, \\ &\psi(r,-d) = \psi(r,d) = 0, \end{aligned} \tag{5.4}$$

$$(\partial\psi / \partial r)_{z=0} = -4 \cdot \pi \cdot j \cdot \omega \cdot \chi^0_{dw} \cdot < H > \cdot d / c \tag{5.5}$$

Condition (5.5) accounts for the assumption that the wall shifts as a whole under the influence of $< H >$, so that $dz / dt \propto \omega \cdot \chi^0_{dw} \cdot < H >$. The solution for ψ which satisfies (5.4) is of the form:

$$\psi = \sum_n D_n \cdot J_0(k_n \cdot r) \cdot \sinh[k_n \cdot (d - z)], \tag{5.6}$$

where $k_n = \lambda_n / a$ are such that $J_1(\lambda_n) = 0$. The constants D_n are determined from (5.5) by using the orthogonality condition from Bessel functions:

$$D_n = -\frac{8 \cdot \pi \cdot j \cdot \omega \cdot \chi^0_{dw} \cdot d \cdot a \cdot < H > \cdot f_n}{c \cdot \lambda_n^3 \cdot J_2^2(\lambda_n) \cdot \sinh(\lambda_n \cdot d / a)}, \tag{5.7}$$

$$f_n = \int_0^{\lambda_n} x \cdot J_1(x) dx.$$

As follows from (5.3), the magnetic field H_{mi} produced by the eddy current has only a circular component, which can be determined by ψ in the form:

$$H_{mi} = -\frac{4 \cdot \pi \cdot \sigma}{c \cdot r} \int_r^a \frac{\partial\psi}{\partial z} r \, dr. \tag{5.8}$$

Then the average value of the magnetic field imposed on the domain boundary is

$$< H >= H^0 - \frac{8 \cdot \pi \cdot \sigma}{c \cdot a^2} \int_0^a dr \int_r^a \frac{\partial \psi}{\partial z} r' dr', \tag{5.9}$$

where ψ is defined by (5.6) and (5.7) and is proportional to $< H >$. From (5.9) the dynamic susceptibility can be found

$$\chi_{dw} = \frac{\chi_{dw}^0 \cdot < H >}{H^0} = \frac{\chi_{dw}^0}{1 - j \cdot \omega / \omega_{dw}}, \tag{5.10}$$

introducing a characteristic relaxation frequency ω_{dw}:

$$\omega_{dw} = c^2 / 64 \cdot \pi^2 \cdot \chi_{dw}^0 \cdot \sigma \cdot a \cdot d \cdot \sum_n g_n, \tag{5.11}$$

$$g_n = \frac{f_n^2 \cdot \coth(\lambda_n \cdot d / a)}{\lambda_n^5 \cdot J_2^2(\lambda_n)}.$$

Here σ is the conductivity. The series in (5.11) rapidly converges and for a=d is equal 0.053. Note that the calculation of χ_{dw} is valid only as long as $\delta / a >> 1$, $\delta = c / \sqrt{2 \cdot \pi \cdot \sigma \cdot \omega}$.

I will demonstrate that in the case of the magneto-inductive effect, the domain processes are most essential.

5.2 Inductive voltage generated by circular magnetisation reversal

In the previous Section, I considered a linear domain wall permeability to demonstrate the relaxation processes due to eddy currents generated by wall motion. In the low frequency approximation, the inductive voltage V_L can be found in a general case of a nonlinear magnetisation due to ac current. This voltage will be defined by a certain non-linear permeability (say, differential permeability). An ac current $i = i_0 e^{-j\omega \cdot t}$ flowing through a wire, generates a circular magnetic field, the radial distribution of which can be considered frequency independent:

$$H_\varphi = 2ir / ca^2 \quad (r \le a). \tag{5.12}$$

This field causes a circular magnetic flux change and generates a longitudinal electric field E_z :

$$\frac{\partial E_Z}{\partial r} = -\frac{1}{c}\frac{\partial B_\varphi}{\partial t} = j\frac{\omega}{c}\mu_{dif} \cdot H_\varphi. \tag{5.13}$$

Here the circular magnetic induction B_φ is a function of H_φ, and μ_{dif} is defined as a differential permeability: $\mu_{dif} = \partial B_\varphi / \partial H_\varphi$. The general solution of (5.13) is of the form:

$$E_Z(r) = j\frac{\omega}{c}\int_0^r \mu_{dif}(r')H_\varphi(r')dr' + E_0 \tag{5.14}$$

The parameter E_0 is found from the condition of constant current amplitude:

$$\begin{aligned} &< E_Z(r) > l = iR_{dc} \\ &E_0 = iR_{dc} - j\frac{\omega}{c}\frac{l}{\pi a^2}\int_0^a rdr\int_0^r \mu_{dif}(r')H_\varphi(r')dr' \end{aligned} \tag{5.15}$$

where R_{dc} is the dc resistance of the wire. The total voltage at constant current amplitude is determined by the value of the field taken at the wire surface:

$$V_w = E_z(a)l = iR_{dc} + V_L \tag{5.16}$$

This gives the following equation for the inductive voltage:

$$\begin{aligned} V_L &= j\frac{\omega}{c}\int_0^a \mu_{dif}(r')H_\varphi(r')dr' - j\frac{2\omega}{c}l\int_0^a rdr\int_0^r \mu_{dif}(r')H_\varphi(r')dr'/\pi a^2 = \\ &= j\frac{\omega}{c}\frac{2l}{\pi a^2}\int_0^a rdr\int_r^a \mu_{dif}(r')H_\varphi(r')dr' \end{aligned} \tag{5.17}$$

Substituting (5.12) for H_φ into (5.17), the inductive voltage can be expressed as

$$\begin{aligned} &V_L = j\cdot\frac{\omega}{c}\cdot L_i \cdot i \\ &L_i = 4\cdot l\cdot\int_0^a rdr\int_r^a \mu_{dif}(r')\cdot r'dr'/a^4. \end{aligned} \tag{5.18}$$

It can be concluded from (5.18) that the inductive voltage is determined by an internal inductance L_i, which depends, in general, on the distribution of the differential permeability inside the wire. For homogeneous materials where μ_{dif} is independent of position, the expression for L_i is reduced to a standard form: $L_i = \mu_{dif}\cdot l/2$. In a general nonlinear case the

differential permeability and, hence, the inductance are functions of current. Therefore, at very low frequencies the change of the material's impedance is exclusively ascribed to the magneto-inductive effect arising from the circular magnetization process. It should be noted that because of large Barkhausen jumps in the domain wall motion the inductive voltage V_L can be very far from the harmonic waveform (especially for high amplitudes of driving current.

5.3 Experimental investigation of inductive voltage (dynamical circular magnetisation reversal).

The inductive voltage across the wire is originated by circular magnetisation reversal, which cannot be measured by conventional magnetometry methods. An approach to the problem is to utilise a balanced bridge circuit, for example Wheatstone, which allows the inductive voltage to be filtered out from the total wire voltage (see Fig. 5.2) [3-6, 10].

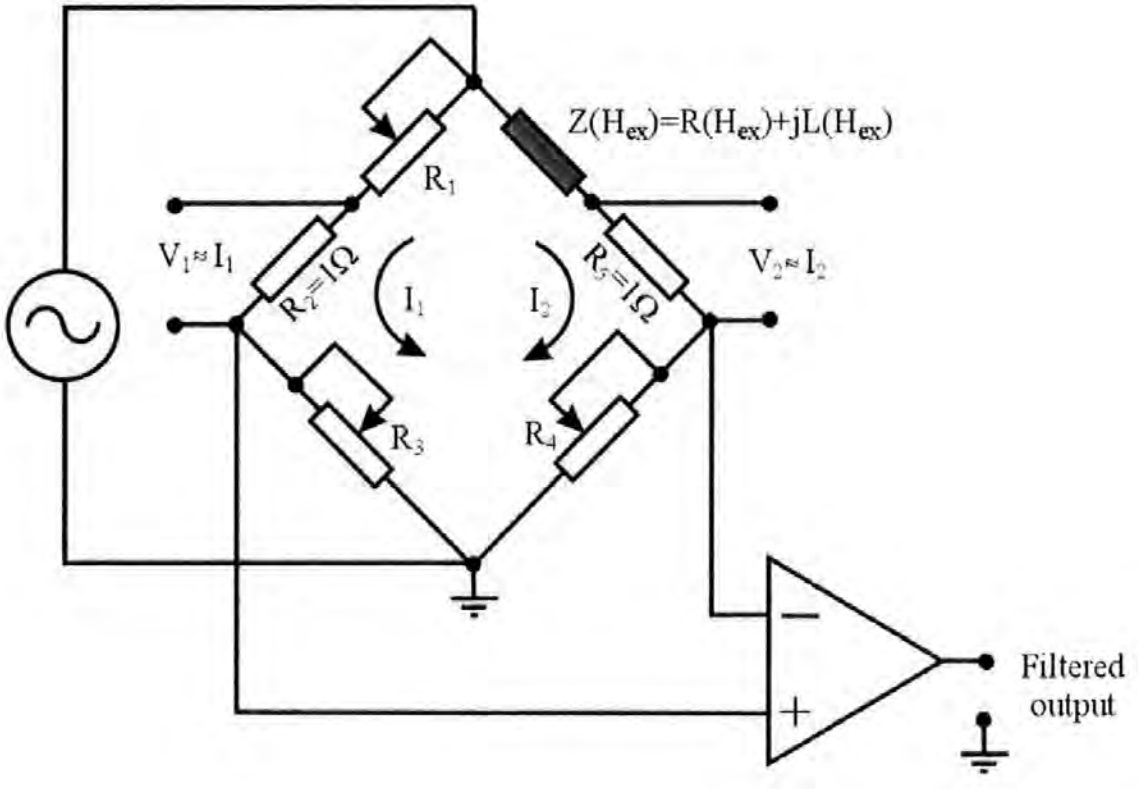

Fig. 5.2 Wheatstone bridge circuit.

Due to its outstanding sensitivity, the Wheatstone bridge circuit is very advantageous for the measurement of resistance and inductance or even complex impedances. It consists of 3 adjustable resistors R_1, R_3 and R_4 and one element under test (magneto-inductive sample) arranged in a diamond orientation. Due to the complex nature (inductive and resistive) of the measured sample, the significant phase shift appears between current I_1 and I_2, which was measured across resistors R_2 and R_5. Measurements of the phase shift allows the non-linear inductive voltage V_L corresponding to the changes of magnetic permeability to be separated from an unwanted ac signal (not related to the hysteresis). Furthermore, careful measurements required the balance of the bridge at each frequency in the presence of a very large axial field (100 Oe) along the sample, since the inductive part of the measured impedance that is related to the magnetic properties dramatically changes with increasing frequency.

The circular flux density was not uniform over the wire cross-section and the measured voltage depends, in general, on its distribution. But at certain condition (say, rigid or flexible domain wall movements) the measured voltage is proportional to the rate of change of the averaged circular flux density. Then, the circular magnetisation loop can be plotted by integrating the inductive voltage signal. The magnetising current amplitude of 30 mA is sufficient to realise almost a complete magnetisation cycle even for frequency up to 250KHz.

The measurements were made for glass covered $Co_{64.6}Fe_{3.5}Si_{15.5}B_{16.4}$ amorphous wires having the metallic amorphous core of 12.6 μm in diameter covered by glass with thickness of 2.3 μm; the wire length was 1.2 cm.

I start with the case when the external dc field along the wire is zero ($H_{ex} = 0$). In the case of circumferential anisotropy, an ac current passing through the wire creates an easy axis circular field H_φ and the circumferential magnetisation proceeds via the wall movements. Figure 5.3 shows the experimental circular hysteresis loops for different frequencies (from 1 kHz to 250 kHz). The loops are nearly rectangular at low frequencies whereas with increasing frequency they progressively widen and the maximal differential permeability drops.

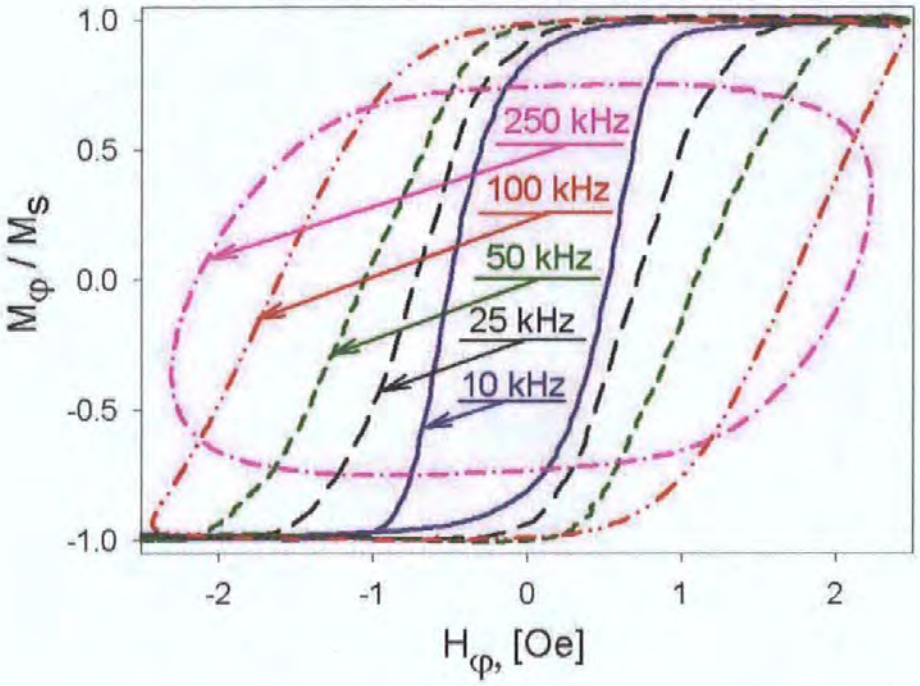

Fig. 5.3. Dynamic circular hysteresis loops in glass-covered amorphous microwires with small negative magnetostriction measured at different frequencies of passing current

Under the effect of the external DC magnetic field applied along the wire the magnetisation inclines towards the wire axis, eventually decreasing the circular flux change. The magnetic field H_{ex} is a hard axis field with respect to the circumferential anisotropy. It suppresses the circular magnetisation via the domain wall movement as can be seen from Fig. 5.4, which shows dynamic circular hysteresis loops at different frequencies at the presence of external field. The external field leads to a gradual transition from almost a square loop to a linear one as the rotation portion of the magnetisation grows. During this process, the coercivity substantially decreases. Figure 5.4 demonstrates good agreement between experiment and Stoner-Wohlfarth rotational model under the effect of a transverse magnetic field (Compare with Fig. 2.4).

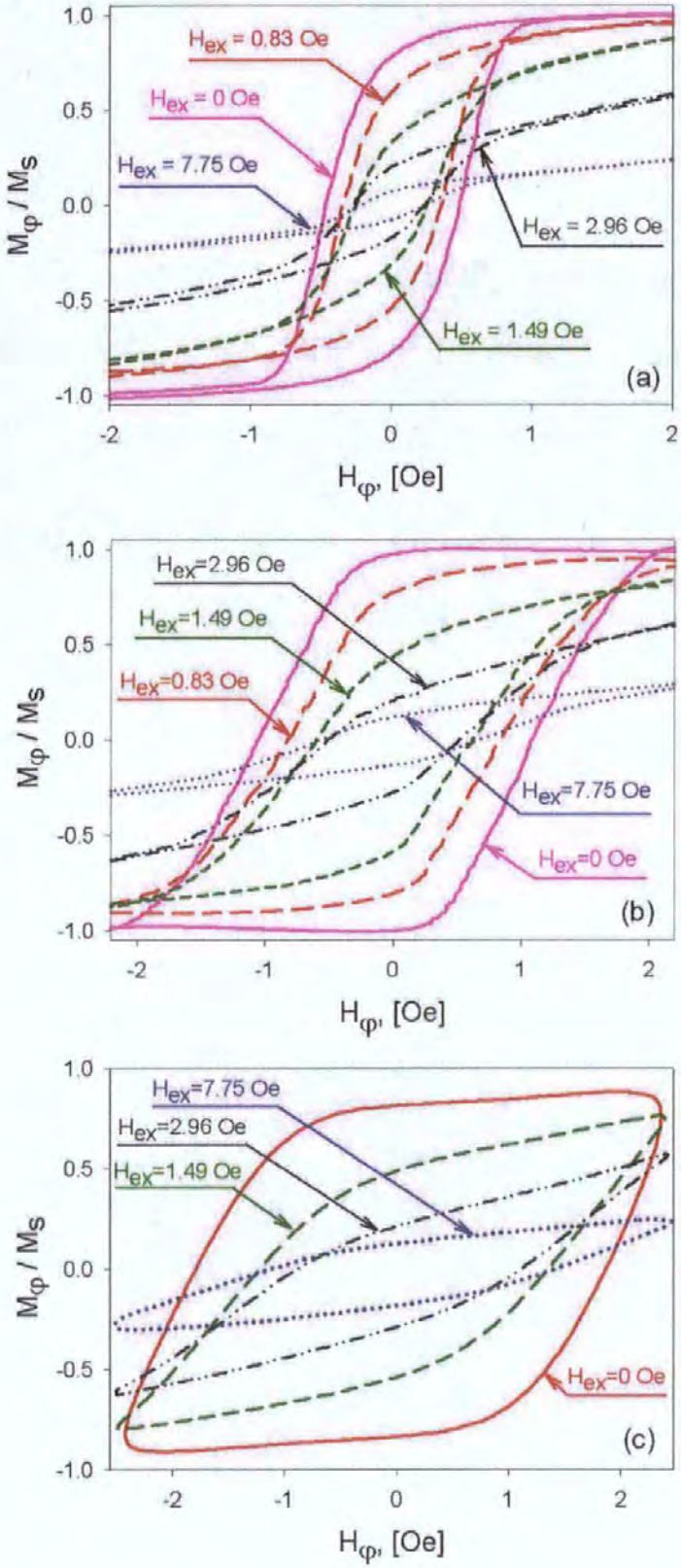

Fig. 5.4. Dynamic circular hysteresis with the axial field as a parameter for three frequencies: 10KHz in (a), 50 KHz in (b) and 150 KHz in (c)

Next, I will look in more details at the behaviour of the parameters describing the hysteresis, such as maximal differential permeability, coercivity and reversible permeability. The transformation in the circular hysteresis under the influence of the axial field indicates, that during this process the maximal differential permeability drops. The normalized plots of this parameter versus external axial field are shown in Fig. 5.5 at different frequencies.

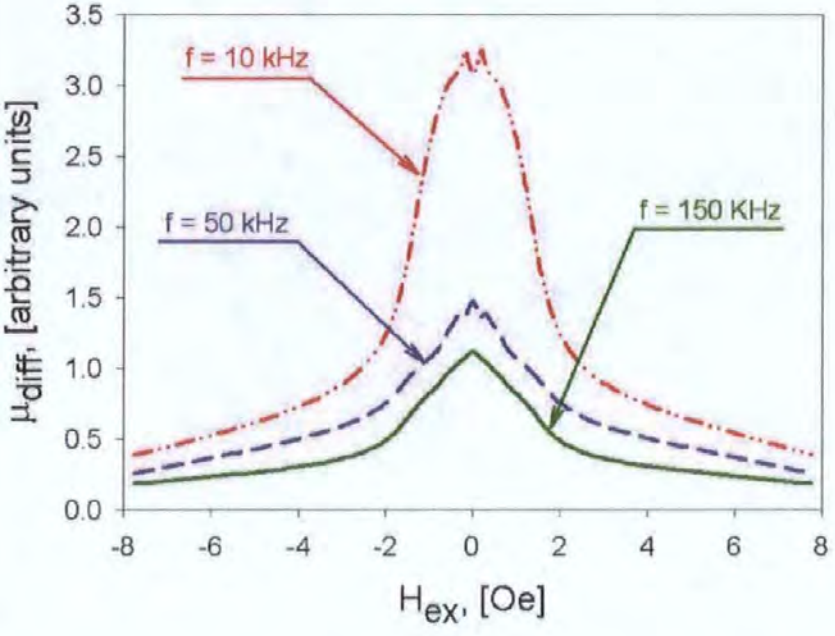

Fig. 5.5 Normalized differential permeability versus external axial field at different frequencies.

In figure 5.6, the plots of coercivity as functions of axial field are shown for different frequencies. The coercivity value increases more then 3 times as frequency is increased from 10KHz to 150KHz. As a function of field, it has a maximum at zero field, quickly decreasing as field is increased. Knowing the coercivity H_c and the remanence magnetisation M_r, which is also a function of the field, I can deduce from these data the behaviour of the reversible domain wall permeability:

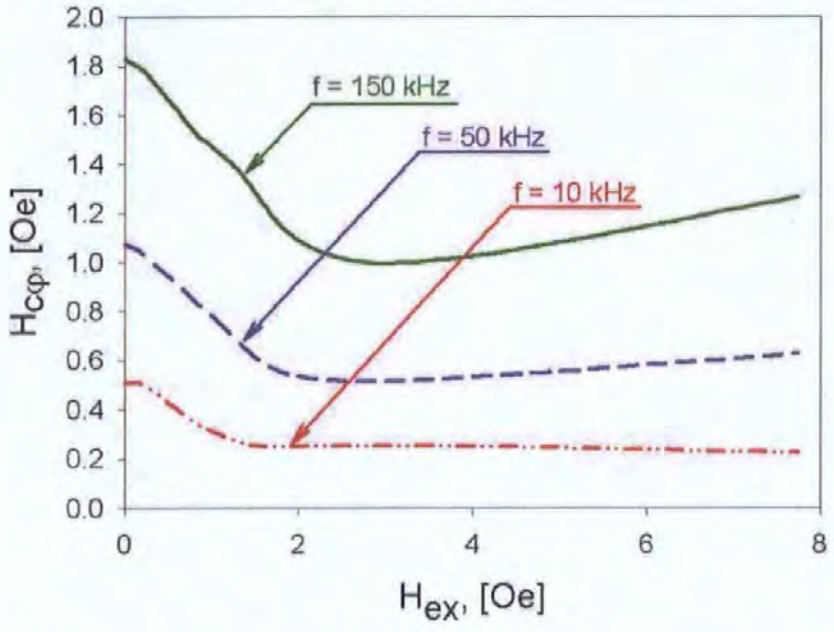

Fig. 5.6. Circumferential coercivity $H_{c\varphi}$ versus external axial field at different freauencies.

$$\mu_{DW} \propto \frac{M_r}{H_c} \tag{5.33}$$

Normalized DW permeability versus external axial field at different frequencies is shown in fig. 5.7. This behaviour exhibits a flat region in the field interval $|H_{ex}| < H_K$. It is important to notice a substantial decrease with frequency in both DW permeability as well as differential permeability.

Observing the hysteresis loops, it is seen that the axial field activates the rotational processes since it results in the magnetisation inclination towards the wire axis. The rotational permeability can be characterised by the following ratio:

$$\mu_{rot} \propto \left.\frac{\partial B_\varphi}{\partial H_\varphi}\right|_{H_\varphi \to 0} \tag{5.19}$$

Fig. 5.8 shows that the rotational permeability increases with the field having a maximum in the region of the anisotropy field. For larger fields, it rapidly drops and at fields more that 10 Oe become insensitive to the axial field.

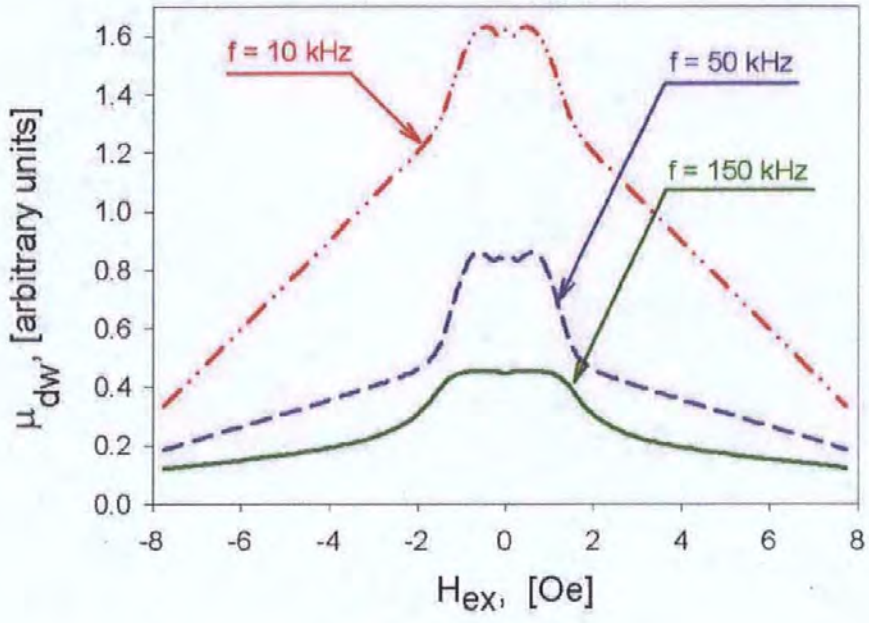

Fig. 5.7. Normalized DW permeability versus external axial field at different frequencies.

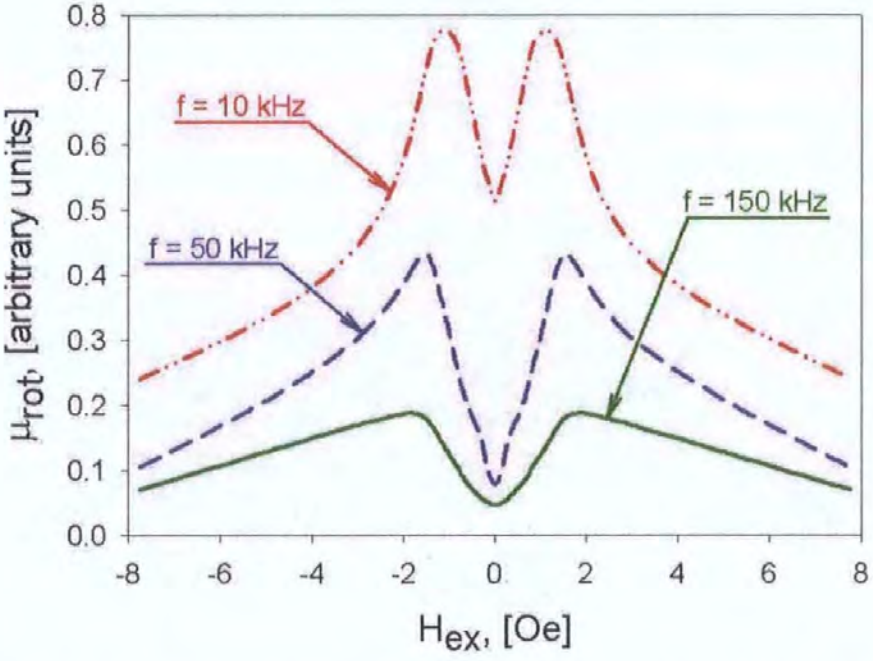

Fig. 5.8. Normalized rotational permeability versus external axial field at different frequencies.

The introduced permeability parameters, although depending upon frequency, does not change their characteristic field dependencies. Therefore, the obtained results are useful to clarify the MI behaviour at higher frequencies and resolve some conflicting results. At relatively low frequencies, the DW processes play a dominant role resulting in MI characteristics with one central peak [1-3], which is in agreement with Figs. 5.5, 5.7. However, the equilibrium between contributions of the DW displacement and rotational permeabilities can be partly controlled by the amplitude of the applied current. If the current amplitude is large enough to activate irreversible DW displacement, the corresponding permeability always decrease with the field, so the impedance does. If the current is relatively small, then only reversible processes contribute to the impedance and the impedance exhibits two peaks near the field of the order of the anisotropy field. The critical current amplitude, which can produce irreversible dynamics, depends mainly on frequency. With increasing frequency, the DW processes become progressively damped and at frequencies of few MHz they are comparable with the rotational ones. At such frequencies, the MI behaviour is characterised by two symmetrical peaks, which are situated at the external field being in the order of the anisotropy field [1]. This is in agreement with the field behaviour of the rotational permeability shown in Fig. 5.8.

References

[1] L. Panina, K. Mohri, T. Uchiyama, M. Noda *"Giant magneto-impedance in Co-rich amorphous wires and films"* IEEE Trans. Magn., (1995) Vol. 31, 1249-1260.

[2] L. Panina, H. Katoh, K. Mohri, K. Kawashima *"Magnetisation processes in amorphous wires in orthogonal fields"* IEEE Trans. Magn., (1993) Vol. 29, 2524-2526.

[3] K. Mohri, K. Kawashima, T. Kohzawa and H. Yoshiba *"Magneto-inductive element"* IEEE Trans. Magn., (1993) Vol. 29, 1245-1248.

[4] K. Kawashima, T. Kohzawa, H. Yoshida and K. Mohri *"Magneto-inductive effect in tension annealed amorphous wires and MI sensors"* IEEE Trans. Magn., (1993) Vol. 29, 3168-3170.

[5] K. Bushida and K. Mohri *"Sensitive magneto-inductive effect in amorphous wires using high-pass filter and micro-field sensor"* IEEE Trans. Magn., (1994) Vol. 30, 1345.

[6] K. Mohri "*Magneto-Impedance Effect in Etched Thin Amorphous Wires*" IEEE Trans. Magn., (1992) Vol. 28, 3150.

[7] F. Humphrey, K. Mohri, J. Yamasaki, H. Kawamura, R. Malmhall *"Re-entrant magnetic flux reversal in amorphous wires"* Proc. Of Symp. On Magnetic Properties of Amorphous Metals, Elsevire Science Publishers B.V., Amsterdam (1987) 110-116.

[8] L. Panina and K. Mohri *"Mechanism of the magneto-impedance effect in negative magnetostrictive amorphous wires"* J. Magn. Soc. of Japan (1994) Vol. 18, 245-249

[9] L. Panina and K. Mohri *"Magneto-impedance effect in amorphous wires"* Appl. Phys. Lett., (1994) Vol. 65, 1189-1191.

[10] A. Hernando and J. Barandiran "*Circular magnetisation measurement in ferromagnetic wires*" J.Phys. D: Appl. Phys, (1978) 11, 1539.

[11] L. Landau and E. Lifshitz *"Electrodynamics of Continuous Media"* Pergamon Press, Oxford (1975) 195.

[12] R. Pry and C. Bean "*The magnetic properties of Fe-based amorphous ribbons coated with various oxides using the sol–gel process*" J. Appl. Phys. (1958) Vol. 29, 532.

[13] J. Velázquez, M. Vázquez, D.-X. Chen, and A. Hernando "*Giant magnetoimpedance in nonmagnetostrictive amorphous wires*" Phys. Rev. B, (1994) Vol. 50, 16737.

[14] R. S. Beach and A. E. Berkowitz "*Sensitive field- and frequency-dependent impedance spectra of amorphous FeCoSiB wire and ribbon*" J. Appl. Phys., (1994) Vol. 76, 6209.

[15] K. L. Garcia, and R. Valenzuela "*Domain wall pinning, bulging, and displacement in circumferential domains in CoFeBSi amorphous wires*" J. Appl. Phys., (2000) Vol. 87, 5257.

[16] T. L. Gilbert "*A Lagrangian Formulation of the Gyromagnetic Equation of the Magnetization Field*" Phys. Rev. (1955) Vol. 100, 1243.

[17] L. Landau and E. Lifshitz *"Electrodynamics of Continuous Media"*, Pergamon Press, Oxford (1975) 195.

[18] L. D. Landau, E. M. Lifshitz and L. P. Pitaevskii *"Quantum Mechanics - Non-Relativistic Theory"* Edition: 3d, Elsevier Science, (1977), Vol. 3.

[19] L. D. Landau and E. M. Lifshitz *"On the theory of the dispersion of magnetic permeability in ferromagnetic bodies"* Phys. Z. Sowjetunion (1935) 8, 153.

[20] L. D. Landau and E. M. Lifshitz *"Electrodynamics of Continuous Media"* Pergamon Press (1975).

[21] A. G. Gurevich *"Ferrites at Microwave Frequencies"* New York: Consultants Bureau (1963).

[22] A. Gurevich *"Magnetic Resonance in Ferrite and Antiferomagnets"*, Nauka, Moscow (1973).

Chapter 6. Magneto-impedance (MI) effect in amorphous microwires with negative magnetostriction.

This Chapter is devoted to the investigation of some special features of the magneto-impedance (MI) effect in amorphous microwires with small negative magnetostriction. The complex-valued impedance of Co-based wires subjected to a static magnetic field, exhibits large and sensitive changes (up to 100%/Oe). Sections 6.1 gives an introduction into MI effect in terms of the surface impedance tensor for wires with a helical anisotropy, when the skin effect is essential and the permeability is due to a coherent magnetisation rotation described by the linearised Landau-Lifshitz equation. The permeability is considered in Section 6.2. Regarding the MI effect at intermediate frequencies, my interest is concentrated on a comparative study of diagonal and off-diagonal impedances, which has a great importance for applications in linear sensing. This is presented in Section 6.3.

At very high frequencies, of the order of GHz, the rotational permeability becomes insensitive to a weak magnetic field and the impedance field behavior is only due to a directional change in the dc magnetization (I exclude effects related to ferromagnetic resonance which require much higher magnetic fields of hundred Oe). In section 6.4 experimental investigation of the MI behaviour in the RF and microwave frequency ranges is presented and analysed by considering the dispersion properties of the effective permeability of the ac linear response combined with the rotational dc magnetization.

6.1 Impedance in magnetic conductors.

The MI effect is typically understood as a large and sensitive change in a voltage response (or complex-valued impedance) measured across a magnetic conductor subjected to an ac current $i=i_0\exp(-j\omega t)$ and a dc magnetic field [1-3]. The voltage vs. field behaviour is due to the redistribution of the ac current density in the presence of the field. In the original theoretical work on MI [3] the current density has been calculated with the assumption that the variable magnetic properties can be described in terms of a total permeability having a

scalar or quasi-diagonal form. This allows the impedance of a magnetic object (and the voltage induced across it by the ac current) to be found essentially in the same way as in the case of a non-magnetic material [4] In this approach, the voltage response V_w is of the form

$$V_w = Z(a/\delta_m)i \tag{6.1}$$

where the impedance Z is calculated as a function of a skin depth

$$\delta_m = c/\sqrt{2\pi\sigma\omega\mu_t} \tag{6.2}$$

Here c is the velocity of light σ is the conductivity and μ_t is the effective transverse permeability (with respect to the current flow), $2a$ is a characteristic cross-section size. If the skin effect is strong $a/\delta_m >> 1$, the impedance is inversely proportional to the skin depth; therefore, the magnetic-field dependence of the transverse permeability controls the voltage behaviour. This simple consideration has provided a qualitative understanding of the MI behaviour, and in certain cases equations (6.1), (6.2) have given a reasonable agreement with the experimental results. For higher frequencies the magnetisation rotation dynamics gives the main impact on the effective permeability as discussed above. The rotational permeability has an essential tensor form, which makes it difficult to use equations (6.1), (6.2) for higher frequencies: the difference between the experimental and theoretical results becomes quite considerable. Further more, it results in the tensor form of the impedance, which from a practical point of view means that the voltage across the wire can be generated by placing the wire into an ac magnetic field h_{ex}. Alternatively, the voltage can be generated in the coil mounted on the wire by a passing ac current along the wire. These excitations can be very important for sensor developments.

In this Section, I will give magneto-impedance analysis in terms of the surface impedance tensor in conjunction with the rotational permeability. In this approach, both an ac current in the wire and an ac axial field (produced by the current in the coil) can be used as a source of excitation. The voltage is measured either across the wire (V_w) or in the coil (V_c), as shown in Fig. 6.1.

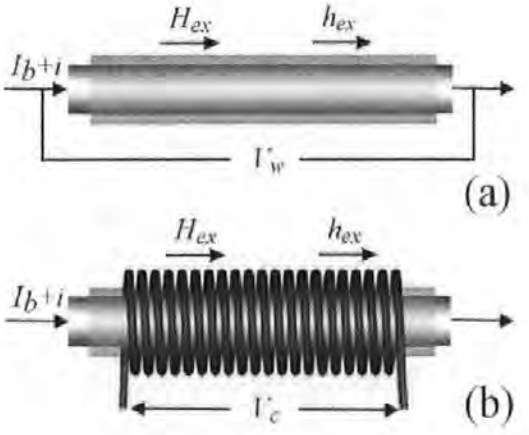

Fig. 6.1 Voltage response due to the ac excitation using current i and field h_{ex}, measured across the wire in (a) and from the coil in (b).

The value of V_w is determined by considering the energy consumption in the wire:

$$iV_w = \frac{c}{4\pi}\int_S (\boldsymbol{e}\times\boldsymbol{h})\,ds \tag{6.3}$$

where the integration is performed along the wire surface, **e** and **h** are the ac electric and magnetic fields. The voltage V_c is found by integrating the field **e** along the coil turns:

$$V_c = \oint \mathbf{e}\,\mathbf{dl} \tag{6.4}$$

As it follows from (6.3), (6.4), the induced voltage can be found by calculating the tangential components of the fields $\bar{\mathbf{e}}_t$, $\bar{\mathbf{h}}_t$ at the wire surface. Since it is assumed that the wavelength is larger than the sample size, the field distribution outside the sample corresponds to the static case. Then, the excitation method imposes the boundary conditions for the magnetic field $\bar{\mathbf{h}}_t$. Using the cylindrical co-ordinates (r, φ, z) with the axis z along the wire, the boundary conditions can be written as:

$$h_\varphi(a) = \bar{h}_\varphi = 2i/ca\,, \quad \bar{h}_z(a) = h_{ex}\,, \tag{6.5}$$

where a is the wire radius. The electric field $\bar{\mathbf{e}}_t$ is related to the magnetic field $\bar{\mathbf{h}}_t$ via the surface impedance matrix $\hat{\varsigma}$ [4]:

$$\bar{\mathbf{e}}_t = \hat{\varsigma}(\bar{\mathbf{h}}_t \times \mathbf{n}) \tag{6.6}$$

where **n** is a unit radial vector directed inside the wire. Comparing (6.3)-(6.6) it is seen that the impedance $\hat{\varsigma}$ is the only characteristic describing the voltage response in the system excited by the external magnetic field **h** (of any origin). In ferromagnetic conductors, $\hat{\varsigma}$ is a two-dimensional matrix.

The present analysis is concerned with the calculation of the surface impedance matrix for a wire with a uniform static magnetisation having a helical orientation. In this case, the matrix $\hat{\varsigma}$ is constant on the surface. Writing vector equation (6.4) in the co-ordinate representation, the components of $\hat{\varsigma}$ can be determined as:

$$\begin{aligned} \bar{e}_\varphi &= -\varsigma_{\varphi\varphi}\,\bar{h}_z + \varsigma_{\varphi z}\,\bar{h}_\varphi \\ \bar{e}_z &= -\varsigma_{z\varphi}\,\bar{h}_z + \varsigma_{zz}\,\bar{h}_\varphi \end{aligned}, \tag{6.7}$$

where $\varsigma_{z\varphi} = \varsigma_{\varphi z}$ because of symmetry. Substituting (6.7) to (6.3) and (6.4) gives the voltage responses:

$$V_w = \bar{e}_z l = (\varsigma_{zz}\frac{2i}{ca} - \varsigma_{z\varphi}\,h_{ex})l, \tag{6.8}$$

$$V_c = \bar{e}_\varphi 2\pi a n l = (-\varsigma_{\varphi\varphi}\,h_{ex} + \varsigma_{\varphi z}\frac{2i}{ca})2\pi a n l, \tag{6.9}$$

where l is the wire length and n is the number of coil turns per unit length.

The MI phenomenon can be explained in terms of classical skin effect in magnetic conductors with a large effective permeability and its strong dependence on the magnitude of an external dc magnetic field [4]. Because the skin depth as well as the characteristic correlation length in a magnetic structure (e.g., domain width) in soft magnetic materials is much larger than the interatomic distances, the classical electrodynamics of continuous media can be used for the description of MI effects. The calculation of $\hat{\varsigma}$ is based on the solution of Maxwell's equations for the fields **e** and **h** together with the equation of motion for the magnetisation vector $\boldsymbol{M}$. An analytical treatment is possible in a linear approximation with respect to the time-variable parameters **e**, **h**, $\mathbf{m} = \boldsymbol{M} - M_0$, where M_0 is the static magnetisation. Assuming a local relationship between **m** and **h**: $\mathbf{m} = \hat{\chi}\mathbf{h}$, the problem is simplified to finding the solutions of Maxwell equations with a given ac permeability matrix $\hat{\mu} = 1 + 4\pi\hat{\chi}$:

$$\nabla \times \boldsymbol{e} = -j\omega\hat{\mu}\boldsymbol{h}/c$$
$$\nabla \times \boldsymbol{h} = 4\pi\sigma\boldsymbol{e}/c \tag{6.10}$$

satisfying the boundary conditions (6.5). In (6.10) the displacement current density $\varepsilon(\partial e/\partial t)$ is neglected inside a conductor. This is permissible since the electric field in conjunction with the dielectric constant is very small, even for rapidly changing fields, when compared with the conduction current. The permeability $\hat{\mu}$ depends on many factors, including the domain configuration, anisotropy and stress distribution, and the mode of magnetisation (domain wall motion or magnetisation rotation). These factors can be complex in real materials, making modelling very difficult. In this analysis, the domain structure is not considered. It can be eliminated by a proper dc bias. It is assumed that M_0 is aligned in a helical direction having a constant angle θ with the wire axis. In this case, $\hat{\mu}$ is determined by the magnetic moment rotation and is independent of the position. This is approximation even for an ideal material, since a circumferential magnetisation near the wire centre results in infinite exchange energy. Then, there is always a radial distribution in permeability, which is stronger in the case of a helical anisotropy due to a stress distribution. Here, when I consider a high frequency case, the permeability is predominantly a surface permeability (not effected by radial changes). In the low frequency case where the radial change in permeability becomes important the magneto-impedance effect is relatively small. The tensor $\hat{\mu}$ has a general form with

$$\mu_{\varphi r} = -\mu_{r\varphi},\ \mu_{rz} = -\mu_{zr},\ \mu_{\varphi z} = \mu_{z\varphi} \tag{6.11}$$

due to the magnetic symmetry. Considering that the time dependence is given by $\exp(-j\omega t)$ and utilising the cylindrical symmetry ($\mathbf{e} = (e_\varphi, e_z)$, $\mathbf{b} = (b_\varphi, b_z)$), Maxwell's equations can be reduced to

$$\frac{\partial e_z}{\partial r} = -\frac{j\omega}{c} b_\varphi,\quad \frac{1}{r}\frac{\partial (r e_\varphi)}{\partial r} = \frac{j\omega}{c} b_z$$
$$\frac{\partial h_z}{\partial r} = -\frac{4\pi\sigma}{c} e_\varphi,\quad \frac{1}{r}\frac{\partial (r h_\varphi)}{\partial r} = \frac{4\pi\sigma}{c} e_z \tag{6.12}$$

where $\mathbf{b} = \hat{\mu}\,\mathbf{h}$ is the vector of magnetic induction. Since $b_r = 0$ (which satisfies the boundary conditions at the wire surface), the material equations are of the form:

$$b_\varphi = \mu_1 h_\varphi + \mu_3 h_z$$
$$b_z = \mu_3 h_\varphi + \mu_2 h_z \tag{6.13}$$

The magnetic parameters are given by

$$\mu_1 = \mu_{\varphi\varphi} + \mu_{\varphi r}^2 / \mu_{rr}$$
$$\mu_2 = \mu_{zz} + \mu_{rz}^2 / \mu_{rr} \tag{6.14}$$
$$\mu_3 = \mu_{\varphi z} - \mu_{\varphi r}\mu_{rz} / \mu_{rr}$$

Substituting (6.13) to (6.12) and eliminating the electric field e gives the equations for the magnetic field components h_z and h_φ:

$$r^2 \frac{\partial^2 h_\varphi}{\partial r^2} + r\frac{\partial h_\varphi}{\partial r} + \left(k_1^2 r^2 - 1\right) h_\varphi = -k_3^2 r^2 h_z$$
$$r^2 \frac{\partial^2 h_z}{\partial r^2} + r\frac{\partial h_z}{\partial r} + k_2^2 r^2 h_z = -k_3^2 r^2 h_\varphi \tag{6.15}$$

where $k_i^2 = \mu_i \left(j\omega\sigma/4\pi\right)$ and $i=1,2,3$. Equations (6.15) are solved imposing following boundary conditions:

$$h_\varphi(a) = 2i/ca$$
$$h_z(a) = h_{ex} \tag{6.16}$$

at the wire surface. The boundary conditions at $r = 0$ must exclude the infinite solutions, requiring

$$h_\varphi(r \le a) < \infty$$
$$h_z(r \le a) < \infty \tag{6.17}$$

Then, the coupled equations (6.15) with conditions (6.5) and (6.17) can be completely determined in two limiting cases: $\delta << a$ and $\delta >> a$, where $\delta = c/\sqrt{2\pi\sigma\omega}$ is the skin depth in a non-magnetic material, as it was shown in [4]. Full theoretical analysis is outside of my investigation and can be found in works of Dr. D. Makhnovskiy and Prof. L. V. Panina [1-4, 17, 20]. Here I will present only final results of low-frequency ($\delta << a$) and high-frequency ($\delta >> a$) solutions for surface impedance $\hat{\zeta}$. The impedance tensor $\hat{\zeta}$ for ($\delta >> a$) can be written as:

$$\hat{\zeta} = \begin{pmatrix} \zeta_{zz} & \zeta_{z\varphi} \\ \zeta_{\varphi z} & \zeta_{\varphi\varphi} \end{pmatrix} = \frac{(1-j)c}{4\pi\sigma\delta} \times \times \begin{pmatrix} \sqrt{\mu_{ef}}\cos^2\theta + \sin^2\theta & \left(\sqrt{\mu_{ef}} - 1\right)\sin\theta\cos\theta \\ \left(\sqrt{\mu_{ef}} - 1\right)\sin\theta\cos\theta & \sqrt{\mu_{ef}}\sin^2\theta + \cos^2\theta \end{pmatrix} \tag{6.18}$$

Here σ is the wire conductivity, and $\mu_{ef} = 1 + 4\pi\chi$ is the ac effective circumferential permeability with respect to the ac current flow.

In the low-frequency case ($\delta << a$) surface impedance $\hat{\zeta}$ can be expressed in the following form:

$$\varsigma_{zz} = \frac{k_1 c}{4\pi\sigma}\frac{J_0(k_1 a)}{J_1(k_1 a)} + \frac{1}{54}\left(\frac{a}{\delta}\right)^4 \frac{c\mu_3^2}{\pi\sigma a} \tag{6.19}$$

$$\varsigma_{\varphi\varphi} = -\frac{k_2 c}{4\pi\sigma}\frac{J_1(k_2 a)}{J_0(k_2 a)} + \frac{1}{36}\left(\frac{a}{\delta}\right)^4 \frac{c\mu_3^2}{\pi\sigma a} \tag{6.20}$$

$$\varsigma_{\varphi z} = \varsigma_{z\varphi} = j\frac{a\omega}{3c}\mu_3 - \left(\frac{a}{\delta}\right)^4 \left[\frac{\mu_1\mu_3}{60} + \frac{\mu_2\mu_3}{30}\right]\frac{c}{\pi\sigma a} \tag{6.21}$$

The second terms in (6.19)–(6.21) depend on the corresponding magnetic parameters μ_i (introduced by (6.14)), demonstrating that the actual expansion parameter involves a sort of magnetic skin depth (but not exactly δ_m). The numerical analysis shows that the first terms in (6.19)–(6.21) can give the main contribution to the impedance even in the case of $(k_i / a) \approx 1$.

6.2 Rotational permeability in a magnetic wire with a helical anisotropy.

In this Section I consider the rotational permeability, which determines the impedance at high frequencies, when the wall motion is strongly damped. I will use a linearised Landau-Lifshitz/Gilbert equation describing the magnetization dynamics in a single domain state [9]:

$$\frac{dM}{dt} = -\gamma M \times H_{eff} + \frac{\tau}{M_0}\left(M \times \frac{dM}{dt}\right) \tag{6.22}$$

where γ is the gyromagnetic ratio, M_0 is the saturation magnetization, $\boldsymbol{H}_{eff}$ is the effective field and τ is the Gilbert damping parameter. In (6.20) the Gilbert form of damping term is used, which for small damping is mathematically equivalent to the original Landau-Lifshitz damping term [9-16]. These dimensionless damping terms conserve the length of the magnetization vector $\boldsymbol{M}$, as required for ferromagnetic systems exhibiting no scattering at impurities.

The effective field $\boldsymbol{H}_{eff}$, which includes all the macro- and microscopic forces acting on the magnetic system, can be calculated from an appropriate free energy density (2.5). The effective field $\boldsymbol{H}_{eff}$ can be defined as a variation derivative of free energy:

$$\boldsymbol{H}_{eff} = -\frac{\partial U_F}{\partial \boldsymbol{M}} \tag{6.23}$$

Equation (6.22) is nonlinear. Its solution can, however, substantially be simplified if the linear approximation is used. The linearization method consists in the representation of all quantities as a sum of a dc and ac additions: $\boldsymbol{M} = \boldsymbol{M}_0 + \boldsymbol{m}$ and $\boldsymbol{H}_{eff} = \boldsymbol{H}_{eff0} + \boldsymbol{h}_{eff}$, where $|\boldsymbol{M}_0| >> |\boldsymbol{m}|$ and $|\boldsymbol{H}_{eff0}| >> |\boldsymbol{h}_{eff}|$. Using these inequalities and (6.20) we obtain the following linearised equations:

$$\boldsymbol{M}_0 \times \boldsymbol{H}_{eff0} = 0 \tag{6.24}$$

which is equivalent to Brown's micromagnetic equation [10] for the static magnetization configuration $\boldsymbol{M}_0$ and the equation

$$\frac{d\boldsymbol{m}}{dt} = -\gamma \boldsymbol{m} \times \boldsymbol{H}_{eff} - \gamma \boldsymbol{M}_0 \times \boldsymbol{h}_{eff} + \frac{\tau}{M_0} \boldsymbol{M} \times \frac{d\boldsymbol{m}}{dt} \tag{6.25}$$

for the ac component of magnetization $\boldsymbol{m}$. For small deviations of the magnetization vector $\boldsymbol{M}$ from its dc value $\boldsymbol{M}_0$ (i.e. $|\boldsymbol{M}_0| >> |\boldsymbol{m}|$) we have also $|\boldsymbol{H}_{eff0}| >> |\boldsymbol{h}_{eff}|$. The second order terms of $\boldsymbol{m}$ and $\boldsymbol{h}_{eff}$ in (6.25) then can be omitted.

Equation (6.25) can be further simplified taking the time dependence as $\exp(-j\omega t)$:

$$-j\omega \boldsymbol{m} + (\omega_H - i\tau\omega)(\boldsymbol{m} \times \boldsymbol{n}_{z'}) + \gamma M_0 ((\hat{N}_{eff} \boldsymbol{m}) \times \boldsymbol{n}_{z'}) = \gamma M_0 (\boldsymbol{h} \times \boldsymbol{n}_{z'}) \tag{6.26}$$

Here $\omega_H = \gamma(\partial U_E / \partial \theta)$, U_E is the overall magnetic energy density (2.5), $n_{z'}$ is a unit vector along the static magnetisation M_0 and $\hat{N}_{eff}$ is the matrix of the effective demagnetising

factors (including anisotropy terms). In the cylindrical coordinate system (z',φ',r) with the axis $z' \| M_0$:

$$N_{z'z'} = -\frac{3\lambda\sigma}{M_0}\cos^2(\theta-\alpha)$$
$$N_{\varphi'\varphi'} = -\frac{3\lambda\sigma}{M_0}\sin^2(\theta-\alpha) \qquad (6.27)$$
$$N_{z'\varphi'} = \frac{3\lambda\sigma}{2M_0}\sin 2(\theta-\alpha)$$

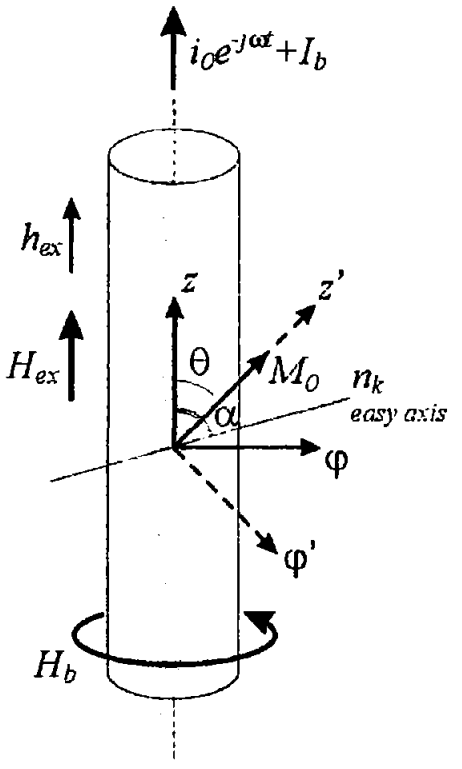

Fig. 6.2 Rotational magnetisation in the wire. Principal quantities and directions. Adapted from [4].

The susceptibility matrix is defined by $\boldsymbol{m} = \hat{\chi}\boldsymbol{h}$. It has a simplest form in the cylindrical co-ordinate system with the axis $z' \| M_0$:

$$\hat{\chi} = \begin{pmatrix} \chi_1 & -j\chi_a & 0 \\ j\chi_a & \chi_2 & 0 \\ 0 & 0 & 0 \end{pmatrix} \qquad (6.28)$$

Solving (6.26) yields:

$$\begin{aligned}
&\chi_1 = \omega_M(\omega_1 - j\tau\omega)/\Delta \\
&\chi_2 = \omega_M(\omega_2 - j\tau\omega)/\Delta \quad \chi_a = \omega\,\omega_M/\Delta \\
&\Delta = (\omega_2 - j\tau\omega)(\omega_1 - j\tau\omega) - \omega^2, \\
&\omega_1 = \gamma[H_{ex}\cos\theta + H_b\sin\theta + H_K\cos 2(\alpha-\theta)], \\
&\omega_2 = \gamma[H_{ex}\cos\theta + H_b\sin\theta + H_K\cos^2(\alpha-\theta)], \\
&H_K = 3\lambda\sigma/M_0 \quad \omega_M = \gamma M_0.
\end{aligned} \tag{6.29}$$

The susceptibility tensor can be converted to the original coordinate representation (z, φ, r) by rotating the prime system by angle θ, which determines the direction of M_0 with respect to the wire axis z,

$$\hat{\chi} = \begin{pmatrix} \chi_1 & -j\chi_a\cos(\theta) & j\chi_a\sin(\theta) \\ j\chi_a\cos(\theta) & \chi_2\cos^2(\theta) & -\chi_2\sin(\theta)\cos(\theta) \\ -j\chi_a\sin(\theta) & -\chi_2\sin(\theta)\cos(\theta) & \chi_2\sin^2(\theta) \end{pmatrix} \tag{6.30}$$

The impedance tensor is determined via the permeability parameters μ_i (low-frequency case) or the parameter μ_{ef} (high-frequency case), all of them are determined by the apparent susceptibility χ

$$\chi = \chi_2 - \frac{4\pi\chi_a^2}{1+4\pi\chi_1}. \tag{6.31}$$

Using this parameter, the introduced permeability values are represented as

$$\begin{aligned}
&\mu_1 = 1+4\pi\cos^2(\theta)\chi, \qquad \mu_2 = 1+4\pi\sin^2(\theta)\chi, \\
&\mu_3 = -4\pi\sin(\theta)\cos(\theta)\chi, \qquad \mu_{ef} = 1+4\pi\chi
\end{aligned} \tag{6.32}$$

Substituting (6.29) into (6.31) gives

$$\chi = \frac{\omega_M(\omega_2 - j\tau\omega) + 4\pi\omega_M^2}{(\omega_1 - j\tau\omega)(\omega_2 + 4\pi\omega_M - j\tau\omega) - \omega^2} \tag{6.33}$$

Equation (6.33) shows that the resonance change in χ can be expected at rather high frequencies (the resonance frequency is roughly equal to $\gamma\sqrt{H_K\,4\pi M_0}/2\pi \sim 500$ MHz for $H_K = 5$ Oe, $4\pi M_0 = 6000$ G), or for very high magnetic fields. Then, the MI effects at are typically not related to ferromagnetic resonance. Yet, a high sensitivity of χ with respect to H_{ex} is needed to obtain large impedance changes. This can be realised by changing the

direction of M_0 under the effect of the field. The magnetisation angle changes for fields of the order of the anisotropy field H_K, which is also the region of the major change in the permeability and the impedance. For higher fields, χ changes little resulting in insensitive impedance behaviour. Therefore, the overall reason for the MI effects is the redistribution of the high-frequency current density when the static magnetic structure is changed. This conclusion is especially important for very high frequencies when the effective susceptibility (6.33) becomes insensitive to both the external field and anisotropy field.

6.3 Experimental magneto-impedance investigation in 1-100 MHz frequency range.

When dealing with measurements at intermediate frequencies, special care must be taken for the correct interpretation of results. At frequencies higher then 10 MHz the impedance match becomes critical to insure the maximum power delivery to the magneto-impedance element.

6.3.1 Experimental set-up

In my case the impedance matrix $\hat{\zeta}$ is measured in a most appropriate way, by means of Hewlett-Packard 8753E Vector Network Analyser configured in the two-ports measurement set for the S_{21}-parameter (forward transmission): $S_{21} = V_{out}/V_{in}$, where V_{in} is the excitation sinusoidal signal from Port 1 and V_{out} is the output signal measured in Port 2. The ac excitation current i and field h_{ex} in (6.8, 6.9) are determined by V_{in}, whereas V_{out} is equal to V_w or V_c in accordance of the excitation method. Thus, the S_{21}-parameter is directly proportional to the specific impedance component. Note that the S_{21}-parameter includes both the normalised amplitude $|V_{out}/V_{in}|$ and phase shift $Arg(V_{out}/V_{in})$ with respect to the excitation signal. The MI effect is assumed to be linear; therefore the excitation signal has to be quite small to exclude any non-linear effects. In my experiments the linear MI effects are investigated using only a few milliamps of excitation current, however, large amplitude excitation (tens of milliamps) can be useful for sensor applications where the improvement of

the signal-to-noise ratio is important. The general view of the measuring system is shown in Fig. 6.3.

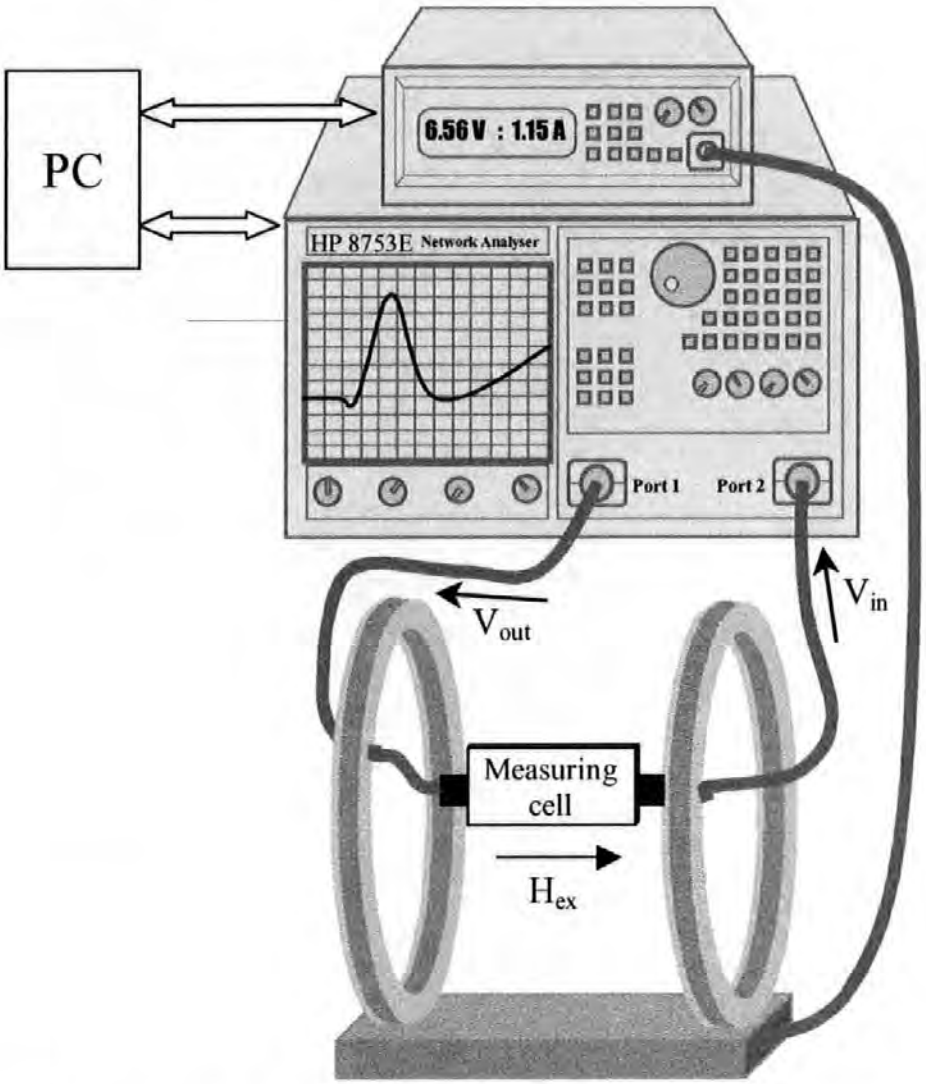

Fig. 6.3 General view of the magneto-impedance measuring system.

The magnetic field (H_{ex}) is produced from a coil driven by a computer controlled dc power supply. The operating processes of the Analyser and power supply are synchronised by a computer program written using VEE software. The power supply is used as a programmable stepwise dc source to provide the field scans. The field was driven in both positive and negative directions to produce the hysteresis plot. The S_{21}-values, obtained within one frequency scan, are saved in the Analyser memory and at the end of a full scan

were transferred to PC. Each frequency scan gives a column of S_{21} taken at some fixed H_{ex}. The total value matrix $\{S_{21}\}_{f,H_{ex}}$ consists of columns of frequency coordinate points (f) and rows of field coordinate points (H_{ex}).

The measured sample was placed onto the open-type cell made of copper-coated fibreglass printed circuit board (PCB), which had the following parameters: 1.8 mm thickness, 35 μm of copper on each side and average dielectric constant of $\varepsilon = 4.5$. All connection stripes were made 2.8 mm in width to provide wave impedance in the order of 50-Ohms over a wide range of frequencies. The microwave track including the cables and adapters was calibrated for the two-port measurements. The cells have 3.5mm connectors and are linked up to the Transmitter/Receiver ports. A wire element (12 mm long) soldered or bonded to the cell is excited by the sinusoidal input voltage V_{in}. The output voltage V_{out} is taken from the wire (Fig. 6.4 (a)) or from a tiny coil (Fig. 6.4 (b)), which has 25 turns and an internal diameter of 120 μm. Blocking capacitor (C) prevents the dc bias current I_b from

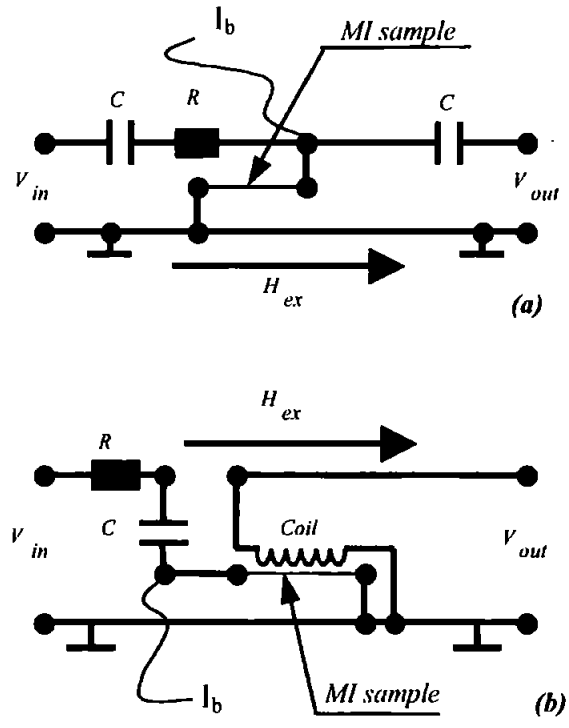

Fig. 6.4 Electrical circuits of the cell for ζ_{zz} in (a) and $\zeta_{\varphi z}$ in (b).

entering the Analyser. Terminal resistors are required for normalising input/output impedance of the measured elements. The S_{21}-parameter (forward transmission) is measured as a function of a sensed magnetic field H_{ex} applied in the wire axial direction. In general, a dc bias current I_b can be applied to the wire. The impedance components ζ_{zz} and $\zeta_{\varphi z}$ $(=\zeta_{z\varphi})$ are determined by measuring the output signal V_{out} from the wire $(V_{out}=V_w)$ or from the coil $(V_{out}=V_c)$, respectively. In both cases the ac current i supplied by V_{in} is applied to the wire. The S_{21}-parameter is defined as a dimensionless quantity $S_{21}=V_{out}/V_{in}$.

6.3.2 Measurements of the diagonal ζ_{zz} and off-diagonal $\zeta_{\varphi z}$ magneto-impedance.

I start my investigation with the longitudinal diagonal magneto-impedance ζ_{zz} in the wire with a circumferential anisotropy. The normalised impedance ζ_{zz} is determined by measuring the voltage V_w across the wire when it is excited by the ac current ($h_{ex}=0$). Putting $h_{ex}=0$ in (6.8) results in $S_{21}=V_w/V_{in}=\zeta_{zz}(H_{ex})(h_\varphi l/V_{in})$. The plots of magnitude of ζ_{zz} versus applied magnetic field H_{ex} at different frequencies are shown in fig. 6.5. The MI patterns change with increasing frequency. At relatively low frequencies (1 MHz, pink curve) there is one central peak. As the frequency is increased, a split occurred and at higher frequencies there are two symmetrical peaks associated with the field in the order of the anisotropy field. This behaviour is governed by comparative contributions of domain wall motion and magnetisation rotation contributions to the overall permeability. These processes have different field dependences. At relatively low frequencies the main contribution to the total permeability is determined by the domain-wall dynamics. The maximum domain permeability corresponds to zero axial magnetic field, which produces one-peak MI plot. This agrees well with the results obtained for domain wall permeability from the analysis of dynamic circular hysteresis (compare pink curve at 1 MHz in Fig. 6.5 and green curves at 150 kHz in figs. 5.5 and 5.7). For higher frequencies the domain wall motion is strongly damped by eddy currents. The corresponding susceptibility χ_{dw} drops, the rotational contribution of remagnetisation grows and becomes important. However, the rotational permeability has completely different field characteristics: it is small at a zero axial field when the dc magnetisation and the excitation high frequency field are in parallel. The application of the

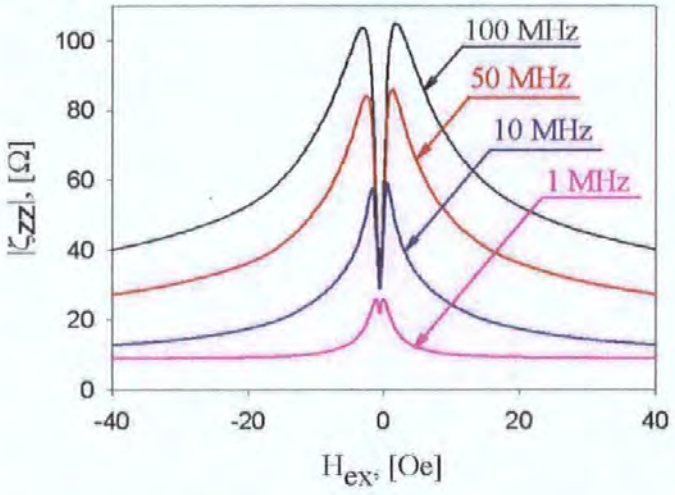

Fig. 6.5 Experimental plots of longitudinal impedance at different frequencies.

axial field rotates the dc magnetisation towards the axis and activates the rotational processes. (Compare with the field behaviour of rotational permeability in Chapter 5). As a result, the MI plots show two sharp maximums at $H_{ex} = H_K \approx 2.8\ Oe$. At high frequencies, both real and imaginary parts of the longitudinal impedance exhibit similar field characteristics, as shown in fig. 6.6. However, the resistive characteristic is sharper and consequently more sensitive to small external magnetic fields. This can be due to the contribution of distributed impedance of lead wires etc, which becomes more essential with increasing frequency. It should be noted, that in the intermediate frequency range the reactive and resistive parts of the impedance are relatively the same and the MI element has to be classified as a low Q-factor device, which makes it not suitable for applications where "a resonance tuning circuit" is required.

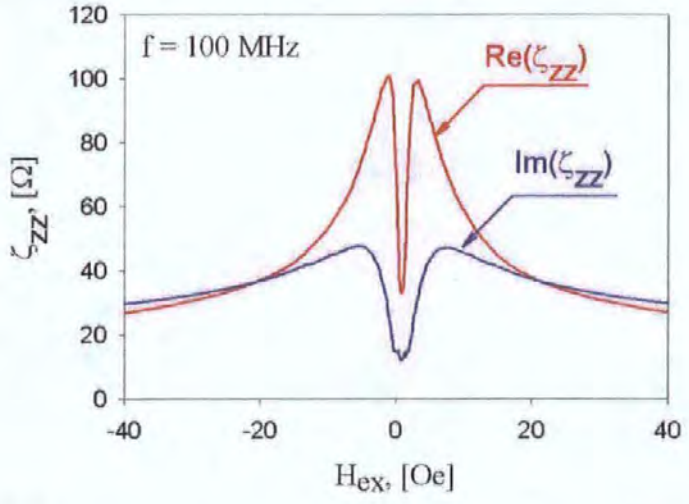

Fig. 6.6 Experimental plot of the real $\mathrm{Re}(\zeta_{zz})$ *and imaginary* $\mathrm{Im}(\zeta_{zz})$ *parts of the longitudinal impedance.*

In the frequency range where the domain contribution is still essential, the low field sensitivity of the MI elements can be improved by applying a dc current, which eliminates the domain structure. This is demonstrated in fig. 6.7. When a dc bias is applied, the impedance value at zero field becomes considerably smaller and the impedance characteristic shows two very sharp peaks. For not very high I_b, the values of the impedance at the maximums are

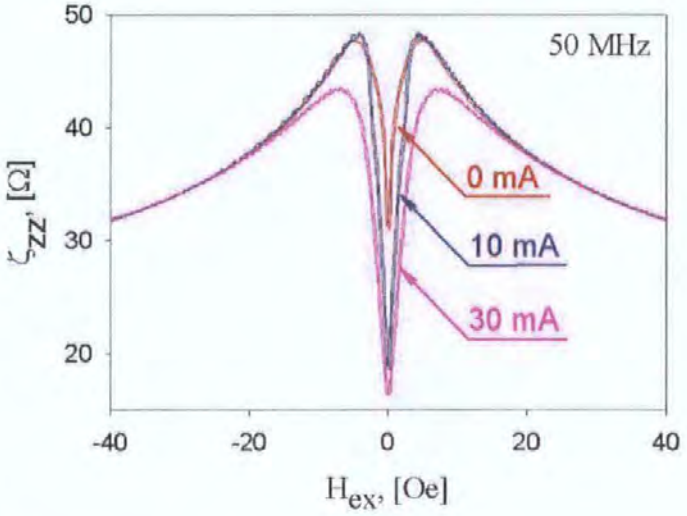

Fig. 6.7 Plots of the longitudinal impedance at different bias currents I_b.

almost constant since they are determined by the rotational processes only. If I_b is increased further the value of the impedance at the maximums becomes smaller and the sensitivity drops, due to an increase in magnetic hardness caused by I_b.

The off-diagonal components $\zeta_{z\varphi}$ and $\zeta_{\varphi z}$ can be determined by measuring the coil voltage V_c when the wire is excited by the ac current i, or measuring the wire voltage V_w in the presence of the ac axial magnetic field h_{ex}. The former is used here (Fig. 6.4(b)). In this case, in equation (6.9) $h_\varphi = 0$ with the result that $S_{21} = V_c/V_{in} = -\zeta_{\varphi z}(H_{ex})(ni\,l/V_{in})$. The off-diagonal impedance $\zeta_{\varphi z}(H_{ex}) \sim S_{21}(H_{ex})$ is shown in Fig. 6.8 at the fixed frequency of 50 MHz for different bias currents. In this case, if no dc bias current is used, the response signal is very small and irregular (it would be zero for an ideal circular domain structure since the average value $\sin\theta\cos\theta$ in (6.27) is zero). The off-diagonal response increases substantially when a small dc current $I_b = 2.5$ mA is applied. Typically, the coercivity in amorphous wires is about a fraction of Oe and applying a small current of a few mA eliminates circular domains. Therefore, in the case of circumferential anisotropy and a circular domain structure, the presence of I_b is the necessary condition for the existence of the off-diagonal components of the impedance tensor. The real and imaginary parts of the off-diagonal component are antisymmetrical with respect to the field H_{ex}, having almost linear behaviour in the field range of ±2 Oe.

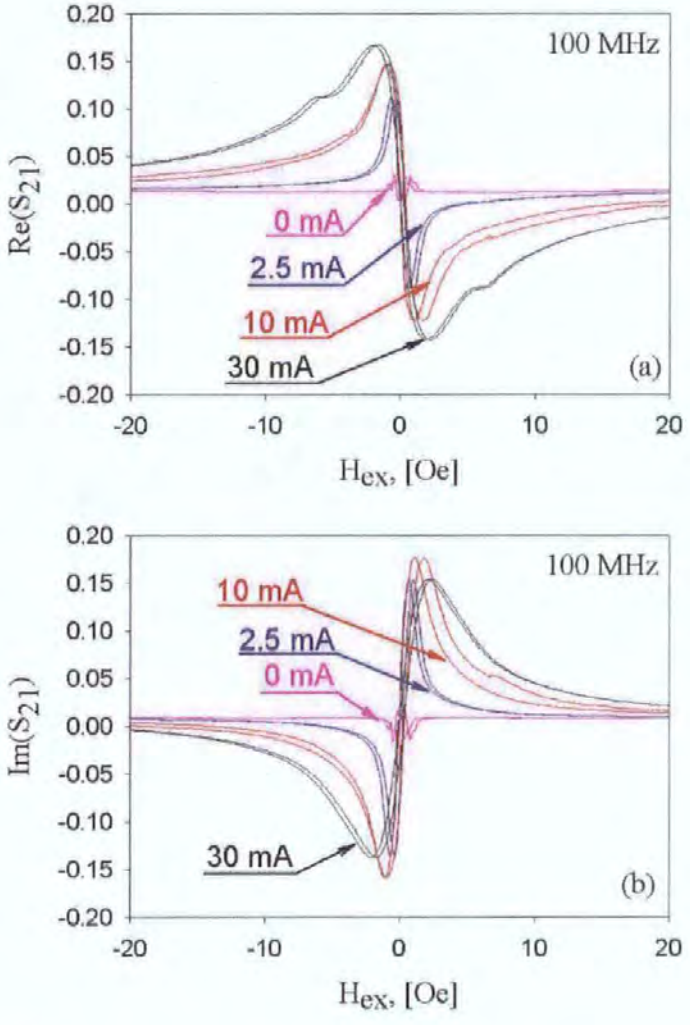

Fig. 6.8 Off-diagonal impedance for different applied bias currents. Real part in (a) and imaginary part of impedance in (b).

6.4 Magneto-impedance in the GHz range.

Recently, Magneto-Impedance at very high frequencies was investigated [19]. The field sensitivity of the surface impedance in the wires with circumferential and helical anisotropies remained very high even in GHz range. This makes the MI effect very useful in the design microwave composites with tunable properties and tunable band-gap structure [20, 21]. It can be also used for designing a new type of high-frequency transponder in radio-frequency identification (RFID) systems [22].

High-frequency modification in magneto-impedance (MI) characteristics in the frequency range of 0.5-3 GHz has been investigated in 10 μm diameter amorphous microwires with a circumferential anisotropy. The circular domain structure results in nearly linear nonhysteretic magnetization curves, as shown in Fig. 6.9.

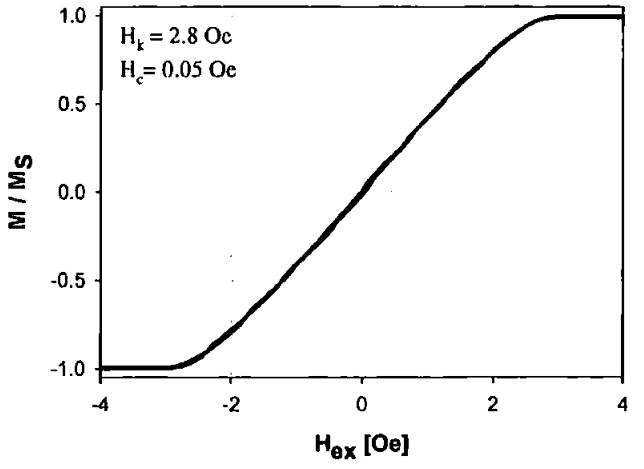

Fig. 6.9. Longitudinal hysteresis loop of microwire with small negative magnetostriction.

The complex-valued of the magneto-impedance $Z = V / i$ is found by measuring S_{11} parameter (reflection coefficient) by means of a Hewlett-Packard 8753E Vector Network Analyser (VNA) with a specially designed microstrip cell (see Fig. 6.10) to minimise the post calibration mismatches originated by bonding the sample. Rather than attempting to quantify the contribution of this error in the wire impedance, my approach was to minimise its effect. The microstrip portion connected to VNA is pre-calibrated with a standard 50 Ω load, which is then removed (Load "1" in Fig. 6.10). During the measurements, the microstrip cell with the bonded sample is matched to a 50 Ω load (Load "2"). This calibration of the microstrip line with a length of 3.5 cm holding the bonded wire of 1.4 cm ensures reliable impedance measurements up to frequencies of about 3 GHz.

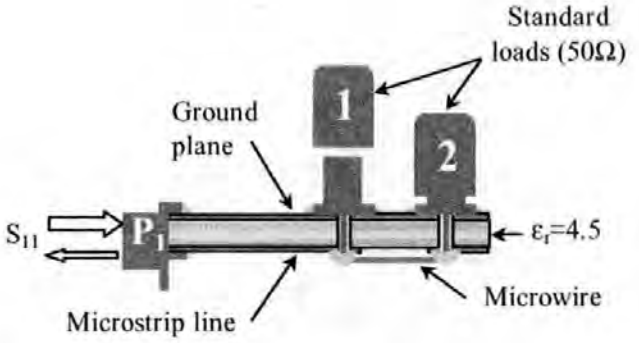

Fig. 6.10. High-frequency measuring cell.

The plots of impedance Z vs. axial low frequency field H_{ex} are shown in Fig. 6.11. Typical MI characteristics with two peaks at the anisotropy field are seen for MHz frequencies. With increasing frequency, the low-field region ($H_{ex} < H_K$) in the impedance plots preserves its high sensitivity although the impedance maximum value at $H_{ex} = H_K$ decreases substantially. The transformations in the high-field ($H_{ex} > H_K$) region are more dramatic. With increasing frequency the impedance looses its sensitivity for higher fields and

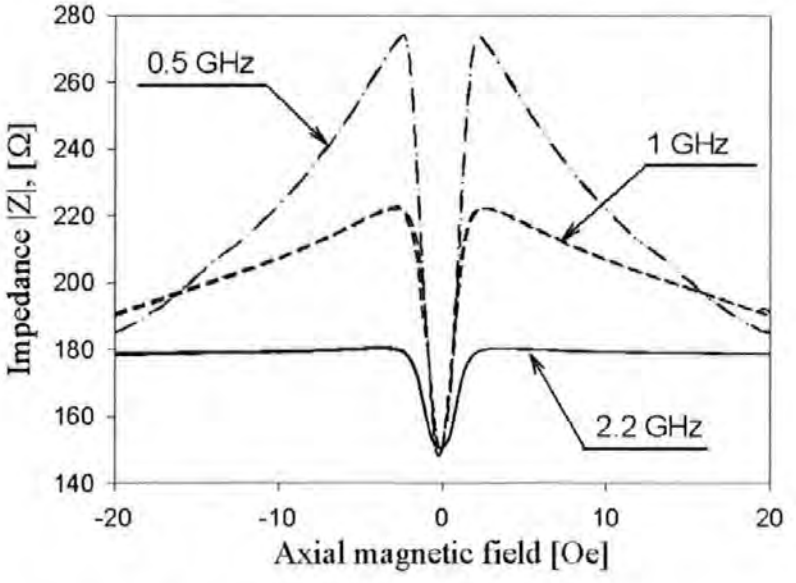

Fig. 6.11. "Valve-like" field-dependence of the axial magneto-impedance at different frequencies in the GHz range.

at frequencies above 2GHz it remains constant for any $H_{ex} > H_K$. This unusual "valve-like" behavior was previously reported in [19] where a rather confusing explanation of this effect was given. It was stated that the microwave MI did not directly depend on the ac permeability (like in MHz range) but on the dc magnetization. My experimental results revealing a gradual transformation of a two-peak plot into that reaching saturation at $H_{ex} = H_K$ allow a consistent explanation to be given.

The analysis of microwave MI is based on the rotational dynamics under the condition of a linear ac excitation with time dependence taken in the form $\exp(-j\omega t)$ [4]. In a wire with a circular domain structure having no averaged helical magnetization, the impedance is represented in a simple form:

$$Z = R_{dc} ka \frac{J_0(ka)}{2J_1(ka)} \tag{6.34}$$

$$k = (1+i)\sqrt{\hat{\mu}} / \delta_0 \tag{6.35}$$

where R_{dc} is the wire dc resistance, $J_{0,1}$ are the Bessel functions, $\delta = \sqrt{2\rho/\omega\mu_0}$ is the skin depth for nonmagnetic material, σ is the conductivity, $\hat{\mu} = 1 + 4\pi\cos^2(\theta)\hat{\chi}$, θ is the angle between the static magnetization M_0 and the wire axis, and $\hat{\chi}$ is the susceptibility parameter:

$$\hat{\chi} = \chi_2 - 4\pi\chi_a / (1 + 4\pi\chi_1) \tag{6.36}$$

In (6.36), the parameters χ_1, χ_2 and χ_a are diagonal and off-diagonal components of the ac rotational susceptibility tensor written in the co-ordinate system with the z-axis parallel to M_0. Assuming that the anisotropy axis is directed at angle α with respect to the wire axis (slightly different from 90°), the susceptibility parameters are given by (6.29).

With increasing frequency beyond the ferromagnetic resonance, the susceptibility $\hat{\chi}$ loses its field sensitivity [20]. Thus, the impedance is entirely related to the static magnetization orientation θ. Then, if θ is a sensitive function of H_{ex}, to insure high field sensitivity of the impedance, it is important only that the condition $|\hat{\mu}| >> 1$ is still held. This conclusion also demonstrates that the condition of the ferromagnetic resonance is not required for the MI effect, contrary to the widely expressed belief [23]. The "valve-like" behavior of $Z(H_{ex})$ at very high frequencies may be of a considerable interest since the impedance switches from one stable level to the other, following the dc magnetization. This

property can find an interesting use in the tunable microwave composite consisting of short ferromagnetic wires embedded into a dielectric matrix [23].

References

[1] L. Panina, K. Mohri, T. Uchiyama, M. Noda, *"Giant magneto-impedance in Co-rich amorphous wires and films"*, IEEE Trans. Magn., (1995) Vol. 31, 1249-1260.

[2] L. Panina and K. Mohri, *"Mechanism of the magneto-impedance effect in negative magnetostrictive amorphous wires"*, J. Magn. Soc. of Japan (1994) Vol. 18, 245-249.

[3] L. Panina and K. Mohri, *"Magneto-impedance effect in amorphous wires"*, Appl. Phys. Lett., (1994) Vol. 65, 1189-1191.

[4] D. P. Makhnovskiy, L. V. Panina, and D. J. Mapps, *"Field-dependent surface impedance tensor in amorphous wires with two types of magnetic anisotropy: helical and circumferential"*, Phys. Rev. B, (2001) Vol. 63, 144424.

[5] L. Panina, H. Katoh, K. Mohri, K. Kawashima, *"Magnetisation processes in amorphous wires in orthogonal fields"*, IEEE Trans. Magn., (1993) Vol. 29, 2524-2526

[6] K. Mohri, K. Kawashima, T. Kohzawa and H. Yoshiba, *"Magneto-inductive element"*, IEEE Trans. Magn., (1993) Vol. 29, 1245-1248.

[7] K. Kawashima, T. Kohzawa, H. Yoshida and K. Mohri, *"Magneto-inductive effect in tension annealed amorphous wires and MI sensors"*, IEEE Trans. Magn., (1993) Vol. 29, 3168-3170.

[8] K. Bushida and K. Mohri, *"Sensitive magneto-inductive effect in amorphous wires using high-pass filter and micro-field sensor"*, IEEE Trans. Magn., (1994) Vol. 30.

[9] T. L. Gilbert *"A Lagrangian Formulation of the Gyromagnetic Equation of the Magnetization Field"* Phys. Rev. (1955) 100, 1243.

[10] L. Landau and E. Lifshitz *"Electrodynamics of Continuous Media"*, Pergamon Press, Oxford (1975) 195.

[11] L. D. Landau, E. M. Lifshitz and L. P. Pitaevskii "*Quantum Mechanics - Non-Relativistic Theory*" Edition: 3d, Elsevier Science, (1977) Vol. 3.

[12] L. D. Landau and E. M. Lifshitz "*On the theory of the dispersion of magnetic permeability in ferromagnetic bodies*" Phys. Z. Sowjetunion (1935) Vol. 8, 153

[13] L. D. Landau and E. M. Lifshitz "*Electrodynamics of Continuous Media*" Pergamon Press, (1975).

[14] A. G. Gurevich, "*Ferrites at Microwave Frequencies*" New York: Consultants Bureau, (1963).

[15] A. G. Gurevich and G. A. Melkov "*Magnetic oscillations and waves*" Boca Ratton: CRC Press, (1996).

[16] A. Gurevich "*Magnetic Resonance in Ferrite and Antiferomagnets*", Nauka, Moscow, (1973)

[17] L.V. Panina, K. Mohri "*Magneto-impedance effect in amorphous wires*" Appl. Phys. Lett. (1994) Vol. 65, 1189.

[18] K. Mohri, L. V. Panina, T. Uchiyama, K. Bushida, M. Noda "*Sensitive and quick response magneto-impedance (MI) sensor using amorphous wire*" IEEE Trans. Magn. (1995) Vol. 31, 1266.

[19] M. Domingues et al "*Magneto-Impedance in VHF range*" J. Magn. Magn. Mater. (2002) Vol. 249, 117.

[20] D. P. Makhnovskiy, L. V. Panina "*Field dependent permittivity of composite materials containing ferromagnetic wires*" J. Appl. Phys. (2003) Vol. 93, 4120.

[21] A. Figotin, Y. A. Godin "*Two-dimensional tunable photonic crystals*" Phys. Rev. B (1998) Vol. 57, 2841.

[22] C. Hausleitner, R. Steindl, A. Pohl, H. Hauser, F. Siefert "*Impedance Loaded SAW Sensors Offer a Wide Range of Measurement Opportunities*" IEEE Microwive theory and Techniques (2001) Vol. 49, 817.

[23] M. R. Britel, D. Menard, L. G. Melo, P. Ciureanu, A. Yelon, R. W. Cochrane, M. Rouabhi, B. Cornut "*Magnetoimpedance measurements of ferromagnetic resonance and antiresonance*" Appl. Phys. Lett. (2000) Vol. 77, 2737.

[24] L. Kraus, M. Vázquez, and A. Hernando "*Creep-induced magnetic anisotropy in a Co-rich amorphous wire*" J. Appl. Phys., (1994) Vol. 76, 5343.

[25] K. Mohri "*Magneto-inductive effect in amorphous wires*" IEEE Trans. Magn., (1992) Vol. 28, 3150.

[26] J. Velázquez, M. Vázquez, D.-X. Chen, and A. Hernando "*Giant magnetoimpedance in nonmagnetostrictive amorphous wires*" Phys. Rev. B, (1994) Vol. 50, 16737.

[27] K. Mohri, K. Kawashima, T. Kohzawa, and H. Yoshida "*Quick response field senor using 200 MHz amorphous MI element FET multivibrator resonance oscillator*" 1993, *IEEE Trans. Magn.*, (1994) Vol. 29, 1245.

[28] R. S. Beach and A. E. Berkowitz "*Sensitive field- and frequency-dependent impedance spectra of amorphous FeCoSiB wire and ribbon*" J. Appl. Phys., (1994) Vol. 76, 6209.

[29] K. L. Garcia, and R. Valenzuela "*Domain wall pinning, bulging, and displacement in circumferential domains in CoFeBSi amorphous wires*" J. Appl. Phys., (2000) Vol. 87, 5257.

[30] A. Yelon, D. Ménard, M. Britel and P. Ciureanu "*Calculations of giant magnetoimpedance and of ferromagnetic resonance response are rigorously equivalent*" Appl. Phys. Lett., (1996) Vol. 69, 3084.

Chapter 7. Magneto-impedance sensors.

I have demonstrated that understanding the magneto-impedance of magnetic wires requires a deep analysis of magnetic structure, magnetisation processes in conjunction with electrodynamics. This generates a considerable interest to MI as a new branch of fundamental research. Along with this the potential of MI in application to the development of new high performance magnetic sensors cannot be overestimated.

In Table 7.1 (mostly based on data produced by Mohri *et al.* [1]), some important characteristics of sensors based on flux detection principles are summarized. SQUID magnetometers have outstanding sensitivity but a very high cost and require special conditions of operation (liquid helium, screen rooms). Regarding magnetoresistive sensors, although the nominal values can be very large (up to 65% in multilayers and spin-tunnelling junctions), the sensitivity to the field typically is relatively low and does not exceed 1%/Oe. Promising results on sensitivity have recently been obtained for STMR showing about 5%/Oe. The sensitivity of flux gate sensors is quite high (field resolution is down to 10^{-8} Oe) but not for localised fields since the sensor head size is a few cm. The MI element can be 30 times smaller exhibiting a similar sensitivity. Furthermore, its response speed up to 10 MHz is more than 10^3 times higher. Therefore, the MI-based sensors present a reasonable compromise on sensitivity, size, response speed and cost; and can satisfy a very broad spectrum of magnetic sensor needs.

Sensor Principle	Head length (m)	Resolution/ Full scale (Oe)	Response speed (Hz)	Power consumption (W)
Hall	$10\sim100\times10^{-6}$	0.5 /± 1000	10^6	10^{-2}
Magnetoresistance (MR)	$10\sim100\times10^{-6}$	0.1 /± 100	10^6	10^{-2}
Giant Magnetoresistance (GMR)	$10\sim100\times10^{-6}$	0.01 /± 20	10^6	10^{-2}

Tunnelling Magnetoresistance (TMR)	10~100 $\times 10^{-6}$	$2 \cdot 10^{-3}$ /± 20	10^{6}	10^{-2}
Fluxgate	10~20 $\times 10^{-3}$	10^{-6}/± 3	5×10^{3}	1
SQUID	10~20 $\times 10^{-3}$	0.6×10^{-12}/ ± 1.25×10^{-8}	5×10^{3}	-
Magneto-impedance (MI)	1~5 $\times 10^{-3}$	10^{-7}/± 3	10^{6}	5~10$\times 10^{-3}$

Table 7.1 Illustrative comparison of several types of magnetic sensors (adapted from [1])

According to the sensing range classification, a MI sensor occupies a mid-sensing range: 10^{-4} Oe for dc field detection and down to 10^{-7} Oe for ac fields. Hundreds of applications can be mentioned which require high performance magnetic sensors operating in this range. The areas of application for sensors based on the MI effect include: automobile industry, industrial measurements and automation, computers & information technology, biomagnetics & health, environmental sensors, power electronics and energy, security and safety, scientific and academic measurements. At present, the demand in such sensors is satisfied by fluxgate, MR and Hall sensors, whereas the MI sensors are at an early stage of their development. On the other hand, they are expected to show more efficient behaviour having much simpler design and lower cost.

In this Chapter, different types of MI sensors will be considered with detailed analysis of their advantages and disadvantages. Up to now, several types of MI sensors have been proposed. One of the first proposed MI sensor is based on self oscillation circuits such as a Colpitts oscillator with the MI element incorporated into it followed by a demodulator detector [7], as considered in Section 7.2. Well-designed Colpitts oscillators are able to produce a low phase noise sine wave that can result in a relatively high performance sensor. However, this type of sensor has certain disadvantages. The second and most common MI sensor is based on a C-MOS pulse excitation technique and a single-ended detection circuit involving Schottky diode or digital switching detection [3, 4]. This type of sensor has a simple design and low power consumption (about 10 mW in all) with typical sensitivity range of 20-100 nT. This type of sensor will be considered in the section 7.3 with detailed analysis of diagonal and off-diagonal sensor configurations. In section 7.4 a new approach for high-

performance MI sensors will be described. I will discuss the importance of such sensor parameters as frequency and temperature stability, phase noise and bandwidth.

7.1. Magneto-Impedance element

As shown in Chapter 6, there are a number of ways of providing an ac excitation to the MI wire and measuring the voltage response, which is associated with the tensor form of the surface impedance. This is important for sensor development, in particular, for obtaining highly sensitive linear characteristics without using high dc bias field. In general, the wire can be excited by a passing ac current, i, or a coil current i_c, which generates the axial excitation field $h_{ex} = ni_c$. Figure 7.1(a) represents the usual way of excitation with current i and measuring the voltage V_w across the wire, which is proportional to the ζ_{zz} *(see equations 6.8 and 6.18).* The voltage V_w appears also if the wire is excited by the coil current, as shown in Fig. 7.1(b), provided that a proper helical magnetisation in the wire is established. This voltage is proportional to the off-diagonal component of the surface impedance $\varsigma_{z\varphi}$. Considering this circuit in terms of usual impedances, I can introduce the ratio $\tilde{Z}_w = V_w / i_c$ and refer to it as off-diagonal impedance. Another way to measure the MI voltage response is

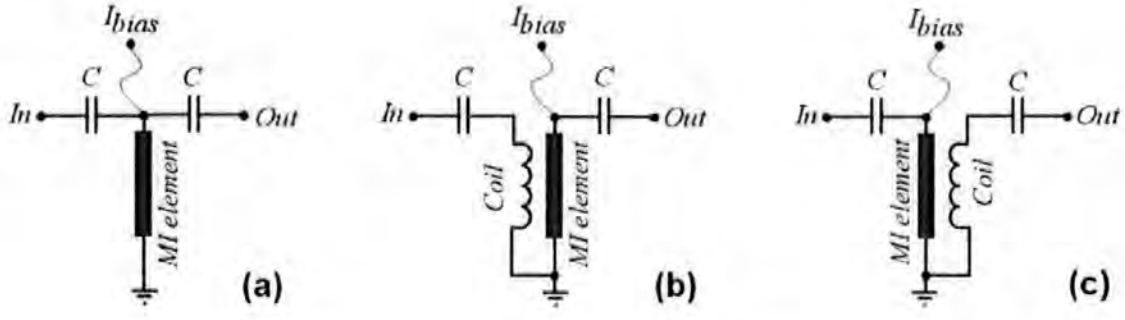

Fig. 7.1 Measuring configurations for Z_W (a), $\tilde{Z}_W$ (b) and Z_C (c). The dc bias current I_{bias} can be applied across the wire to establish a proper dc magnetisation. Blocking capacitors C in the circuits prevent I_{bias} from entering the driving and detecting circuits.

to measure a voltage V_c in the coil mounted around the wire. The excitation can be still provided by a passing current as shown in Fig. 7.1(c). This also corresponds to the off-diagonal impedance configuration determined by the ratio $Z_c = V_c / i$.

According to the theoretical calculations (6.18) and experimental results (see fig 7.2(a)), the diagonal impedance $Z_w(H_{ex})$ is symmetrical having two identical peaks at $H_{ex} = \pm H_K$, where H_K is the characteristic anisotropy field, whilst $Z_c(H_{ex})$ and $\widetilde{Z}_w(H_{ex})$ are antisymmetrical with a near-linear region around zero field point (see fig. 7.2(b)). In a wire with circumferential anisotropy, the axial magnetic field produces a linear magnetisation

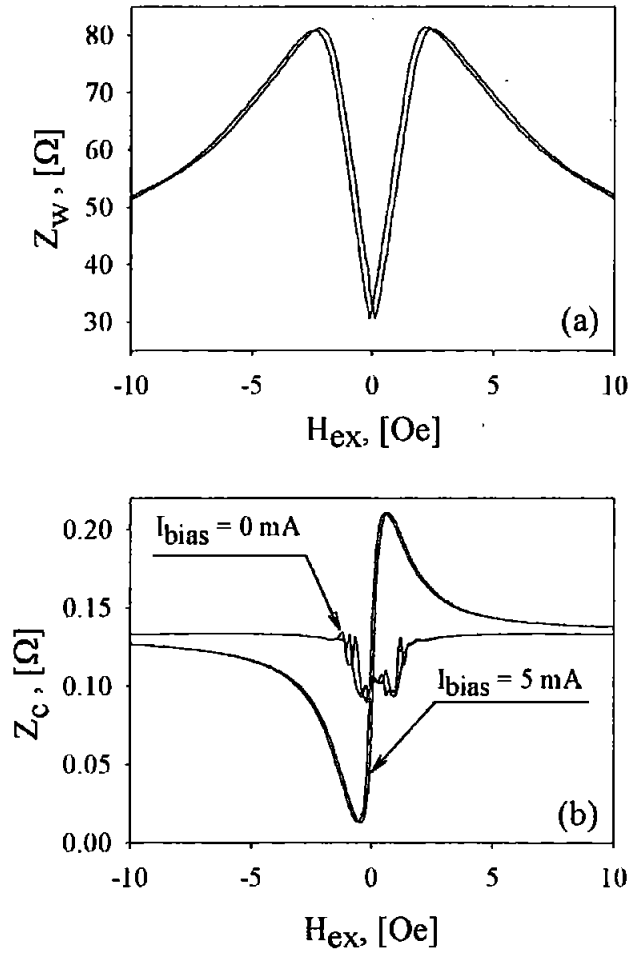

Fig.7.2. The plot of the diagonal (a) and off-diagonal (b) magneto-impedance Z vs. axial magnetic field H_{ex} at frequency 56 MHz. Off-diagonal magneto-impedance measured with (5 mA) and without bias current.

curve in the range of $-H_K < H_{ex} < H_K$. Therefore, I can expect linear field behaviour of the off-diagonal impedances in this field interval for such magnetic configuration (6.18). Some deviation from linearity may be due to the field dependence of the permeability parameter μ_{ef}. However, if the wire has a circular domain structure the off-diagonal components averaged over domains are zeroed, because of the factor $\sin\theta$ (see 6.18), which has an opposite sign in the domains with the opposite circular magnetisation. It implies that a dc bias current will be needed to eliminate the circular domain structure (Fig. 7.2 (b)). With the theoretical and experimental developments in mind, we are ready to focus on different types of MI sensors.

7.2 MI sensor embedded into a Colpitts oscillator

Figure 7.3 shows a typical sensor design, in which the wire is embedded into a Colpitts oscillator – high frequency self-oscillation circuit [7]. Well-designed Colpitts

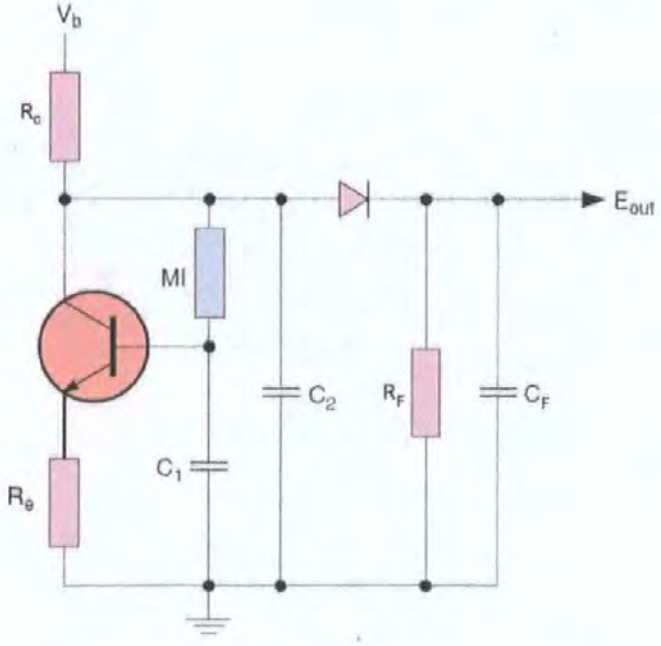

Fig. 7.3 Principle MI sensor design on the basis of the Colpitts oscillator.

oscillators are able to produce a low phase noise sine wave that can result in a relatively high performance sensor. The MI element (wire or thin film) and two capacitors $C_{1,2}$ constitute a resonant circuit whose oscillation is maintained by the transistor. The amplitude of ac current flowing through the MI element will strongly depend on H_{ex} because the oscillations are near the resonance. The amplitude-modulated voltage due to H_{ex} is detected through a diode and low-frequency R_FC_F-filter.

Here I will present a brief analysis of the MI sensor based on Colpitts oscillator. It is convenient to represent the oscillator circuit by a small signal equivalent circuit. To simplify the analysis, the collector and emitter resistors are omitted and a load resistor R_L is introduced. The small-signal equivalent circuit is shown in Figure 7.4. In the case of not very complex oscillator configurations, *the node voltage analysis* [41, 42] can be applied to this circuit.

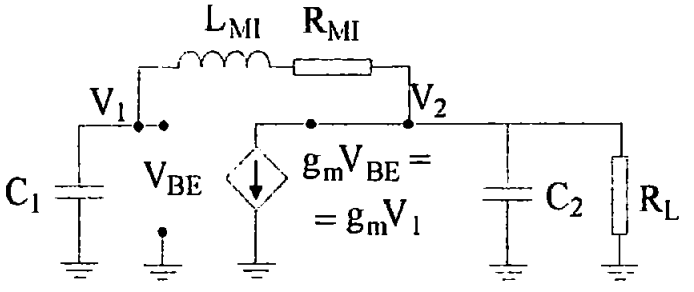

Fig. 7.4 Small-signal equivalent circuit of the Colpitts oscillator with an embedded MI element. Here parameter g_m is transconductance determining the gain of the transistor.

Here the MI element is represented as complex impedance containing the real R_{MI} and imaginary ωL_{MI} parts. Summing the current at node 1, we obtain:

$$j\omega C_1 V_1 + \frac{V_1 - V_2}{R_{MI} + j\omega L_{MI}} = 0 \tag{7.1}$$

Similar at node 2, we have

$$g_m V_1 + \frac{V_2}{R_L} + j\omega C_2 V_2 + \frac{V_2 - V_1}{R_{MI} + j\omega L_{MI}} = 0 \tag{7.2}$$

Groping terms results in

$$V_1(j\omega C_1 + \frac{1}{R_{MI} + j\omega L_{MI}}) - V_2 \frac{1}{R_{MI} + j\omega L_{MI}} = 0$$
$$V_1(g_m - \frac{1}{R_{MI} + j\omega L_{MI}}) + V_2(\frac{1}{R_L} + j\omega C_2 + \frac{1}{R_{MI} + j\omega L_{MI}}) = 0 \quad (7.3)$$

The obtained equations set a linear system of two algebraic equations with the right-hand sides set to be zero. Thus, there is always a trivial solution $V_1=V_2=0$. For non-zero values for V_1 and V_2 the equations have to be linear dependent. It means that the determinant of the system is set to zero:

$$\begin{vmatrix} j\omega C_1 + \frac{1}{R_{MI} + j\omega L_{MI}} & -\frac{1}{R_{MI} + j\omega L_{MI}} \\ g_m - \frac{1}{R_{MI} + j\omega L_{MI}} & \frac{1}{R_L} + j\omega C_2 + \frac{1}{R_{MI} + j\omega L_{MI}} \end{vmatrix} = 0 \quad (7.4)$$

This yields the following equation:

$$\left(j\omega C_1 + \frac{1}{R_{MI} + j\omega L_{MI}}\right)\left(\frac{1}{R_L} + j\omega C_2 + \frac{1}{R_{MI} + j\omega L_{MI}}\right) - \left(-\frac{1}{R_{MI} + j\omega L_{MI}}\right)\left(g_m - \frac{1}{R_{MI} + j\omega L_{MI}}\right) = 0 \quad (7.5)$$

Grouping real and imaginary parts gives:

$$\frac{\omega^2 L_{MI}(C_1 + C_2) + g_m R_{MI} + R_{MI}/R_L - \omega^2 C_1 C_2 (R_{MI}^2 + \omega^2 L_{MI}^2)}{R_{MI}^2 + \omega^2 L_{MI}^2} + j\omega \frac{R_{MI}(C_1 + C_2) - L_{MI}(\frac{1}{R_L} + g_m) + C_1 \frac{R_{MI}^2 + \omega^2 L_{MI}^2}{R_L}}{R_{MI}^2 + \omega^2 L_{MI}^2} = 0 \quad (7.6)$$

Then, equation (7.5) corresponds to two equations:

$$\omega^2 L_{MI}(C_1 + C_2) + g_m R_{MI} + R_{MI}/R_L - \omega^2 C_1 C_2 (R_{MI}^2 + \omega^2 L_{MI}^2) = 0 \quad (7.7)$$

$$j\omega\left(R_{MI}(C_1 + C_2) - L_{MI}(\frac{1}{R_L} + g_m) + C_1 \frac{R_{MI}^2 + \omega^2 L_{MI}^2}{R_L}\right) = 0 \quad (7.8)$$

Neglecting the resistive part of the MI impedance ($R_{MI} << R_L$, $R_{MI} << \omega L_{MI}$), frequency of oscillation is found from (7.7):

$$\omega = \sqrt{\frac{C_1 + C_2}{L_{MI} C_1 C_2}} \tag{7.9}$$

and the transconductance g_m can be found from equation (7.9):

$$g_m = \frac{C_1}{C_2 R_L} \tag{7.10}$$

Equations (7.9) and (7.10) correspond to the typical Colpitts oscillator characteristic parameters and stable oscillation can be achieved by choosing right values for capacitors and load resistor.

However, as shown in Chapter 6 (Fig. 6.6), the real and imaginary parts of the magneto-impedance load are of the same order and the real part of the impedance can't be neglected. In this case the characteristic oscillator parameters are not so obvious. Solving the imaginary part for ω, we obtain an expression for frequency of oscillation for the case when R_{MI} and L_{MI} are of the same order:

$$\omega = \sqrt{\frac{L_{MI} + g_m R_L L_{MI} - R_{MI} R_L (C_1 + C_2) + C_1 R_{MI}^2}{C_1 L_{MI}^2}} \tag{7.11}$$

The second unknown parameter, transconductance g_m, as can be seen from (7.7) and (7.8), is not so simple to obtain. By solving (7.7) with fixed ω, g_m can be determined as a function of L_{MI}, R_{MI} and frequency. Due to large changes in both inductive and resistive parts as a response to the applied (sensed) magnetic field, g_m will also change its value. These changes will affect stability of the oscillator and may generate spurious distortion signals, induce rapid slope changes in the tuning curve or even cause the oscillations to stop. Higher stability can be achieved by using buffering between oscillation circuit and the field-dependant MI element.

Another important feature of the magneto-impedance sensor based on the Colpitts oscillator is a non-linear mode of operation. Since the circuit operates in the resonance mode,

the current flowing through the MI element is quite large. Such a circuit can give several times more sensitive output than the classical characteristics obtained at the condition of constant current amplitude.

An interesting schematic solution was proposed by group of Prof. K. Mohri [3, 4] based on C-MOS pulse excitation circuit, which will be considered in the next Section. I have further developed this MI sensor circuit by proposing utilizing the off-diagonal impedance, which gives a linear behaviour of the output voltage.

7.3 C-MOS pulse-type MI sensor

In this Section I consider a pulse excitation of the wire samples using C-MOS digital circuits, shown in Fig. 7.5. This corresponds to a practical MI sensor circuit design [3-6]. The circuit with a C-MOS IC multivibrator produces sharp-pulsed current of duration 5–20 ns. Pulse excitation provides: simplicity of electronic design, low cost components, and reasonably good stability since C-MOS multivibrator oscillation frequency almost does not depend on the impedance characteristics of the MI elements. Power consumption of this circuit is also small (10mW). In addition, such a pulsed current involves both high (20–100 MHz) and low (quasi-dc) frequency harmonics. Therefore, it can be ideally used for the asymmetrical and off-diagonal MI requiring dc bias.

The circuit operates as follows. The 74AC04 is a C-MOS TTL device used for its high-speed switching and low current capability. *U1:A* and *U1:B* are configured as a multivibrator with capacitor C_1 and resistor R_1 forming the timing network to give an approximate 250 KHz square wave pulse generator (shown in Fig. 7.6 (lower signal)). The output of the multivibrator is fed to a differentiating circuit comprising R_3 and C_3 that causes the leading edge of the square wave to become a positive going 5 ns pulse (as shown in Fig. 7.6 (upper signal)). This pulse is applied to *U1:E* to improve its shape and is applied directly to the MI element. Analysing the MI characteristics obtained under a sinusoidal excitation the optimal frequency of 50 MHz has been identified, for which the maximal sensitivity (and the best linearity in the case of the off-diagonal impedance) has been achieved. In the case of pulsed

excitation, such parameters as a rise time and a fall time determine the frequency of the principle harmonic. The time parameter of 5 ns corresponds also to the optimal frequency of 50 MHz. The rise and fall times of the pulse signal are determined by the construction of HEX Inverters. The 74HCT04 inverter possesses the needed characteristics. Further more, this microchip has a minimal distortion and high temperature stability.

To demonstrate the principles of the MI sensor operation, the output pulse voltages are obtained for different sensed field H_{ex}. The voltage signal taken across the wire (using MI cell configuration shown in Fig. 7.1(a)) corresponding to the diagonal impedance Z_w. Figures 7.7 show the diagonal voltage response (V_w) before the rectifier (SW1, R4, C4) for $H_{ex}=0$ and $H_{ex}=2.6\,\mathrm{Oe}$, respectively. The amplitude of the main pulse is increased almost twice in the presence of the field. If the field is applied in the reversed direction, the pulse amplitude and sign do not change. This is in line with the result obtained for a sinusoidal excitation: the real and imaginary parts of the diagonal impedance are symmetrical with respect to the axial sensed field. A high-speed digital switch *SW1* filters out a background noise along with an unwanted pulse voltage portion and charges up *C15* via *R4* (10 kHz low pass filter) to give a DC voltage proportional to the applied magnetic field. The integrating element (*R4, C15*) produces a smooth quasi-dc signal proportion to the pulse amplitude. The parameters are chosen such that the integrating time is much larger than the pulse train period. Amplification of the DC is achieved by U3 (AD524). The final DC output signal is taken from the *J7* connector. It is envisaged that the basic components of the system would be a pulse generator, rectifier, and filter.

Typically, the MI characteristics have low sensitivity along with a strong nonlinearity in the vicinity of zero field. Then, an additional dc bias field is needed to set an operational point within a sensitive linear regime. In this case the electronic scheme will include an additional bias coil.

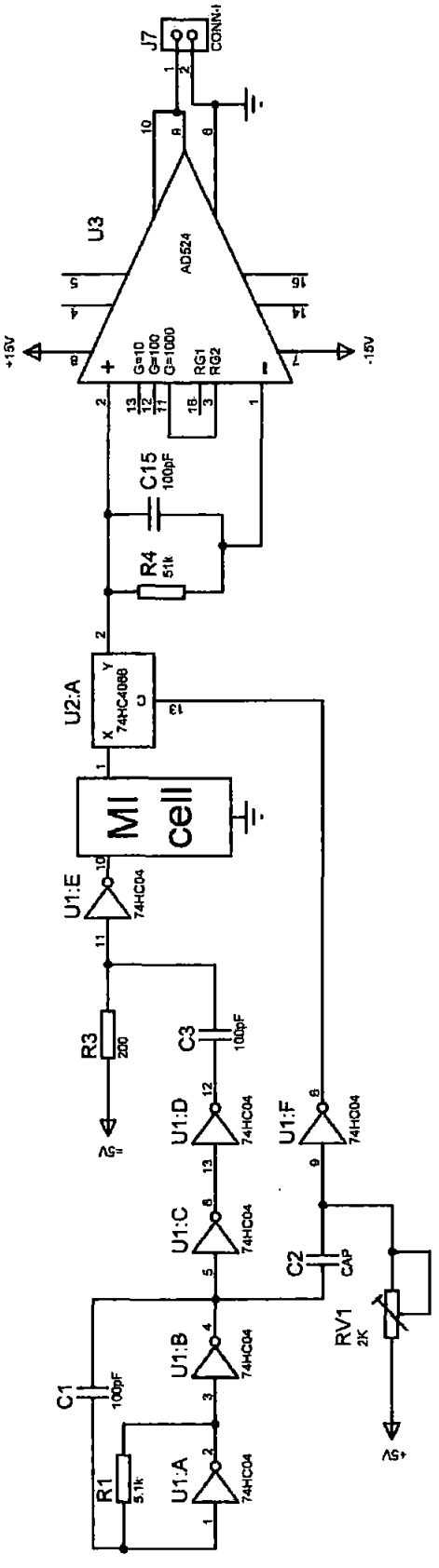

Fig. 7.5 Principle MI sensor design with a C-MOS IC multivibrator.

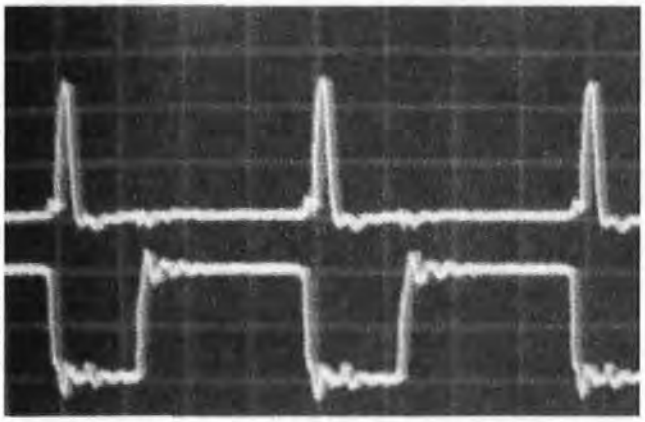

Fig. 7.6. Rectangular signal produced by the square-wave generator (U1:A, U1:B) (bottom signal) and the positive pulses after the differential circuit (C3, R3) upper signal). Vertical resolution: 2V/div, horizontal resolution: 50 ns/div.

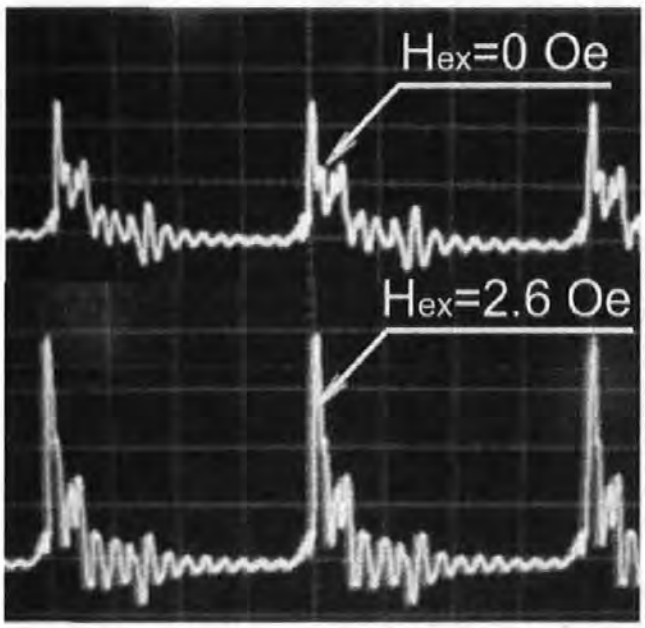

Fig. 7.7. Diagonal voltage response (V_w) before the rectifier (SW1, R4, C4). Vertical resolution: 40 mV/div, horizontal resolution: 50 ns/div.

Next, I consider a circuit configuration where the off-diagonal response ($\varsigma_{\varphi z}$ or ς_{yz}) is taken from the pick-up coil (V_c) and a single MI element (the measuring cell shown in fig 7.1(b) or 7.1(c) is used in the C-MOS sensor circuit). In the case of the output taken from the coil (off-diagonal response V_c), the signal is very small if no axial magnetic field is applied. In the presence of the field, the voltage pulse increases and when the field is

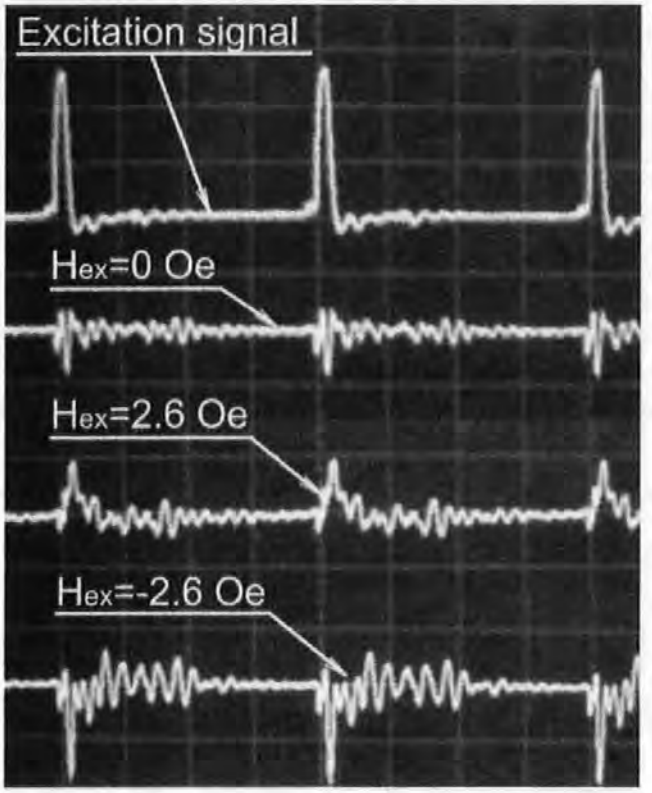

Fig. 7.8. Off-diagonal response V_c before the rectifier (SW1, R4, C4) measured from the pick-up coil. Horizontal resolution: 50ns/dev. Vertical resolution: 2V/dev for the top signal and 50 mV/dev for the lower signal.

reversed the direction of the pulse is also reversed. The off-diagonal behaviour is demonstrated in Fig. 7.8, where the top signal is the excitation pulse on the wire and signals below are the output voltage before the rectifier (SW1, R4, C4) as a function of the sensing field H_{ex}. The off-diagonal voltage response shows antisymmetrical field characteristics as predicted.

Figure 7.9 shows the integrated diagonal (V_w) and off-diagonal (V_c) responses after the rectification and amplification as a function of H_{ex}. In the case of the diagonal response (Fig. 7.9(a)), the field characteristics are symmetrical showing two maximums at $H_{ex} = \pm 4$ Oe. This behaviour is very similar to that shown in Fig. 7.2(a) for the diagonal impedance. The off-diagonal voltage output as a function of H_{ex} shown in Fig. 7.9(b) has an almost linear portion in the field interval $H_{ex} = \pm 2$ Oe. This is similar to the off-diagonal impedance versus H_{ex} shown in Fig. 7.2(b). Therefore, I can conclude that the off-diagonal voltage response in

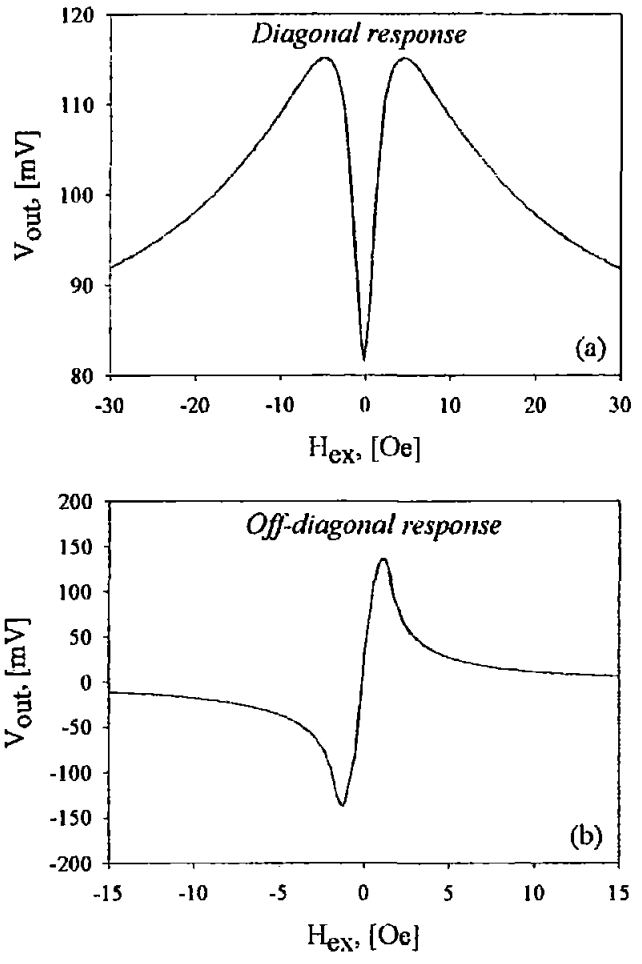

Fig. 7.9. Integrated diagonal in (a) and off-diagonal responses in (b) after rectification (SW1, R4, C4) and amplification as a function of H_{ex}.

amorphous wires with a circumferential anisotropy obtained under pulsed excitation can be linear with respect to the sensed axial field without using any bias fields or currents. In fact, the pulse current applied to the wire itself does two jobs: it causes a high frequency magnetisation that is responsible for the voltage-field dependence, and it also partially eliminates circular domains making the off-diagonal response possible.

The C-MOS MI sensor is a simple, low consumed power, cheap and easy integrable device. For many applications such as portable magnetic field detectors or car compasses it can be 'worth weight in gold'. However for applications where precision measurements are critical C-MOS MI sensor is not very good solution because of the large high frequency distortion produced by digital electronics. This distortion, which is a result of using digital electronics, is seen in figures 7.7, 7.8.

The main disadvantage of the C-MOS circuit is that its pulse mode operation produces a lot of digital distortion (up to 10 mV/V/Oe) that significantly degrades the measured signal resolution. Another important disadvantage of the C-MOS sensor is that the pulse excitation circuit induces a small unpredictable dc offset current (up to 10 mA) even in 'idle-mode' (period between pulses), which changes the MI characteristics. This dc bias current applied to the MI device changes the magnetic structure and as a consequence the MI response. Additional information on the dc offset current can be found in datasheets on HEX invertors (74HCT04, parameters V_{OL} and I_{OL}) used as pulse generator in [3-6].

7.4. High-performance MI sensor using sine-wave excitation and magnitude-phase detection.

The high sensitivity sensor requires good linearity, frequency stability and low noise electronics. I analysed two types of sensors utilising the MI effect. In this Section, I consider a new type of magneto-impedance (MI) sensor using sine excitation and magnitude-phase detection. Employing high-stable sine excitation circuit and high-sensitive analogue demodulator with input range –60 dBm to 0 dBm, this sensor is able to measure dc magnetic

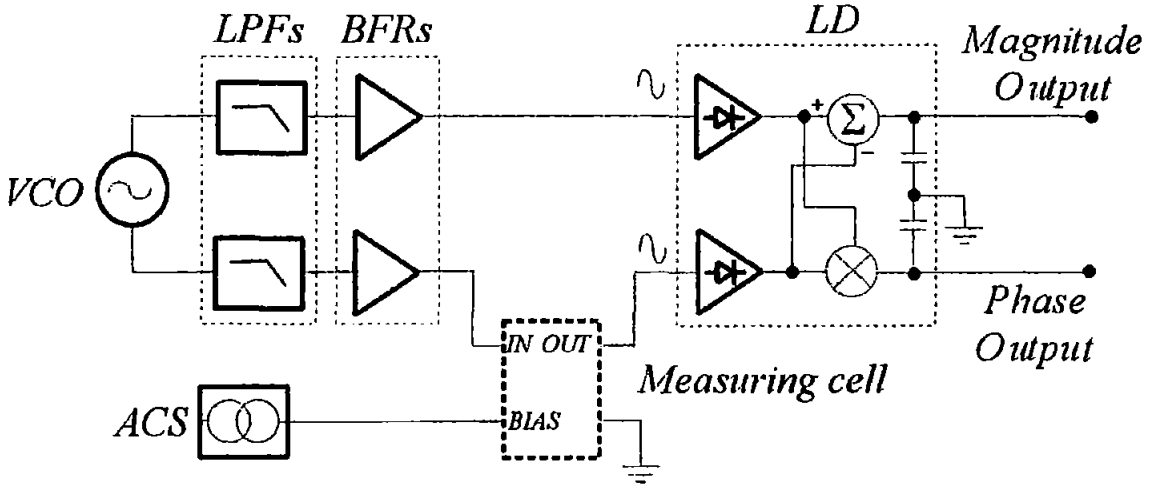

Fig. 7.10. MI sensor circuit based on sine-wave excitation. The following abbreviations are used: Voltage Controlled Oscillator (VCO, MAX2605), low-pass filters (LPFs, P3LP-606), buffers (BFRs, MAX2470), logarithmic demodulators (LDs, AD8302) and adjustable current source (ACS).

fields with resolution down to 10^{-5} Oe (1 nT) for the full scale of ±2 Oe (0.2 mT). Future advantages of proposed sensor include low phase noise (-117 dBc/Hz at 100 kHz offset), long-term temperature stability of 360 ppm/°C for the -40°C to +85°C temperature range and in relatively wide output bandwidth (up to 10 MHz). A schematic view of sensor is shown on Figure 7.10.

a. Driving part

A compact, low-cost, low power consumption and reasonably high-performance Voltage Controlled Oscillator (VCO) with two differential buffered outputs has been used as a driving circuit. The core of the VCO is based on the varactor tuned Colpitts topology. This topology is useful for a wide range of operating frequencies, from intermediate to microwave frequencies. To tune the oscillator to the desired frequency (in our case the optimum between maximum sensitivity, sensor stability and power consumption was chosen near 55 MHz) a parallel-resonant tank controlling the oscillation frequency has been used. The parallel-mode network allows the use of small-value varactors and a large inductor having high quality factor Q around 50 at 60MHz. The parallel-mode configuration also permits a straightforward analysis of the oscillator. Measured phase noise at 100 kHz offset was -117 dBc/Hz. In order to suppress higher harmonics of the signal produced by VCO a passive low-pass filtering network (LPFs on fig. 7.10) has been used with –3 dB attenuation at cut-off frequency of 60 MHz. After filtering the third harmonic becomes as low as –58 dBm. The designed VCO delivers about –15 dBm to the following stage. A VCO is not able to deliver much power to other circuits; it needs a following intermediate stage. Buffer amplifiers (BFRs in fig. 7.10) improve the frequency stability of the oscillator and phase noise performance by isolating it from the load. I have used low-noise, low-power buffers with high reverse isolation $|S_{12}|^2 > 65dBm$ in the driving circuit. The buffer amplifiers are placed immediately after the passive filtering network. Having high input impedance the buffer amplifiers draw very little power from the oscillator. Sufficiently low output impedance of the buffer amplifier provides enough gain to supply the following MI load. An adjustable current source (ACS) providing

stable dc current has been designed to establish a helical magnetic structure in the MI element (wire with initial circumferential anisotropy).

b. Magnitude-Phase Detector

Up to the present, most proposed MI detectors (demodulators) have been based on single-ended amplitude demodulator involving Schottky diodes. The semiconductor diode has the property that the current through it increases exponentially as the applied voltage increases linearly. In general use, this means that a silicon diode experiences an internal voltage drop of about 0.65 to 0.7 volt for a reasonable circuit current range (for germanium diodes, it is about 0.3 V). A practical problem with a simple diode is the inherent internal resistance of any semiconductor material. This resistance is also subject to change with temperature, and may actually cause some internal heating in some applications. To avoid the problem, a transistor may be substituted for the diode. The relatively high base resistance of the transistor is bypassed, as most of the emitter current will flow through the collector region instead. Nevertheless, the logarithmic voltage/current characteristics of the emitter-base junction will still be in effect, so the circuit will perform quite well as a logarithmic converter.

In our design I used a new approach. A monolithic logarithmic demodulator (LDs in fig. 7.9) using a 7-stage "parallel-detection" technique has been chosen. Demodulator has two inputs: one is connected to the well-matched reference signal from VCO and second loaded with the MI element. The detector comprises a closely matched pair of demodulating logarithmic amplifiers, each having 60 dBm measurement range. By taking the difference of their outputs, a measurement of the magnitude ratio or gain/loss between the two inputs signals is available. Since subtraction in the logarithmic domain corresponds to the ratio in the linear domain, the resulting output becomes:

$$V_{MAG} = V_{SLP} \log(V_{IN1} / V_{IN2}) \tag{7.12}$$

where V_{IN1} is well-matched reference signal from VCO and V_{IN2} is an analogous signal from buffer output loaded with the MI element, V_{MAG} is the output corresponding to the difference

in input signals magnitude, and V_{SLP} is a slope. Unlikely the measurements of power, when measuring a dimensionless quantity such as relative signal level, no independent reference or intercept need to be invoked. In essence, one signal serves as the intercept for the other. Variation in intercept due to frequency, temperature, and supply voltage affect both channels identically and hence do not affect the difference. This technique depends on the pairs of logarithmic amplifiers being well matched in slope and intercept to ensure cancellation.

The outputs of the 7 logarithmic amplifiers, connected in series for each channel, are fully limited signals over most of the input dynamic range. The limited outputs from both log amps drive an exclusive-OR style digital phase detector. Operating strictly on the relative zero crossing of the limited signals, the extracted phase difference is independent of the original input signal levels. The phase output has the general form:

$$V_{PHS} = V_{\Phi}\left[\Phi(V_{IN1}) - \Phi(V_{IN2})\right] \tag{7.13}$$

where V_{PHS} is the phase slope and Φ is each signal's relative phase in degrees.

By connecting different measuring cells shown in Figure 7.1 different types of response can be obtained. Figure 7.11, 7.12 shows the diagonal (V_w) and off-diagonal (V_c) responses at the output of the sensor as a function of H_{ex}. In the case of the diagonal response (the cell shown on fig 7.1 (a) is used), the field characteristics are symmetrical showing two maximums at $H_{ex} = \pm 2$ Oe (Fig. 7.11). This behaviour is very similar to that shown in Fig. 7.2 (a) for the diagonal impedance. This type of sensor is useful for indirection measurements. The off-diagonal voltage output, obtained by using cells shown in figure 7.1(b) or 7.1(c), as a function of H_{ex} shown in Fig. 7.11 has an almost linear portions in the field interval H_{ex}=±1 *Oe*. This is similar to the off-diagonal impedance versus H_{ex} shown in Fig. 7.2 (b). Therefore, I can conclude that the off-diagonal voltage response in amorphous wires with a circumferential anisotropy can be linear and bi-directional with respect to the sensed axial field in the presence of a small bias current.

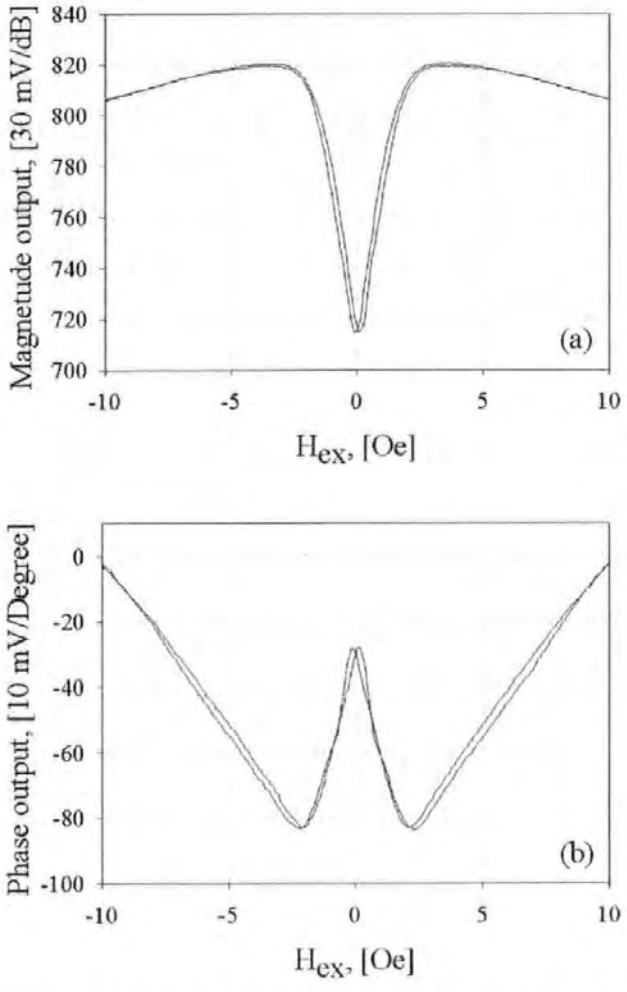

Fig. 7.11. The plot of the magnitude (a) and phase (b) output of the sensor measuring diagonal impedance versus axial magnetic field H_{ex}.

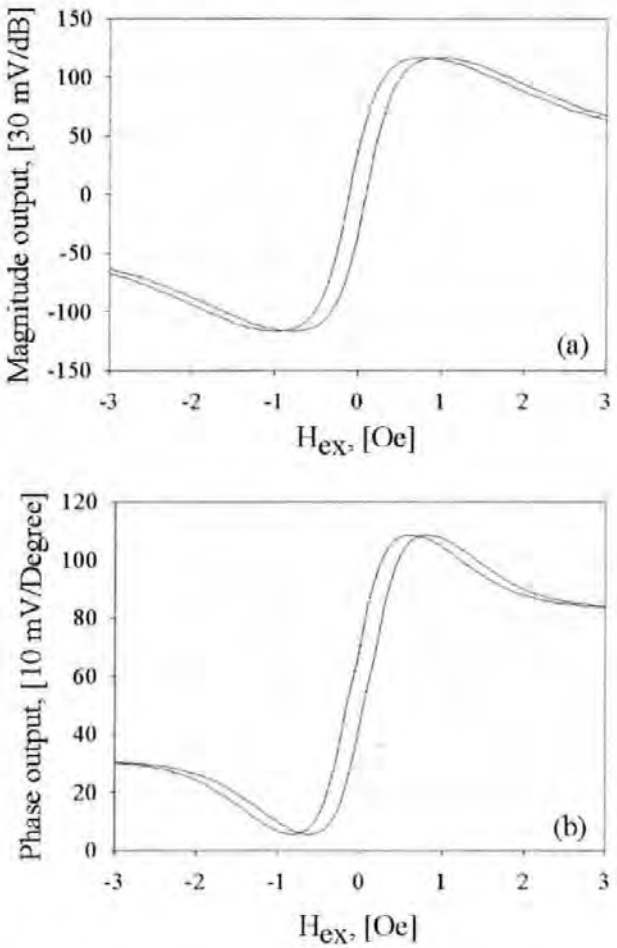

Fig. 7.12 The plot of the magnitude (a) and phase (b) output of the sensor measuring off-diagonal impedance versus axial magnetic field H_{ex}. Applied dc bias current was 5 mA.

We are now in a position for testing performances of the designed sensor. Due to the high sensitivity of the MI sensor, a precision measurement in a magnetically shielded environment is required.

The first series of experiments was dedicated to the measurements of noise spectrum of the MI element (microwire). The main source of noise of the MI element is associated with magnetic core, a part of which has an excess "*1/f*" component. A preliminary study was made on the impedance of the wire between the frequencies 0.01 Hz to 500 MHz. The wire was 1 cm long and 10 μm in diameter embedded into a specially designed measuring cell. It was placed at the end of a 50Ω coaxial line, the second end of which was connected to the HP 4195A Network/Spectrum Analyser, measuring noise spectrum at fixed current excitation frequency. The DC field was applied using calibrated Helmholtz coils.

The largest sensitivity was found above 50 MHz, mainly on the real part of the impedance, with a maximum value of the field to impedance transfer coefficient of 0.5Ω/nT (or 100%/Oe). The noise spectrum measured across the MI element is shown in Fig. 7.13. The noise level obtained between 20 kHz and 1 MHz fall in the range of $5-10\,pT/\sqrt{Hz}$, a promising value, which is limited, mostly, by the detection electronics. Some work has to be done with respect to the low-frequency noise, but noise reduction techniques as developed earlier for SQUIDs systems may be adopted. The goal of $0.1\,pT/\sqrt{Hz}$ at 1 Hz then appears realistic. This level of noise would really open interesting applications in non-destructive testing, magneto-cardiography, and bio-magnetism.

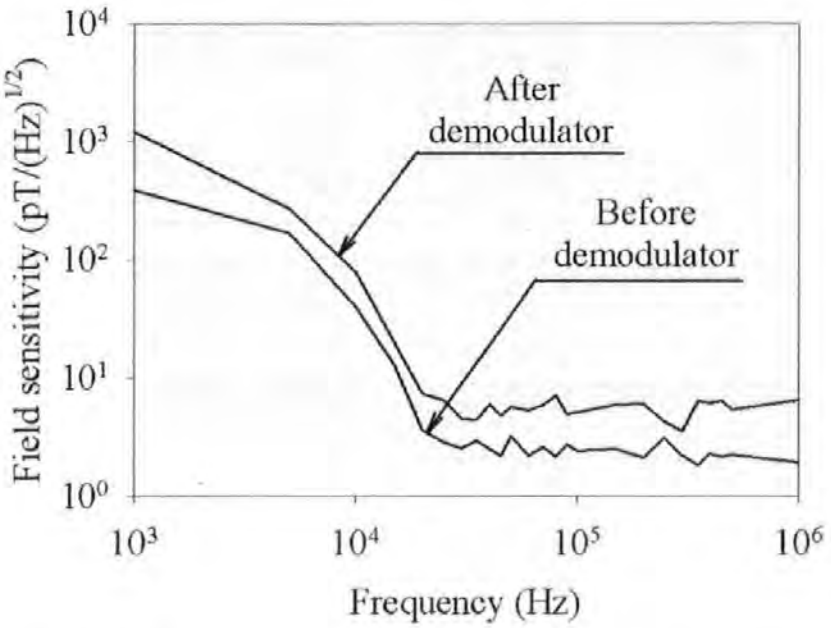

Fig.7.13. Noise spectrum measured after MI element and after demodulation stage.

References

[1] L. V. Panina, K. Mohri, K. Bushida, and M. Noda, "*Giant magneto-impedance and magneto-inductive effects in amorphous alloys*", J. Appl. Phys., (1994) Vol. 76, 6198.

[2] K. Mohri, L. V. Panina, K. Bushida, M. Noda, and T. Uchiyama, "*Sensitive and Quick Response Micro Magnetic Sensor Utilizing Magneto-Impedance in Co-rich Amorphous Wires*", IEEE Trans. Magn., (1995) Vol. 31, 1266-1275.

[3] M. Vazquez and A. Hernando, "*A soft magnetic wire for sensor application*", J. Phys. D: Appl. Phys., (1996) Vol. 29, 939.

[4] K. Mohri, T. Uchiyama, and L. V. Panina, "*Recent advances of micro magnetic sensors and sensing application*", Sensors and Actuators A, (1997) Vol. 59, 1.

[5] K. Mohri, T. Uchiyama, L. P Shen, C. M. Cai, and L. V. Panina, "*Sensitive micro magnetic sensor family utilizing magneto-impedance (MI) and stress-impedance (SI) effects for intelligent measurements and controls*", Sensors and Actuators A, (2001) Vol. 91, 85.

[6] Y. Honkura, M. Yamamoto, Y. Kohtani, and K. Mohri, "*Mass produced amorphous wire type MI sensor*", IEEE Trans. Magn., (2002).

[7] P. Ripka, L. Kraus, "*Magnetoimpedance and magnetoinductance. Chap. 9. Other principles. Chap. 9.1 In: Monografie Magnetic Sensors and Magnetometers*", ed. Pavel Ripka, Boston, Artech House Publishers, Norwood (England), ISBN I-58053-057-5, (2001), 349-367.

[8] R. A. Hambley "*Electronics*" ISBN 0-13-691982-0 (2000).

[9] J Everard "*Fundamentals of RF Circuit Design with low noise oscillators*" ISBN 0-471-49793-2 (2002).

[10] K. Mohri, T. Uchiyama, L. P Shen, C. M. Cai, and L. V. Panina, "*Sensitive micro magnetic sensor family utilizing magneto-impedance (MI) and stress-impedance (SI) effects for intelligent measurements and controls*", Sensors and Actuators A, (2001) Vol. 91, 85.

[11] K. Mohri, T. Uchiyama, L. P. Shen, C. M. Cai, L. V. Panina, Y. Honkura, and M. Yamamoto "*Amorphous Wire and CMOS IC-Based Sensitive Micromagnetic Sensors Utilizing Magnetoimpedance (MI) and Stress-Impedance (SI) Effects*" IEEE Trans. Magn., (2002) Vol. 38, 3063.

[12] *Aichi Steel Brochure.* (2002) Catalog.

[13] H. Hauser, L. Kraus, and P. Ripka "*Giant magnetoimpedance sensors*" IEEE Instrumentation & Measurement Magazine, (2001) Vol. 69, 28.

[14] T. Uchiyama, K. Mohri, M. Shinkai, A. Ohshima, H. Honda, T. Koayashi, and T. Wakabayashi "*Position Sensing of Magnetic Gel Using MI Sensor for Brain Tumor Detection*" IEEE Trans. Magn., (1997) Vol. 33, 4266.

[15] N. Kawajiri, M. Nakabayashi, C. M. Cai, K. Mohri, and T. Uchiyama, "*Highly stable micro sensor using C-MOS IC multivibrator with synchronous rectification*", IEEE Trans. Magn., (1999) Vol. 35, 3667.

[16] Y. Honkura, M. Yamamoto, Y. Kohtani, and K. Mohri, "*Mass produced amorphous wire type MI sensor*", IEEE Trans. Magn. (2002).

[17] T. Kitoh, K. Mohri, and T. Uchiyama, "*Asymmetrical magneto-impedance effect in twisted amorphous wires for sensitive magnetic sensors*", IEEE Trans. Magn., (1995) Vol. 31, 3137.

[18] D. P. Makhnovskiy, L. V. Panina, and D. J. Mapps, "*Field-dependent surface impedance tensor in amorphous wires with two types of magnetic anisotropy: helical and circumferential*", Phys. Rev. B (2001) Vol. 63, 144424.

[19] D. P. Makhnovskiy, L. V. Panina, and D. J. Mapps, "*Measurement of field-dependent surface impedance tensor in amorphous wires with circumferential anisotropy*", J. Appl. Phys. (2000) Vol. 87, 4804.

[20] D. P. Makhnovskiy, L. V. Panina, and D. J. Mapps, "*Asymmetrical magneto-impedance in as-cast CoFeSiB amorphous wires due to ac bias*", Appl. Phys. Letters, (2000) Vol. 77, 121.

[21] L. V. Panina, D. P. Makhnovskiy, D. J. Mapps, K. Mohri, and P. I. Nikitin, "*Effect of frequency and dc current on ac-biased asymmetrical magneto-impedance in wires*", Materials Science Forum, (2001) Vol. 373/376, 741.

[22] E. Lenz "*A Review of Magnetic Sensors*" Proc. IEEE Trans. Magn. (1990) Vol. 78, 973.

[23] J.-S. Lee, K.-H. Ahn, Y. H. Joeng, and D. M. Kim "*Highly sensitive $Al_{0.25}Ga_{0.75}As/In_{0.25}Ga_{0.75}As/GaAs$ quantum well Hall devices with Si-deltadoped GaAs layer grown by LP-MOCVD*" Sensors and Actuators **A** (1996) Vol. 57, 183.

[24] M. Behet, J. Bekaert, J. De Boeck, and G. Borghs "*Comparative Study on the Performance of InAs/Al0.2Ga0.8Sb Quantum Well Hall Sensors on Germanium and GaAs Substrates*" Sensors and Actuators **A** (2000) Vol. 81, 13.

[25] R. P. Hunt "*A magnetoresistive readout transducer*" IEEE Trans. Magn. **MAG-7**(1), (1971).

[26] M. N. Baibich, M. Broto, A. Fert, F. Nguyen Van Dau, F. Petroff, P. Etienne, G. Creuzei, A. Frederic, and J. Chazelas "*Giant Magnetoresistance of (001)Fe/(001)Cr Magnetic Superlattices*" Phys. Rev. Lett., (1988) Vol. 61, 2472.

[27] R. Coehoorn "*Giant magnetoresistance in exchanged-biased spin-valve layered structures and its application in read heads*" U. Hartmann (Ed.), Magnetic Thin Film and Multilayer Systems: Physics, Analysis and Industrial Applications, Springer Series in Materials Science, (1996).

[28] P. P. Freitas, F. Silva, N. J. Oliveira, L. V. Melo, L. Costa, and N. Almedia "*Spin Valve Sensors*" Sensors and Actuators **A** (2000) Vol. 81, 2.

[29] S. S. Parkin "*Dramatic enhancement of interlayer exchange coupling and giant magnetoresistance in $Ni_{81}Fe_{19}/Cu$ multilayers by addition of thin Co interface layers*" Appl. Phys. Lett. (1992) Vol. 61, 1358.

[30] B. Rodmacq, G. Pulumbo, and Ph. Gerard "G*iant magnetoresistance in $Ni_{81}Fe_{19}/Cu$ multilayers*" J. Magn. Magn. Mat. (1993) Vol. 118, 11.

[31] T. L. Hylton, K. R. Coffey, M. A. Parker, and J. K. Howard *"Giant magnetoresistance at low fields in discontinuous NiFe-Ag multilayer thin films"* Science (1993) Vol. 261, 1021.

[32] J. S. Moodera, L. R. Kinder, T. M. Wong, and R. Meservey "*Large Magnetoresistance at Room Temperature in Ferromagnetic Thin Film Tunnel Junctions*" Phys. Rev. Lett. (1995) Vol. 74, 3273.

[33] Z. G. Wang and Y. Nakamura "*Spin-tunnelling random access memory (STram)*" IEEE Trans. Magn. (1996) Vol. 32, 4022.

[34] S. A. Wolf, et al. "*Spintronics: A Spin-Based Electronics Vision for the Future*" Science (2001) Vol. 294, 1488.

[35] Y. Ohno et al. "*Electrical Spin Injection in a Ferromagnetic Semiconductor Heterostructure*" Nature (1999) Vol. 402, 790.

[36] F. Primdahl *"The Fluxgate Mechanism, Part I: The Gating Curves of Parallel and Orthogonal Fluxgates"* IEEE Trans. Magn. (1970) **MAG-6**, 376.

[37] P. Ripka "*Review of fluxgate sensors*" Sensors and Actuators **A** (1992) Vol. 33, 129.

[38] P. Ripka "*New Directions in Fluxgate Sensors*" J. Magn. Magn. Mater. (2000) Vol. 215/216, 735.

[34] O. Dezuari, E. Belloy, S. E. Gilbert, and M. A. M. Gijs *"Printed circuit board integrated fluxgate sensor"* Sensors and Actuators **A** (2000) Vol. 81, 200.

[39] S. Choi and S. Kawahito "*A planar fluxgate magnetic sensor for on-chip integration*" Sensors and Materials (1997) Vol. 9, 241.

[40] P. Kejik, L. Chiesi, B. Janossy, and R. S. Popovic "*CMOS planar 2D micro-fluxgate sensor*" Sensors and Actuators **A** (2000) Vol. 81, 180.

[41] K. Mohri "*Application of amorphous magnetic wires to computer peripherals*" Mater. Sci. Eng. A, (1994) Vol. 185, 141.

[42] K. Mohri, T. Uchiyama, L. P. Shen, C. M. Cai, and L. V. Panina "*Sensi- tive micromagnetic sensor family utilizing amorphous ferromagnetic wires*" J. Magn. Magn.

Mater., (2002) Vol. 249, 351.

Chapter 8. Stress-impedance effect and application to the stress-sensing media.

As described in Chapters 2 and 3, the magneto-elastic interaction plays a dominant role in establishing magnetic anisotropy in amorphous wires. Then, applying a certain external stress will change the magnetic anisotropy, and hence, equilibrium magnetic structure. This can lead to large variations in the high frequency impedance. This effect is often referred as a *stress-impedance (SI)*. Thus, in Co-based wires having a negative magnetostriction and a large axial tensile stress the easy anisotropy axis is along a circumferential direction. The application of a torsion stress induces a helical anisotropy, which can be detected by the impedance change. On the contrary, the external tensile stress does not change the direction of the easy anisotropy, and the impedance is insensitive to this kind of stress. To obtain a large change in impedance under the effect of tensile stress in wires with a negative magnetostriction, a helical anisotropy needs to be induced by a corresponding annealing procedure. It can be also achieved by biasing the wire with a dc axial magnetic field.

The stress dependence of magneto-impedance can be used for the development of stress sensors. This principle has been successfully employed on a stress annealed CoFeSiB amorphous ribbon achieving stress sensitivity of 214 MPa/Oe at 1 MHz frequency, and for measuring small loads on membranes with annealed glass-coated low magnetostrictive microwire [1, 2]. In the case of microwires, the DC electrical resistance is quite large so that GMI results in large variations in voltage induced by mechanical loading. [3]. Strain-gauges using a stress-impedance element can achieve gauge factors of around 4000, which can be compared with the gauge factors of 2 and 140 for resistive gage and semiconductor, respectively [4]. A sensitive stress sensor based on CMOS IC circuit was developed by Kusumoto et al. [5] with a strain gauge factor of 4000. Chiriac et al. [6] developed a finger-tip blood vessel pulsation sensor for diagnosis of blood circulation and health conditions. Also, as reported by Atkinson et al. [7], mechano-encephalogram based on stress impedance detects small skin deformation at a forehead centre reflecting brain activity.

Remote interrogation of the stress state of GMI material can be performed by a free-space interogation technique. Various materials with microwire or thin film shape have been successfully employed to evaluate the material undergoing stress for frequencies in the range 300 MHz to 3 GHz. In this Chapter I consider the effect of applied tensile stress on magneto-

impedance in glass-coated CoMnSiB amorphous wires at Ultra-High frequencies (UHF) band (300MHz-3GHz). This effect could be of a considerable interest for applications in smart composite materials filled with ferromagnetic wires for remote stress monitoring, where the effective permittivity depends on stress or strain in a narrow frequency band with a characteristic frequency of few GHz.

8.1 Experimental investigation of the magnetisation rotation under the effect of external stress.

In the Chapter 2 the rotational magnetisation reversal under the effect of various stresses has been described for a single-domain amorphous ferromagnetic sample with a circumferential or helical anisotropy. However, the proposed rotational model can be applied for multi domain samples as it describes the rotational processes within the domains (reversible portions of the magnetisation curves, which is the predominant process at high frequencies). Hereafter I will present experimental results of the magnetisation reversal under the effect of tensile stress. The experimental results are provided for $Co_{68.5}Mn_{6.5}Si_{10}B_{15}$ amorphous glass-coated wires having the total diameter of 14.5 μm and the metallic core diameter of 10.2 μm. For this alloys composition $\lambda \approx -2 \cdot 10^{-7}$ [3]. For dc magnetisation measurements (see measurements set in Chapter 4, fig. 4.3), the wire length was 6 cm and the stress was applied by hanging a load of 1–10 g at the wire end. The longitudinal magnetisation curves under the effect of stress are shown in Fig. 7.2. The original curve for an unloaded wire shows a steep hysteresis but with a rather small remanence to saturation value $M_r / M_s = 0.2$, which corresponds to almost circumferential anisotropy with a small helical angle $\alpha \approx 12^0$. Applying the tensile stress strengthens the circumferential anisotropy: the magnetisation curve becomes almost linear with $M_r / M_s \approx 0$, the hysteresis disappears and the effective anisotropy field H_K increases. For the unloaded wire $H_K = 2.6$ Oe, and it becomes 9 Oe, when a load of 8.5 g is applied. This magnetisation behaviour corresponds to the magnetostrictive energy given by equation (2.7) with parameters $\sigma_1 = 200$ MPa, $\sigma_2 = 44$ MPa provided that $\lambda = -2 \cdot 10^{-7}$ and load of 1 g corresponds to a tension of 65 MPa.

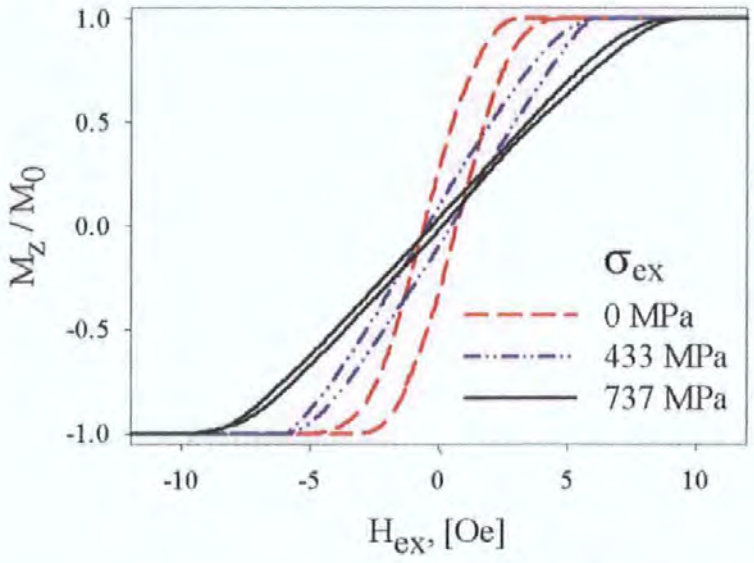

Fig. 8.1 Axial dc magnetization curves $M_z / M_0 = \cos(\theta)$ with the applied stress as a parameter. The wire length was 6 cm and the load was attached at the wire free end.

Experimental hysteresis loops shown in Fig. 8.1 are in very good agreement with the model presented in Chapter 2. Enlargement of the anisotropy field and vanishing of coercivity on applying tensile stress has been predicted by the modelling magnetisation reversal process in amorphous wires under the effect of applied tensile stresses.

8.2 Experimental investigation of the stress-impedance in amorphous microwires at GHz frequencies.

Next I consider the stress effect on the magneto-impedance behavior at the UH frequencies band. The complex-valued stress impedance is found by measuring S_{11}-parameter by means of the Hewlett-Packard 8753E Vector Network Analyzer (VNA), as shown in Fig. 8.2a. The measurement technique is similar to the UHF measurements of the filed-dependant Magneto-Impedance described in the Chapter 6. When dealing with measurements at UHF band, special care must be taken for the correct interpretation of results. At frequencies higher then 500 MHz impedance matching becomes critical since half wavelength becomes relatively small (<30 cm). I designed a special microstrip cell to minimise the post calibration mismatches (Fig. 8.2b). Rather than attempting to quantify the contribution of the error in the wire impedance, my approach is to minimise its effect. The microstrip portion connected to

VNA is pre-calibrated with a standard 50Ω load, which is then removed (Load "1" in Fig. 8.2b). During the measurements, the microstrip cell with the soldered sample is terminated with a 50Ω load (Load "2"). This calibration of the microstrip line with a length of 3.5 cm holding the soldered up wire of 1.4 cm ensures reliable impedance measurements up to frequencies of about 3 GHz. The wire is loaded with a weight in its middle (in this case 1 g load corresponds to a tension estimated to be 320 MPa, see Caption for Fig. 8.2b). The cell with the sample is placed into the Helmholtz coil producing a dc magnetic field.

Figure 8.3 shows plots of impedance vs. applied tensile stress for three frequencies 500 MHz 1.5 GHz and 2.5 GHz. If no field is applied, the stress effect is small being about 12% at 500 MHz and almost not noticeable at GHz frequencies. Since a negative magnetostriction wire has a nearly circumferential anisotropy (if no large frozen-in torsion exists), the applied tensile stress alone will not cause the change in M_0 direction, and as a result, will not produce noticeable changes in the impedance at high frequencies.

For a large stress effect on the MI, the ability of σ_{ex} to change the direction of $\mathbf{M}_0$ is needed. In the case when $H_{ex}=0$, this is possible if the anisotropy axis has a helical angle α nearly equal to 45^0, which is achieved by a proper annealing (current annealing or annealing under torsion) to establish a substantial frozen-in torsion ($\sigma_2 >> \sigma_1$, $\alpha \approx 45^0$ at $\sigma_{ex}=0$). Another possibility of the directional change in the magnetisation under the external stress is to use the axial field bias. In the presence of H_{ex} the magnetisation rotates towards the wire axis whereas the application of σ_{ex} strengthens the circumferential anisotropy (for $\lambda<0$) and hence acts in the opposite way. Then, the magnetisation rotates back to the circular direction. The highest stress sensitivity is obtained for $H_{ex} \approx H_K$, which is sufficient to saturate the wire. Further increase in H_{ex} is unnecessary since a larger stress will be required to move the magnetisation back. I utilise the assistance of H_{ex} to realise very large impedance change when the external tensile stress is applied.

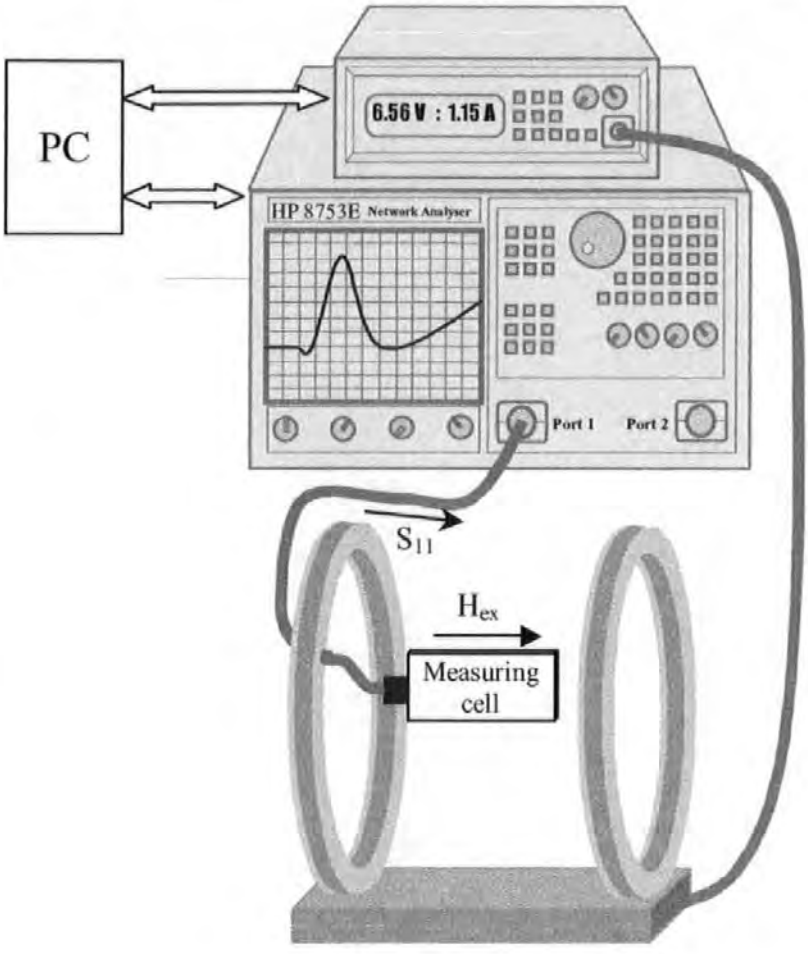

(a)

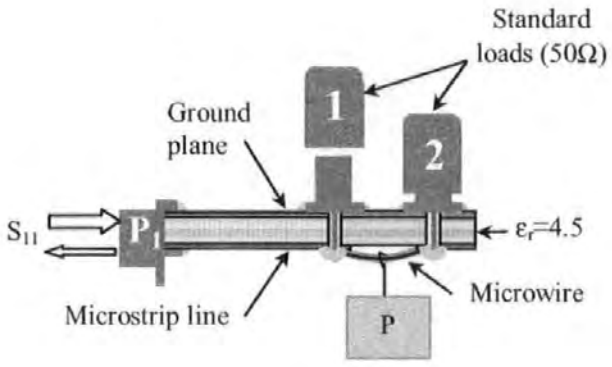

(b)

Fig. 8.2 Stress-impedance measurement setup in (a) and sketch of the microstrip cell with a wire sample loaded in its centre with a weigh P in (b). This imposes a stress of $P/2\pi a^2 \sin\psi$ *where* $\psi \approx 6^0$ *is the angle between the bent wire and the horizontal direction.*

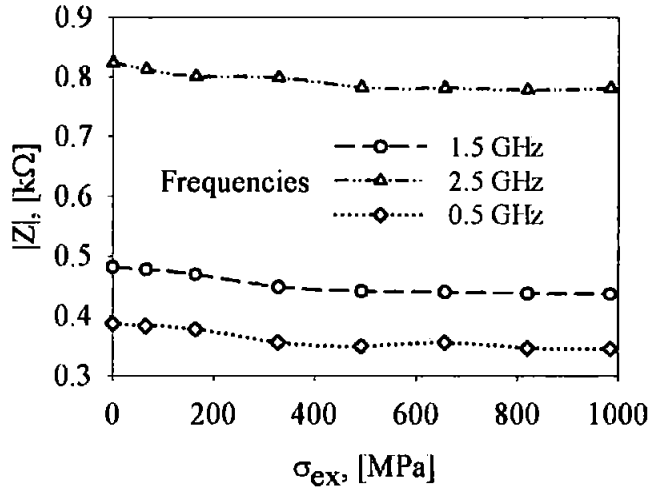

Fig. 8.3 Experimental plots of impedance vs. applied stress in a CoMnSiB wire with a circumferential anisotropy. The load of 1 g applied at the middle of the wire is estimated to impose a stress of 320 MPa.

In the presence of H_{ex}, the wire impedance shows large changes in response to the application of the tensile stress (Fig. 8.4). The highest stress sensitivity of *100%* per *180 MPa* at *500 MHz* and *60%* per *180 MPa* at *2.5 GHz*, respectively obtained for H_{ex}=*3 Oe* that is about the same value as the anisotropy field for the unloaded wire.

The microwave MI/SI phenomenon can be explained in terms of classical skin effect in magnetic conductors with a large effective permeability and its strong dependence on the magnitude of the external dc magnetic field [8]. Because the skin depth as well as the characteristic correlation length in a magnetic structure (e.g., domain width) in soft magnetic materials is much larger than the inter-atomic distances, the classical electrodynamics of continuous media can be used for the description of MI/SI effects. The calculation of the complex-valued impedance $\hat{\varsigma}$ is based on the solution of Maxwell's equations for the fields $\boldsymbol{e}$ and $\boldsymbol{h}$ together with the equation of motion for the magnetisation vector $\boldsymbol{M}$.

The voltage response measured across a ferromagnetic wire (z-axis) carrying a high frequency current $i = i_0 \exp(-j\omega t)$ is expressed in terms of the longitudinal component ς_{zz} of the surface impedance tensor ($\varsigma_{zz} = e_z / h_\varphi$, where e_z and h_φ are the axial electric and circular magnetic fields at the wire surface)

$$V = \frac{2l}{ca}\varsigma_{zz} i . \tag{8.1}$$

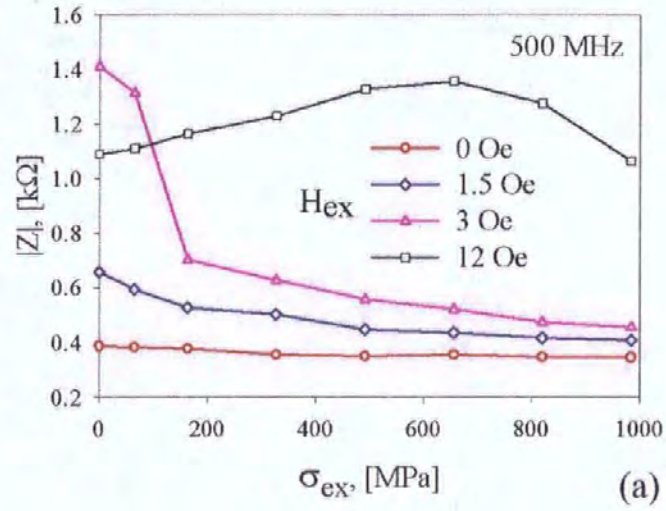

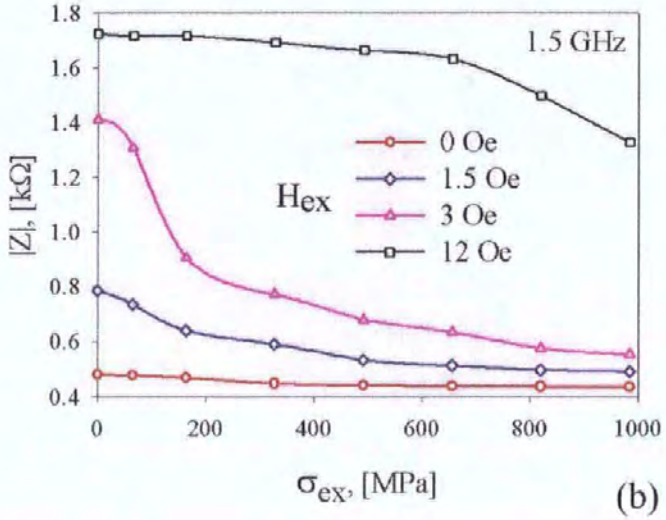

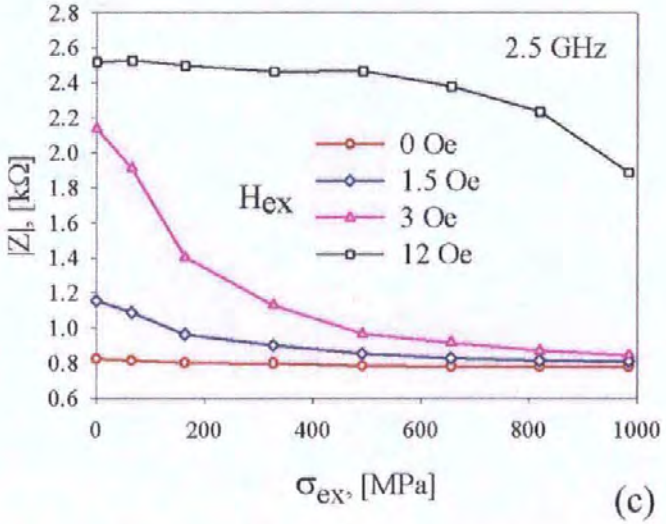

Fig. 8.4 Experimental plots of impedance vs. applied stress with the external magnetic field as a parameter.

Here l is the wire length, a is the wire radius, and c is the velocity of light. Strictly speaking, equation (3) is valid for a wire with a uniform magnetisation but can be applied for a multidomain wire provided that ς_{zz} is averaged over domains and the domain wall displacements are damped. In the case of a strong skin effect, the following equation holds [8]

$$\varsigma_{zz} = \frac{c\rho(1-j)}{4\pi\delta_0}(\sqrt{\mu}\cos^2\theta + \sin^2\theta) \tag{8.2}$$

Here ρ is resistivity, $\delta_0 = c(\rho/2\pi\omega)^{1/2}$ is a non-magnetic skin depth, μ is the circular permeability describing the magnetisation precession around the equilibrium magnetisation $\mathbf{M_0}$ having an angle θ with the wire axis. Equation (8.2) demonstrates that the longitudinal surface impedance depends on both the dynamic permeability μ and the static magnetisation angle θ. The parameter μ has a very broad dispersion region. At high frequencies (higher than the frequency of the ferromagnetic resonance) μ changes very little with both the external axial magnetic field H_{ex} and anisotropy field H_K, although preserving its relatively high values ($|\mu| \approx 10$ in the GHz range for Co-based wires with $H_K = 2-5$ Oe). In this case, the dependence of the impedance on magnetic properties is entirely determined by the static magnetisation angle θ. Thus, the impedance vs. stress behaviour can be quantitatively modelled using (8.2) and (2.21) and assuming that the dynamical permeability μ in Eq. (8.2) is related to a uniform precession of the magnetisation around the equilibrium magnetisation $\mathbf{M_0}$ (see model in Chapter 2). The theoretical plots showing $Z(\sigma_{ex})$ with H_{ex} as a parameter for frequency of 2.5 GHz are shown in Fig. 8.5, demonstrating very good quantitative agreement with the experimental results.

The effect of stress on microwave MI in amorphous fine wires is proposed to be used for the creation of a new stress-tuneable composite medium for remote stress monitoring by microwave spectroscopy technology. The composite material consists of short wire inclusions (exhibiting stress-impedance effect) embedded into the dielectric matrix with the permittivity ε. The wire inclusions behave as the electric dipole "scatterers". This dipole response of the composite system can be characterised by some effective permittivity ε_{eff}. Then, ε_{eff} can have a resonance or relaxation dispersion (depending on the wire impedance) seen near the antenna resonance for an individual wire. For a moderate skin-effect ($\delta \approx a$) the dispersion characteristics of ε_{eff} depend on the longitudinal surface impedance ς_{zz}. Therefore, in a

composite containing ferromagnetic wires exhibiting MI/SI effect the effective permittivity may depend on the external magnetic field and stress/strain via the corresponding dependence of ς_{zz}. The changes in ε_{eff} can be detected by microwave scanning techniques, in particular, microwave loss spectroscopy.

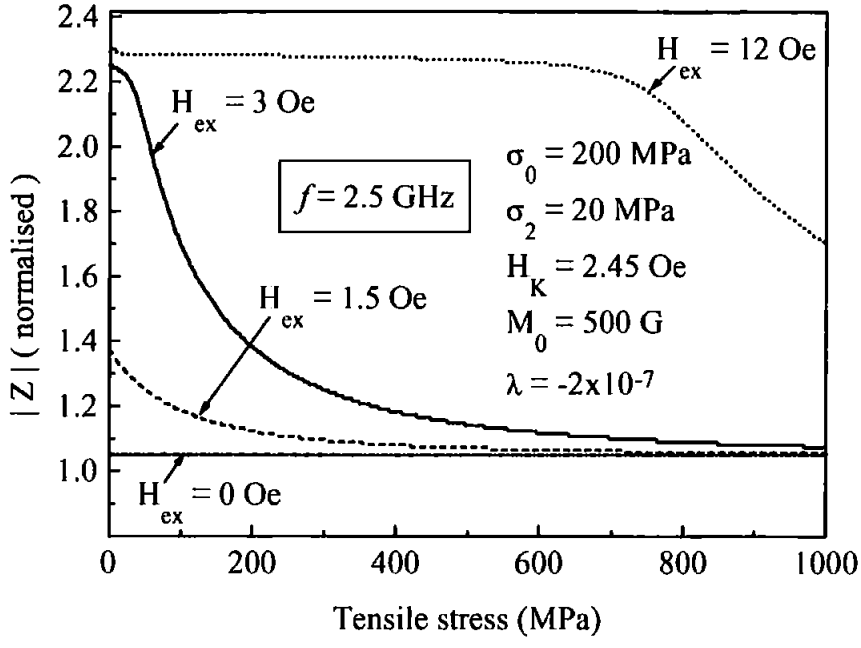

Fig. 8.5. Theoretical plots showing $Z(\sigma_{ex})$ with H_{ex} as a parameter for frequency of 2.5 GHz.

References

[1] Cobeño, A. F., Blanco, J. M., Zhukov, A., and González, J. "*Sensitive magnetoelastic properties of glass-coated CoMnSiB amorphous microwires for magnetoelastic sensors*" J. Magn. Magn. Mater., (2002) Vol. 249, 402.

[2] Shen, L. P., Uchiyama, T., Mohri, K., Kita, E., and Bushida, K. *"Sensitive Stress-Impedance Micro Sensor Using Amorphous Magnetostrictive Wire"* IEEE Trans. Magn., (1997) Vol. 33, 3355.

[3] Cobeño, A. F., Zhukov, A., Blanco, J. M., Larin, V., and González, J. "*Magnetoelastic sensor based on GMI of amorphous microwire*" Sens. Act. A, (2001) Vol. 91, 95.

[4] Mohri, K., Uchiyama, T., Shen, L. P., Cai, C. M., Panina, L. V., Honkura, Y., and Yamamoto, M. "*Amorphous Wire and CMOS IC-Based Sensitive Micromagnetic Sensors Utilizing Magnetoimpedance (MI) and Stress-Impedance (SI) Effects*" IEEE Trans. Magn., (2002) Vol. 38, 3063.

[5] Kusumoto, D., Shen, L. P., Naruse, Y., Mohri, K., and Uchiyama, T. "*Detection of Finger-Tip Blood Vessel Pulsation Using CoSiB Thin Amorphous Wire CMOS-IC SI Sensor*" IEEE Trans. Magn., (1999) Vol. 35, 4115.

[6] Chiriac, H., Colesniuc, C. N., Óvari, T. A., and Ticusan, M. "*In suit investigation of the magnetization processes in amorphous glass-covered wires by ferromagnetic resonance measurements*" J. Appl. Phys., (1999) Vol. 85, 5453.

[7] Atkinson, D., Squire, P. T., Maylin, M. G., and Gore, J. "*An integrating magnetic sensor based on the giant magneto-impedance effect*" Sens. Act. A, (2000) Vol. 81, 82.

[8] D. P. Makhnovskiy, L. V. Panina, and D. J. Mapps "*Field-dependent surface impedance tensor in amorphous wires with two types of magnetic anisotropy: helical and circumferential*" Phys. Rev. **B** (2001) Vol. 63, 144424.

[9] D. P. Makhnovskiy and L. V. Panina "*Field dependent permittivity of composite materials containing ferromagnetic wires*" J. Appl. Phys. (2003) Vol. 93, 4120.

[10] M. Vazquez "*Giant magneto-impedance in soft magnetic wire*" J. Magn. Magn. Mater. (2001) Vol. **226**, 693.

[11] M Knobel "*Giant Magnetoimpedance: Concepts and Recent Progress*" J. Magn. Magn. Mater. (2002) Vol. 242-245, 33.

[12] V. Zhukova, A. Chizhik, A. Zhukov, A. Torcunov, V. Larin, and J. Gonzalez "*Optimisation of giant magneto-impedance in Co-rich amorphous microwires*" IEEE Trans. Magn. (2002) Vol. 38, 3090.

[13] M. Dominguez, J. M. Garcia-Beneytez, M. Vazquez, S. E. Lofland, and S. M. Bhagat "*Microwave response of amorphous microwires: magnetoimpedance and ferromagnetic resonance*" J. Magn. Magn. Mater. (2002) Vol. 249, 117.

[14] S. I. Sandacci, D. P. Makhnovskiy, and L. V. Panina "*Valve-like behaviour of magnetoimpedance at GHz frequencies*" J. Magn. Magn. Mater. (2004) Vol. 272/276, 1855.

[15] K. Mohri, T. Uchiyama, L. P. Shen, C. M. Cai, L. V. Panina, Y. Honkura, and M. Yamamoto "*Amorphous Wire and CMOS IC-Based Sensitive Micromagnetic Sensors Utilizing Magnetoimpedance (MI) and Stress-Impedance (SI) Effects*" IEEE Trans. Magn. (2002) Vol. 38, 3063.

[16] H. Hauser, R. Steindl, C. Hausleitner, J. Nicolics, and A. Pohl "*Miniaturized Magnetic Field Sensors Utilizing Giant Magneto-Impedance [GMI] Effect and surface Acoustic Wave [SAW] Technology*" Sens. and Mater. (2001) Vol. 13, 25.

[17] O. Reynet, A.-L. Adent, S. Deprot, O. Acher, and M. Latrach "*Magnetism - Effect of the magnetic properties of the inclusions on the high-frequency dielectric response of diluted composites*" Phys. Rev. **B** (2002) Vol. 66, 94412.

Chapter 9. Conclusions and future work.

The first part of my research was dedicated to the theoretical and experimental study of a magnetic microwire with positive magnetostriction. This type of wire exhibits very rapid magnetisation reversal (also called a large Barkhausen jump) as a response to the periodical remagnetisation process. The idea of using this feature for security applications has been known for many years. However, until recently, systems using these properties existed only in close range prototypes (less then a few millimetres between the magnetic wire and reading apparatus).

Within, the first part of the PhD program, a deep and detailed investigation of the properties of microwires with positive magnetostriction was carried out. I applied stochastic methods for modelling the remagnetisation reversal in the microwires with axial anisotropy. To my knowledge, it is a first attempt to analyse the microwires behaviour by means of stochastic methods. While the eddy current approach, widely discussed in literature, is based on the single domain model, proposed stochastic approach takes into account a multi-domain state of the studied samples. A modified stochastic Néel-Brown model of the magnetisation reversal has been proposed enabling the explanation of number of characteristic parameters of the microwires with axial magnetisation [1]. Such important parameters of Barkhausen discontinuity as a mean switching field and a standard deviation of the switching field distribution have been investigated to understand the influence of extrinsic factors such as slew rate of the alternating magnetic field on application's operation.

As a result of this detailed investigation the reading system developed within my PhD research project allows the large Barkhausen jump to be detected without an actual contact between the magnetic microwire and the magnetic field detector. Experiments show that the detection will be possible at a distance of approximately 100-150 mm from the detecting sensor.

As an extension of the investigation of microwires with positive magnetostriction, I took part in development of a new method of coding the wire using a localised laser annealing treatment [2]. Using a multi-pulse magnetic label is one of the practicable methods of improving security and reliability of the magnetic remote sensing systems. While the collaborators (Aston University, Birmingham) carried out the laser treatment, my contribution was to develop a magnetic measurement system based on a compensation differential

magnetometer circuit, carry out accurate measurements of the treated microwires and to analyse the magnetic behaviour before and after the laser treatment.

Another part of my research had been devoted to study of the Magneto-Impedance effect in amorphous wires. The investigation carried out at low-frequency (LF) band (10kHz-300kHz) allows analysing the different magnetisation processes such as domain walls displacements (reversible and irreversible) in the wires with circumferential anisotropy [3]. This analysis was helpful in understanding the various characteristics obtained at different frequencies and excitation conditions. In a very high-frequency (VHF) range (30 MHz-300 MHz) our research was focused on the design of high-performance sensors utilising MI effect. A new high-performance sensor using microwires with circumferential anisotropy has been developed [4-8]. Whilst other MI sensors (as was discussed in Chapter 7) produce symmetrical response with respect to the applied field, my sensor produces antisymmetrical response. It can be useful if field direction is important. The proposed sensor employing a novel RF measurement technique allows optimising sensitivity, bandwidth, linearity, simplicity and cost.

Another interesting outcome of my PhD research are a stress-sensitive composites. Investigation of the amorphous wires behaviour in the ultra high-frequency (UHF) band (300MHz-3 GHz) shows that the MI effect remains very high in a microwave frequency range [8-10]. On the basis of the experimental investigation carried out a new type of stress-sensitive composite material is proposed, the microwave effective permittivity of which depends on the mechanical stress. This composite material opens up new possibilities for a remote monitoring of stress with the use of microwave "free-space" techniques. This kind of the composite material can be characterised as a "sensing medium", which images the mechanical stress distribution inside construction or on its surface.

List of related publications

[1] S. I. Sandacci et al., `*Dynamic Hysteresis in Magnetostrictive Amorphous Microwires*`, IEEE Trans. on Magn. (2002) Vol. 38, N 5, 2409- 2411.

[2] A. N. Grigorenko, L. V. Panina, S. I. Sandacci, D. P. Makhnovskiy, and D. J. Mapps, `*Laser Processing Effect on Magnetic Properties of Amorphous Wires*`, Applied Physics Letters (2002) Vol. 81, N 25, 4790.

[3] A. Radkovskaya, S. I. Sandacci, L. V. Panina, D. J. Mapps 'Dynamic Circular Hysteresis in Co-based Amorphous microwires', Journal of Magnetism and Magnetic Materials, (2004) Vol. 272-276, N 3, 1841-1843.

[4] S. I. Sandacci et al., *'Off-diagonal impedance in amorphous wires and application to linear magnetic sensors'*, IEEE Trans. Magn. (2004) Vol. 40, N 6, 1.

[5] S. I. Sandacci et al., *'Linear magnetic sensor based on off-diagonal impedance in amorphous wires'*, accepted to IEEE Circuits and Systems (ICECS 2003) December 2003.

[6] S. I. Sandacci et al., *'High-performance magneto-impedance sensor using magnitude-phase detection for measuring magnetic field in nano Tesla region.'*, submitted to IEEE Sensors 2004 in April 2004.

[7] S. I. Sandacci et al., *'Valve–like behaviour of the magneto-impedance in the GHz range'*, J. Magn. Magn. Mater., (2004) Vol. 272-276, N 3, 1855-1857.

[8] S. I. Sandacci et al., *'Very high stress sensitivity of magneto-impedance (MI) in CoMnSiB amorphous wires at GHz frequencies'*, submitted to the Journal of Magnetism and Magnetic Materials (EMSA2004), March 2004.

[9] L. V. Panina, S. I. Sandacci, and D. P. Makhnovskiy, *'Stress effect on magneto-impedance (MI) in amorphous wires at GHz frequencies and application to stress-tuneable microwave composite materials'*, J. Appl. Phys. (2005) Vol. 97, N 1, 13701.

[10] S. I. Sandacci et al., *'Magnetic permeability of the glass-coated microwires'*, Mathematical Modelling in Education science and industry (2001) Vol. 27, 238.

[11] N. Fry, D.P. Makhnovskiy, L.V. Panina, S.I. Sandacci, M. Akhter, D.J. Mapps, *'Field dependance of the off-diagonal impedance in NiFe/Au/NiFe layered film with a planar microcoil'*, IEEE Trans. Magn. (2004) Vol. 40, 3358.

[12] S. A. Baranov, M. Vazquez, V. S. Larin, A. V. Torcunov, S. I. Sandacci, *'Magnetic permeability of Co-based glass-coated microwire'*, Moldavian Journal of the Physical Sciences, (2002) Vol. 1, N 3, 5-8.

APPENDIXES

APPENDIX A

Low-Frequency Identification System (LFIDS). Circuits and diagrams.

Appendix A.1 Power generator circuit for 1-D interogation system

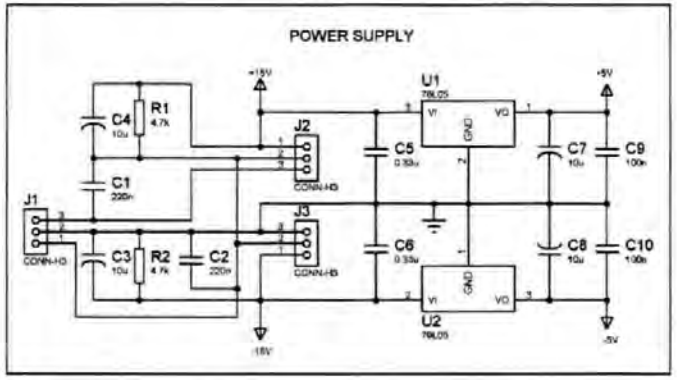

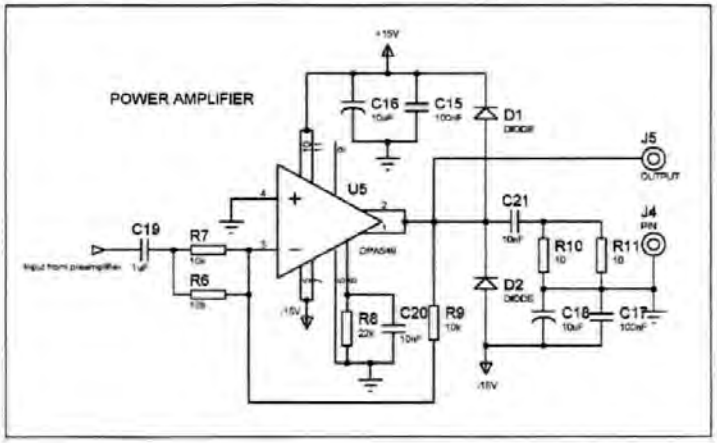

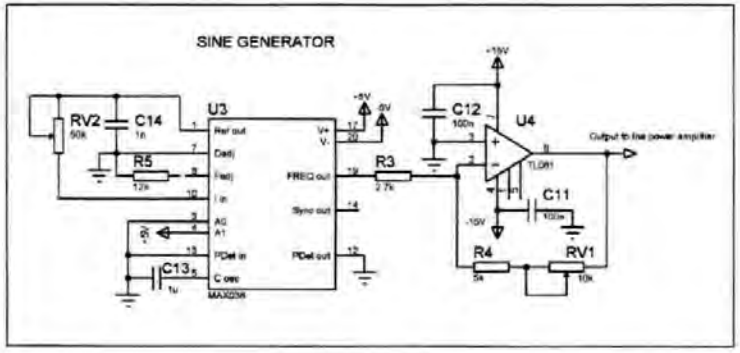

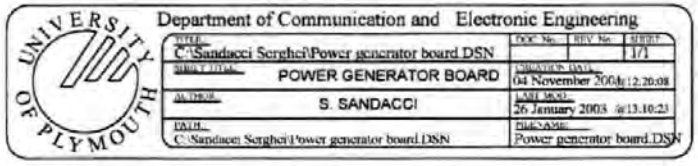

Appendix A.2 Amplification and filtering circuit

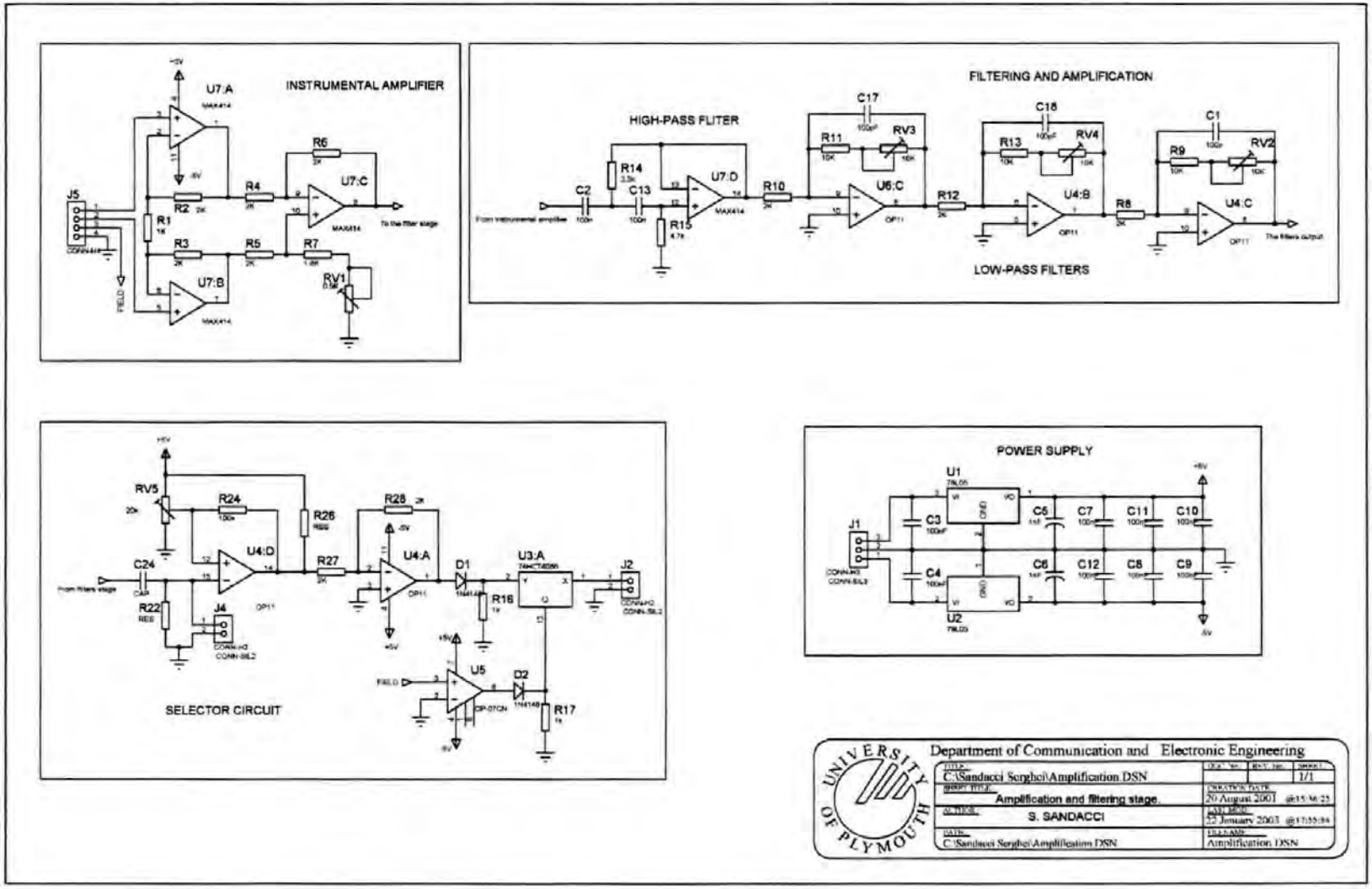

Appendix A.3 Storing and displaying circuit

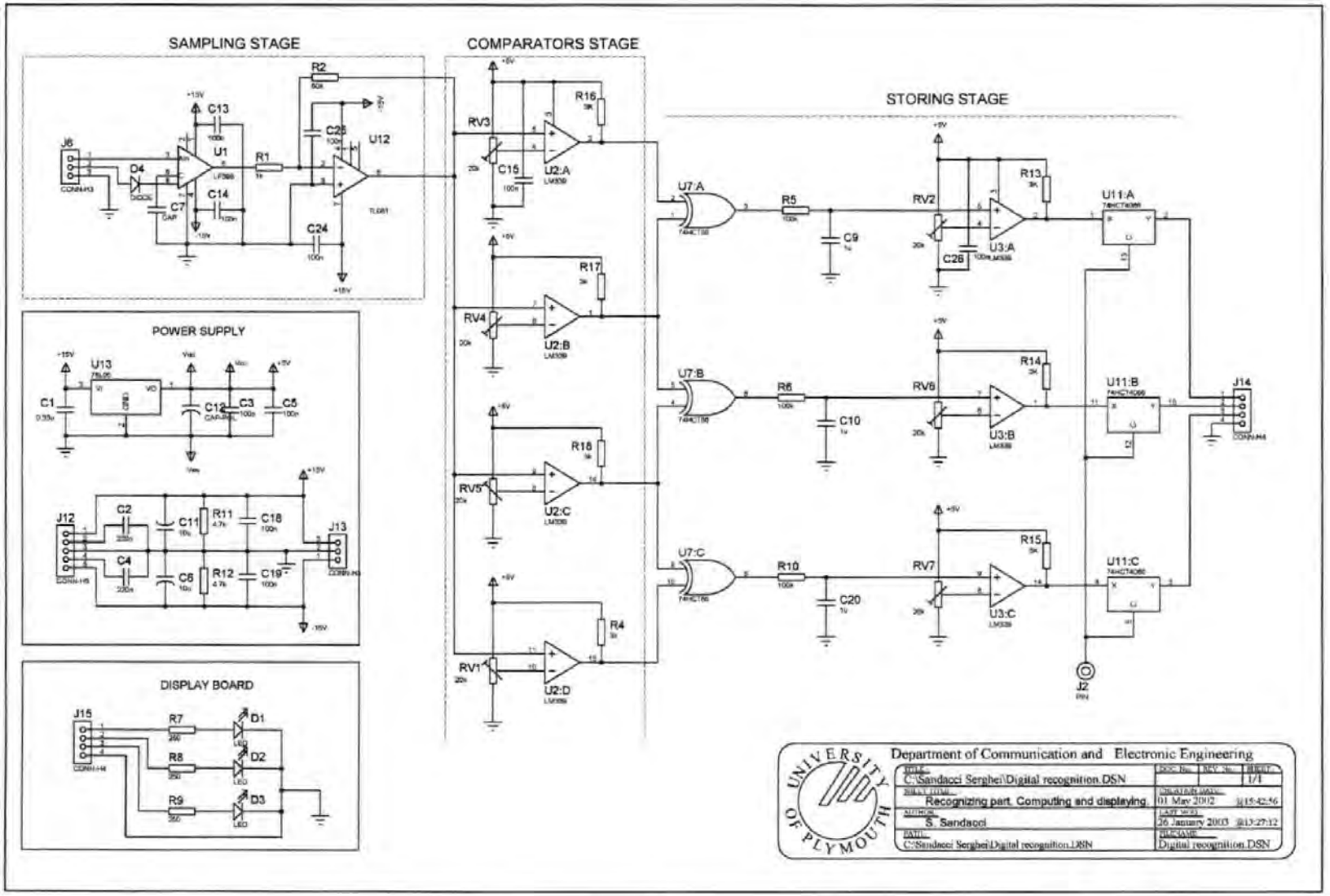

Appendix A.4 Power generator circuit for 2-D interrogation system

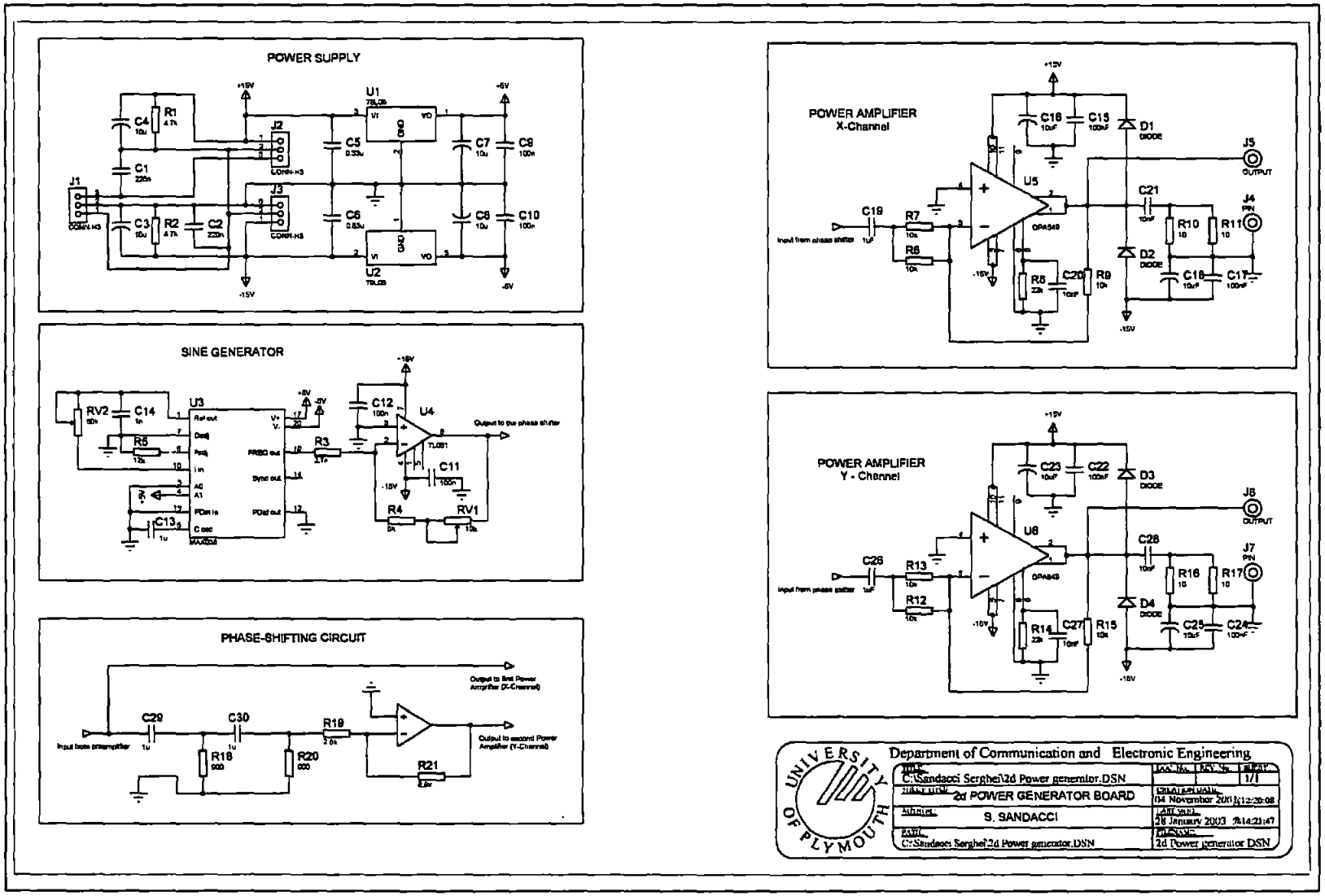

APPENDIX B

(Publications)

Dynamic Hysteresis in Magnetostrictive Amorphous Microwires

Sergei I. Sandacci, Alexander N. Grigorenko, Larissa V. Panina, and Desmond J. Mapps

Abstract—**Dynamic hysteresis in bistable amorphous wires is studied at frequencies up to 200 kHz. As frequency is increased, the magnetization loop exhibits progressive widening, maintaining its bistable property. The switching process is analyzed within the Néel–Brown theory of the magnetization reversal due to activation over an energy barrier. The frequency dependence of the switching field is evaluated by considering a "waiting time" for closure domain wall to escape the pinned state, which gives a very good agreement with the experiment. The time of the magnetization reversal decreases with frequency down to few microseconds at 200 kHz, owing to the switching field increase.**

Index Terms—**Amorphous wires, dynamical hysteresis, Néel–Brown model.**

I. Introduction

AMORPHOUS magnetostrictive wires exhibit very rapid bistable magnetization reversal (large Barkhausen jumps). This property makes them unique for applications in security sensors and pulse generators. As operational frequencies become progressively higher, there is an interest in studying the magnetization reversal in bistable wires at corresponding frequencies. On the other hand, most of experiments of hysteresis in these materials (and in general) are performed under dc or quasi-dc conditions. In this paper, the hysteresis loops in glass-covered amorphous wires have been measured for frequencies up to 200 kHz. The results are analyzed in terms of stochastic activation over domain wall (DW) pinning barrier [1], [2].

Generally, the modification of the hysteresis curves in conducting magnetic materials due to higher frequency magnetizing fields is described introducing an additional energy dissipation resulting from eddy-current losses [3], [4]. However, in regard to bistable systems, within this approach it is not possible to explain an increase in the switching field with a frequency since the rate of the magnetization change is zero before the flip. On the other hand, DW dynamics in ferromagnetic systems exhibit intrinsic stochastic properties [5], [6]. Magnetic viscosity can be understood in terms of thermal or other noise activation over energy barriers introducing "waiting time" for DW to break away from the pinning site. This mechanism leads to higher switching fields H_B as frequency is increased. The calculated frequency dependence of H_B agrees very well with the experiment.

Manuscript received February 19, 2002; revised June 6, 2002.

The authors are with the Department of Communications and Electronic Engineering, University of Plymouth, Drake Circus, Plymouth PL4 8AA, U.K. (e-mail: ssandacci@plymouth.ac.uk; agrigorenko@plymouth.ac.uk; lpanina@plymouth.ac.uk; dmapps@plym.ac.uk).

Publisher Item Identifier 10.1109/TMAG.2002.803609.

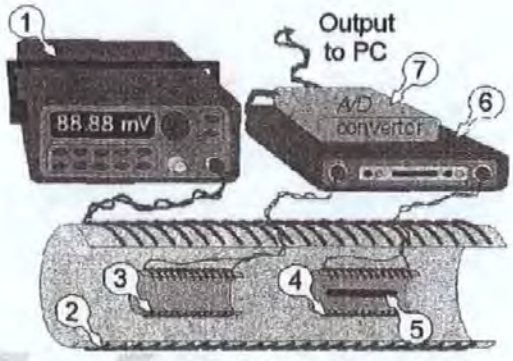

Fig. 1. Compensation magnetometer. (1) Signal generator. (2) Driving solenoid. (3) Compensation coil. (4) Pickup coil. (5) Sample. (6) Processing electronics. (7) A/D converter.

II. Experiments

A special hysteresis loop tracer was designed for high-frequency measurements. Care was taken to decrease the dimensions of the system shown in Fig. 1. Two pickup coils, (3) and (4), of 0.05 cm in diameter, 1 cm long with 30 turns are placed inside a driving solenoid, (2), of 0.75 cm in diameter, 6 cm long with 180 turns. The driving solenoid is connected to a signal generator, (1), and produces the ramping fields of different forms and frequencies. The wire element (5) of 2 cm long was placed in one pickup coil, (4), which was used for detection of magnetization changes while the other, (3), is designed for compensation of the driving field. A differential detection system, (6), contains amplifiers and high-frequency bandpass filters to suppress noise. For frequencies higher than few kilohertz, the effect of distributed inductance and capacitance becomes significant introducing distortions into the output voltage signal. The hysteresis tracer was calibrated using an integro-differential correction function. The parameters of the correction function at different frequencies were calculated and checked by measuring the system response to various periodic input signals (of sinusoidal, rectangular, triangular forms). The driving field amplitude was 7 Oe, which was sufficient to realize the magnetization switching at frequencies up to 200 kHz.

We have studied glass covered $Fe_{15}Co_{55.4}Mn_{7.2}B_{12.4}Si_{10}$ amorphous wires produced by Taylor–Ulitovski method kindly provided by "AmoTec" Ltd. The wires had a core of 12.4–16.1 μm in diameter covered by glass with total diameter of 18.6–22.1 μm. Fig. 2 shows a typical set of hysteresis loops reconstructed from measured signals at different frequencies of the periodic driving field of a constant amplitude. At low frequencies, the magnetization process is well described in terms

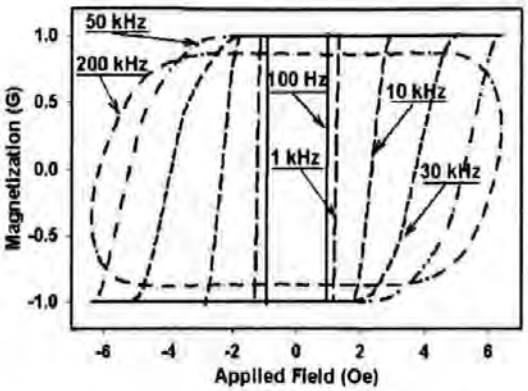

Fig. 2. Dynamic hysteresis loops in a glass covered amorphous wire.

of a large Barkhausen jump, which happens at a switching field of about 1 Oe. Three important features characterize the dynamic hysteresis. First, the field at which the large Barkhausen jumps occur (switching field) considerably increases with frequency and changes from 1 Oe at low frequencies to 2 Oe at a frequency of 20 kHz. Second, the time of magnetic field ramping becomes comparable with the time of magnetization changes at frequencies above 10 kHz and the hysteresis loop opens up. Third, the DWs that carry magnetization reversal fail to reach the sample edges at frequencies above 200 kHz and hysteresis loops acquire an elliptical shape. It was also found that the time of the large Barkhausen jump decreases with an increase of frequency of driving field.

We believe that all these features of dynamic hysteresis can be understood in terms of DW activation and propagation. To our knowledge, this approach to analyze the magnetic bistability in magnetostrictive amorphous wires has not been used before. The initial switching field is described by an activation of a closure DW over an initial barrier. Larger times of field sweep correspond to larger numbers of activation attempts (larger "waiting times"). As a result, DW overcomes an initial barrier at smaller fields for lower frequencies, which corresponds to the lower switching fields. An activation process always leads to the distribution of the switching field, which was observed in our experiments. The detailed discussion of the distribution and waiting time measurements will be given elsewhere. The increase of the switching field at higher frequencies implies an increase of the average driving field acting on DW and leads to the decrease of the time for DW to complete the Barkhausen jump. Time of magnetization reversal is determined by an average field acting on the DW(s) and its (their) mobility as well as by the distance the DW has to cover.

III. Modified Néel–Brown Model

To quantify the frequency dependence of the switching field, we make use of the Néel–Brown model of magnetization reversal, which was originally developed for description of the magnetization flip in uniaxial magnetic particles due to thermal activation over the anisotropy barrier. We suggest that the switching field H_β in our experiments is defined by the closure DW activation over the initial barrier ΔU and modify the Néel–Brown model to account for this scenario.

According to the model, the probability rate $p(t)$ of DW to overcome the barrier is given by

$$p(t) = \nu_0 \exp\left(-\frac{\Delta U - H(t)MV}{D}\right) \tag{1}$$

where ν_0 is the attempt frequency, $H(t)$ is the ramping magnetic field, M is the magnetization, V is the activation volume, and D is the noise parameter. Assumptions are made here that the initial energy barrier ΔU does not depend upon magnetic field, the frequency of magnetic field is much lower than the attempt frequency and the magnetic field is treated as perturbation for simplicity. The probability $Q(t)$ of DW to stay in the pinned state obeys the following equation:

$$dQ/dt = -p(t) \cdot Q. \tag{2}$$

Assuming that a jump will eventually happen at some small value of Q_0 and using (1), we obtain an implicit equation for the jump time t_j

$$\int_{t_0}^{t_j} \exp\left(\frac{H(t)MV}{D}\right) dt = \frac{\ln(1/Q_0)}{\nu_0} \exp\left(\frac{\Delta U}{D}\right) \tag{3}$$

where t_0 is the time at which a reversal nucleus appears and DW is able to jump. Taking a sawtooth dependence of the magnetic field $H(t) = H_0\omega t$ and assuming that time t_0 corresponds to some field $H_{\beta 0}$ (when ω tends to be zero), we finally get the switching field of the large Barkhausen jump

$$H_\beta = \frac{D}{MV} \ln\left(\frac{\omega}{\omega_0} + 1\right) + H_{\beta 0} \tag{4}$$

where

$$\omega_0 = \frac{D\nu_0}{\ln(1/Q_0)H_0MV} \exp\left(-\frac{\Delta U - H_{c0}MV}{D}\right).$$

The behavior of the switching field versus frequency given by (4) is compared with the experimental one, as shown in Fig. 3. In the experiment, the distribution of H_β was nearly Gaussian (in accordance with the model), and the average value was taken to make an accurate comparison.

It is seen that the agreement between theory and experiment extends over the frequency range of two decades (where the ramping field amplitude was sufficient to drive the sample into saturation). Equation (4) worked well for different bistable wires in a large temperature range down to the temperature of liquid nitrogen. Careful comparison of the change in the logarithm slope with decrease of temperature shows that the temperature activation accounts for only less than 10% of total noise. This implies that fluctuating external magnetic fields were the main source of noise. A lower limit of an activation volume can be estimated by considering that the noise factor is of thermal origin $D = 3k_bT/2 = 6.2 \cdot 10^{-15}$erg. Extracting the logarithmic prefactor from the graph shown in Fig. 3 and taking $M = 500$ G, we estimate $V \approx 4.1 \cdot 10^{-16}$ cm^3 which gives the linear dimension of activation as $d \approx 7 \cdot 10^{-6}$ cm. This scale is close to the DW width in this material.

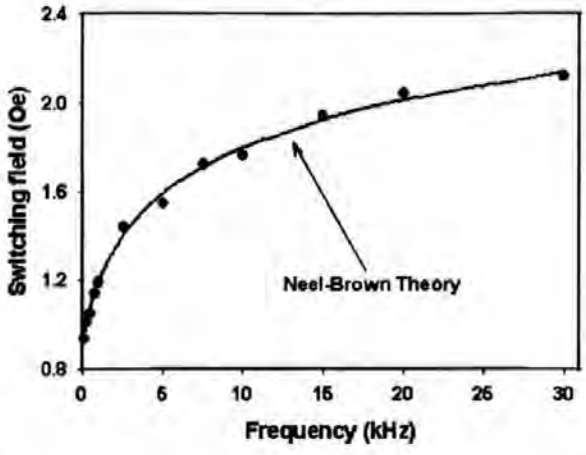

Fig. 3. Average switching field of a large Barkhausen jump as a function of frequency at room temperature. Solid line is the prediction of Néel–Brown theory. Simulation equation is $H_B = 0.3\ln(1 - \omega/624.5) - 0.93$.

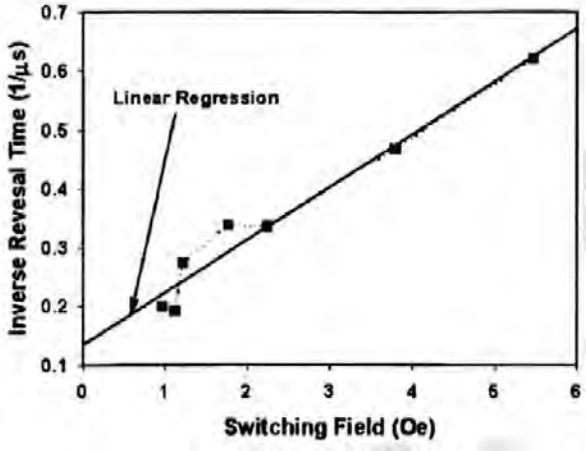

Fig. 4. Inverse of reversal time as a function of switching field. Solid line is the linear regression curve.

IV. Time of Magnetization Reversal

Once activated, DW propagates forming an elongated shape to minimize the demagnetizing energy [7]. During this process, some additional demagnetizing field H_d assists its movement. For a moving wall, the damping essentially balances the effective field H_{eff}, which includes the applied field, demagnetization field and coercivity field. The DW velocity is of the form

$$u = (2M/\beta)H_{\text{eff}}(t) \tag{5}$$

where β is the damping parameter. Since the switching field increases with the frequency of field ramping, it means that DW moves in higher fields at higher frequencies. Considering that the damping parameter does not change essentially with frequency, (5) leads to an increase of an average DW velocity $\langle u \rangle$ and, hence, to a decrease of the time of magnetization reversal which can be estimated as $l/\langle u \rangle$, where l is the sample length (or distance between nucleation sites). For fast reversal processes, we can assume that the external field does not change during the jump and take $H(t) \approx H_B$. Then, it follows from (5) that the time of magnetization reversal τ has to be inversely proportional to the switching field H_B. This is proven in Fig. 4 where the plot $1/\tau$ versus H_B is given. The data used cover the frequency range from 100 Hz to 100 kHz. The interception with the field axis of the linear regression to the experiment gives an average demagnetization field of about 1.6 Oe. Finally, we can combine the expression for switching field (4) with linear dependence for the inverse time and estimate the frequency at which τ becomes in the range of the period of the driving field. A straightforward evaluation gives the frequency of about 100 kHz for our samples. This coincides with the experimental results showing elliptical hysteresis loops at frequencies higher than 100 kHz.

V. Conclusion

We have found that the dynamic hysteresis in bistable amorphous wires under a periodic magnetic field is described well by Néel–Brown theory of activation of a closure DW over a pinning barrier. The switching field follows a logarithmic function of frequency. The evaluated size of an activation volume is comparable to the size of the DW in amorphous materials. The change of the magnetization reversal time with frequency is attributed to the change of the switching field.

References

[1] L. Neel, *C. R. Acad. Sci.*, 1949, vol. 228, pp. 664–671.
[2] W. F. Brown, *Micromagnetics*. New York: Wiley, 1963.
[3] D. C. Jiles, "Frequency dependence of hysteresis curves in conducting magnetic materials," *J. Appl. Phys.*, vol. 76, pp. 5849–5855, 1994.
[4] J. Szczyglowski, "Influence of eddy currents on magnetic hysteresis loops in soft magnetic materials," *J. Magn. Magn. Mater.*, vol. 223, pp. 97–102, 2001.
[5] P. Gaunt, "The frequency constant for thermal activation of a ferromagnetic domain wall," *J. Appl. Phys.*, vol. 48, pp. 3470–3474, 1977.
[6] A. N. Grigorenko, "Experimental observation of magnetostochastic resonance," *J. Appl. Phys.*, vol. 76, pp. 6335–6337, 1994.
[7] L. V. Panina *et al.*, "Domain dynamics at large Barkhausen discontinuity in magnetostrictive amorphous wires," *IEEE Trans. Magn.*, vol. 27, pp. 5331–5333, 1991.

Laser processing effect on magnetic properties of amorphous wires

A. N. Grigorenko,[a] L. V. Panina, S. I. Sandacci, D. P. Makhnovskiy, and D. J. Mapps
Department of Communications and Electrical Engineering, University of Plymouth, Drake Circus, Plymouth PL4 8AA, United Kingdom

I. Y. Khrushchev and M. V. Dubov
Department of Electronic Engineering, Aston University, Aston Triangle, Birmingham B4 7ET, United Kingdom

V. Larin and A. Torkunov
Amotec Ltd., Kishinev, Moldova

(Received 18 June 2002; accepted 21 October 2002)

Controllable, spatially selective treatment of glass-covered amorphous magnetic wires by laser irradiation is demonstrated. Local annealing by an argon laser has resulted in the formation of weakly interacting heterogeneous structures with different magnetic properties. Two large and stable Barkhausen jumps were detected in the magnetization reversal of high and positive magnetostriction wires with treated portions of 200 μm and 0.5 cm. The local annealing of negative magnetostrictive wires has modified wire magnetoimpedance: the maximum of the impedance plot flattens and the working field interval increases. These favorable changes are due to the creation of local stresses and structure interfaces. © *2002 American Institute of Physics.* [DOI: 10.1063/1.1528724]

Amorphous thin wires are among the most interesting materials for applications as magnetic sensing elements, owing to their unique properties related to reentrant magnetic flux reversal[1–3] and giant magneto impedance.[4,5] These properties are influenced by domain structures that exist in the as-cast state and can be modified by various annealing methods.[6–8] Amorphous materials do not possess magnetocrystalline anisotropy. Therefore, the anisotropy and the domain structure are determined by the balance between the magnetoelastic and magnetostatic (shape) contributions. The alloy composition determines the value and sign of the magnetostrictive constant whereas the fabrication process and annealing under stress and/or magnetic field results in a particular magnetoelastic energy. Then, various kinds of magnetic structures can be realized by a suitable postproduction treatment, which normally affects the whole sample. A local processing, which influences only a part of an amorphous material, is also possible. For example, laser radiation was used to achieve local crystallization of amorphous CoP alloys,[9] to change locally the anisotropy of ferromagnetic amorphous ribbons,[10] and to cause local phase transitions to the ferromagnetic state in thin amorphous nonmagnetic CoC films.[11] However, little work has been done to investigate the effect of a local treatment of amorphous materials with the aim to produce heterogeneous magnetic structures. In particular, the development of a method for the predetermined, spatially patterned modification of glass covered amorphous wires would be a very attractive proposition.

In this letter we present our results on local annealing of glass-covered amorphous magnetic wires by laser light. We demonstrate that magnetic properties of amorphous wires can be locally and controllably tuned by argon laser processing due to the formation of magnetic heterostructures. This can be of great interest for application of amorphous wires as magnetic labels and tags.

The sketch of the installation is shown in Fig. 1. In the experiment, the magnetic wires were exposed to the emission of an argon laser operating at a wavelength of 488 nm. The laser beam was focused into an elliptical spot, aligned with the wire, by a positive cylindrical lens. The width of the spot across the wire was about of 25 μm. An additional negative cylindrical lens was used for expanding the laser spot along the wire. Depending on the position of the negative lens, the spot length varied from ~2 to 10 mm. It was possible to focus the beam tighter, down to a length of 30 μm, by substituting the negative lens with a microscope objective.

A glass-covered amorphous wire was fixed on a bracket holder that allowed an exposure of the middle section of the wire. A three-coordinate translation stage provided precise alignment of the holder. The maximal power in the beam was 6.5 W, corresponding to the maximum intensity in the focus in excess of 10^4 W/cm^2.

We used wires of the following compositions: $Fe_{74}B_{13}Si_{11}C_2$ (sample 1), $Fe_{36}Co_{40}B_{13}Si_{11}$ (sample 2), and $Co_{68}Fe_4B_{11}Si_{14}(NiMoGe)_3$ (sample 3). Depending on Co/Fe content, these materials have large positive magnetostriction

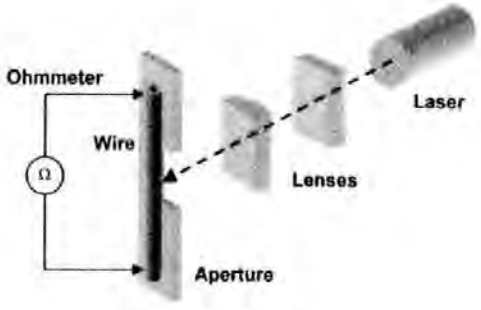

FIG. 1. Schematic of installation.

[a]Electronic mail: a.grigorenko@plymouth.ac.uk

(samples 1 and 2) or small negative magnetostriction (sample 3), which results in different magnetic anisotropies. The general magnetic properties and the fabrication method of glass-covered amorphous wires are summarized in Refs. 12 and 13. An axial anisotropy and a longitudinal domain structure are typical of positive magnetostrictive wires, whereas a circumferential anisotropy and circular domain structure exist in the outer region of negative magnetostrictive wires. In the first case, the longitudinal magnetization is characterized by a large Barkhausen jump leading to bistable rectangular magnetization loops. In the second case, the wire impedance can be sensitively controlled by a small axial magnetic field owing to the circular magnetization process. Both types of wires have been laser processed to investigate the effect of this treatment on the bistability and giant magnetoimpedance (GMI).

In the experiment, we exposed both types of wires to the laser light and investigated the changes in the bistable behavior of samples 1 and 2 as well as the giant magnetoimpedance (GMI) in sample 3 before and after the treatment.

A change in the wire resistance was used as a reference parameter for the laser treatment. The dependence of the wire resistance upon temperature has been calibrated in a thermal bath prior to processing. The wire resistance changed with temperature at a rate $\eta = \Delta R/(R \cdot \Delta T) = 1.2 \times 10^{-4}\ C^{-1}$. Therefore, knowing the length of the exposed section, we can roughly evaluate the local temperature of the treated wire from the total resistance of the sample. When a wire was exposed to relatively low laser intensity below 10^3 W/cm^2, its resistance changed reversibly, i.e., the resistance increased and returned to the initial value after irradiation. At a higher level of exposure, the wire resistance dropped irreversibly by 1%–3%. The likely reason for that is crystallization of the sample and a better conductivity of a crystalline state. During the experiments, care was taken to avoid the crystallization process. The annealing procedure consisted of an increase and a decrease of laser power until the total wire resistance fell to a predetermined value below the initial value. The exposure time was typically of a minute.

In the wires with positive magnetostriction (samples 1 and 2), we investigated the effect of laser treatment on the magnetic reversal characteristics. The magnetization curves were measured by a conventional inductive method using two differential pickup coils of 30 turns, 0.5 mm in inner diameter (0.8 mm in outer diameter) and 1 cm long. Figures 2(a) and 2(c) show the measured differential response of an unprocessed wire and that of a partially laser treated wire (sample 1), respectively. The total sample length was 2 cm and the length of the treated portion was about 5 mm. For as-cast wires, a sharp voltage pulse was detected at a magnetic field of 0.7 Oe [see Fig. 2(a)]. This pulse is characteristic of a large Barkhausen jump. Placing the processed wire in such a way that the detection coil contained both treated and nontreated portions, we detected two voltage pulses (two large Barkhausen jumps) shown in Fig. 2(c). The first pulse corresponds to that of Fig. 2(a) and the other occurs at higher field of 1.9 Oe. On the other hand, if the treated portion was outside the detection coil there was no change in the magnetization reversal behavior in comparison with as-cast wires

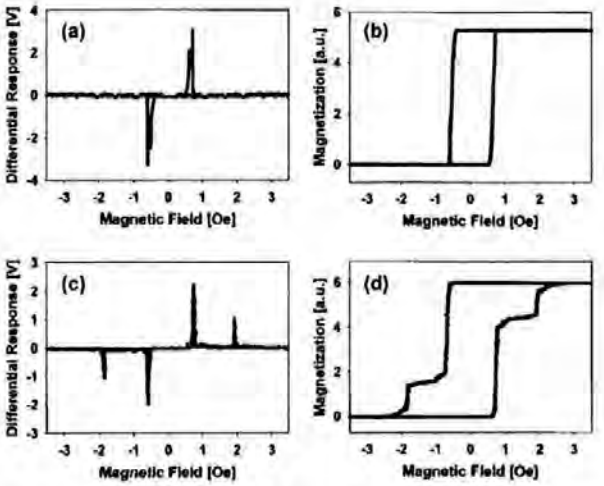

FIG. 2. Magnetic responses of a laser treated bistable amorphous wire-sample 1. The differential signals and reconstructed magnetization loops of the as-cast wire (a) and (b) and the processed wire (c) and (d). The laser treated portion is about 0.5 cm, evaluated annealing temperature is about 500 °C.

[Fig. 2(a)]. Therefore, the laser annealing induced a local change in coercivity and produced no measurable effect on the adjacent areas. By reducing the width of the pickup coils and measuring local magnetization loops, we confirmed that the magnetization reversal happens in treated and nontreated portions by means of a large Barkhausen jump occurring at different fields. As a result, the differential response shown in Fig. 2(c) has two pulses corresponding to the coercivity of processed and unprocessed material. Similarly, one can compare the reconstructed hysteresis loops in Fig. 2(b) (unprocessed wire) and Fig. 2(d) (partially annealed sample 1). The hysteresis loop of sample 1 consists of a superposition of two rectangular hysteresis loops with two distinctly different coercivities. It means that a locally laser treated bistable wire represents an interesting prototype of a simple 2-bit element for product labeling.

Next we studied the effect of the length of the annealed portion on the appearance of the second magnetization jump. Using the resistance change to control annealing, we can reliably monitor the resistance changes (and hence temperature) of a wire with a treated portion down to about 100 μm. Even in this case, two voltage pulses appear at the magnetization reversal, which is demonstrated in Fig. 3(a) for sample 2 with the annealed part of 200 μm. The treated area was reduced further by making use of spherical optics. The resistance control was unreliable for small dimensions of the treated part because the wire resistance changes were small.

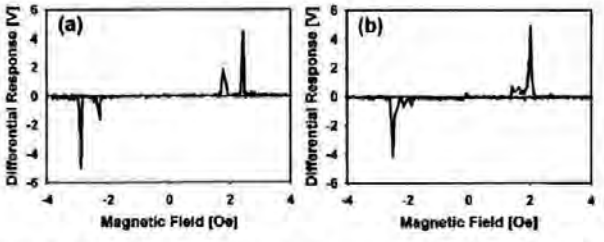

FIG. 3. Magnetic responses of a laser treated bistable amorphous wire-sample 2. The differential signals of the processed wire: (a) the annealing length of 200 μm, (b) the annealing length 30 μm.

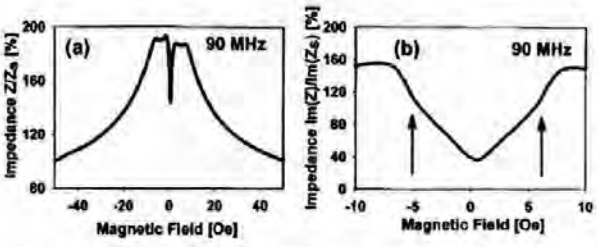

FIG. 4. Magnetoimpedance characteristic of a laser annealed GMI wire at frequency 90 MHz-sample 3: (a) impedance dependence upon magnetic field, (b) the imaginary part of impedance as a function of small fields. Impedance is normalized by the saturation impedance value Z_s. The laser treated portion is about 0.5 cm, evaluated annealing temperature is about 500 °C.

Instead, an intensity of the laser beam was taken as an indicator of the annealing temperature. Figure 3(b) demonstrates that there is no second large Barkhausen jump at the magnetization process after annealing of a 30 μm portion of sample 2. This gives ~100 μm as the upper limit of the wire laser treated length at which distinct magnetic properties are developed and the second magnetization jump is achieved.

It is interesting to note that the amplitude of the pulse related to the annealed portion [seen in Fig. 3(a) at smaller fields and in Fig. 2(b) at higher fields] is relatively large despite a small contribution of this area to the total interrogated region. This observation is very useful for wire applications as a label. It is explained by the fact that the reversal domains have an elongated shape[14] and local laser annealing creates interfaces which act as pinning or nucleation sites for those domains. Also, the measured pulse time is proportional to the length of the "reversing" portion of the wire inside the pickup coil, which makes peaks of Fig. 2(c) narrower than those of Fig. 2(a).

In the case of amorphous wires with a circular domain structure (sample 3) the laser treatment also forms a heterogenic magnetic system, which can be seen from GMI characteristics. Figure 4(a) plots the relative change in impedance as a function of axial magnetic field for a processed wire with the total length of 1 cm and treated portion of about 5 mm. A notable feature of this dependence is the existence of a flat insensitive region in the field range from 2 to 7 Oe. The plateau comes from the superposition of the GMI characteristics from the laser annealed and unprocessed parts of the wire, which peak at different values of the external field. Figure 4(b) shows the plot of the imaginary part of the wire impedance for low fields, where two regions with different GMI slopes and field ranges are clearly seen. The up and down magnetoimpedance curves shown in Fig. 4 coincide. This implies that the treated part of the wire changed the magnitude but conserved the circumferential nature of anisotropy. Such GMI characteristics can be useful for applications in magnetic proximity and switching sensors.

We briefly discuss a possible mechanism of the observed effect. The favorable changes of the magnetic properties cannot be attributed to the partial crystallization of the wires. When crystallization took place and the wire resistance dropped considerably after processing, we found that magnetization reversal of magnetic wires with positive magnetostriction did not happen in one large Barkhausen jump and hysteresis loops lost their rectangular shape. This is due to the fact that crystallization usually results in multiple pinning centers instead of homogeneous local changes. The local change in the magnetic properties is most likely connected with the stress induced by the glass cover in the metallic core. During irradiation the laser power is absorbed mainly inside the core. The core expands and heats up the surrounding glass. As a result, the mechanical equilibrium and local stress of the glass-covered wires are changed when radiation is removed and sample is cooled to an ambient temperature. Scanning electron and optical microscopy of laser-annealed wires revealed that the glass cover changed its form in the laser treated parts of the wire and there is a tendency of developing of microgaps between the glass and the core. This may induce nucleation centers in the amorphous material and influence its magnetic characteristics. It is worth noting similar magnitudes of the switching fields for treated portions obtained for samples 1 and 2, which may suggest that the energy barriers associated with the produced nucleation centers are mostly determined by the annealing characteristics. Further investigation is required to clarify the mechanism of laser annealing.

In conclusion, we applied laser radiation for local, reliable, and controllable treatment of different glass-covered amorphous wires. We have shown that the formation of heterogeneous magnetic structures with uniform properties can be realized by this method. The magnetic properties of these materials such as a large Barkhausen jump and giant magnetoimpedance can be locally adjusted in order to match a particular application. The proposed technique is suitable for mask or multistage laser microprocessing and can be used for fabrication of micro- (nano-) structures based on amorphous magnetic materials.

This work was supported in part by EPSRC Grant Nos. GR/N02283/01 and GR/M23977/01.

[1] R. C. O'Handley, J. Appl. Phys. **46**, 4996 (1975).
[2] F. B. Humphrey, K. Mohri, J. Yamasaki, K. Kawamura, R. Malmhall, and I. Ogasawara, Magnetic Properties of Amorphous Metals, New York, (1987).
[3] H. Chiriac, T. A. Ovari, M. Vazquez, and A. Hernando, J. Magn. Magn. Mater. **177**, 205 (1998).
[4] L. V. Panina and K. Mohri, Appl. Phys. Lett. **65**, 1189 (1994).
[5] M. Vazquez, J. Magn. Magn. Mater. **226**, 693 (2001).
[6] R. Malmhal, K. Mohri, F. B. Humphrey, T. Manabe, H. Kawamura, J. Yamasaki, and I. Ogasawara, IEEE Trans. Magn. **23**, 3242 (1987).
[7] J. Gonzalez, N. Murillo, V. Larin, J. M. Barandiaran, M. Vazquez, and A. Hernando, Sens. Actuators A **59**, 97 (1997).
[8] V. Zhukova, A. F. Cobeno, A. Zhukov, J. M. Blanco, S. Puerta, J. Gonzalez, and M. Vazquez, J. Non-Cryst. Solids **287**, 31 (2001).
[9] M. Zheng, M. Yu, Y. Liu, R. Skomski, S. H. Liou, D. J. Sellmyer, V. N. Petryakov, Y. K. Verevkin, N. I. Polushkin, and N. N Salashchenko, Appl. Phys. Lett. **79**, 2606 (2001).
[10] M. Garcia and M. C. Sanchez, Rev. Phys. Appl. **21**, 207 (1986).
[11] C. Aroca, M. C. Sanchez, I. Tanarro, P. Sanchez, E. Lopez, and M. Vazquez, Phys. Rev. B **42**, 8086 (1990).
[12] H. Chiriac, Mater. Sci. Eng., A **304**, 166 (2001).
[13] A. Zhukov, J. Gonzalez, J. M. Blanco, M. Vazquez, and V. Larin, J. Mater. Res. **15**, 2107 (2000).
[14] L. V. Panina, H. Katoh, M. Mizutani, K. Mohri, and F. B. Humphrey, IEEE Trans. Magn. **28**, 2922 (1992).

ELSEVIER
SCIENCE

Dynamic circular hysteresis in Co-based amorphous microwires.

Anna A. Radkovskaia[a,b], Serghei I. Sandacci[b], Larissa V. Panina[b] and Desmond J. Mapps[b]

[a] *Faculty of Physics, Moscow State University, Vorob'evi Gory, Moscow, 117192, Russia*

[b] *Department of Communication and Electrical Engineering, University of Plymouth, Drake Circus, Plymouth, Devon PL4 8AA, UK*

Elsevier use only: Received date here; revised date here; accepted date here

Abstract

The circular hysteresis loops in CoFeSiB negative magnetostrictive amorphous wires with glass cover have been measured at frequencies up to 300 kHz under the effect of axial dc magnetic field. The loops are partitioned into reversible and irreversible portions assigning them corresponding permeability parameters. It is demonstrated that the introduced permeabilities are characterised by different field-frequency behaviour. This analysis is helpful to understand the variety of magnetoimpedance characteristics reported for different frequency ranges and excitation conditions. © 2001 Elsevier Science. All rights reserved

Keywords: amorphous wire; circumferential anisotropy; dynamic hysteresis; magnetoimpedance
PACS: 75.50. Kj; 76.60.Es; 06.30.Ft; 07.55.w

The magnetoimpedance (MI) effect is based on a very large and sensitive change in dynamic circular magnetisation caused by axial magnetic field H_{ex}. Therefore, there is an interest in studying the circular magnetisation reversal at corresponding frequencies. On the other hand, the most of experiments of hysteresis in these materials are performed under quasi dc conditions [1-3]. In this paper, the circular hysteresis loops in CoFeSiB amorphous wires with glass cover have been measured for frequencies up to 300 kHz under the effect of H_{ex}. The essential features of different magnetisation processes such as domain wall displacements (reversible and irreversible) and magnetisation rotation can be deduced by introducing the corresponding permeability parameters. This analysis has been proven to be helpful to explain various MI characteristics obtained at different frequencies and excitation conditions. Along with this, the obtained hysteresis loops can be useful to clarify the theoretical models of the dynamic hysteresis in general [4].

A $Fe_{4.35}Co_{68.15}Si_{12.5}B_{15}$ amorphous wire with slightly negative magnetostriction was used in these experiments. The metallic core diameter was 24 μm, the glass thickness was 3.4 μm and the wire length was 20 mm. An ac current is applied to the wire, which produces an easy-axis driving circular magnetic field. The induced circular magnetisation

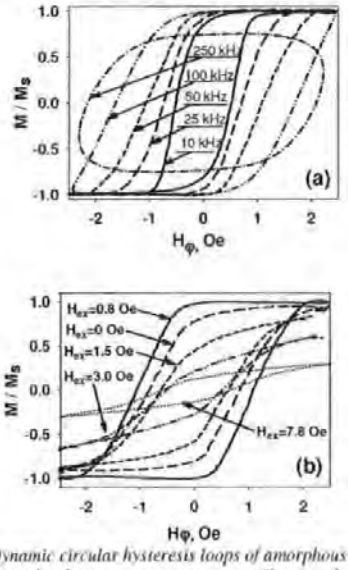

Fig.1. Dynamic circular hysteresis loops of amorphous microwire (a) with a frequency as parameter at H_{ex}=0 and (b) with H_{ex} as parameter at 50kHz of circular.

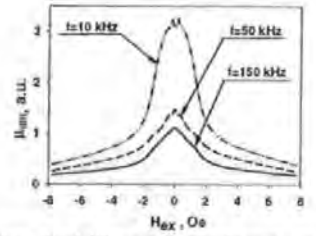

Fig.2. Normalised differential permeability μ_{dif} vs. external axial field H_{ex} with a frequency as a parameter.

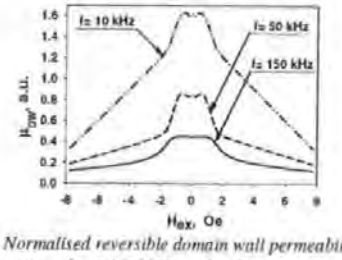

Fig.3. Normalised reversible domain wall permeability μ_{rot} vs. external axial field H_{ex} with a frequency as a parameter.

reversal can be measured by filtering out an inductive voltage signal across the wire using well-known balanced bridge circuit technique. The circuit was balanced at each frequency in the presence of a very large axial field of 100 Oe, which is sufficient to magnetise the wire in the axial direction. Then, only the magnetic contribution to V_1 is measured. Integrating the voltage signal yields the circular magnetisation loops. The driving current amplitude was 30 mA allowing the wire to be remagnetized at higher frequencies.

Figure 1a shows the circular hysteresis loops with a frequency as a parameter whilst the external field is fixed (in particular, H_{ex}=0). The hysteresis loops show progressive widening as frequency is increased. At frequencies higher than 200 kHz, the magnetisation reversal is not complete producing rounded loops. The application of H_{ex} suppresses the circular hysteresis: the coercivity decreases and rotational portion increases, as shown in Fig 1b.

It is informative to analyse the hysteresis in terms of its reversible and irreversible portions and assigning them the corresponding permeability parameters: maximal differential permeability, reversible domain wall permeability and rotational permeability. The differential permeability $\mu_{diff}=\partial B_\varphi/\partial H_\varphi$ reaches a maximum when the driving field H_φ is in the range of circular coercivity. At this point, irreversible domain wall motion mainly contributes to this parameter. Figure 2 shows the field behaviour of the maximal deferential permeability for different frequencies. It peaks at zero field, rolling down very rapidly as H_{ex} is increased. A plausible mechanism explaining this behaviour was proposed in Ref. 1, which is based on the distribution of the anisotropy axes. The peak value drops considerably with increasing frequency

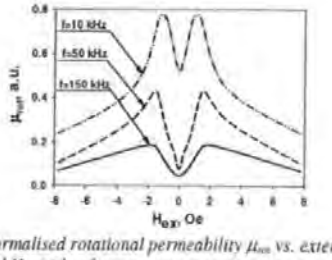

Fig.4. Normalised rotational permeability μ_{rot} vs. external axial field H_{ex} with a frequency as a parameter.

indicating that the irreversible domain wall processes are strongly damped by eddy currents. On the contrary, the field behaviour of the reversible domain wall permeability exhibits a flat region in the field interval $|H_{ex}| < H_k$ as shown in Fig.3. This parameter can be characterised by the ratio $4\pi M_r/H_c$ of the remnant magnetisation M_r to coercivity H_c. Since the external field H_{ex} reduces both M_r and H_c, their ratio exhibits little change.

Examining the hysteresis loops shown in Fig. 1b, it is seen that the application of H_{ex} activates the rotational processes, since it results in the magnetisation inclination towards the wire axis. The rotational processes are reasonable to characterised by the value of the differential permeability determined at H_φ=0. Figure 4 shows the plots of μ_{rot} vs. H_{ex} with a frequency as a parameter. This characteristics shows two peaks at $H_{ex}=\pm H_k$. For larger fields, it rapidly drops and at fields more that 10 Oe becomes insensitive to the axial field.

The analysis made has demonstrated that different magnetisation processes contributing to circular hysteresis may respond differently upon the application of the external field. Accordingly, the field behaviour of the corresponding permeability parameter may have one central peak, or two symmetrical peaks situated at the anisotropy field, or flat region at $|H_{ex}| < H_k$, depending on the predominant mechanism.

All these features can be observed in impedance vs. H_{ex} plots depending on frequency and amplitude of the driving current, which resolves some conflicting results. At relatively low frequencies (lower than 1-3 MHz) and sufficiently large driving current amplitudes one-peak MI characteristic is typical. As frequency is increased and domain wall processes are strongly damped, the MI plots have two peaks at the anisotropy field. At certain conditions, there may be very insensitive MI behaviour. If the ac driving current is biased with dc bias current, which eliminates domain structure, the MI paten is always of two-peak type.

References

[1] L. V. Panina, H. Katoh, and K. Mohri, IEEE Trans. Magn. 29, (1993) 2524.

[2] K. Mohri, L.V. Panina, T. Uchiyama, K. Bushida, M. Noda, *IEEE Trans. Magn.* 31 (1995) 1266

[3] M.Vazquez and A. Hernando, *J. Phys. D: Appl. Phys.*, 29 (1996) 939

[4] DC Jiles, J.Appl. Phys., vol. 76, (1994) 5849-5855

ELSEVIER
SCIENCE

Valve–like behavior of the magnetoimpedance in the GHz range

Serghei I. Sandacci,[a] Dmitriy P. Makhnovskiy,[a] and Larissa V. Panina [a *]

[a]*Department of Communication and Electrical Engineering, University of Plymouth, Drake Circus, Plymouth, Devon PL4 8AA, United Kingdom.*

Elsevier use only: Received date here; revised date here; accepted date here

Abstract

High-frequency modification in magneto-impedance (MI) characteristics in the frequency range of 0.5-3 GHz has been investigated in 10 micron diameter amorphous microwires with a circumferential anisotropy. As frequency is increased, the peaks in the MI behavior observed at the anisotropy field reduce and become less sharp, disappearing completely at frequencies higher than 1.6GHz. This "valve-like" behavior can be explained by considering the dispersion properties of the effective permeability of the ac linear response combined with the rotational dc magnetization.

Keywords: Magneto-impedance, ferromagnetic wires, microwave materials.
PACS: 75.30.Cr; 75.30.Gw; 75.40.Gb; 75.50.Cc; 75.50.Kj.

Co-based microwires with circular magnetization in the surface region exhibit the most sensitive magneto-impedance (MI) effect [1]. The continued and growing interest in these materials is mainly due to their application as high-performance magnetic sensors. Typically, MI sensors are designed for MHz frequencies [2], due to the limitations of the associated electronics. However, the field sensitivity of the surface impedance in wires with circumferential anisotropy remains very high even at the GHz range [3]. This makes the MI effect very useful to design microwave composites with tunable properties and tunable band-gap structure [4,5]. It can be also used for designing a new type of high-frequency transponders in radio-frequency identification (RFID) systems [6].

Co-rich glass-coated amorphous wires of 10 μm in diameter with vanishing negative magnetostriction were used in our experiments. The circular domain structure results in nearly linear nonhysteretic magnetization curves, as shown in Fig.1. The loops were measured by means of compensation magnetometer at 130 Hz [7]. The anisotropy field H_K estimated from Fig. 1 is 2.8 Oe. The MI characteristics were deduced from S_{11} parameter measurements with the use of Network Analyzer HP 8753E

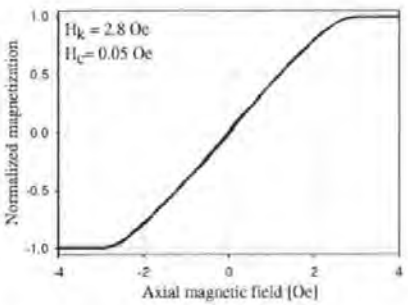

Fig. 1. Longitudinal magnetization curve in Co-based microwires

operating at frequencies up to 6 GHz. As frequency is increased beyond 500 MHz, an extra care is needed to decrease the spurious resonance of the cable leads and matching network. Since measurements were taken above 500MHz, recalibration was required to account for the spurious resonance of the total line-impedance network. The plots of the ral part of impedance Z vs. axial low frequency field H_{ex} are shown in Fig. 2. Typical MI

* Corresponding author. Tel.: +44-1752-232599; fax: +44-1752-232583; e-mail: lpanina@plymouth.ac.uk.

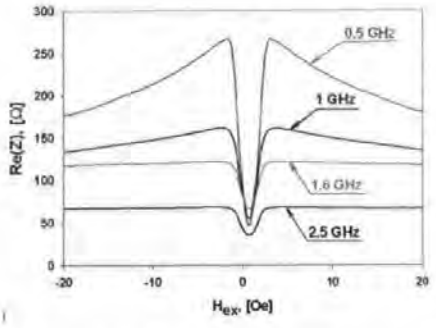

Fig. 2. "Valve-like" field-dependence of the axial magneto-impedance at different frequencies in the GHz range.

characteristics with two peaks at the anisotropy field are seen for MHz frequencies. With increasing frequency, the low-field region ($H_{ex} < H_K$) in the impedance plots preserves its high sensitivity although the impedance maximum value at $H_{ex} = H_K$ decreases substantially. The transformations in the high-field ($H_{ex} > H_K$) region are more dramatic. With increasing frequency the impedance looses its sensitivity for higher fields and at frequencies above 1.6GHz it remains constant for any $H_{ex} > H_K$. This unusual "valve-like" behavior was previously reported in Ref. 3 where a rather confusing explanation of this effect was given. It was stated that the microwave MI did not directly depend on the ac permeability (like in MHz range) but on the dc magnetization. Our experimental results revealing a gradual transformation of a two-peak plot into that reaching saturation at $H_{ex} = H_K$ allow a consistent explanation to be given. Namely, the impedance always depends on the dc magnetic quantities via the ac permeability.

The analysis of microwave MI is based on the rotational dynamics under the condition of a linear ac excitation with time dependence taken in the form $\exp(-j\omega t)$ [8]. In a wire with a circular domain structure having no averaged helical magnetization, the impedance is represented in a simple form:

$$Z = R_{dc} ka \frac{J_0(ka)}{2J_1(ka)}, \tag{1}$$

$$k = (1+j)\sqrt{\tilde{\mu}}/\delta_0 \tag{2}$$

where R_{dc} is the wire dc resistance, $J_{0,1}$ are the Bessel functions, $\delta_0 = c/\sqrt{2\pi\sigma\omega}$ is the skin depth for nonmagnetic material, σ is the conductivity, c is the velocity of light (Gaussian units are used), $\tilde{\mu} = 1 + 4\pi\cos^2(\theta)\tilde{\chi}$, θ is the angle between the static magnetization $\mathbf{M}_0$ and the wire axis, and $\tilde{\chi}$ is the susceptibility parameter:

$$\tilde{\chi} = \chi_2 - 4\pi\chi_a^2/(1+4\pi\chi_1). \tag{3}$$

In (3), the parameters χ_1, χ_2 and χ_a are diagonal and off-diagonal components of the ac rotational susceptibility tensor written in the co-ordinate system with the z-axis parallel to $\mathbf{M}_0$. Assuming that the anisotropy axis is directed at angle α with respect to the wire axis (slightly different from 90°), the susceptibility parameters are given by:

$$\begin{aligned}
&\chi_1 = \omega_M(\omega_1 - j\omega\tau)/\Delta,\\
&\chi_2 = \omega_M(\omega_2 - j\omega\tau)/\Delta,\\
&\chi_a = \omega\omega_M/\Delta,\\
&\Delta = (\omega_1 - j\omega\tau)(\omega_2 - j\omega\tau) - \omega^2\\
&\omega_1 = \gamma[H_{ex}\cos\theta + H_K\cos 2(\alpha-\theta)],\\
&\omega_2 = \gamma[H_{ex}\cos\theta + H_K\cos^2(\alpha-\theta)],\\
&\omega_M = \gamma M_0
\end{aligned} \tag{4}$$

where, γ is giromagnetic constant, and τ is the relaxation parameter. With increasing frequency beyond the ferromagnetic resonance, the susceptibility $\tilde{\chi}$ loses its field sensitivity [4]. Thus, the impedance is entirely related to the static magnetization orientation θ. Then, if θ is a sensitive function of H_{ex} as in the present case, to insure high field sensitivity of the impedance it is important only that the condition $|\tilde{\mu}| >> 1$ is still held. The analysis of (4) shows that for Co-based wires (H_K =2Oe, $4\pi M_0$ =6000G) $|\tilde{\mu}| \approx 25$ for a frequency of 3 GHz,. This conclusion also demonstrates that the condition of the ferromagnetic resonance is not required for the MI effect, contrary to the widely expressed belief [9].

The "valve-like" behavior of $Z(H_{ex})$ at very high frequencies may be of a considerable interest since the impedance switches from one stable level to the other, following the dc magnetization. This property can find an interesting use in the tunable microwave composite consisting of short ferromagnetic wires embedded into a dielectric matrix [4].

References

[1] L.V. Panina, K. Mohri, Appl. Phys. Lett. 65 (1994) 1189.
[2] K. Mohri, L. V. Panina, T. Uchiyama, K. Bushida, M. Noda, IEEE Trans. Magn. 31 (1995) 1266.
[3] M. Domingues et al, J. Magn. Magn. Mater. 249 (2002) 117.
[4] D. P. Makhnovskiy, L. V. Panina, J. Appl. Phys. 93 (2003) 4120.
[5] A. Figotin, Y. A. Godin, Phys. Rev. B 57 (1998) 2841.
[6] C. Hausleitner, R. Steindl, A. Pohl, H. Hauser, F. Siefert, IEEE Microwive theory and Techniques 49 (2001) 817.
[7] S. I. Sandacci, A. N. Grigorenko, L. V. Panina, D. J. Mapps, IEEE Trans. Magn. 38 (2002) 2409.
[8] D. P. Makhnovskiy, L. V. Panina, D. J. Mapps, Phys. Rev. B 63 (2001) 144424.
[9] M. R. Britel, D. Menard, L. G. Melo, P. Ciureanu, A. Yelon, R. W. Cochrane, M. Rouabhi, B. Cornut, Appl. Phys. Lett. 77 (2000) 2737.

Off-diagonal Impedance in Amorphous Wires and Application to Linear Magnetic Sensors

S. I. SANDACCI, D. P. MAKHNOVSKIY, L. V. PANINA, K. MOHRI, Y. HONKURA

Abstract - **The magnetic-field behaviour of the off-diagonal impedance in Co-based amorphous wires is investigated under the condition of sinusoidal (50 MHz) and pulsed (5 ns rising time) current excitations. For comparison, the field characteristics of the diagonal impedance are measured as well. In general, when an alternating current is applied to a magnetic wire the voltage signal is generated not only across the wire but also in the coil mounted on it. These voltages are related with the diagonal and off-diagonal impedances, respectively. It is demonstrated that these impedances have a different behaviour as a function of axial magnetic field: the former is symmetrical and the latter is antisymmetrical with a near linear portion within a certain field interval. In the case of the off-diagonal response, the dc bias current eliminating circular domains is necessary. The pulsed excitation that combines both high and low frequency harmonics produces the off-diagonal voltage response without additional bias current or field. This suits ideal for a practical sensor circuit design. The principles of operation of a linear magnetic sensor based on C-MOS transistor circuit are discussed.**

Index Terms - **ferromagnetic wire, magneto-impedance sensor, magneto-impedance tensor, diagonal impedance, off-diagonal impedance, antisymmetrical impedance.**

I. Introduction

Magneto-impedance (MI) is an expanding area of current research because of its importance for micro magnetic sensor applications [1-6]. Recently developed MI sensor technology uses CoFeSiB amorphous wires as MI-element incorporated into C-MOS IC multivibrator pulse current circuit. Typical parameters of sensor operation with 1 mm long MI head are: a field resolution of 10^{-6} Oe (0.1 nT) for the full scale of ±1 Oe (0.1 mT), a response speed of 1 MHz, and a power consumption of about 10 mW. The sensor sensitivity is at least an order of magnitude higher than that for GMR sensors. These advanced characteristics are associated with a large change in the range of 100% in high-frequency impedance of Co-based amorphous wires subjected to a moderate magnetic field (1-5 Oe). Sensor operation needs high sensitivity combined with linearity. On the other hand, the impedance vs. field behaviour in amorphous wires is essentially non-linear especially near zero-field point. Customarily, applying a dc bias field or utilising an asymmetric MI effect [7-9] achieves linearity. On the other hand, off-diagonal impedance may have almost linear region near zero-field point [10,11] and hence can be used for linear sensing, as demonstrated in this paper.

Generally, impedance Z_w in a wire is understood as a ratio of voltage V_w measured across it to a passing ac current i (see Fig. 1(a)). In wires with a circumferential anisotropy this quantity is very sensitive to a dc axial magnetic field H_{ex}, as a result of the skin effect and ac transverse magnetisation. The real and imaginary parts of the function $Z_w(H_{ex})$ are symmetrical having either a peak at a zero field or two

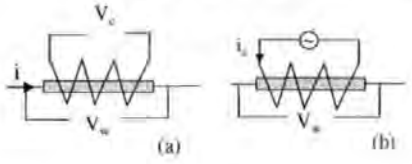

Fig. 1. Voltage responses due to the ac excitation using current i and field h_{ex}, measured and in the coil in (a) and across the wire in (a,b).

identical peaks at $H_{ex} = \pm H_K$, where H_K is the characteristic anisotropy field. For a helical static magnetisation, the ac current i induces also a voltage V_c in the coil mounted on the wire (see Fig. 1(a)), since the current flow gives rise to ac axial magnetisation. The ratio $Z_c = V_c / i$ may be called the off-diagonal impedance. In contrast, if the wire is placed in an ac longitudinal magnetic field $h_{ex} = ni_c$ induced by the coil current i_c (n is the number of coil turns per unit length), the circulatory ac magnetisation contributes to V_w (see Fig. 1(b)). The ratio $\tilde{Z}_w = V_w / i_c$ also may be called the off-diagonal impedance. The crossed magnetisation processes that are responsible for the voltages V_w and V_c are known as the inverse Wiedemann and Matteucci effects [3,10,11]. In single-domain wires with a circumferential anisotropy, the real and imaginary parts of the functions $Z_c(H_{ex})$ and $\tilde{Z}_w(H_{ex})$ are antisymmetrical with a near-linear region around zero field point [10,11]. These off-diagonal field characteristics can be used in linear sensing. A practical design of such a sensor is reported in [12] where the wire element is exited by a pulse current of C-MOS IC multivibrator and the output signal is measured in a wire coil (the off-diagonal component $Z_c(H_{ex})$). Therefore, the sensor operation is based on the off-diagonal impedance. This has not been made clear and no analysis of the related impedance components as functions of the sensed field has been carried out.

In this paper, we investigate the field behaviour of the off-diagonal impedance $Z_c(H_{ex})$ in CoFeSiB glass covered amorphous wires by means of two types of measurements. The wire is excited with a sinusoidal current using a HP 8753E Network Analyser, and with a pulse current using C-MOS multivibrator circuit. We demonstrate that for a multidomain state in a wire, the off-diagonal impedance is almost zero for any value of H_{ex}. Biasing the ac current with a dc one which saturates the outer shell of the wire in the circular direction is essential to get the off-diagonal properties in the case of the circumferential anisotropy. The discussion is made using the concept of the surface impedance tensor and generalised Ohm's law. In the case of the pulse current excitation, which contains both low and high frequency harmonics the off-diagonal impedance is large without applying any additional dc bias. A practical sensor design is analysed as well.

II. Voltage Response and Impedance Tensor

The SI system of units will be used in the equations throughout the paper. An ac current $i = i_0 \exp(-j\omega t)$ flowing in a wire with a helical magnetisation induces voltages V_w across the wire and V_c in the coil mounted on the wire, as shown in Fig. 1(a). The voltage V_c appears as a result of the change in the ac axial magnetisation m_z caused by the circular field h_φ produced by the current i (at the wire surface $h_\varphi = i/2\pi a$, a is the wire radius). A helical type of the equilibrium magnetisation is needed to make possible such cross-magnetisation process $m_z - h_\varphi$. Furthermore, if the wire is placed in a variable longitudinal field $h_{ex} = n i_c$, the voltage V_w across the wire will be generated due to a similar cross-magnetisation process $m_\varphi - h_z$ (see Fig. 1(b)).

In general, the voltage response in a magnetic wire (V_w, V_c) is related to the current vector (i, i_c) via the surface impedance tensor $\hat{\zeta}$ [10]. This is convenient since the tensor $\hat{\zeta}$ represents the relationship between the electric field (which determines the voltage) and magnetic field (which determines the current) on the wire surface. The following equations are hold [10,11]:

$$V_w = e_z l = (\zeta_{zz} \frac{i}{2\pi a} - \zeta_{z\varphi} h_{ex}) l , \quad (1)$$

$$V_c = e_\varphi 2\pi a n l = (-\zeta_{\varphi\varphi} h_{ex} + \zeta_{\varphi z} \frac{i}{2\pi a}) 2\pi a n l . \quad (2)$$

Here l is the wire length, $h_{ex} = n i_c$, n is the number of coil turns per unit length, e_z and e_φ are the longitudinal and circumferential electrical fields on the wire surface, respectively. This can be understood as generalised Ohm's law introducing the impedance matrix $\hat{\mathbf{Z}}$, which relates the voltage vector $\mathbf{V} = (V_w, V_c)$ to the current vector $\mathbf{i} = (i, i_c)$:

$$\mathbf{V} = \hat{\mathbf{Z}}\mathbf{i}, \quad \begin{aligned} V_w &= Z_{zz} i + Z_{z\varphi} i_c \\ V_c &= Z_{\varphi z} i + Z_{\varphi\varphi} i_c \end{aligned} \quad (3)$$

In a wire with a dc uniform equilibrium magnetisation $\mathbf{M}_0$ in the surface shell inclined towards the axis by angle θ the surface impedance tensor has a simple form in the high frequency limit and considering linear ac magnetisation, which are of interest here. Taking the result of [10] for $\hat{\zeta}$ and comparing Eqs. (1)-(3) the impedance tensor $\hat{\mathbf{Z}}$ can be written as:

$$\hat{\mathbf{Z}} = \begin{pmatrix} Z_{zz} & Z_{z\varphi} \\ Z_{\varphi z} & Z_{\varphi\varphi} \end{pmatrix} = \frac{(1-j)R_{dc}a}{2\delta} \times \times \begin{pmatrix} \sqrt{\mu_{ef}}\cos^2\theta + \sin^2\theta & 2\pi a n\left(\sqrt{\mu_{ef}} - 1\right)\sin\theta\cos\theta \\ 2\pi a n\left(\sqrt{\mu_{ef}} - 1\right)\sin\theta\cos\theta & (2\pi a n)^2 / \sqrt{\mu_{ef}}\sin^2\theta + \cos^2\theta) \end{pmatrix} \quad (4)$$

Here $R_{dc} = \rho l / \pi a^2$ is the dc wire resistance, $\delta = \sqrt{2\rho / \omega\mu_0}$ is the non-magnetic skin depth, μ_0 is the vacuum permeability, ρ is the wire resistivity, and μ_{ef} is the ac effective circumferential permeability with respect to the ac current flow [10]. Observing Eq. (4) the important conclusion can be made. The impedance tensor components have a different symmetry with respect to the dc magnetisation: the diagonal components Z_{zz} and $Z_{\varphi\varphi}$ do not change when the direction of the equilibrium dc magnetisation $\mathbf{M}_0$ is reversed whereas the off-diagonal components $Z_{z\varphi}$ and $Z_{\varphi z}$ change the sign together with $\mathbf{M}_0$. Therefore, the off-diagonal impedances are antisymmetrical with respect to $\mathbf{M}_0$. In fact, the permeability parameter also depends on the magnetisation angle θ but this does not alter the conclusion made.

In a wire with a circumferential anisotropy, the axial magnetic field is a hard axis field that will produce a linear magnetisation curve in the range of $-H_K < H_{ex} < H_K$. Therefore, we can expect a linear field behaviour of the off-diagonal impedances in this field interval for such magnetic configuration. Some deviation from linearity may be due to the field dependence of the permeability parameter μ_{ef}. However, if the wire has a circular domain structure the off-diagonal components averaged over domains are zeroed, because of the factor $\sin\theta$, which has opposite signs in the domains with the opposite circular magnetisation. It implies that a dc bias current will be needed to eliminate circular domain structure. A typical field behaviour of the off-diagonal impedance is demonstrated in Fig. 2 where the result of calculations for a single domain wire with a circumferential anisotropy is given [10].

III. Impedance Investigation

In this Section we consider the impedance characteristics under sinusoidal current excitation. Glass covered $Co_{64.6}Fe_{3.5}Si_{15.5}B_{16.4}$ amorphous wires produced by Taylor-Ulitovsky method (kindly provided by **MFTI Ltd**, Moldova) have been used as an MI element in all the experiments. The wire has a metallic amorphous core of 29.6 μm in diameter (d_w) covered by glass with thickness of 2.3 μm, as sketched in Fig. 3. The equilibrium magnetisation is mainly determined by

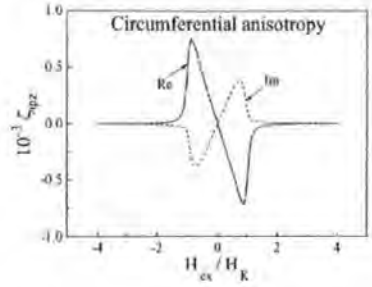

Fig. 2. Typical field dependence of the off-diagonal impedance in the megahertz range for wires with a circumferential anisotropy. The real and imaginary parts are antisymmetrical with respect of H_{ex}.

the negative magnetostriction coupled with the axial stress, which results in a circumferential anisotropy and a circular domain structure. This structure is confirmed by dc longitudinal magnetisation measurements, which show almost a non-hysteretic linear curve, as seen in Fig. 4. The anisotropy field is estimated to be about 1.4 Oe.

Fig. 3. Sketch of the glass covered wire. The core has a diameter d_m, whilst the total diameter of the micro wire, i.e. core and the glass coating, is D_w.

A HP 8753e Network Analyser with a specially designed high frequency measuring cells (seen in Figs. 5(a),(b)) is used for the impedance measurements. The cells have 3.5-mm connectors and are linked up to the Transmitter/Receiver ports. A wire element (8 mm long) soldered or bonded to the cell is excited by the sinusoidal input voltage V_{in}. The output voltage V_{out} is taken from the wire (Fig. 5(a)) or from a tiny coil (Fig. 5(b)), which has 25 turns and a diameter of 120 μm. Blocking

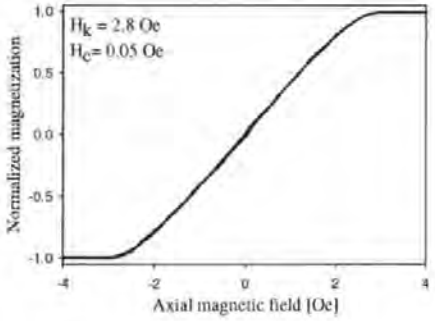

Fig 4. Longitudinal dc magnetisation loop for the wire with a circumferential anisotropy used in measurements.

capacitor (C) prevents the dc bias current I_b from entering the Analyser. Terminal resistors are required for normalising input/output impedance of the measured elements. The S_{21}-parameter (forward transmission) is measured as a function of a sensed magnetic field H_{ex} applied in the wire axial direction. In general, a dc bias current I_b can be applied to the wire. By frequency scanning we have chosen optimal frequency of 50 MHz for our simples, when the impedance characteristics are most sensitive to H_{ex}. The impedance components Z_{zz} and $Z_{\varphi z}$ ($\equiv Z_{z\varphi}$) are determined by measuring the output signal V_{out} from the wire ($V_{out}=V_w$) or from the coil ($V_{out}=V_c$), respectively. In both cases the ac current i supplied by V_{in} is applied to the wire. The S_{21}-parameter is defined as dimensionless quantity $S_{21}=V_{out}/V_{in}$. Then, putting $i_c=0$ in Eq. (3), both Z_{zz} and $Z_{\varphi z}$ are calculated as the ratio $V_{out}/i=S_{21}\cdot V_{in}/i$.

Figure 6 shows the longitudinal impedance Z_{zz} versus applied magnetic field H_{ex} at the fixed frequency 50 MHz. As it could be expected from Eq. (4), both the real and imaginary parts are symmetrical with respect to H_{ex}, exhibiting two maximums at the field in the range of the anisotropy field $H_{ex}=\pm H_K$. The off-diagonal impedance $Z_{\varphi z}(H_{ex})\sim S_{21}(H_{ex})$ is shown in Fig.

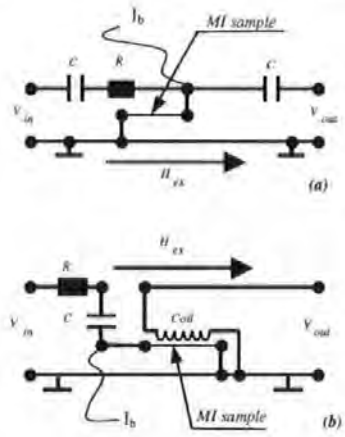

Fig. 5. Electrical circuits of the cells for Z_{zz} in (a) and $Z_{\varphi z}$ in (b). The cells have input and output 3.5-mm connectors. The dc bias current I_b is applied across the wire. Blocking capacitor (C) prevents I_b from entering the Analyser.

7 at the fixed frequency of 50 MHz for different bias currents. In this case, if no dc bias current is used, the response signal is very small and irregular. It increases substantially when a small dc current $I_b=2.5$ mA is applied. Typically, the coercivity in amorphous wires is about a fraction of Oe and applying a small current of few mA eliminates circular domains. Therefore, in the case of a circumferential anisotropy and a circular domain structure, the presence of I_b is the necessary condition for the existence of the off-diagonal components of the impedance

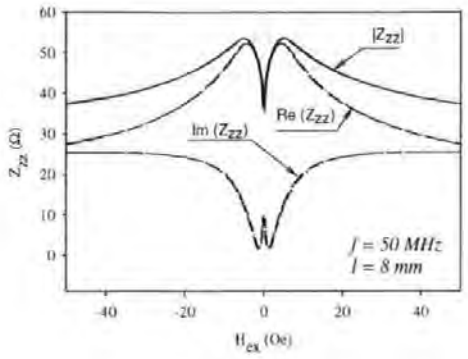

Fig. 6. Longitudinal impedance Z_{zz} versus applied magnetic field H_{ex} at the fixed frequency 50 MHz. Both the real and imaginary parts are symmetrical with respect to H_{ex}, exhibiting two maximums at the field in the range of the anisotropy field $H_{ex} = \pm H_K$.

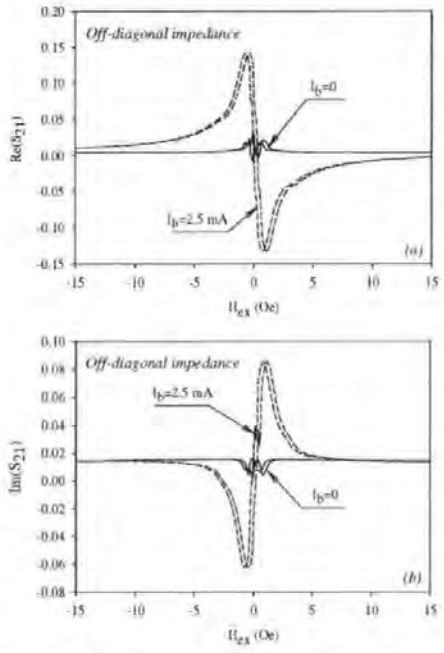

Fig. 7. Real in (a) and imaginary in (b) parts of the field dependence of the off-diagonal response for $f = 50$ MHz. Without bias current I_b, the off-diagonal response is very poor and irregular due to the averaging over the stripe domain structure. With $I_b = 2.5$ mA the off-diagonal response increases significantly and becomes antisymmetric, as predicted theoretically.

tensor. The real and imaginary parts of the off-diagonal component are antisymmetrical with respect to the field H_{ex}, having almost linear behaviour in the field range of ±2 Oe.

IV. C-MOS SENSOR – PULSE EXCITATION OF MI WIRES

In this Section we consider a pulse excitation of the wire samples using C-MOS transistor circuits, shown in Fig. 8. This corresponds to a practical MI sensor circuit design.[12] As in Section III, the output signal is taken from the wire or from the coil. The real and imaginary parts of the impedance components measured by the Analyser correspond to the signal amplitude and its phase (time shifting with respect to the excitation signal) in a physical device. The amplitude includes the signal value and its sign. We will be interested only in the amplitude with sign since the phase is not important for the field dependence of the output voltage.

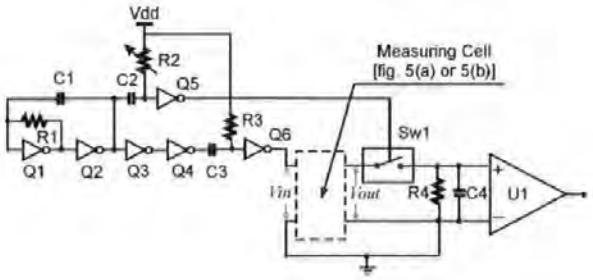

Fig. 8. Principle electronic circuit for a sensor with a pulse excitation, which can utilise the off-diagonal impedance. The circuit includes: C-MOS IC multivibrator with invertors (Q1, Q2), differential circuit (C3, R3), analogous synchronised switch (SW1), integrator (R4, C4), and differential amplifier. The ac signal is taken from the wire (V_w) or pick-up coil (V_c) using the analogous synchronised switch (SW1) and converted to a dc voltage by the integrator (R4, C4).

The circuit operates as follows. Square-wave generator (Q1, Q2) produces rectangular signal as shown in Fig. 9 (bottom signal). Differential circuit (C3, R3) transfers the squire-wave signal into the positive pulses, which are applied to the wire (Fig. 9, top signal). Analysing the MI characteristics obtained under a sinusoidal excitation the optimal frequency of 50 MHz has been identified, for which the maximal sensitivity (and the

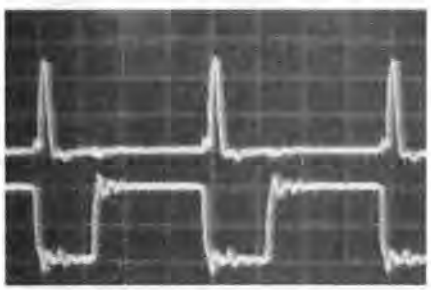

Fig. 9. Rectangular signal produced by the square-wave generator (Q1, Q2) (bottom signal) and the positive pulses after the differential circuit (C3, R3) (top signal). The sharp pulse excitation containing the high frequency harmonics and dc bias (zero harmonic) is applied to the wire. Vertical resolution: 2V/dev, horizontal resolution: 50 ns/dev.

best linearity in the case of the off-diagonal impedance) has been achieved. In the case of a pulsed excitation, such parameters as a rise time and a fall time determine the frequency of the principle harmonic. The time parameter of 5ns corresponds to the optimal frequency of 50 MHz. The rise and fall times of the pulse signal are determined by the construction of HEX Inverters. The 74HCT04 inverter possesses the needed characteristics. Further more, this microchip has a minimal distortion and high temperature stability.

To demonstrate the principles of the MI sensor operation, the output pulse voltages are obtained for different sensed field H_{ex}. The voltage signal taken across the wire (using cell of Fig. 5(a)) corresponds to the diagonal impedance Z_{zz}. Figures 10(a),(b) show the diagonal voltage response (V_w) before the rectifier (SW1, R4, C4) for $H_{ex}=0$ and $H_{ex}=2.6$ Oe, respectively. The amplitude of the main pulse is increased almost twice in the presence of the field. If the field is applied in the reversed direction, the pulse amplitude and sign do not change. This is in line with the result obtained for a sinusoidal excitation: the real and imaginary parts of the diagonal impedance are symmetrical with respect to the axial sensed field. In the case of the output taken from the coil (off-diagonal response V_c), the signal is very small if no axial magnetic field is applied. In the presence of the field, the voltage pulse increases and when the field is reversed the direction of the pulse is reversed as well. This behaviour is demonstrated in Fig. 11, where the top signal is the excitation pulse on the wire and the bottom signal is the output voltage before the rectifier (SW1, R4, C4) as a function of the sensing field H_{ex}. Therefore, in the case of a pulse excitation, the off-diagonal voltage response shows antisymmetrical field characteristics, similar to that for the off-diagonal impedance. Note that the pulse excitation does not require the use of the dc bias current I_b to make the off-diagonal voltage be induced since such excitation already involves low-frequency harmonics.

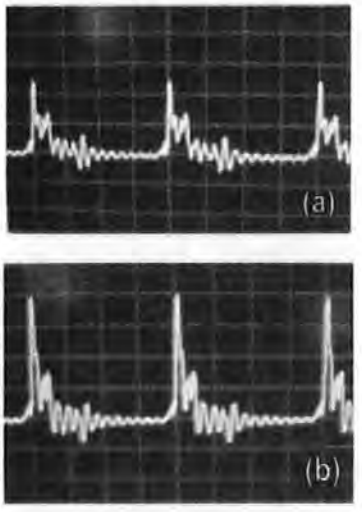

Fig. 10 Diagonal voltage response (V_w) before the rectifier (SW1, R4, C4) for $H_{ex}=0$ in (a) and $H_{ex}=2.6$ Oe in (b). Vertical resolution: 40 mV/dev, horizontal resolution: 50 ns/dev. The amplitude of the main pulse is increased almost twice in the presence of the field. If the field is applied in the reversed direction, the pulse amplitude and sign do not change.

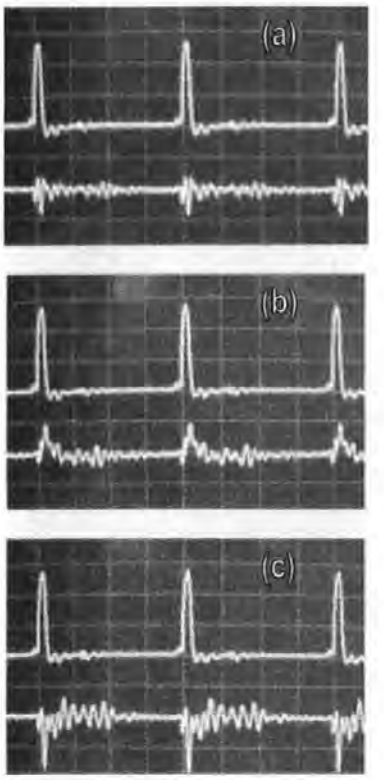

Fig. 11. Off-diagonal response V_c before the rectifier (SW1, R4, C4) measured from the pick-up coil. Horizontal resolution: 50ns/dev. Vertical resolution: 2V/dev for the top signal and 50 mV/dev for the bottom signal. The top signal in (a), (b) and (c) is the excitation pulse at the wire. The bottom signal in (a), (b) and (c) is the off-diagonal response from the pick-up coil. V_c is very small if no axial magnetic field H_{ex} is applied (see (a)). In the presence of H_{ex}, the voltage pulse increases (see (b), and (c)) and when the field is reversed the direction of the pulse is reversed as well (see (c)). Therefore, in the case of a pulse excitation, the off-diagonal voltage response shows antisymmetrical field characteristics, similar to that for the off-diagonal impedance.

The rest of the circuit is needed to obtain a rectified output depending on the field H_{ex}. Digital switch (SW1) filters away a background noise signal along with an unwanted pulse voltage portion. Its output impedance is loaded by 50 Ω. The integrating element (R4, C4) produces a smooth quasi-dc signal in proportion to the pulse amplitude (with sign). The parameters are chosen such that the integrating time is much larger than the pulse train period. The circuit does not contain

a detector (diode) because we would like to measure the signal amplitude along with its sign. Figure 12 shows the integrated diagonal (V_w) and off-diagonal (V_c) responses after the rectification and amplification as a function of H_{ex}. In the case of the diagonal response (Fig. 12(a)), the field characteristics are symmetrical showing two maximums at $H_{ex} = \pm 4$ Oe. This behaviour is very similar to that shown in Fig. 6 for the diagonal impedance. The off-diagonal voltage output as a function of H_{ex} shown in Fig. 12(b) has almost linear portion in the field interval $H_{ex} = \pm 2$ Oe. This is similar to the off-diagonal impedance versus H_{ex} shown in Fig. 7. Therefore, we can conclude that the off-diagonal voltage response in amorphous wires with a circumferential anisotropy obtained under pulsed excitation can be linear with respect to the sensed axial field without using any bias fields or currents. In fact, the pulse current applied to the wire itself does two jobs: it causes a high frequency magnetisation that is responsible for the voltage-field dependence, and it also partially eliminates circular domains making the off-diagonal response possible.

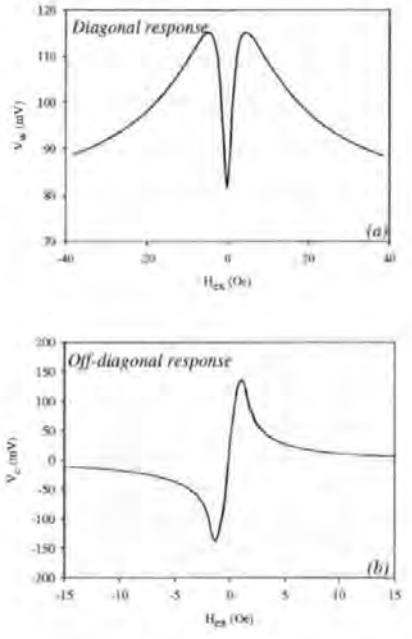

Fig. 12 Integrated diagonal (V_w) and off-diagonal (V_c) responses after the rectification (SW1, R4, C4) and amplification as a function of H_{ex}. In the case of the diagonal response in (a), the field dependence is symmetrical showing two maximums at $H_{ex} = \pm 4$ Oe. The off-diagonal voltage output as a function of H_{ex} shown in (b) has almost linear portion in the field interval $H_{ex} = \pm 2$ Oe.

V. Conclusion

The principles of operation of a linear magnetic sensor circuit based on magneto-impedance (MI) in glass-covered Co-based amorphous wires have been revealed by considering sinusoidal and pulsed current excitations. In the first case, the voltage response detected across the wire and in the coil mounted on it directly proportional to the complex impedance (diagonal or off-diagonal, respectively). It was shown that the off-diagonal response is realised under the application of a dc bias current. The diagonal and off-diagonal impedances have different field behaviour: the former is symmetric and the latter is antisymmetric within respect to the axial sensed field. This property is very important for linear magnetic sensing. A practical C-MOS transistor circuit producing pulsed current excitation of the wire is analysed. In this case, the pulse current contains both low and high frequency harmonics and can induce the off-diagonal response without additional dc bias. This configuration is especially advantageous to realise sensitive linear sensing.

References

[1] L. V. Panina, K. Mohri, K. Bushida, and M. Noda, "Giant magneto-impedance and magneto-inductive effects in amorphous alloys", *J. Appl. Phys.*, vol. 76, p. 6198, 1994.

[2] K. Mohri, L.V. Panina, K. Bushida, M. Noda, T. Uchiyama, "Sensitive and Quick Response Micro Magnetic Sensor Utilizing Magneto-Impedance in Co-rich Amorphous Wires", 1995, *IEEE Trans. on Magnetics*, Vol.31, No2, 1266-1275

[3] M. Vazquez and A. Hernando, "A soft magnetic wire for sensor application", *J. Phys. D: Appl. Phys.*, vol. 29, p. 939, 1996.

[4] K. Mohri, T.Uchiyama, L.V. Panina, "Recent advances of micro magnetic sensors and sensing application", *Sensors and Actuators A*, vol. 59 , p. 1, 1997

[5] K. Mohri, T.Uchiyama, L. P Shen, CM Cai, L.V. Panina, "Sensitive micro magnetic sensor family utilizing magneto-impedance (MI) and stress-impedance (SI) effects for intelligent measurements and controls", *Sensors and Actuators A*, vol.91, p.85, 2001

[6] Y. Honkura, M. Yamamoto, Y. Kohtani, K. Mohri, "Mass produced amorphous wire type MI sensor", IEEE Trans.Magn., 2002 (in press).

[7] T. Kitoh, K. Mohri, T. Uchiyama, *IEEE Trans. Magn.* **31** (1995) 3137

[8] D. P. Makhnovskiy, L. V. Panina, and D. J. Mapps, "Asymmetrical magneto-impedance in as-cast CoFeSiB amorphous wires due to ac bias", *Appl. Phys. Letters*, vol. 77, p. 121 2000.

[9] L. V. Panina, D. P. Makhnovskiy, D. J. Mapps, K. Mohri, and P. I. Nikitin, "Effect of frequency and dc current on ac-biased asymmetrical magneto-impedance in wires", *Materials Science Forum*, vol. 373/376, p. 741, 2001

[10] D. P. Makhnovskiy, L. V. Panina, and D. J. Mapps, "Field-dependent surface impedance tensor in amorphous wires with two types of magnetic anisotropy: helical and circumferential", *Phys. Rev. B*, vol. 63, p. 144424, 2001.

[11] D. P. Makhnovskiy, L. V. Panina, and D. J. Mapps, "Measurement of field-dependent surface impedance tensor in amorphous wires with circumferential anisotropy", *J. Appl. Phys.*, vol. 87, p. 4804, 2000.

[12] N. Kawajiri, M. Nakabayashi, C. M. Cai, K. Mohri, and T. Uchiyama, "Highly stable micro sensor using C-MOS IC multivibrator with synchronous rectification", *IEEE Trans. Magn.*, vol. 35, p. 3667, 1999.

ELSEVIER SCIENCE

Very high stress sensitivity of magneto-impedance in CoMnSiB amorphous wires at the UHF frequency band.

S. I. Sandacci, R. Craig, D. P. Makhnovskiy, and L. V. Panina

School of Computing, Communications and Electronics, University of Plymouth, Drake Circus, Plymouth, PL4 8AA, United Kingdom

Elsevier use only: Received date here; revised date here; accepted date here

Abstract

Co-rich amorphous magnetic microwires exhibit a very large change in high frequency impedance, when subjected to a dc axial magnetic field H_{ex} [1]. This magneto-impedance (MI) effect originates from the skin effect in conjunction with the transverse magnetisation processes, which is very sensitive to H_{ex} for certain magnetic structures. Applying a stress or a torque may also cause a change in the wire transverse magnetisation producing very large variations in impedance [2]. Here the effect of applied tensile stress on MI in glass-coated $Co_{68.5}Mn_{6.5}Si_{10}B_{15}$ amorphous wires is investigated at the UHF frequency band. In the presence of a dc bias magnetic field near the anisotropy field strength, the impedance shows very large changes when the wire is subjected to a tensile stress of 100% per 180 MPa at 500 MHz and 60% per 180 MPa at 2.5 GHz, respectively. This new effect can be used for creating wireless stress/pressure sensors and stress-tunable microwave media for use in structural health monitoring and defect detection applications.

Keywords: Stress-tuneable composites, Amorphous microwires, Magneto-impedance, Stress-impedance, Structural health monitoring.
PACS: 75.30.Cr; 75.30.Gw; 75.40.Gb; 75.50.Cc; 75.50.Kj.

1. Introduction

For the last 10 years Co-based amorphous microwires having small negative magnetostriction have been intensively investigated because of their importance in low-magnetic field sensing applications. Amorphous magnetic wires having Co-alloy compositions exhibit a very large change in the complex-valued impedance, when subjected to a high frequency current and dc magnetic field [1-3]. This effect is known as the *magneto-impedance (MI) effect.* It is caused by the dependence of the high frequency current distribution in the wire on its magnetic properties, in particular, equilibrium magnetic structure and dynamic transverse magnetisation (with respect to the current flow).

Co-based amorphous wires have a circumferential anisotropy due to its coupling between the negative magnetostriction and residual stress. Applying a stress or a torque causes a change in the wire magnetic structure and consequently very large variations in impedance. This effect is commonly called *stress-impedance (SI).* It has been reported that CoSiB amorphous wires with a helical anisotropy have a strain gauge factor of 1200–2000 at 1–10 MHz and can be used as highly sensitive stress sensors [12, 13]. The helical magnetic structure was induced by physically twisting a wire that initially had circumferential magnetisation.

This paper investigates the effect of applied tensile stress on the magneto-impedance of glass-coated $Co_{68.5}Mn_{6.5}Si_{10}B_{15}$ amorphous wires over the microwave frequency range, demonstrating relative changes in

impedance of about 60% for an applied stress of approximately 180 MPa at frequencies as high as 2–3 GHz.

This effect could be of considerable interest for remote stress monitoring applications using smart composite materials filled with ferromagnetic wires. Here, the effective permittivity in a narrow UHF frequency band depends on the stress or strain applied to the composite media.

2. Experimental results

The experimental results are provided for $Co_{68.5}Mn_{6.5}Si_{10}B_{15}$ amorphous glass-coated wires having the total diameter of 14.5 μm and the metallic core diameter of 10.2 μm. The wire diameter is chosen such that it would be suitable for microwave applications. For this alloy composition, $\lambda_s \approx -2 \cdot 10^{-7}$ [13]. For dc magnetisation measurements, the wire length was 6 cm and the stress was applied by hanging a load of *1–10 g* at the wire end. The longitudinal magnetisation curves under the effect of stress are shown in Fig. 1. The original curve for an unloaded wire shows a steep hysteresis but with a rather small remanence-to-saturation value $M_r/M_s=0.2$, which corresponds to almost circumferential anisotropy with a small helical angle $\alpha \approx 12^0$. Applying the tensile stress strengthens the circumferential anisotropy: the magnetisation curve becomes almost linear with $M_r/M_s \approx 0$, the hysteresis disappears and the effective anisotropy field H_K increases. For the unloaded wire H_K =2.6 *Oe*, and it becomes 9 Oe, when a load of 8.5 g is applied.

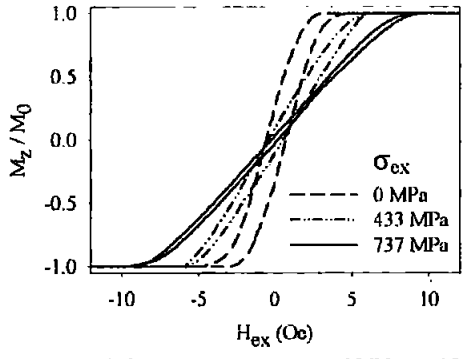

Fig. 1. Axial dc magnetization curves $M_z/M_0=\cos(\theta)$ with the applied stress as a parameter. The wire length was 6 cm and the load was attached at the wire free end. In this case the tension created by 1 g is estimated to equal 65 MPa.

The complex-valued impedance is found by measuring S_{11}-parameter by means of the Hewlett-Packard 8753E Vector Network Analyzer (VNA). When dealing with measurements at UHF frequency band, special care must be taken for the correct results interpretation. At frequencies higher then 500 MHz the impedance match becomes critical since half wavelength become relatively small (<30 cm). We designed a special microstrip cell to minimise the post calibration mismatches (Fig. 2). Rather than attempting to quantify the contribution of the error in the wire impedance [14], our approach is to minimise its effect. The microstrip portion connected to VNA is pre-calibrated with a standard 50Ω load, which is then removed (Load "1" in Fig. 2). During the measurements, the microstrip cell with the soldered up sample is terminated with 50Ω load (Load "2"). This calibration of the microstrip line with a length of 3.5 cm holding the soldered up wire of 1.4 cm ensures reliable impedance measurements up to frequencies of about 3 GHz. The wire is loaded with a weight in its middle (in this case 1 g load corresponds to a tension estimated to be 320 MPa, see Caption for Fig. 2). The cell with the sample is placed into the Helmholtz coil producing a dc magnetic field.

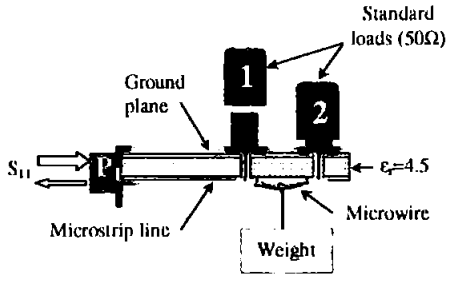

Fig. 2. Sketch of the microstrip cell with a wire sample for impedance measurement. The wire is loaded at the middle with a weight P, which imposes a stress of $P/\pi a^2 \sin(\psi)$, where $\psi \approx 6^0$ is the angle between the bent wire and the horizontal direction.

Figure 3 shows plots of impedance vs. applied tensile stress for three frequencies 500 MHz 1.5 GHz and 2.5 GHz. If no field is applied, the stress effect is small being about 12% at 500 MHz and almost not noticeable at GHz frequencies. Since a negative magnetostriction wire has a nearly circumferential anisotropy (if no large frozen-in torsion exists), the applied tensile stress alone will not cause the change in M_0 direction, and as a result, will not produce noticeable changes in the impedance at high frequencies.

Applying the field H_{ex} of the order of the anisotropy field saturates the wire in the axial direction. The tensile stress which enlarges the circumferential anisotropy in the case of negative magnetostriction acts in opposite way and rotates the magnetisation back to the circular direction. The highest stress sensitivity is obtained for $H_{ex} \approx H_K$, which is sufficient to saturate the wire.

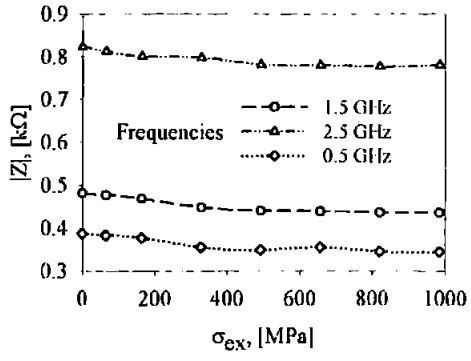

Fig. 3. Experimental plots of impedance vs. applied stress. The load of 1 g applied at the middle of the wire is estimated to impose a stress of 320 MPa.

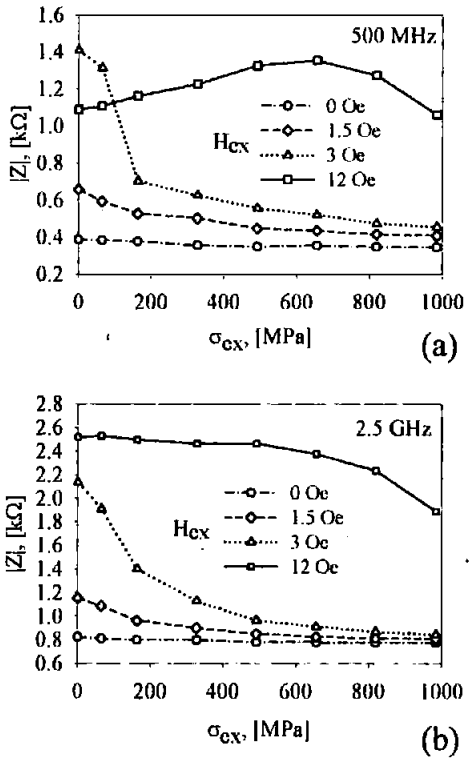

Fig. 4. Experimental plots of impedance vs. applied stress with the external magnetic field as a parameter at 500 MHz in (a) and 2.5 GHz in (b).

Further increase in H_{ex} is unnecessary since a larger stress will be required to return the magnetisation back. In the presence of H_{ex}, the wire impedance shows large changes in response to the application of the tensile stress (Fig. 4). The highest stress sensitivity of ***100%*** per ***180 MPa*** at ***500 MHz*** and ***60%*** per ***180 MPa*** at ***2.5 GHz***, respectively obtained for H_{ex}=***3 Oe*** that is about the same value as the anisotropy field for the unloaded wire.

3. Theoretical approach

The microwave MI/SI phenomenon can be explained in terms of classical skin effect in magnetic conductors with a large effective permeability and its strong dependence on the magnitude of external dc magnetic field [4]. Because the skin depth as well as the characteristic correlation length in a magnetic structure (e.g., domain width) in soft magnetic materials is much larger than the inter-atomic distances, the classical electrodynamics of continuous media can be used for the description of MI/SI effects. The calculation of the complex-valued impedance $\hat{\varsigma}$ is based on the solution of the Maxwell's equations for the fields e and h together with the equation of motion for the magnetisation vector M .

3.1. Equation of motion for the magnetisation vector

In amorphous ferromagnetic alloys, the preferable magnetisation direction is set by the combined effect of the shape anisotropy and the magnetoelastic anisotropy arising from the coupling between magnetostriction λ and internal stresses σ. The sign and value of λ depend on the alloy composition, whereas σ is induced during the fabrication process. Negative magnetostriction, which is proven to be essential for the MI wire element, is typical for Co-based alloys having relatively small λ, of about $-3\cdot10^{-6}$ that can be reduced to -10^{-7} by small additions of Fe or Mn. In the case of amorphous wires produced by rapid solidification technique, the internal stresses (axial, radial, and azimuth) are originated by a strong thermal gradient existing during the fabrication process. This results in a substantial stress distribution over radius and a complicated core and sheet domain structure. The stress distribution is more uniform in glass-coated wires where the drawing process induces an additional large tensile stress. Then, there is a predominant easy anisotropy direction almost in the entire wire: axial for $\lambda>0$ and circular for $\lambda<0$. The latter has a particular interest for the MI/SI effect since the equilibrium magnetic structure can be sensitively monitored by applying such external factors as an axial magnetic field, stress or torque.

In amorphous ferromagnetic materials where magnetostrictive processes play the main role in establishing the magnetic anisotropy, the applied stress may influence the magnetisation reversal substantially. The

stress effect on the rotational hysteresis of an amorphous wire with a negative magnetostriction has two types of internal (or applied) stresses: an axial tension and a twist.

The former has intensity σ_1 and the latter represents the combination of tension and compression σ_{2+} and σ_{2-} with equal intensity ($\sigma_{2+} = \sigma_{2-} = \sigma_2$) at 90^0 to each other and at 45^0 to the wire axis, as shown in Fig. 2.5.

The combined action of all the stresses results in the effective magnetostrictive energy of the form:

Further we assume that in general the internal stress in a wire consists of an axial tension (σ_1) and a torsion which is a combination of a tension and compression with equal intensity σ_2 at 90^0 to each other and at 45^0 to the wire axis. Then, for $\lambda < 0$, the easy anisotropy is directed in a helical way having an angle $\alpha < 45^0$ with respect to the circumference. The static magnetisation direction can be changed by the application of the external axial magnetic field H_{ex} and tensile stress σ_{ex}. The stable direction of $\mathbf{M}_0$ is found by minimising the energy U

For a large stress effect on MI, the ability of σ_{ex} to change the direction of $\mathbf{M}_0$ is needed. In the case $H_{ex} = 0$, this is possible if the anisotropy axis has a helical angle nearly equal to 45^0, which is achieved by a proper annealing (current annealing or annealing under torsion) to establish a substantial frozen-in torsion ($\sigma_2 >> \sigma_1$, $\alpha \approx 45^0$ at $\sigma_{ex} = 0$). Another possibility of the directional change in the magnetisation under the external stress is to use the axial field bias. In the presence of H_{ex} the magnetisation rotates towards the wire axis whereas the application of σ_{ex} strengthens the circumferential anisotropy (for $\lambda < 0$) and hence acts in the opposite way. Then, the magnetisation rotates back to the circular direction. In this paper, we utilise the assistance of H_{ex} to realise very large impedance change when the external tensile stress is applied.

3.2. Microwave surface impedance

The voltage response measured across a ferromagnetic wire (z-axis) carrying a high frequency current $i = i_0 \exp(-j\omega t)$ is expressed in terms of the longitudinal component ς_{zz} of the surface impedance tensor ($\varsigma_{zz} = e_z / h_\varphi$, where e_z and h_φ are the axial electric and circular magnetic fields at the wire surface)

Here l is the wire length, a is the wire radius, and c is the velocity of light. Strictly speaking, equation (1) is valid for a wire with a uniform magnetisation but can be applied for a multidomain wire provided that ς_{zz} is averaged over domains and the domain wall displacements are damped. In the case of a strong skin effect, the following equation is held[1]

Here ρ is resistivity, $\delta_0 = c(\rho / 2\pi\omega)^{1/2}$ is a non-magnetic skin depth, μ is the circular permeability describing the magnetisation precession around the equilibrium magnetisation $\mathbf{M}_0$ having an angle θ with the wire axis. Equation (2) demonstrates that the longitudinal surface impedance depends on both the dynamic permeability μ and the static magnetisation angle θ. The parameter μ has a very broad dispersion region. At high frequencies (higher than the frequency of the ferromagnetic resonance) μ changes very little with both the external axial magnetic field H_{ex} and anisotropy field H_K, although preserving its relatively high values ($|\mu| \approx 10$ at GHz range for Co-based wires with $H_K = 2-5$ Oe). In this case, the dependence of the impedance on magnetic properties is entirely determined by the static magnetisation angle θ.

4. Conclusion

The effect of stress on microwave MI in amorphous fine wires is proposed to utilise for the creation of a new stress-tuneable composite medium for remote stress monitoring by microwave spectroscopy technology. The composite material consists of the short wire inclusions (exhibiting stress-impedance effect) embedded into the dielectric matrix with the permittivity ε. The wire inclusions behave as the electric dipole "scatterers". This dipole response of the composite system can be characterised by some effective permittivity ε_{eff}. Then, ε_{eff} can have a resonance or relaxation dispersion (depending on the wire impedance) seen near the antenna resonance for an individual wire. For a moderate skin-effect ($\delta \approx a$) the dispersion characteristics of ε_{eff} depend on the longitudinal surface impedance ς_{zz}. Therefore, in composite containing ferromagnetic wires exhibiting MI effect the effective permittivity may depend on the external magnetic field and stress/strain via the corresponding dependence of ς_{zz}. The theoretical approach for such field-tunable composite materials was developed in our previous work.[10] The model is based on solving the scattering problem for a ferromagnetic wire with the impedance boundary conditions to find the current (and electric charge) distribution along the wire as a response to the incident electromagnetic wave. In the frequency band with the characteristic antenna resonance frequency, the induced dipole moment in a wire will depend on the surface impedance and hence on the wire magnetic properties which can be modified sensitively by H_{ex} or σ_{ex}. Figure 5 shows the frequency plots for the effective permittivity with H_{ex} and σ_{ex} as parameters, demonstrating very large change (almost twice) in the imaginary part of ε_{eff} at the antenna resonance. The real part also undergoes considerable transformations at slightly shifted frequencies. These large changes in ε_{eff} can be detected by microwave scanning techniques, in particular, microwave loss spectroscopy. The detailed analysis of stress-tuneable composite material will be published elsewhere.

References:

[1]D. P. Makhnovskiy, L. V. Panina, and D. J. Mapps, Phys. Rev. B 63, 144424 (2001).
[2]M. Vazquez, J. Magn. Magn. Mater. 226, 693 (2001).
[3]M Knobel, J. Magn. Magn. Mater. 242-245, 33 (2002).
[4]V. Zhukova, A. Chizhik, A. Zhukov, A. Torcunov, V. Larin, and J. Gonzalez, IEEE Trans. Magn. 38, 3090 (2002).
[5]M. Dominguez, J. M. Garcia-Beneytez, M. Vazquez, S. E. Lofland, and S. M. Bhagat, J. Magn. Magn. Mater. 249, 117 (2002).
[6]S. I. Sandacci, D. P. Makhnovskiy, and L. V. Panina, J. Magn. Magn. Mater., accepted (2004).
[7]K. Mohri, T. Uchiyama, L. P. Shen, C. M. Cai, L. V. Panina, Y. Honkura, and M. Yamamoto, IEEE Trans. Magn. 38, 3063 (2002).
[8]H. Hauser, R. Steindl, C. Hausleitner, J. Nicolics, and A. Pol, Sens. and Mater. 13, 25 (2001).
[9]O. Reynet, A.-L. Adent, S. Deprot, O. Acher, and M. Latrach, Phys. Rev. B 66, 94412 (2002).
[10]D. P. Makhnovskiy and L. V. Panina, J. Appl. Phys. 93, 4120 (2003).
[11]L. V. Panina, D. P. Makhnovskiy, and K. Mohri, J. Magn. Magn. Mater., accepted, (2004).
[12]L. P. Shen, T. Uchiyama, K. Mohri, and K. Bushida, IEEE Trans. Magn. 33, 3355 (1997).
[13]A. F. Cobeno, A. Zhukov, J. M. Blanco, V. Larin, and J. Gonzalez, Sens. and Actual. A 91, 95 (2001).